Neutrino treatment in multidimensional astrophysical simulations: a new spectral scheme

Inauguraldissertation

zur
Erlangung der Würde eines Doktors der Philosophie
vorgelegt der
philosophisch-naturwissenschaftlichen Fakultät
der Universität Basel
von

Albino Perego

aus Italien

Basel, 2014

Genehmigt von der philosophisch-naturwissenschaftlichen Fakultät

auf Antrag von

Prof. Dr. Friedrich-Karl Thielemann, PD Dr. Matthias Liebendörfer und Prof. Dr. Stephan Rosswog.

Basel, den 11. Dezember 2012

Prof. Dr. Jörg Schibler

Namensnennung-Keine kommerzielle Nutzung-Keine Bearbeitung 3.0 Schweiz
(CC BY-NC-ND 3.0 CH)

Sie dürfen: **Teilen** — den Inhalt kopieren, verbreiten und zugänglich machen

Unter den folgenden Bedingungen:

Namensnennung — Sie müssen den Namen des Autors/Rechteinhabers in der von ihm festgelegten Weise nennen.

Keine kommerzielle Nutzung — Sie dürfen diesen Inhalt nicht für kommerzielle Zwecke nutzen.

Keine Bearbeitung erlaubt — Sie dürfen diesen Inhalt nicht bearbeiten, abwandeln oder in anderer Weise verändern.

Wobei gilt:

- **Verzichtserklärung —** Jede der vorgenannten Bedingungen kann **aufgehoben** werden, sofern Sie die ausdrückliche Einwilligung des Rechteinhabers dazu erhalten.
- **Public Domain (gemeinfreie oder nicht-schützbare Inhalte) —** Soweit das Werk, der Inhalt oder irgendein Teil davon zur Public Domain der jeweiligen Rechtsordnung gehört, wird dieser Status von der Lizenz in keiner Weise berührt.
- **Sonstige Rechte —** Die Lizenz hat keinerlei Einfluss auf die folgenden Rechte:
    - Die Rechte, die jedermann wegen der Schranken des Urheberrechts oder aufgrund gesetzlicher Erlaubnisse zustehen (in einigen Ländern als grundsätzliche Doktrin des **fair use** bekannt);
    - Die **Persönlichkeitsrechte** des Urhebers;
    - Rechte anderer Personen, entweder am Lizenzgegenstand selber oder bezüglich seiner Verwendung, zum Beispiel für **Werbung** oder Privatsphärenschutz.
- **Hinweis —** Bei jeder Nutzung oder Verbreitung müssen Sie anderen alle Lizenzbedingungen mitteilen, die für diesen Inhalt gelten. Am einfachsten ist es, an entsprechender Stelle einen Link auf diese Seite einzubinden.

Quelle: http://creativecommons.org/licenses/by-nc-nd/3.0/ch/ Datum: 12.11.2013

Abstract

Neutrinos play a central role in modern physics and astrophysics. Their extremely weak interaction rate with baryons and other leptons makes their detection on the Earth difficult and challenging. At the same time, it implies that the emission and the absorption of neutrinos are the dominant radiative processes in hot and dense astrophysical environment (such as core-collapse supernovae and the merger of binary compact objects), where photons are completely trapped and diffuse out on much longer timescales. The implementation of neutrino-transport schemes in hydrodynamics simulations is a subtle problem, especially in multi-dimensions, where an accurate solution of the transport equations can be, computationally speaking, extremely expensive.

In this work, we have developed a new approximate neutrino-radiation treatment, the Advanced Spectral Leakage (ASL) scheme; after having tested and calibrated it, we have shown a variety of applications, both in the context of core-collapse supernovae and of binary neutron star mergers.

The ASL scheme was derived from previous grey leakage schemes, and it retains the conceptual and the computational simplicity that characterize leakage schemes. Different from its predecessors, the new treatment is spectral (i.e. it retains information on the particle energy), and it includes the modeling of a neutrino trapped component in optically thick conditions and of neutrino absorption terms in optically thin conditions. The scheme has been tested against detailed neutrino-transport in the context of spherically symmetric models of collapsing stellar cores. We have shown that it is able to capture, with reasonable accuracy, the main expected features during the collapse phase, at core bounce and in the first hundreds of millisecond after bounce, both for the fundamental hydrodynamics and neutrino quantities.

The optical depth is a central quantity in leakages schemes. We have also developed a new algorithm to compute the optical depth in multi-dimensional domains, without any symmetry constraint. We called it Multidimensional Optical Depth Algorithm (MODA).

The major application of the ASL scheme in this work has been the study of the development of a neutrino-driven wind from the hot and dense disc resulting from the merger of two neutron star. This process has been studied for the first time in 3D Cartesian simulations, performed with the FISH code. The intense (10^{53} erg/s) neutrino emission coming from the (probably, unstable) hyper massive neutron star and from the disc itself is partially re-absorbed by low density ($< 10^{10}$g/cm^3), neutron-rich ($Y_\mathrm{e} < 0.1$) matter inside disc. This energy deposition drives a baryonic wind, mainly perpendicular to the disc plane, on a timescale of ~ 50 ms. Neutrino-matter interactions in the wind modify significantly the electron fraction of matter: the resulting distribution shows a broad range of Y_e, from 0.2 to 0.4, with larger values along the polar directions than along the equatorial one. At ~ 100 ms after the merger, the amount of ejecta is of the order of 2% the initial mass of the disc, thus it represents a significant channel for mass ejection from binary neutron star mergers. The broad range in Y_e represents an interesting signature in the context of r-process nucleosynthesis.

Furthermore, we have shown other applications of the ASL scheme. First, we have implemented it in the MHD version of the FISH code to study the electron fraction in jets resulting from magneto-rotationally driven supernovae. In the case of strong and fast jet formation (~ 30 ms after core bounce), the electron fraction in the ejecta is low enough ($Y_\mathrm{e} < 0.3$) to produce robust r-process nucleosynthesis.

Second, we have implemented the ASL scheme inside the SPH code SPHYNCS, to perform core-collapse simulations. The results we have obtained are compatible with what we have obtained with grid codes. This model shows that the scheme is of easy implementation also in Lagrangian, multidimensional SPH codes.
Finally, we have designed a new prescription to explode artificially spherically symmetric core-collapse models, using the IDSA scheme for electron neutrinos and the ASL scheme for μ and τ neutrinos. The extra energy deposition required to trigger the explosion is obtained by the parametrized absorption of heavy flavour neutrinos inside the gain region. The model has shown promising results and it is well suited to study the explosive nucleosynthesis for broad stellar progenitor samples, including detailed neutrino treatment.

Contents

Acknowledgements

It is a great pleasure for me to acknowledge here the persons that, in various form and in different ways, provided me the necessary support during my PhD in Basel.

- Prof. Dr. M. Liebendörfer (University of Basel), as my PhD advisor. I really appreciate his expertises and and his kindness, as a model of human and scientific integrity.
- Prof. Dr. F. Thielemann (University of Basel), as my PhD co-advisor, for his extraordinary capability of providing the best working environment for young researchers and his never-ending enthusiasm.
- Prof. Dr. S. Rosswog (University of Stockholm), as my PhD co-advisor, for his competences and for his capacity to transmit energy and ideas.
- Dr. C. Winteler and Dr. R. Käppeli, as my historical colleagues. Thanks for the nice and enjoyable time spent together, and for the mutual help.
- Dr. Rubén Cabezón and Prof. Dr. A. Arcones, as always happy and always available scientific guides; thanks to Rubén also for reading some important parts of the thesis.
- Dr. M. Pignatari, Dr. A. Carrera and Chiara Biscaro, as Italian colleagues and friends, who are always able to make me feel at home. Special thanks to Chiara for the Monday cakes.
- Dr. M. Hempel, Dr. N. Nishimura, Dr. T. Rauscher and Dr. C. Fröhlich as senior scientists in the group and scientific reference points.
- Dr. S. Scheidegger, Dr. U. Frischknecht, Dr. T. Fischer, Dr. C. von Arx, Dr. S. C. Whitehouse and Dr. N. Vasset, as former colleagues, for the nice time spent together.
- M. Heichler, M. Frensel, K. Ebinger, as my new office colleagues. Thanks for your patience with me (and my poor German).
- Prof. Dr. C. Pethick, Prof. Dr. A. Schwenk and E. Gafton, for the fruitful collaborations we have started.
- U. Battino, S. Fehlmann, A. Sarangi, D. Gobrecht, as nice PhD colleagues in the group in Basel.
- The secretaries and the administrative staff at the Department of Physics, for their efficiency and kindness.
- All the friends I met in Basel.
- My wife Maddalena, for her constant, lovely support and help (some of the pictures in the thesis are from her).
- My family, for their solid and close support, despite the distance from home.

Introduction

The major topic of my PhD thesis was the study of neutrino emission from astrophysical systems. In many astrophysical scenarios, neutrinos do not play an important role or, if they do, their very small interaction cross sections allow to model them simply as a cooling source, assuming that all produced neutrinos are emitted from the system and leave it without further interactions. In the next chapter, I will introduce two very relevant astrophysical situations where the previous argument is not true and where neutrinos have to be modeled as a radiation field, strongly coupled with the surrounding fluid and its dynamics: Core Collapse Supernovae and Neutron star Mergers. These systems represent interesting scenarios, due to the large variability of scales, physical phenomena and interactions which characterize them. They both are among the most energetic and violent events in the Universe, releasing on timescales smaller than one second, an amount of energy comparable to the rest mass energy of ~ 0.1 Solar masses (hereafter $M_\odot$); and most of it in form of neutrinos. They both involve Neutron stars, which represent one of the most extreme conditions under which large amount of matter can be found nowadays in the Universe. A correct and complete model of these systems requires the inclusion of all fundamental interactions, as we presently know them: the strong force and the electromagnetic interaction for the equation of state of matter at high density and temperature; the dynamics of macroscopic intense magnetic fields, which can affect the motion and the properties of the plasma; the weak interaction to model neutrinos and electrons, as well as the fundamental ratio between protons and neutrons. And, finally, the gravitational interaction, which is the true engine driving the events towards their inescapable fate. Curiously, Core Collapse Supernovae and Neutron star Mergers represent two (possible) extremes in the life of a Neutron star. However, as it happens often in Nature, even the catastrophic death of a celestial body can be the origin of new ones. Even more, the conditions in which matter is ejected from those systems allow the synthesis of new elements and their dispersion in the interstellar medium. These elements are the necessary ingredients to form, for example, planets and, ultimately, life.

Due to the large complexity of the problem, numerical simulations have been extensively developed during the last decades to model neutrino radiation hydrodynamics. The first steps in this direction were modelled using simple grey (i.e., non-spectral) leakage schemes, whose aim was to estimate the emission rates (both for particles and energy) from each point of the system (see, for example, [33]). Then, more demanding schemes were developed, and in particular the Multi Group Flux Limited Diffusion (MGFLD) [80], which tackles the radiative transport problem by solving the relevant transport equation in the two relevant limiting cases, i.e. the diffusive limit and the free streaming limit. This scheme allowed the treatment of neutrino interactions with a high

degree of accuracy (see, for example, [12] and [99]). During the 90s', due to the increase in computational power, two different paths were explored: on one side, the solution of the full Boltzmann equation became possible in spherically symmetric systems (see. for example, [99] and [86]), well designed for CCSN models. On the other side, the modeling multidimensional systems (like, for example, the merger of compact objects) became feasible with a significant resolution, and there neutrinos were taken into account again with grey leakage schemes, which benefited from the knowledge that emerged from more accurate one dimensional transport problems (see, for example, [143, 137]). Up to now, these grey schemes have been implemented and extensively applied in Core Collapse Supernova models (see, for example, [114, 115]) and in Neutron star Merger simulations (see, for example, [139]). Even more, the last years have seen the development of different techniques to obtain detailed neutrino treatment also in two and three dimensions. These were obtained using, for example, ray-by-ray schemes (where a one-dimensional problem is solved along different rays covering the whole solid angle, see for example [16, 13]) or S_n schemes (see, for example, [116]). Their major drawback is that, when moving from one dimensional problems to multidimensions, the computational cost of the calculation increases dramatically. This latter aspect conflicts with the large variability of possible initial conditions, provided by progenitor masses, metallicity, rotation and magnetic fields in the CCSN case, and by NS masses, spins and orbital parameters in the NS merger scenario. Overall, large uncertainties still characterize essential input physics, like the nuclear equation of state, the neutrino physics and the modeling of strong gravitational fields. The `ELEPHANT` code (see, for example, [174]), developed by Matthias Liebendörfer and Stuart C. Whitehouse at the University of Basel, represents already a significant improvement in this direction, because it guarantees an accurate spectral treatment of neutrino transport, coupled with high resolution hydrodynamics, at a much lower computational cost in three dimensional core collapse supernova simulations [83].

The main objective of this thesis is to develop and test a new leakage scheme, which tends to keep a relatively low computational cost, avoiding the solution of the expensive diffusion equation. The price of this simplification is a reduced accuracy; but, compared with other previous leakage schemes, we wanted 1) to improve significantly its reliability and completeness; and 2) to design a scheme which can be easily exported in different dimensions and in different codes. In this sense, this scheme allows us to efficiently explore wide parameter space for several astrophysical scenarios where neutrinos play a role, and provide useful information to perform detailed studies with more accurate neutrino transport schemes.

The following thesis is essentially oriented towards the exposition of the new scheme, its validation and its very first applications.

In Chapter 1, we briefly present the astrophysical scenarios that motivated our work and where the new scheme will be applied. Together with the physical description and explanation of the knowledge we presently have, we will summarize the major aspects of the numerical investigations that have been performed up to now.

Chapter 2 is devoted to explain in detail the new scheme (ASL), starting from the exposition of its parent scheme, its applications and its extension to the new algorithm. In the second part of the chapter, the scheme is tuned and validated via direct comparison with solutions of the Boltzmann equation in spherically symmetric Core Collapse Supernova.

In the new scheme (as well as in previous leakage schemes), a special role is reserved to neutrino optical depth. In Chapter 3, we present a new algorithm (MODA) to calculate the optical depth in multidimensional hydrodynamical simulations, without any assumption about the symmetry of the system.

In Chapter 4 we will present the status of the implementation of the ASL scheme in three dimensional simulations modeling the aftermath of Neutron star Mergers with the grid code `FISH`, as it is at the moment. This project benefits also of the collaboration of Prof. Stephan Rosswog (University of Stockholm).

Finally, in Chapter 5 other applications of the new scheme are explained. They are 1) the implementation of the ASL scheme in models of magnetically-driven Core Collapse Supernovae, performed with the grid code `FISH`. 2) The implementation of the scheme in Core Collapse models performed with the SPH code `SPHYNX`. 3) The development of a new way to trigger artificially explosions in spherically symmetric supernova models; this new method uses the deposition of a fraction of the luminosities associated with mu and tau neutrinos, treated with the ASL scheme.

Chapter 1

Astrophysical background and motivations

Neutrinos play a central role in contemporary physics. Already their theoretical prediction by Wolfgang Pauli in 1930 offered an enlightening example of how modern physics proceeds and how powerful the simple axioms (that we call conservation laws) are.
The neutrino was postulated as an electrically neutral particle, produced, but not detected, during a beta decay reaction. The reason for such an extreme hypothesis was that, studing the decay of radioactive nuclei, the energy spectrum of the emitted electron was not the one expected from the kinematics of a two body decay problem. For example, for a two body decay such as

$$(A, Z) \rightarrow (A, Z + 1) + e^{-}, \tag{1.1}$$

assuming energy and linear momentum conservation, the electron energy in the center of mass frame should be

$$E_{e^-} = \left(\frac{M^2_{(A,Z)} - M^2_{(A,Z+1)} + m^2_{e^-}}{2M_{(A,Z)}} \right) c^2. \tag{1.2}$$

Instead E_{e^-} showed a continuum spectrum, ranging from 0 to E_{e^-}, as shown in Figure 1.2. Such an unexpected behavior could have been explained with two opposite hypothesis: the first one (suggested, among the others, by Niels Bohr) assumes the possibility for microphysical reactions to violate conservation principles (which, then, have only a statistical meaning); the second one assumes the presence of an undetected particle, which could take away the electron's missing energy . In this case, the detected energy spectrum could have been easily referred to a reaction of this kind:

$$(A, Z) \rightarrow (A, Z + 1) + e^{-} + X \tag{1.3}$$

where X is the unknown particle. Due to charge conservation, the new particle should have been neutral and Pauli proposed the name *neutron*. This idea was accepted with skepticism and, when James Chadwick in 1932 discovered a new particle, neutral and (roughly) as massive as the proton, he "stole" the name and he called it neutron. But in the following year, Enrico Fermi formulated his theory of the beta decay, which incorporates Pauli's particle and proved so brilliantly successful that Pauli's idea was

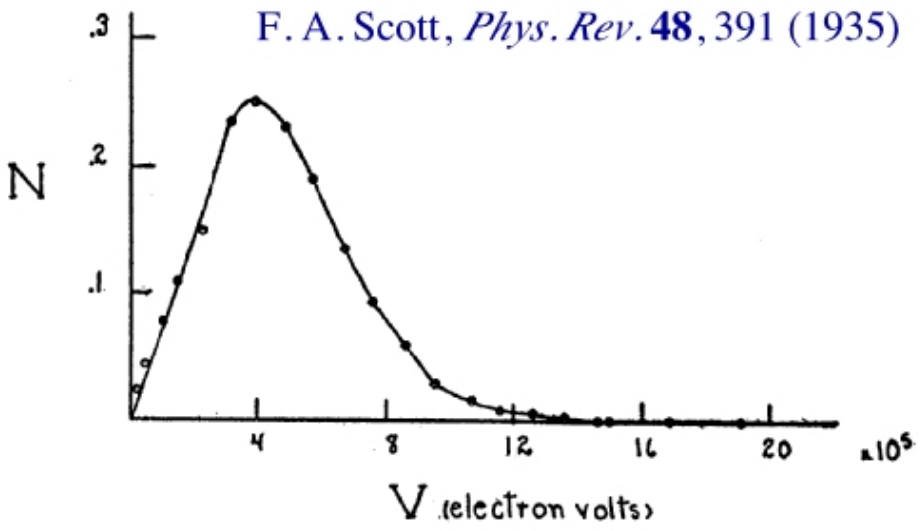

FIG. 5. Energy distribution curve of the beta-rays.

Figure 1.1: Energy spectrum of the electrons emitted in the beta decay of Radium, from [148].

taken more and more seriously. Fermi re-named the still mysterious particle *neutrino*, ν. The fact that the electron energy in the β decay was (experimentally speaking) equal to the maximum kinematically allowed energy suggested that the new particle was extremely light, at most with no rest mass, like the photon. As all the other particles, it admits an antiparticle, which is called antineutrino, $\bar{\nu}$. Actually, with the modern convention, the particle X in reaction 1.3 is an electron antineutrino. Other decays, studied during the 1940s', seemed also to point to the mysterious Pauli particles. Among the others, the decay of the muon was compatible with the emission of two neutral, very light (even massless) particles.
The first detection of the new particle happened only several years later, in 1956, when Clyde Cowan, Frederick Reines and collaborators detected antineutrinos coming from an intense source (a nuclear reactor) and absorbed by a proton:

$$\bar{\nu} + p \rightarrow n + e^{+}. \tag{1.4}$$

An interesting question at that time was if neutrinos are the same as antineutrinos. From the experimental result of Cowan and Reines, it was clear that the cross reaction

$$\nu + n \rightarrow p + e^{-} \tag{1.5}$$

should happen. If neutrino and antineutrino were the same particle, an analogous reaction with antineutrino should occur:

$$\bar{\nu} + n \rightarrow p + e^{-}. \tag{1.6}$$

But Davies found experimentally that this reaction does not occur, so neutrino and antineutrino are distincted particles.
In the next years (1962), a detailed study of the muon decay established that one of the particles emitted in that decay was not a neutrino nor an antineutrino, of the type

already observed. The puzzle was solved introducing different families of leptons: the electron and the positron, associated with *electron* neutrino and antineutrino, ν_e and $\bar{\nu}_e$; and the muon $\mu^{\pm}$, associated with the *muon* neutrino and antineutrino, ν_μ and $\bar{\nu}_\mu$. Finally, after the discovery of the heaviest lepton $\tau^{\pm}$ in 1975, missing energy and momentum in its decay led to the conclusion of the existence of a third neutrino family, ν_τ and $\bar{\nu}_\tau$. This indirect evidence was found in 2000, at Fermi Lab; due to it, tau neutrinos were the last detected particles in the context of the Standard Model (SM) theory of elementary particles.

According to the SM, neutrinos are massless fermions, with 1/2 spin, which can interact with quarks (and, consequently, baryons and mesons) and leptons via weak interaction. From a fundamental point of view, the weak interaction is described as a gauge theory, mediated by massive, spin 1 bosons; these bosons are the so called $W^{\pm}$ and Z particles. Due to their large masses (80.385 GeV for the charged $W^{\pm}$ and 91.1876 GeV for the neutral Z), the weak interaction has a very short interaction range at energies far below the bosons mass, and a small coupling constant. Typical neutrino cross section are of the order of

$$\sigma_0 \equiv \frac{4}{\pi}\left(\frac{\hbar}{m_e c}\right)^{-4}\left(\frac{G_F}{m_e c^2}\right)^2 = 1.76 \times 10^{-44}\,\mathrm{cm}^2. \tag{1.7}$$

For instance, nuclear cross sections are typically measured in barn ($10^{-24}\mathrm{cm}^2$); this simple comparison gives an idea of the weakness of the interaction and a measure of the elusiveness of those particles.

The clean picture representing neutrinos in the framework of the SM has been recently shaken by very interesting experimental results and theoretical ideas. The amount of neutrinos emitted from the Sun and detected on the Earth has always been affected by a systematic discrepancy between the predicted and the measured values: the detected flux is roughly one third of the one expected from detailed models of the Sun, which seem to describe our star very well. A possible solution for this problem is the possibility for neutrinos to oscillate from one flavor to another: the conversion of electron neutrinos in other flavor could explain the missing flux. The mathematical description of this oscillation mechanism was first suggested by Bruno Pontecorvo in 1957 and assumes that neutrinos have a mass (even if very small). The basic idea behind this mechanism is that the interaction eigenstates describing neutrinos emitted in weak processes, are not equal to the mass eigenstates, which are three and are the proper basis to describe the time evolution (i.e., the propagation) of the particle. Thus, a neutrino emitted as an electron neutrino ν_e (and the same holds for all types of neutrinos) is a superposition of the three possible mass eigenstates, and it has a certain probability to be detected as a ν_e or ν_μ or ν_τ during its propagation. These probability are oscillating functions; that is the reason why this phenomenon is call neutrino oscillations.

Nowadays neutrinos oscillations have been observed in several experiments and from different sources (mainly, solar neutrinos, atmospheric neutrinos and reactor - accelerator neutrinos); their combined results (will) allow to determine the free parameters in the model, and, hopefully, the values of the neutrino masses (actually, neutrino oscillations depend on the mass squared splitting). Apart from vacuum oscillation, neutrinos can oscillate between different flavours also when they travel in a medium, due to the Mikheyev-Smirnov-Wolfenstein effect; more recently, it has been postulated also the

possibility for neutrinos, when they form a trapped Fermi gas (like the one which forms in the core of exploding stars, as we will see later) to undergo collective neutrino oscillations.
In this work, we will consider neutrinos as they are in the SM (massless and without oscillations). The study of the impact of oscillations in astrophysical contexts is under fast development; nevertheless, we assume that this impact is small on the scale we are going to consider. A full treatment, which includes also oscillations, is necessary to predict neutrino observables.

Detection of neutrinos on Earth is very challenging, mainly due to their incredible low cross section. Being very rare events, the dimensions of the detectors, as well as their screeing properties and sensitivity, have highly improved in the last years. Now, all over the world, we are potentially able to detect every day a few neutrinos coming from nuclear reactors, from particle collisions in the atmosphere or from the space. But where do space neutrinos come from?

There are several places in the Universe where neutrinos are produced and emitted, typically in huge amounts. Actually, the whole Universe is filled by cosmological neutrinos, relic of a much hotter epoch. According to the Big Bang theory describing the evolution of our Universe, the Universe expanded from a very hot and dense primordial state. At a time around 10^{-2}s after the beginning of the expansion, the temperature was around $\sim 10^{11}$K, corresponding to $k_B T \sim 8.6\,\mathrm{MeV}$ in energy units. All the particles (and their antiparticles) whose masses are lower or almost equal to this thermal energy are continuously produced and annihilated. At this stage, the cosmological plasma is composed of nucleons, photons, electrons, positrons and all kind of neutrinos. The leptons are kept in thermal equilibrium by neutral current (i.e., mediated by the neutral Z boson) pair production reactions

$$e^+ + e^- \leftrightarrow \nu + \bar{\nu}, \tag{1.8}$$

active for all neutrino flavours. The interactions that keep baryons in equilibrium with leptons are the charged current (i.e., mediated by the charged $W^\pm$ bosons) weak interactions

$$p + e^- \leftrightarrow n + \nu_e \qquad n + e^+ \leftrightarrow p + \bar{\nu}_e \qquad n \leftrightarrow p + e^- + \bar{\nu}_e. \tag{1.9}$$

At a given temperature, the mass difference between neutron and protons sets their relative abundances, favoring more and more the conversion of neutrons into protons. When the plasma temperature drops to around and below 1 MeV, photons are no more energetic enough to produce electron-positron pairs, and electrons are no more energetic enough to overcome easily the mass difference between neutrons and protons. As a consequence, thermal neutrinos are no more produced and the pre-existing ones decouple from the plasma, now transparent for them. These neutrinos should be still present in the Universe in form of a very cold gas, permeating everything, very similar to the cosmic microwave background, but emitted much earlier.
Another place where neutrinos are copiously produced and emitted is the center of the Sun (and of stars, in general). The energy generation inside the Sun is due to hydrostatic hydrogen burning. This nuclear burning proceeds via the proton-proton chain and the Carbon-Nitrogen cycle. In both cases, the net reaction is

$$4p \rightarrow {}^4He + 2e^+ + 2\nu_e \tag{1.10}$$

Hydrogen burning necessarily involves the emission of neutrinos: they arise when weak interactions convert a proton into a neutron. Due to the very low weak cross sections, the produced neutrinos do not interact intensively with the plasma, and they can leave the star at the speed of light. Under these conditions, the Sun is said to be transparent to neutrinos, and the neutrinos stream out freely from it. Considering the luminosity necessary to sustain steadily the Sun from Hydrogen burning, it is possible to estimate the amount of reactions in the center, and, consequently, the amount of emitted neutrinos. On the Earth, the expected flux is quite high, $\sim 6.5\,10^{10}$particles/cm^2/s. On average, their energy is $\sim 0.42\,$MeV.
The emission of neutrinos from stars is not only related to nuclear reactions. In very massive stars, in advanced burning stages, the central temperature and density rise (for example, during silicon burning, $T_c \sim 0.4$MeV and $\rho_c \sim 3\,10^{10}$g/cm^3). In those conditions, neutrinos are increasingly produced by pair production (1.8). Still, the density and temperature are not high enough to trap them; so, the star is transparent and they can leave the star freely (like in the case of the Sun). Under this conditions, neutrinos represent the most effective cooling source of the star; the energy emitted in neutrinos is by far larger then the one emitted in photons. Keeping in mind that the rate of production of nuclear energy in stars is directly governed by the rate of energy loss, it is easy to understand why the late burning phases of massive star proceed faster and faster, due to neutrino cooling (for example, the Silicon burning phase in a $25M_\odot$ star lasts $\sim$ 1day).

In this work, we are interested in two very appealing astrophysical scenarios, where the production and the emission of neutrinos play a major role, for the energetics, for the dynamics and for the chemical composition of the system. They are core collapse supernovae and the merger of neutron stars in binary systems. Differently from the neutrino emitted from the Sun and from more massive star in burning phases, here the thermodynamical conditions of matter are so extreme that neutrinos of all flavours are not only produced, but they can be trapped and diffuse out of the system on the longer diffusion timescale. Moreover, they are energetic enough to be partially re-absorbed in the outer, more dilute regions. Due to the huge neutrino luminosities, this neutrino heating can have important implication for the dynamics and for the composition of the plasma. In the case of core collapse supernovae, a (at least, qualitative) confirmation that we do understand the basic aspects of the process and the role of neutrinos in it came from the very first neutrino detection from a Galactic source, which was the very famous SN1987a supernova, in the Large Magellanic Cloud.
In the next pages, we are going to introduce and to present the main physical aspects of these two scenarios. For core collapse supernovae, we refer to some complete and detailed reviews, like [7, 178, 67, 60], and references therein; for the mergers of compact objects and their connection with Gamma ray burst, we refer, for example, to [137, 34, 30, 152, 139] and references therein.

1.1 Core collapse supernovae

After millions of years of (almost hydrostatic) stellar evolution, during which a massive star has burnt its core of hydrogen into heavier and heavier elements, the iron core (which represents the final stage of nuclear burning) collapses in a few hundreds of milliseconds,

and, eventually, produces the explosion of the progenitor star. Only massive stars are expected to undergo all the stellar burning stages and, finally, to present favorable conditions to trigger a gravitational collapse. According to our present understanding, this depends mainly on the mass of the star at the beginning of its life, and secondary on its metallicity and on the fact that the star belongs or not to a multiple star system (which is, in most of the cases, a binary system). Differently from the other class of supernovae (type Ia SNe, which should consist in the thermonuclear explosion of a compact white dwarf), core collapse supernovae are typically expected to leave a compact object behind them, in addition to the remnant produced by the ejection of the outer layers of the star. According to the original mass and metallicity of the progenitor, and to the details of the explosion itself, the relic object can be a neutron star or a stellar-mass black hole. For example, at zero metallicity, stars with an initial mass between $\sim 8M_{\odot}$ and $\sim 100M_{\odot}$ undergo gravitational core collapse of their core, followed by a supernova explosion and the ejection of their hydrogen-rich envelop and, partially, of their helium-rich shell. The less massive ones (for initial masses lower than $\sim 25M_{\odot}$) are expected to form a neutron star; on the other hand, for initial masses in the range between $\sim 25M_{\odot}$ and $\sim 40M_{\odot}$, the fallback material of the explosion accretes on the neutron star, causing it to reach its maximum stable mass and inducing its further collapse to a black hole. For stars in the mass range between $\sim 40M_{\odot}$ and $\sim 100M_{\odot}$, a stellar black hole forms directly from the iron core collapse. The defining characteristic of very massive stars (which means with an initial mass of more then $\sim 100M_{\odot}$) is their electron-positron instability after carbon burning, which gives rise to the so called pair instability supernovae. For solar metallicity this picture becomes more complicated, due to larger uncertainties on the stellar evolution and on the explosion mechanism. Stars with an initial mass between $\sim 8M_{\odot}$ and $\sim 25M_{\odot}$ are, again, expected to form a neutron star; stellar black holes should form from more massive stars (again, up to $\sim 100M_{\odot}$). Nevertheless, according to the mass-loss rate in Wolf-Rayet stars, there could be a window (centered around $\sim 50M_{\odot}$) where the mass loss is so effective in depleting mass from the progenitor star, that a neutron star could still form. As it has been recently shown (see, for example, [168] and [167]), the impact of three dimensional effects in supernova explosions, as well as the differences in stellar evolution induced by binary system dynamics, can introduce large uncertainties and new features in this picture. Even more, stellar magnetic fields and rotation are expected to play an important role in the fate of massive stars, but a systematic and robust study of their effects is still missing.

1.1.1 Massive star evolution and progenitor structure

The life of a star is governed, during all its history, by its self-gravity. It is due to gravity that a portion of an interstellar cloud (mainly formed by cold molecular hydrogen) contracts and forms a protostar, in a process whose details are still mostly unknown. The amount of gravitational energy released by the contracting system is used to dissociate the hydrogen molecules into atoms and, then, to ionize the atoms. When the gas has been significantly ionized, the protostar has still a radius several hundreds of time larger the the solar radius, and an internal temperature of $30,000\,\mathrm{K}$. Due to the increase of photon opacity, any subsequent release of gravitational energy can be also converted to and stored as internal energy. The subsequent increase in pressure slows the contraction

down and settles an almost hydrostatic equilibrium inside the protostar. On a longer timescale of $10^7 - 10^8$yr, the system still contracts and heats, converting half of the released gravitational energy into internal energy (the other half is radiated away at the surface of the protostar). The contraction stops when the temperature and the density at the centre increase until the conditions are suitable for thermonuclear fusion of hydrogen. The energy released by nuclear fusion lessens the need for the release of gravitational energy, and the protostar ceases to contract. From this point on, the star enters the hydrostatic burning phase: nuclear species of increasing atomic and mass number are fused at larger and larger temperature, the ashes of a burning step being often the fuel of the next one. At the end of this phase, an initially massive star (i.e. a star which can undergo all the possible nuclear fusions) consists of concentric shells with different nuclear composition. Each shell is characterized by its most abundant element; proceeding from the outer to the inner part, there are the hydrogen, helium, carbon, neon, oxygen and silicon shells. Silicon burns in the center, producing a core of iron group elements (with mass number around 56). In particular, following silicon burning, the composition consists of the most tightly bound iron-group nuclei compatible with the actual thermodynamical condition (density, temperature and electron fraction). Iron-group nuclei are the final stage of nuclear hydrostatic fusion, because any further nuclear fusion reaction does not release energy (it rather depletes internal energy, storing it into nuclear binding energy). When the silicon has been depleted and its abundance has become small enough, all nuclear and electromagnetic reactions are in equilibrium with their inverse reactions, and all abundances can be expressed by a nuclear Saha equation as a function of the local thermodynamical properties of the stellar plasma. Then, the plasma can be considered in Nuclear Statistical Equilibrium (NSE). At the interface between the silicon shell and the iron core, the silicon is continuously burnt and the mass of the core increases. At this stage, the density inside the core can reach $5 \cdot 10^9 \mathrm{g/cm^3}$ and the temperature exceeds 0.5 MeV. Due to electron captures on nuclei, the electron fraction Y_e reduces from 0.5 to 0.48 at the core edge, and up to 0.42 in the core center. After helium burning, neutrino emission from thermal processes and from electron captures is the most effective source of cooling for the star interior. During silicon burning, it is so effective (due, for example, to the strong temperature dependence of processes like electron-positron annihilation) that the entropy of the iron core is kept relatively low (from $0.4\,k_B$/baryon in the center up to $1\,k_B$/baryon at the core edge). In these extreme thermodynamical conditions, the typical Fermi energy of electrons is larger than their rest mass energy and electrons form a relativistic degenerate gas, which provides the largest contribution to pressure,

$$P \sim P_e \propto (Y_e \rho)^{4/3} \tag{1.11}$$

A self-gravitating system sustained by a degenerate relativistic electron gas has a maximum mass, above which there is no solution for the hydrostatic equilibrium (i.e. no stable configurations; see, for example, [150]). This maximum mass is called *Chandrasekhar mass*. Traditionally, for a full degenerate relativistic gas, it is equal to:

$$M_{\mathrm{Ch,T=0}} = 1.44 \left(\frac{Y_e}{0.5}\right)^2 M_\odot \tag{1.12}$$

Keeping into account the first order correction for the finite temperature (entropy), the effective Chandrasekhar mass can be expressed as:

$$M_{\rm Ch} \approx M_{\rm Ch,T=0} \cdot \left(1 + \left(\frac{s_e}{\pi Y_e}\right)^2\right) \tag{1.13}$$

where s_e is the electron entropy per baryon in units of the Boltzmann constant k_B. For typical values of entropy and electron fraction, a $15M_\odot$ main sequence star has a Chandrasekhar mass of about $1.34M_\odot$.

1.1.2 The collapse

A degenerate iron core with a mass exceeding its own Chandrasekhar mass will be gravitationally unstable and collapse. Pre-supernova models develop already during the silicon burning phase an infalling velocity profile, due to the continuous release of neutrinos, releasing gravitational binding energy out of the core. The collapse is, then, accelerated by two instabilities. The first is the significant increase of electron capture on iron-group nuclei,

$$^{56}\mathrm{Fe} + e^- \rightarrow {}^{56}\mathrm{Mn} + \nu_e \tag{1.14}$$

mainly due to the increase of density, which translates into an increase of the Fermi energy of the electron gas (see, for example, [150]):

$$\mu_e = 11.1\,\mathrm{MeV}\left(\frac{\rho Y_e}{10^{10}\,\mathrm{g/cm^3}}\right). \tag{1.15}$$

Together with an obvious depressurization effect, electron capture changes the nuclear composition toward neutron rich nuclei: when Y_e decreases below 0.41, the mean mass number of heavy nuclei increases well above 70. The second instability (dominant in hotter, more massive stars) is photodisintegration: at higher temperature and densities, nuclear statistical equilibrium favors a large abundance of free α nuclei,

$$\gamma + {}^{56}\mathrm{Fe} \rightarrow 13\,\alpha + 4\,n \tag{1.16}$$

with a negative Q-value of $Q = -124.4\,\mathrm{MeV}$. The corresponding increase in ion entropy is compensated by a decrease in electron entropy (the collapse, apart from the variation of entropy due to neutrino emission, can be considered adiabatic), which in turn reduces the Chandrasekhar mass and helps the collapse. The collapse proceeds faster and faster, on the free fall timescale:

$$t_{\rm dyn} \sim t_{\rm freefall} \sim \sqrt{\frac{1}{G\bar{\rho}}} \sim 10^2\mathrm{ms} \tag{1.17}$$

where $\bar{\rho}$ is the average density of the core, increasing mainly the central density. Neutrinos produced with increasing degeneracy energy can escape freely, up to the point where a density of a few times $10^{12}\mathrm{g/cm^3}$ is reached. Above this density, neutrinos (now with a typical energy of a few MeV or even larger), interact more and more often with infalling matter. As a result, they cannot escape from the core on the shortest free streaming timescale $t_{\rm fs}$, but they diffuse out on the longer diffusion timescale $t_{\rm diff}$. In particular,

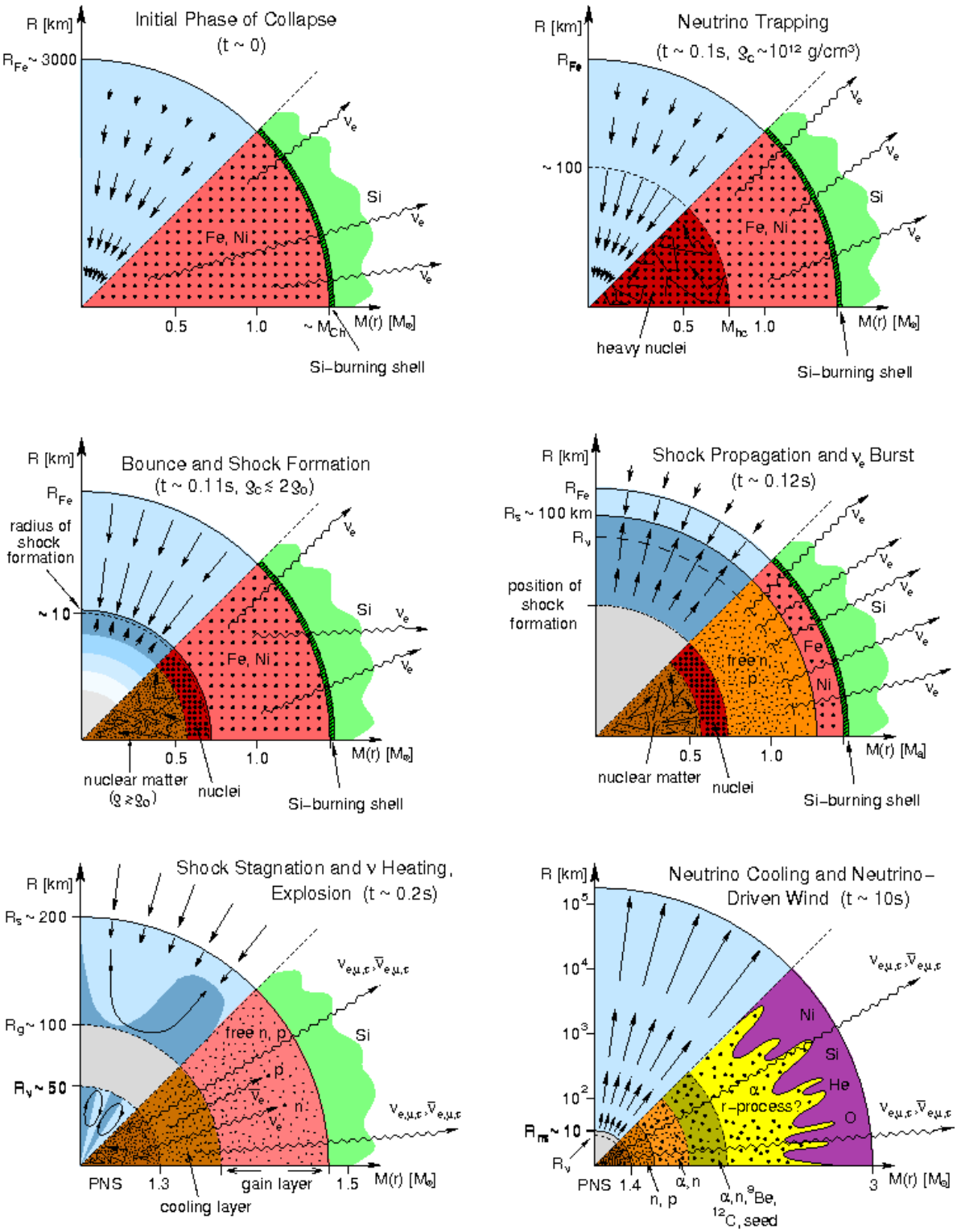

Figure 1.2: Schematic and pictorial representation of the evolutionary stages, from core collapse to the onset of the explosion and the development of a neutrino-driven wind, during the neutrino cooling phase of the protoneutron star. This Figure was taken from [60].

above 10^{12}g/cm^3, the diffusion timescale becomes larger than the dynamical timescale and neutrinos can be considered trapped inside the collapsing core. The result of the neutrino trapping is the formation of an electron neutrino gas inside the star; as density and temperature increase, neutrino reaction rates increase as well, and thermal and weak equilibrium are established. The formation of an antineutrino gas is initially suppressed by the large electron neutrino chemical potential (which, at equilibrium, translates into a large, negative chemical potential for electron antineutrinos). The main reactions which provide weak and thermal equilibrium are the electron and positron capture on nuclei and nucleons

$$(A, Z) + e^- \rightarrow (A, Z-1) + \nu_e \tag{1.18}$$

$$p + e^- \rightarrow n + \nu_e \tag{1.19}$$

$$n + e^+ \rightarrow p + \bar{\nu}_e. \tag{1.20}$$

Neutrino scattering on nuclei and nucleons are major sources of opacity,

$$(A, Z) + \nu \rightarrow (A, Z) + \nu \tag{1.21}$$

$$N + \nu \rightarrow N + \nu, \tag{1.22}$$

where (A, Z) is a nucleus of mass number A and atomic number Z, while $N = p, n$. These processes can be considered as elastic processes in a first approximation. Neutrino-electron scattering is another relevant reaction,

$$\nu + e^- \rightarrow \nu + e^- \tag{1.23}$$

which has been shown to improve the speed of the thermal equilibrium establishment, leading to softer neutrino spectra and increasing the neutrino luminosity (as low energy neutrino are expected to interact less and diffuse faster out of the core, [99]). Other thermal or very degenerate processes, like neutrino pair production and neutrino bremsstrahlung, become relevant at the end of the collapse and in the after bounce phase, because they require much higher temperature and densities. After neutrino trapping, neutrinos cannot escape from the core; as a consequence, the lepton number and the total entropy stay constant. Nevertheless, weak equilibrium at the proper thermodynamical conditions sets the ratio between electrons and neutrinos. If before trapping the central electron abundance is around $Y_e \sim 0.39$ and the neutrino abundance is negligible, when the collapse has proceeded and the central density is around 10^{14}g/cm^3, one forth of the electrons has been converted into neutrinos, so that $Y_e \sim 0.31$ and $Y_{\nu_e} \sim 0.08$. In the main while, the collapse of the inner part of the core proceeded homologously [48] and, because of that, this part of the star is referred as the homologous core. Here, the infall fluid speed is proportional to the radius ($v_r \propto r$) and below the sound speed. Outside the homologous core, the collapse is supersonic and follows a free fall profile, $v_r \propto 1/r$. The two parts of the core have approximately the same mass. Due to the proceeding collapse, the central density becomes supernuclear, reaching a few times nuclear saturation density ($\rho_0 \approx 2 \times 10^{14}$g/cm^3). As a consequence of the short range repulsive nuclear interaction, the fluid becomes harder to compress and the homologous core start to decelerate and bounces. Sonic waves reach the sonic point, at the edge of the homologous core, but they cannot proceed further. Then, a shock wave is launched from that point (within an enclosed mass of $\sim 0.7 M_\odot$), toward the outer part of the core.

1.1.3 The prompt shock

The shock wave forms at the edge of the homologous core and it starts to travel inside the supersonically infalling iron core. A shock wave is a dissipative, irreversible process in a fluid. Unshocked matter passing through the shock front increases its entropy. Assuming that the shock is weak ($p_1 \lesssim p_2$, in opposition to strong shocks, where $p_1 \ll p_2$, where p_1 is the pressure of the unshocked matter and p_2 of the shocked one), the variation of entropy per baryon can be estimated by

$$\Delta s \approx \frac{\gamma\,(\gamma+1)}{12}\left(\frac{v_r}{c_s}\right)^3, \tag{1.24}$$

where γ is the adiabatic exponent of the equation of state (roughly 4/3 at the shock formation, since this is the exponent associated with a relativistic gas of degenerate fermions). Starting from a relatively low value of the entropy ($s \approx 1\,k_\mathrm{B}$/baryon) for the unshocked part, it rises between 6 and 12 k_B/baryon below the shock. This increase in entropy corresponds to a large increase in temperature too, passing from ~ 2 MeV to $\sim 20-15$ MeV. At those values of entropy ($s > 3k_\mathrm{B}$), heavy nuclei are photodissociated into nucleons. The dissociation of an iron nucleus into neutrons and protons costs the shock wave 8.8 MeV per nucleon. Considering an outer iron core of $0.7M_\odot$, the shock has not enough energy to travel through the whole core.
The sudden increase in temperature and the change in matter composition have a large impact on neutrino reactions and behavior. Large abundances of free protons increase highly the electron capture rate on proton. High temperatures provide a large density of positrons, which can be captured by very abundant neutrons or can annihilate with electrons into neutrino pairs. As a consequence, neutrinos of all flavours (even if with different rates and on different timescale) are copiously produced and, eventually, re-absorbed by the fluid, forming fermion gases in equilibrium with matter. All these reactions, together with the equally increased scattering off free nucleons, provide a very high neutrino opacity inside the shock wave: initially, all the neutrinos inside the shock can be considered trapped and they move together with the wave. But few milliseconds after bounce ($3-5$ms), the shock has traveled enough in the core to reach the relevant neutrinosphere (i.e. the surface corresponding to the last scattering or interacting surface), corresponding to a density of a few times 10^{11}g/cm^3 and a radius of about ≈ 70km. At this point, the neutrinos produced in the core, advected with the fluid and diffusing out from the core are no more trapped and can be released. This produces the so called neutrino burst, which can be seen as a sudden increase in neutrino luminosity, up to a few times 10^{53}erg/s, and which lasts for a few ms. The formation of neutrino gases inside the core, together with the neutrino burst and the increase in neutrino luminosity, happen again at the expense of the shock wave energy. The copious electron capture on protons leads to a further neutronization of the shocked matter, whose electron fraction decreases down to ~ 0.1. The combined action of iron dissociation and neutrino emission weaken the shock wave so much that it finally stalls between 100 and 200 km, and converts into an accretion shock (a shock wave with both shocked and unshocked down streaming flows).
The shock forms at a radius corresponding (in good approximation) to the mass of the homologous core; this means that this amount of relatively cold matter (i.e. low entropy nuclear matter) will stay cold and unshocked, with an initial electron fraction of about

0.3 and with copious neutrinos diffusing out on long timescales (roughly, of the order of 1-10 seconds for the relevant neutrino energies). This relic is called proto-neutron star. When the shock wave converts into an accreting front, matter falls and piles up on the central object with a very high accretion rate (up to $\sim 2M_{\odot}$/s, depending very much on the progenitor mass and model), rapidly increasing its mass until the explosion sets in. Depending on the progenitor mass, the accretion rate and the explosion timescale change, leading to different remnant masses. As already point out above, star with a progenitor mass less than 25 $M_{\odot}$ are expected to form a neutron star; for larger masses, the mass of the proto-neutron star probably exceeds the maximum allowed neutron star mass, triggering the collapse to a stellar black hole.

1.1.4 Explosion mechanism(s)

Delayed neutrino-driven explosion

The fact that the shock wave stalls few tens of milliseconds after core bounce, converting into a standing accretion shock deep inside the star core, is usually referred as the failure of the prompt shock explosion. The problem of how and when the standing shock gains enough energy to convert itself into an outward moving wave, producing a supernova explosion and, ultimately, the destruction of the progenitor star, can be presently defined as the central, long standing problem in core collapse supernova theory.
Several different possible mechanisms have been explored, both theoretically and numerically. One of the first ideas is the so called *neutrino-driven explosion*. Colgate and White [24] were first to suggest that high energy neutrinos coming from the hot proto-neutron star can be absorbed by the shocked material above the neutrinospheres. These neutrinos carry most of the gravitational energy released by the collapse and deposit a fraction of it just behind the shock front. The reactions which are mainly responsible for the absorption of both ν_e and $\bar{\nu}_e$ are the charge current reactions on free nucleons:

$$\nu_e + n \rightarrow e^- + p \qquad \bar{\nu}_e + p \rightarrow e^+ + n. \tag{1.25}$$

This neutrino heating increases the internal energy and the pressure of the fluid behind the shock, which starts to expand, pushing the shock forward. The persistent neutrino flux can potentially sustain this mechanism and, eventually, leads to an explosion. The very low values of the neutrino cross sections require both high neutrino fluxes (of the order of 10^{52} erg/sec) and relatively long timescales (of the order of a few 100 ms): an absorption efficiency of $10-20\%$ for both ν_e and $\bar{\nu}_e$ is expected to be necessary to trigger an explosion. The final success of the neutrino-driven mechanism turns out to be crucially dependent on the balance between the neutrino cooling and the neutrino heating. Cooling rates depend very sensitively on the matter temperature ($Q^- \propto T^6$), while the heating rates outside the neutrinosphere decreases with increasing radius $Q^+ \propto R^{-2}$. As the decrease of temperature in the relevant region can be roughly described by a power law of the radius (approximately, $T \propto R^{-1.2}$), it turns out that the cooling process is dominant just above the neutrinosphere (corresponding also to the surface of the protoneutron star), while the heating process just below the shock. The radius where the cooling and the heating curve cross is called *gain radius*. As it can be easily foreseen, only if the heating is strong enough an explosion can be triggered. Two related factors

which influence the success of the neutrino-driven mechanism are the value of the neutrino luminosity and the hardness of their spectra. The neutrino heating has a positive feedback, because a strong heating on an infalling fluid element decelerates it, increasing the time spent above the gain radius, and, finally, the probability more absorption.
Since its introduction during the 60's, the neutrino-driven explosion has been tested in spherically symmetric computational models of increasing complexity and accuracy. Several remarkable improvements have been performed in the hydrodynamical schemes, in the neutrino transport and physics, in the treatment of gravity and in the description of matter at the very high density and temperature which characterize core collapse supernova. All state-of-the-art spherically symmetric simulations of core collapse supernova with detailed neutrino transport, performed in Newtonian gravity, as well as in approximated or full General Relativity, using appropriate hadronic equations of state, confirm the presence of an important heating effect, due to the hot neutrino emission from the proto-neutron star, between the gain and the shock radius (see, for example [164, 86, 154], and references therein). Nevertheless, no delayed explosions could be obtained for progenitor heavier than $10M_{\odot}$. The failure of the delayed neutrino-driven mechanism in spherically symmetric models can have several different explanations and can potentially open a series of questions, for example concerning our understanding of the behavior of matter under extreme conditions, as well as our knowledge of the challenging neutrino interactions. However the spherical symmetry can be a potential limiting factor. In fact, this assumption prevents the developing of multi-dimensional hydrodynamical effects (like instabilities and convection), as well the inclusion of intrinsically multidimensional physics inputs (like magnetic field). The importance of these ingredients was known since the beginning (see, for example, [106, 8]), but the lower computational power limited strongly the possibility of a deep and extensive investigation until the 90's. The first steps toward accurate multi-dimension core collapse supernova simulations was performed developing axisymmetric hydrodynamics code, with an approximated gray transport scheme for neutrinos. The first simulations (see, for example, [61, 100]) showed the developing of violent convection in the gain region, due to the negative entropy gradient behind the accretion shock; this was generated by the strong deposition of heat just above the gain radius, larger compared to the energy deposition at the outer shock front. The effect of this convection is to increase the efficiency of the heating mechanism, because it increases the time spent by a fluid element in the gain region, and because the convective motion overturns the shocked material, refilling continuously the gain region with relatively cold matter. Those simulations resulted in promising explosions; however, more recent axisymmetric simulations with more accurate, energy dependent neutrino transport did not reproduce these results for all stellar progenitors (see, for example, [16, 28, 116, 92, 107]). While simulations based on progenitor model with an initial mass of $11.2M_{\odot}$ seem to explode (even if with a rather weak explosion energy), simulations with heavier progenitors failed. However, considering important aspects like the explosion timescale and the explosion energy, the results of different groups have not converged yet. Together with expected convective instabilities, axisymmetric simulations showed a new kind of potentially important instabilities; this was a generic instability of the accretion shock to non-radial deformation, which has been called Standing Accretion Shock Instability (SASI, see [38, 10]). Expanding the non-radial component of the motion in spherical harmonics, it appeared that SASI

was linked with the growth rates of the $l = 1, 2$ modes. The instability results in a pulsational oscillation (i.e. contraction and expansion) of the shock front in the polar directions. Similarly to the convective instabilities, the main effect is the increase of the time spent by a fluid element in the gain region; differently, the phase difference in the oscillation between the two poles (i.e. while a pole expands the other contracts) seeds an intrinsically asymmetric heating enhancement, which can potentially results in a strong degree of asymmetry in the explosion. The growth of SASI and the details of its strongly non-linear mechanism are still under investigation and are matter of debate.
In the last few years, an increasing effort has been devoted to develop three dimensional simulations, with different degrees of neutrino treatment. Considering that a full three-dimensional Boltzmann treatment of the neutrino distribution functions (at the level of detailed spherically symmetric simulations) is nowadays impossible both for the expected CPU-time demands and for the huge memory required in such a simulation (even for the largest supercomputers), several approximate treatments have been developed [44, 112, 108, 50, 70]. In this respect, the Isotropic Diffusion Source Approximation (IDSA) has been developed and tested by Matthias Liebendoerfer and the Basel group [88] in spherically symmetric simulations; later, it has been extended to three dimensional Cartesian simulations in the `ELEPHANT` code [174, 175]. Other interesting methods are currently under development (see, for example, [1]).

Currently, several groups are investigating the first results coming from their very large three dimensional simulations. Even though there is not yet a publication with a large sample of three dimensional, self-consistent delayed neutrino-driven exploding models, it seems that the heating mechanism benefits from the larger variety of hydrodynamical instabilities and their coupling with neutrino transport. The actual degree of neutrino heating enhancement, as well as the impact on the neutrino critical luminosity, passing from axisymmetric to three dimensional simulations is still matter of debate [112, 50].
Recent simulations, both performed in axisymmetry and in three dimensions, with a tuned neutrino luminosity imposed at the surface of the proto-neutron star, showed that random perturbations (artificially included in a spherically symmetric profile, obtained by a detailed spherically symmetric simulation, a few milliseconds after bounce develop) grow and can develop strong asymmetric explosions. These instabilities and the resulting dynamics of the fluid can potentially explain the recoil velocity of the proto-neutron star, as well as its spinning velocity; moreover, the asymmetry at the onset of the explosion causes strong instabilities also during the shock expansion in the outer shell of the massive star. These instabilities are potentially relevant for the subsequent nucleosynthesis in the ejecta.

Other possible explosion mechanisms

Three dimensional hydrodynamics simulations with sophisticated spectral neutrino transport are definitely necessary to understand if neutrino-heating mechanism is responsible for the explosion of stars more massive than $15M_{\odot}$. Nevertheless it is also not excluded that other mechanisms can trigger the explosion or contribute to it, together with neutrino absorption. One of the first alternative scenarios which was invoked in the context of core collapse supernova is the so called *magnetically-driven explosion mechanism* (see, for example, [106, 19]); it assumes that the core rotates fast and differentially, and that

an initially high poloidal stellar magnetic field can be highly amplified by compression and by local instabilities (for example, magneto-rotational instabilities, MRI) during or a few milliseconds after the collapse. Under these special conditions, free rotational energy in the nascent proto-neutron star can be extracted and converted into magnetic energy, rising from the winding of the poloidal filed into a strong toroidal component; the resulting magnetic pressure can push and lift strongly the matter along the rotational axis, forming a fast expanding jet inside the shock. Recent progenitor models which tried, for the first time, to mimic the impact and the evolution of rotation and magnetic field in massive star [52], seem to disfavor this scenario: the contemporary presence of high magnetic field and high rotational rates should have a brake effect which is very effective in transporting angular momentum out of the stellar core; moreover, the magnetic field evolution seems to favor a larger toroidal component in the final iron core. However, stars with very large mass and very low metallicity (i.e. primordial stars) are expected to transport their angular momentum much less effective, thus leaving a faster rotating iron core [177]. And, overall, the uncertainties in these progenitor models are still quite large. So, the exploration of this mechanism looks still interesting, even if, probably, it cannot be assumed to be the standard explosion mechanism, for all progenitor masses and all possible metallicities, but maybe an alternative explosion scenario for peculiar progenitors. The hypothesis of an infrequent explosion mechanism in primordial stars could be also compatible with the abundances of r-process elements in the early Universe, assuming that these jets are very promising sites for r-process nucleosynthesis [176].

The presence and the evolution of magnetic fields in massive (collapsing) stars is not the only alternative explosion scenario. Several uncertainties characterize also the behavior of matter at very high densities and temperatures. The effect on stellar core collapse of a phase transition between hadronic and quark matter at densities a few times above nuclear density and finite temperature has been recently investigated in spherically symmetric models [145, 36]. For some of the obtained equations of state, the phase transition inside the proton-neutron star generates a second strong shock, some hundreds of milliseconds after the first bounce, which is able to explode the star. The recent discovery of a almost $2M_{\odot}$ neutron star [27] has seriously challenged the possibility of this phase transition at relatively low baryon density, reducing the possible parameter space, but without ruling it out completely [74].

1.2 Binary neutron star mergers

1.2.1 General description of the GRB scenario

Gamma-ray bursts (GRBs hereafter) are intrinsically powerful flashes of collimated high energy radiation, whose isotropized values is typically $\sim 10^{51}$ erg (see, for example, [41]). They happen in various types of galaxies and they are isotropically distributed at cosmological distances [93]. Since they were accidentally discovered in 1967 by the Vela satellites [65], they have obstinately resisted against a definitive theoretical understanding of the mechanism that triggers such enormous energy release. Their discovery has nourished a furious research activity which gave birth to a large number of theoretical models trying to explain the broad diversity in the behavior of GRBs, none of them being fully conclusive. Nevertheless a general consensus exists on some basic facts:

- **A neutron star or a black hole is the main responsible of the explosion.** Even though the radiation energy observed in GRBs already characterizes them among the most energetic events in the Universe, the amount of energy globally released by each of them is probably even larger: neutrinos, gravitational waves, ejected matter and magnetic field can, in principle, store or release a meaningful fraction of the initially available energy, which can rise up to a few times 10^{53}erg. Catastrophic events associated with the collision between stellar compact objects (black holes and neutron stars) or the death of a massive star (which, in the end, leads to the formation of a black hole or a neutron star) seem to be the best candidates to explain the huge amount of energy which characterizes GRBs.

- **GRBs are divided into two categories: short and long.** Short ones have typical durations of ~ 0.3 s, while long ones last about ~ 30 s. Approximately 25% of all observed GRBs belong to the first group.

- **There are strong correlations between duration, spectra and redshift distribution.** Short GRBs have a spectrum that is harder (i.e. with a larger fraction of high-energy photons) than long ones [69]. They are mainly detected at lower redshift ($z_{\rm short} \lesssim 2$), while long ones have a more uniform redshift distribution and are among the most distant events observed in the Universe ($z_{\rm long} \lesssim 10$) [40, 47]. These correlations suggest the existence of two different central engines, each one associated to each category of GRBs.

Independently from the actual central engine, the GRBs emission has two phases: the erratic gamma ray *prompt* phase and the smoother *afterglow* phase. According to the most accepted model for the electromagnetic emission, these phases are powered by a so-called *fireball* [93], which originates due to the injection of a large amount of energy ($> 10^{49}$ erg) in a small, relatively baryon-free volume (of the order of several Schwarzschild radii of size). The resulting fireball consists in an optically thick plasma that accelerates to ultra-relativistic speeds ($\Gamma > 100$) under its own pressure. This flow of electron-positron pairs, photons and baryons cools by adiabatic expansion until it becomes optically thin at large distances from the source ($\gtrsim 10^{13}$ cm). At this point, the prompt electromagnetic emission is produced by the dissipation of part of the energy in highly relativistic electrons, which in turn interact with the magnetic field or the

radiation field via internal shocks in the flow, emitting the detected gamma rays. The afterglow is generated later, when the remaining flow energy is transmitted to the ambient medium at larger radii ($\sim 10^{16} - 10^{18}$ cm) and decelerates producing electromagnetic emission. This scenario poses a serious constraint to any central engine model: in order to obtain a high relativistic motion, the mass of the baryonic ejecta has to be small enough, compared to the injected energy (for a typical GRB, smaller than $\sim 10^{-6}\ M_{\odot}$). Therefore the study of how a system can inject a high amount of energy in a small volume, without polluting it with baryonic matter, is one of most important issues to understand the GRB scenario.

Any central engine model has to fulfill a list of constrains, which come directly from GRB observations:

- the engine must provide the large energy reservoir, which is necessary to account for the observed photon luminosity, as well as to explain its own dynamics; more precisely, it has to explain how a fraction of the available energy is deposited in a relatively baryon free region, in order to produce a highly relativistic outflow;

- the engine model and its dynamics must explain both the duration of the burst and the small scale variability of the observed lightcurves;

- the compact objects associated with the engine, and the related events triggering the burst, have to be compatible with the types of observed host galaxies and with the GRB redshift distributions;

- the model has to provide an intrinsic variability, which could be correlated with the huge diversity in GRB observations.

Considering all these constrains and the few basic facts about which there is a broad consensus, the most promising basic ingredient needed to launch a GRB event should be a rapidly accreting compact object (a solar mass black hole or a neutron star, eventually highly magnetized), surrounded by a massive disk of accreting matter. Two main astrophysical scenarios are compatible with this recipe: 1.- A rapidly rotating, massive Wolf-Rayet star that has lost its hydrogen envelope and has a massive 10 $M_{\odot}$ helium core, which afterwards collapses, forming finally a black hole surrounded by a thick disk of accreting matter. Or 2.- A binary system of two neutron stars (or a neutron star and a black hole) that merge, due to the loss of angular momentum via gravitational wave emission, forming, in the end, a black hole and a massive accretion disk.

Since the observation of an unambiguous re-brightening of the optical light curve of GRB 030329 in 2003 by BEPPOSAX, it is generally accepted that at least some of the long GRBs are related to certain supernovae events, and therefore to massive young stars. This was also supported by the fact that long GRBs only occur in galaxies with an active star formation. On the other hand, the observation of the first afterglow of short GRBs in 2005 by the SWIFT satellite [11] showed that these can also occur in host galaxies without star formation, pointing to an old progenitor population. Hence, long GRBs are mainly supposed to be generated by the collapse of a massive star, or *collapsar* model, while short GRBs are produced by the merger of compact objects, namely the *compact binaries* model [117].

1.2.2 Double neutron star mergers

Double neutron star binary system formation

Since their first direct detection, in 1967 by Anthony Hewish and his student Jocelyn Bell who discovered the first pulsar, the number of observed neutron star has largely increased, and it will certainly do so in the future. They appear in a large variety of situations: they can be isolated or in binary systems, they can have an intrinsic pulsating emission (typically, in the radio band, but not only) or they can have intense X-ray emission, due to the accretion of matter from a standard companion star. Among all these cases, a binary system formed of two neutron stars is certainly a system of high scientific interest. Double neutron star systems are rare, because the original binary system has to survive two supernova explosions. There are several evolutionary path which can explain the existence of such systems. In the standard scenario, they originate from a close binary system of two massive stars, with initial masses between $\sim 8M_{\odot}$ and $\sim 25M_{\odot}$. The most massive star (the primary) will evolve faster than the other. During the red giant phase, it will probably expand and fill its Roche-lobe, transferring mass to the companion. Once the iron core of the primary has reached the Chandrasekhar limit, the core will collapse, the star will explode, and a hot neutron star will be formed. The kick imparted to the neutron star and the (probably related) asymmetric ejection of matter can destroy the binary system. If the system survives, it likely has a very high eccentricity. If the secondary star is still in its main sequence, it can transfer mass to the neutron star and, eventually, be observed as a (high mass) x-ray binary system. When the secondary evolves and, after its main sequence phase, expands, the compact companion can be engulfed in a common envelope phase. This phase is very critical for the binary system. Dynamical friction of the compact object over the dilute envelope can lead to accretion over it and to a rapid shrink of the orbit. The angular momentum and the energy released by the binary decay is carried away by the envelope, which evaporates, leaving behind the naked core of the secondary (which is called He-star). If the accretion on the neutron star is too intense, it may collapse into a black hole, changing the nature of the primary compact object (whatever is the fate of the secondary). In another extreme case, if the orbital decay is too effective, the neutron star can fall on the He-star before the latter can undergoes any core collapse explosion. Assuming that none of the previous cases happens, the neutron star descending from the primary orbits in a very close orbit around a He-star, which explodes as a CCSN and forms a second neutron star. If the binary system survives also the second explosion, a binary system of neutron star has formed. A possible way to avoid problems arising from the motion of a neutron star in a dilute envelope is to assume that the two initial masses are almost equal. Under these conditions, the secondary star expands before the primary explodes; the common envelope phase is characterized by the motion of two He-cores in a dilute gas, and it ends with a close binary system of two He-cores. If the binary system survives the two (close in time) explosions, a binary neutron star system has formed.

Today, the number of observed double neutron star binary systems in our Galaxy is around 10 (see, for example,[73] for the situation up to 2007). The first one was observed already in 1973, and it is the famous Hulse-Taylor binary pulsar PSR 1913+16. This system is truly considered as a wonderful laboratory to test gravitational physics in the

strong field limit. Actually, several different effects have been observed, and the most famous is the inspiral of the components, one towards the other. This effect is in excellent agreement with the prediction from General Relativity [172]. Another remarkable aspect of this binary system is that the mass of the two neutron star can be measured with an accuracy of $\sim 0.014\%$: $M_{\mathrm{puls,PRS1913+16}} = 1.4414 \pm 0.0002 M_\odot$ and $M_{\mathrm{puls,PRS1913+16}} = 1.3867 \pm 0.0002 M_\odot$ [173].

Inspiral and coalescence

Nowadays, the most important supports to the existence of coalescing neutron star binaries are the observed decrease of the orbital period of the Hulse-Taylor binary pulsar PSR 1913+16 [56, 159]. If the orbital period T_{orb} continuously decreases, together with the orbital distance (measured by the semi-major axis of the orbit, a), the two neutron stars will finally collide. According to General Relativity, this change in the orbital parameter is due to the emission of gravitational waves, which extract orbital angular momentum and energy out of the system. Losing angular momentum and energy, the orbit shrinks and the velocity increases. As a consequence, the gravitational emission becomes more intense and increases its frequency. It is easy to understand that such a process will have a positive feedback, reducing faster and faster the orbital period. This phase is called the *inspiral phase* and it proceeds slowly, due to the weak emission of gravitational radiation at initial separation distances. Actually, the initial phase is the bottleneck of the whole process. From the decay rate of the major semi-axis,

$$\frac{\mathrm{d}a}{\mathrm{d}t} = -\frac{64}{5}\frac{G^3 \mu M^2}{c^5}\frac{1}{a^3}\left(1-e^2\right)^{-7/2}\left(1-\frac{73}{24}e^2+\frac{37}{96}e^4\right) \tag{1.26}$$

where M is the total mass of the system, μ the reduced mass, and e the eccentricity, and assuming initially Keplerian motion, it is possible to fit the inspiral timescale:

$$t_{\mathrm{insp}} = 10^7 \mathrm{yr}\left(\frac{T_{\mathrm{orb}}}{1\mathrm{h}}\right)\left(\frac{M}{M_\odot}\right)^{-2/3}\left(\frac{\mu}{M_\odot}\right)^{-1}\left(1-e^2\right)^{-7/2}. \tag{1.27}$$

For PRS1913+16, $t_{\mathrm{insp}} \sim 3 \times 10^8\,\mathrm{yr}$ from now. From equation (1.27), it is clear that eccentricity plays a relevant role: systems with high eccentricity can inspiral much faster, compared with circular binaries. Nevertheless, this tendency is partially contrasted by the fact that, together with the reduction of the orbital period, the emission of gravitational waves reduces also the eccentricity and tends to circularize the orbit (for a fixed a, a circular orbit is the one which minimizes the angular momentum). But the fact that

$$\frac{\mathrm{d}e}{\mathrm{d}t} \propto \frac{1}{a^4} e\left(1-e^2\right)^{-5/2}\left(1+\frac{121}{304}e^2\right) \tag{1.28}$$

implies that the circularization is more effective in the last (shorter) phase of the inspiral motion. Thus, a large eccentricity can potentially reduce the inspiral timescale.
After the inspiral phase, the two neutron stars form a close binary system of compact objects: in the last seconds before coalescence, their relative distance reduces from $\sim$ 100km up to a few radii (which are expected to be $\sim$ 10km), and the orbital period goes from 0.1s to $\sim$ 1ms. Finally, when the relative separation is only a few times their radii,

the merger process starts. The mutual tidal interaction deforms the objects, which touch each other in a few milliseconds. After their contact, most of the mass falls in the center, while two tails of matter (which become spiral arms due to the fast orbital motion) form and spread away, removing the excess angular momentum. In the end, a very massive (with a baryon mass of $\sim 2.7 M_{\odot}$) and hot ($T \sim 10$MeV) neutron star-like object has formed in the center, surrounded by a thick torus of dense and hot matter (it has a mass of $\sim 0.1 M_{\odot}$, but cooler and less dense, compared with the central object). The fast rotating supermassive neutron star (SMNS hereafter) is initially supported against gravity by differential rotation. Due to viscosity and angular momentum redistribution, it will collapse soon into a stellar black hole, with an expected gravitational mass of $\sim 2.5 M_{\odot}$; but the timescales and the details of this process are still matter of debate (see, for example, [128]). Matter in the disk orbits very fast, almost in Keplerian motion. Nevertheless, the disk is far from a steady configuration, being characterized also by strong turbulent motions and fast accretion onto the central object. The sudden rise in temperature, as well as the high densities, trigger a copious neutrino production and emission, for all neutrino favors. In the SMNS, Fermi gas of neutrinos of all flavors are expected to form relatively fast after the coalescence. Similarly to the after bounce phase of core collapse supernova, neutrinos are expected to diffuse out from the very opaque regions, and to stream from the less dense outer part. This emission is the most efficient way for the system to release energy, both the internal energy of the SMNS and the gravitational energy converted into internal by the accretion process. Electron antineutrino luminosity is expected to be the largest one, because the neutron rich matter is expected to favor positron absorption on neutrons, Equation 1.20, over electron absorption on protons, Equation 1.19. Thermal processes (like neutrino bremsstrahlung or neutrino pair production) are also expected to be relevant for the all flavor production, an in particular for $\nu_{\mu,\tau}$ and $\bar{\nu}_{\mu,\tau}$.
In this scenario, the energy reservoir is mainly due to the gravitational energy released passing from a binary system of orbiting NSs (mass $\sim 1.4\, M_{\odot}$, radius $\sim 10\,$km) to an single SMNS (mass $\sim 2.7\, M_{\odot}$, radius $\sim 20\,$km), and it can be estimated to be a few times 10^{53}erg. Then, assuming that the emission will last for ~ 1s (as a typical diffusion timescale from the SMNS), we can already foresee that the total neutrino luminosity is expected to be similar to the CCSN case ($\sim 10^{53}$erg/s). The major source of opacity for neutrinos is expected to be elastic scattering on nucleons, Eq. (1.22). As we have already said, due to the high density in the SMNS and in the inner regions of the disk, neutrinos will not simply escape freely, but they will diffuse out on longer timescales. The relevant neutrino surfaces (which are the equivalent of the neutrinospheres in the CCSN case) forms in different locations, according to the flavor. The most interactive ν_e's and $\bar{\nu}_e$'s will have last production and last scattering surfaces in the inner part of the accretion disk, but far from the SMNS surface; for $\nu_{\mu,\tau}$'s and $\bar{\nu}_{\mu,\tau}$'s, these surfaces are expected to be much closer to the central SMNS (almost inside it). These differences have a large impact on the places where neutrinos are finally expected to be emitted and, consequently, on their spectrum: $\nu_{\mu,\tau}$ and $\bar{\nu}_{\mu,\tau}$ are expected to be harder, coming from the hot SMNS, while ν_e and $\bar{\nu}_e$ should be softer, coming from the inner part of the disk. Similarly to what happens at the material behind the shock wave in the core collapse supernova context, along their paths, there will be a non-negligible probability (in particular, for high energy neutrinos) of being re-absorbed by the nucleons in the disk.

Few neutrino absorptions can cause a baryon to be ejected from the disk in the external space: this is the so-called *neutrino-driven wind*. Because of the stronger centrifugal force, the regions along the rotational axis (polar regions) are expected to have a lower baryonic pollution. On the other hand, these are the regions where neutrinos coming from the disk are expected to deposit more energy by neutrino-antineutrino annihilation, [137] and [29]. This strong energy deposition in a relatively baryon-free region can be a promising mechanism for the formation of the relativistic jet required by short GRBs production. Together with neutrinos, magnetic field is expected to play a major role during the collapse and in its aftermath. As it has been shown in detailed numerical simulations [121], during the merger of a binary system of magnetized neutron stars, magnetic fields inside the SMNS are strongly and quickly amplified, up to $\sim 10^{15} - 10^{16}$ Gauss, on a timescale of $\sim$ 1ms. Moreover, more recent full general relativistic MHD simulations [129] have revealed that, on longer timescale ($\sim$ 30ms) the magnetic field can reorganize it-self, creating a strong ($\sim 10^{15}$ Gauss) poloidal field along the rotational axis of the newly formed black hole. The interaction between the spinning black hole and the magnetic field can, in principle, power a relativistic jet via the Blandford-Znajek mechanism.

Even though both the neutrino and the magnetic field mechanism look promising for the formation of a relativistic jet, the details of each of them are still poorly known. In particular, it is not clear if the two mechanisms can act together or one dominates over the other. But, in both cases, the degree of baryonic pollution above the poles of the SMNS/BH represents a severe and crucial constraint, which requires a detailed analysis.

Gravitational waves, neutrinos, baryonic wind and electromagnetic radiations are not the only possible outcomes and observables of a double neutron star merger. The highly neutronized material is a suitable environment to produce heavy nuclei, as a result of rapid neutron captures; this scenario makes neutron star mergers a promising candidate site for r-process elements nucleosynthesis [42, 4, 49]. Three possible stages can lead to a yield of escaping heavy nuclei within the coalescence process: 1.- The merger phase, where a long tail of mass can be ejected during the decompression of the stars; 2.- The accretion phase, when a small amount of mass is lost from the outer part of the disk; and 3.- The baryonic neutrino-driven wind itself. Even more, the r-process represents a non-negligible energy contribution to the thermal evolution of the accreting mass onto the SMNS, which may explain the extended emission of X-rays that follows the prompt burst in some short GRBs [94].

The problem of the coalescence of two neutron stars (and, more in general, the problem of the coalescence of compact objects) is a complex problem, in which several different interactions have to be considered at the same time. Altogether, they set the physical scales for the relevant dynamical, thermodynamical and chemical quantities. These scales usually span many orders of magnitude. Although this scenario is conceptually very different from the CCSN case, the main ingredients and the relevant scales are very similar. Thus, as for the stellar collapse and explosion, numerical simulations are a powerful tool to model and to investigate quantitatively the merger of two neutron stars and their aftermath. The history of numerical simulations of double neutron star merger is long and rich. Differently from CCSN simulations, the intrinsic non-sphericity of the problem has prevented the possibility to simulate it in spherically symmetry. Due to the larger computational power requested by axisymmetric simulations or full

three dimensional models, and to the fact that the existence and the evolution of binary neutron star systems have been investigated only after the 70's, the first simulations were performed only in the late 80's. The list of ingredients which should be necessary to be included in a full satisfactory model includes (magneto)hydrodynamics, General Relativity, detailed microphysics and neutrino transport. Unfortunately, nowadays a simulation which includes all these aspects in a satisfactory way is far behind our actual computational capabilities. Then, several different approximated approaches have been adopted. The first merger simulations were performed with three dimensional Newtonian codes, without taking into account neutrino emission or General Relativity (for example: [109, 136] and references therein). Ruffert et al, [143, 144] included neutrino emission, using a grid code; a similar approach was employed also by [137] in SPH codes. The impact of magnetic fields in Newtonian models was included for the first time in SPH simulations by [121] and [140].
The main goals of these simulations were to study, with increasing degree of accuracy and reliability, 1) the dynamics of all the phases of the merger (from the final moments of the inspiral motion, up to the dynamics in the accretion disk); 2) the properties of the central SMNS, as well as the properties of the fast ejected matter; 3) the signal from the gravitational wave emitted during the coalescence; 4) the neutrino luminosity and spectrum during the merger and in the aftermath of it.
Recently, axisymmetric simulations of the neutrino emission and of the neutrino-driven baryonic wind in the aftermath of neutron star mergers were performed, using a detailed spectral neutrino treatment [29]. The main outcome of this study was that neutrino absorption can lead to the formation of a baryonic neutrino driven-wind. This wind can pollute the regions above the disk and, partially, also the polar regions, while the energy deposition due to neutrino annihilation is not enough to power a relativistic jet from the poles. This study assumed always the presence of the SMNS (i.e., a long timescale for the SMNS to collapse to a BH). This was probably a very important and relevant hypothesis, because most of the neutrino emission and a good fraction of the baryonic pollution in the polar funnels came from the surface of the SMNS.

Chapter 2

ASL, an advanced spectral leakage treatment for neutrinos in astrophysical simulations

2.1 General concepts

The idea behind a leakage scheme for treating neutrino emission from an astrophysical object is simple: the scheme has to provide a computationally inexpensive, but physically robust and motivated estimation of the amount of neutrinos emitted, and, together with it, the energy released by them. This quantity has to be calculated in any point of the system. Leakage schemes have a long history in computational astrophysical, especially the ones regarding neutrino emission from core collapsing supernovae, from forming black holes or from neutron star mergers.
In the context of radiation hydrodynamics, the requirement of a low computational cost is often not compatible with the exact solution of the equations governing the system: the diffusion equation and, even more, the Boltzmann equation require large computational effort, increasing dramatically with the dimensions of the problem: then, if state-of-the-art spherically symmetric simulations of core collapse supernovae can be performed solving the full Boltzmann equation, axisymmetric and, even more, three dimensional simulations have to find a compromise between accuracy and performances. In this respect, many different approximations have been developed, starting from Multi Group Flux Limited Diffusion (MGFLD), application of multiple one-dimensional Boltzmann transports in many rays, S_N method and, in the last years, the Isotropic Diffusion Source Approximation (IDSA), developed in Basel [88], in the context of one and three dimensional models of CCSNe.
A leakage scheme can be considered as an *effective* scheme. The reason is that, strictly speaking, it is not based on the solution a fundamental set of equations, but it assumes to know qualitatively their solutions in different part of the domain, and it tries to mimic them accordingly. In this respect, the scheme has to be dynamic and to follow consistently the evolution of the fluid. Then, even if the solutions are supposed to be known, the detection of the conditions where they can be applied is on the most challenging part of the scheme. If this aspect is what makes these schemes very efficient from a computational point of view, it is also their biggest limit: a leakage scheme, to

be accurate, requires a calibration solution, where its free parameters can be set and the overall agreement can be checked. Its reliability far from the calibration solution can be, in principle, questioned.
A leakage scheme can be defined as a top-bottom way to treat radiation: from the knowledge of the global behavior of neutrinos, it is possible to define a minimal scheme, including only the most relevant reactions and a few physical processes. Once the very basic scheme works, it is possible to add, in a progressive and controlled way, other reactions and other details, which should increase the agreement with the calibration solution. The robustness of the scheme is in its capacity to include new physics, without changing its previous, basic structure. On the other hand, the reduced amount of ingredients and their inclusion in an effective way make the evolution of the system sometimes sensitive to the details of the implementation.
Another good point of these schemes is that their general picture is usually independent of the number of spatial dimensions. Thus, even if they are often developed in one dimension, they can be adapted and exported to multi-dimensions with a relatively low effort. Moreover, their basic concepts are usually not dependent on specific aspects or details of the hydrodynamical code. So, the scheme can be passed from one code to a different one again with a reduced amount of modifications, and without changing the major aspects.
Despite its computational simplicity, such a scheme that provides accurate enough solutions, spanning different hydrodynamical regimes and long evolution periods, is not trivial to develop and to calibrate.
All these properties make the choice of developing an accurate leakage scheme an interesting and fruitful one: due to its relatively low computational cost, it can be used for large parameter space exploration; due to its adaptivity, it can be implemented in very elaborate hydrodynamical codes in multi-dimensions, or in codes where a standard treatment for neutrino transport is still not available.

Modern leakage schemes have a central quantity, on which almost all the others depend: the *optical depth*. The optical depth τ (which will be discussed in more detail in the next Chapter) is defined as the path integral of the inverse mean free path:

$$\tau_\gamma = \int_\gamma \frac{1}{\lambda}\,\mathrm{d}s \tag{2.1}$$

calculated on a suitable path γ. From a physical point of view, it is a measure of the global opacity of a certain radiation (photons or neutrinos), where "global" means that it is measured in relation with the whole system, and not just on the local properties of matter. It counts the number of interactions that a radiation particle experiences, before leaving the system. Let's assume to consider a neutrino emitted in one point of the system, of which we know everywhere the optical depth τ. We distinguish between three cases:

- $\tau \gg 1$; in this case, the radiation particle is in a diffusive regime, because it can not stream out freely, but it has to diffuse, interacting several times with matter, before reaching more transparent areas. In the case where the diffusive timescale is even larger than the typical dynamical timescale, the radiation can be considered *trapped*. Due to the kind of interactions that provide neutrino opacity, the radiation can be in thermal equilibrium or not with the matter: in case of

production processes (like the production of an electron neutrino due to electron capture on a proton) or scattering with particles with (total) energy similar to the energy of the neutrino, the interaction is very effective in exchanging energy between the radiation and the fluid, and neutrinos are in thermal equilibrium; if the interaction is not able to exchange energy in an efficient way (like in the case of scattering on very massive particles), the radiation field is practically thermically decoupled from matter. Due to the very low cross section of neutrino interactions, a plasma needs extreme conditions of densities and temperature to be able to trap neutrinos.

- $\tau \sim 1$; this is the most complicated regime, known as *semi-transparent* regime, where neutrinos just make a few interactions, before leaving. A detailed balance between the local radiation density, the rate of production and a rate of diffusion is here needed.

- $\tau \lesssim 1$; this is called *free streaming* regime. In this case, radiation particles that are produced just stream out freely, almost with no interaction with matter.

From the local properties of matter, it is possible to calculate the rates at which neutrinos are emitted (and also absorbed); we call these rates production (absorption) rates, $R_{\mathrm{prod},\nu}$ ($R_{\mathrm{ab},\nu}$), and we assume to express them in units of [particles/g/s]. In the diffusive regime, we have that, due to the high temperature and high density, the production rates are extremely high, as well as their inverse absorption reactions. If the interactions with matter limit the possibilities for neutrinos to stream away, they will stay within the fluid elements, forming a Fermi gas in thermal equilibrium with matter. If the rates are high enough (and this has to happen in order to have a diffusive neutrino gas in thermal equilibrium), they almost cancel each other. The net difference is just the necessary rate to form the gas and, eventually, replace neutrinos leaving the fluid element. Due to temperature and density (both matter and electron density) gradients inside the plasma, the rates are not the same everywhere, but vary locally. The random motions of radiation particles, together with these slightly different rates, create a net flux of neutrinos from the more to the less opaque regions. This rate is called *diffusion rate*, $R_{\mathrm{diff},\nu}$, expressed, for example, in [particles/g/s]. If t_{diff} is the diffusion timescale, the rate and the timescale are related by

$$R_{\mathrm{diff},\nu} \approx \rho \frac{n_\nu}{t_{\mathrm{diff}}} \tag{2.2}$$

where n_ν is the volume density of neutrinos and ρ the density of matter.
On the other hand, in the opposite extreme case of free streaming neutrinos, the reaction rates are not high enough to provide equilibrium between emission and absorption, as well as to limit the effective speed of neutrinos. In these conditions, the emitted neutrinos do not interact locally with matter, do not form a gas, but they leave the fluid element keeping their properties untouched (for example, maintaining their production energy spectrum). In this regime, the definition of a diffusion rate could be inconsistent. However, it is possible to extend the previous definition, estimating the diffusion rate that a neutrino gas *should* have if it were trapped and in equilibrium with matter at the typical thermodynamical conditions characterizing the free streaming regime. Considering the fact that the diffusive timescale tends to the smaller free streaming one

in a transparent medium, and that the production rate is usually not high enough to contrast neutrino emission in forming a local gas, the (potential) diffusive rates is here expected to be larger than the production one.
Thus, we can summarize these two situations in the table 2.1.

τ	Expected regime and rate	R_{prod}, R_{ab}	R_{diff}
$\tau \gg 1$	diffusive: R_{diff}	very high, to provide opacity and a Fermi gas of ν	much lower than the production rate
$\tau < 1$	free streaming: R_{prod}	relatively low production, and lower absorption	(potentially) higher than the production

Table 2.1: Summary of the main rates properties in the optically thick and optically thin regimes.

The intermediate situation (the semitransparent regime, where $\tau \sim 1$) does not fall in any of the previous cases. The modeling of that regime is very challenging, and probably only a detailed solution of the Boltzmann equation can describe the subtle behavior of the neutrino distribution functions in that regions, where production, absorption and diffusion really compete. Every leakage scheme has to provide a smooth, conservative interpolation in that regime, without pretending to describe what really happens there; but just contenting of not overestimating the emission of neutrinos from that area.

Traditionally, leakage schemes have been associated with the treatment of the main aspects of neutrino cooling processes. The inclusion of heating terms, both for the diffusive and the free streaming regime, has posed always great problems. We mention, mainly, two of them: the first one is the non-local aspect of the heating process: neutrino re-absorption usually happens in a place far from the production place. The modeling of non-local phenomena usually limits the computational efficiency of a scheme. The second one is the fact that the process of absorption in relatively cold regions is very sensitive to the energy of the neutrino emitted by the hot and dense cooling regions. Being based on the local properties of matter, the energy of the emitted neutrinos are not affected by the important thermalization processes which usually happens during diffusion. This lack translates into too hard neutrino spectra, which enhance artificially (i.e., overestimating) the absorption rates.

The new treatment we have developed would like to be a synthesis of all the aspects we have briefly mentioned: a computationally and conceptually inexpensive scheme, which includes all the relevant neutrino physics and processes, and which can be adapted to different codes, different dimensions, different geometries and even different astrophysical scenarios. It differs from most of the previous leakage schemes because it retains information, not only about the neutrino flavor, but also about the neutrino energy (i.e., it is a spectral scheme, where neutrinos with different energies are treated separately). Moreover, we tried also to include a simplified, but physically motivated, model of the diffusion and thermalization process, in order to take into account also a heating term. In the next section, we will describe the grey scheme, which has been our staring point.

Then, we will describe the new spectral, advance scheme we have developed, and we will calibrate/validate it against detailed spherically symmetric core collapse supernova simulation, performed solving the Boltzmann equation for neutrino transport.

2.2 Our starting point: a previous leakage scheme

The starting point of the new treatment is a grey leakage scheme, currently used by Stephan Rosswog in his SPH simulations. This scheme has been developed by Stephan Rosswog and Matthias Liebendörfer, and its description can be found in the appendix of [137]. This appendix is here summarized and reported, in the spirit of introducing some relevant concepts for the new scheme.
We mention also that this scheme is similar to another leakage scheme, which was developed also in the context of neutron star merger, and whose description can be found in the appendix of [143]. Nevertheless, some important differences are present.

The goal of the scheme is to provide effective neutrino cooling rates, both for energy and for particles emission. The *effective* emission rates are obtained as smooth interpolations between *diffusion* and local *production* rates. If we denote for a given neutrino species ν_i the number emission rates by R_{eff,ν_i} per volume and energy emission rates per volume by Q_{eff,ν_i}, the prescription for the effective rates reads

$$R_{\mathrm{eff},\nu_i} = R_{\mathrm{prod},\nu_i}\left(1+\frac{R_{\mathrm{prod},\nu_i}}{R_{\mathrm{diff},\nu_i}}\right)^{-1} \tag{2.3}$$

$$Q_{\mathrm{eff},\nu_i} = Q_{\mathrm{prod}\nu_i}\left(1+\frac{Q_{\mathrm{prod},\nu_i}}{Q_{\mathrm{diff},\nu_i}}\right)^{-1}. \tag{2.4}$$

The quantities labeled by "prod" denote the locally produced rates of number and energy, while the label "diff" refers to the diffusion rates. In the transparent regime, where the diffusion timescale t_{diff,ν_i} is short, and therefore $R_{\mathrm{diff},\nu_i} \gg R_{\mathrm{prod},\nu_i}$ and $Q_{\mathrm{diff},\nu_i} \gg Q_{\mathrm{prod},\nu_i}$, all the locally produced neutrinos stream out freely. In the very opaque regime, where t_{diff,ν_i} is large, the neutrinos leak out on the diffusion timescale. Therefore both limits are treated correctly, the regime in between these limits is handled via interpolation.
In the following, we will present the way in which the different rates are calculated.

2.2.1 Free Emission Rates

In the following expressions, the electron mass and the nucleon mass difference, $Q = m_n - m_p = 1.2935$ MeV have been neglected, in all the cross sections [166]. Moreover, neutrinos are assumed to be in thermal equilibrium with matter; thus, the neutrino temperature is identical to the local matter temperature; where it is needed, neutrinos are assumed to follow a Fermi-Dirac distribution. The chemical potentials of the $\nu_{\mu,\tau}$ are generally assumed to vanish, while for ν_e and $\bar{\nu}_e$ weak equilibrium values apply

$$\mu_{\nu_e} = -\mu_{\bar{\nu}_e} = \bar{\mu}_e - \hat{\mu} - Q, \tag{2.5}$$

wherever they occur in the sequel. Here $\bar{\mu}_e$ is the electron chemical potential (with rest mass) and $\hat{\mu}$ is the difference in the neutron and proton chemical potentials (without

rest mass). Degeneracy parameters μ_i/T are denoted by η_i, (temperatures are always in units of energies).
With these approximations and ignoring momentum transfer to the nucleon, the *electron capture* rate per volume reads

$$R_{\mathrm{EC}} = \beta\, \eta_{pn} T^5 F_4(\eta_e),, \tag{2.6}$$

with

$$\beta = \frac{\pi}{h^3 c^2} \frac{1+3\alpha^2}{(m_e c^2)^2} \sigma_0. \tag{2.7}$$

Here h is Planck's constant and c the speed of light, $\alpha \approx 1.25$, m_e is the electron mass, $\sigma_0 \approx 1.76 \cdot 10^{-44}\mathrm{cm}^2$. F_n is a Fermi integral given by

$$F_n(z) = \int_0^\infty \frac{x^n dx}{e^{x-z}+1}. \tag{2.8}$$

The factor η_{pn} given by

$$\eta_{pn} = \frac{n_n - n_p}{\exp(\hat{\mu}/T) - 1}, \tag{2.9}$$

takes into account the nucleon final state blocking and reduces in the non-degenerate limit to the proton number density n_p, n_n refers to the neutron number density. Following the analogous procedure, one finds for the energy emission rate

$$Q_{\mathrm{EC}} = \beta\, \eta_{pn} T^6 F_5(\eta_e), \tag{2.10}$$

and for the mean energy of the emitted neutrinos

$$\langle E_{\nu_e} \rangle_{\mathrm{EC}} = \frac{Q_{EC}}{R_{EC}} = T \frac{F_5(\eta_e)}{F_4(\eta_e)}. \tag{2.11}$$

The corresponding rates for *positron captures* read

$$R_{\mathrm{PC}} = \beta\, \eta_{np} T^5 F_4(-\eta_e), \tag{2.12}$$

$$Q_{\mathrm{PC}} = \beta\, \eta_{np} T^6 F_5(-\eta_e), \tag{2.13}$$

$$\langle E_{\bar{\nu}_e} \rangle_{PC} = T \frac{F_5(-\eta_e)}{F_4(-\eta_e)}, \tag{2.14}$$

where η_{np} is obtained from η_{pn} by interchanging the neutron and proton properties.
The "thermal" processes are taken into account via fit formula. For the energy emission from the *pair process*, the prescription of [57] can be easily used. The number emission rate is obtained by dividing by the mean energy per neutrino pair, given by [25]:

$$\langle E_{\nu_i \bar{\nu}_i} \rangle_{\mathrm{pair}} = T \left(\frac{F_4(\eta_e)}{F_3(\eta_e)} + \frac{F_4(-\eta_e)}{F_3(-\eta_e)} \right). \tag{2.15}$$

The total production rate is obtained just summing up all the rates of the relevant reactions:

$$R_{\mathrm{prod},\nu_e} = R_{\mathrm{EC}} + \frac{1}{2} R_{\mathrm{pair}} \tag{2.16}$$

$$R_{\mathrm{prod},\bar{\nu}_e} = R_{\mathrm{PC}} + \frac{1}{2} R_{\mathrm{pair}} \tag{2.17}$$

$$R_{\mathrm{prod},\nu_{\mu,\tau}} = \frac{1}{2} R_{\mathrm{pair}} \tag{2.18}$$

2.2.2 Diffusive Emission Rates

The dominant sources of opacity are

(i) neutrino nucleon scattering:

$$\nu_i + \{n, p\} \rightarrow \nu_i + \{n, p\} \tag{2.19}$$

with $\sigma_{\nu_i,\mathrm{nuc}} = \frac{1}{4}\sigma_0 \left(\frac{E_{\nu_i}}{m_e c^2}\right)^2$

(ii) coherent neutrino nucleus scattering:

$$\nu_i + A \rightarrow \nu_i + A \tag{2.20}$$

with $\sigma_{\nu_i,A} = \frac{1}{16}\sigma_0 \left(\frac{E_{\nu_i}}{m_e c^2}\right)^2 A^2(1 - Z/A)^2$.
Here A and Z are the nucleon and proton number of the average nucleus provided by the nuclear equation of state. Due to the A^2-dependence of the cross section this process will dominate as soon as a substantial fraction of heavy nuclei is present.

Electron type neutrinos additionally undergo

(iii) neutrino absorption:

$$\nu_e + n \rightarrow p + e^- \tag{2.21}$$
$$\bar{\nu}_e + p \rightarrow n + e^+ \tag{2.22}$$

with $\sigma_{\nu_e,n} = \frac{1+3\alpha^2}{4}\sigma_0 \left(\frac{E_\nu}{m_e c^2}\right)^2 \langle 1 - f_{e^-}\rangle$,
and $\sigma_{\bar{\nu}_e,p} = \frac{1+3\alpha^2}{4}\sigma_0 \left(\frac{E_{\bar{\nu}}}{m_e c^2}\right)^2 \langle 1 - f_{e^+}\rangle$,

where

$$\langle 1 - f_{e^-}\rangle \approx (\exp(\eta_e - F_5(\eta_{\nu_e})/F_4(\eta_{\nu_e})) + 1)^{-1}$$

and

$$\langle 1 - f_{e^+}\rangle \approx (\exp(-\eta_e - F_5(\eta_{\bar{\nu}_e})/F_4(\eta_{\bar{\nu}_e})) + 1))^{-1}$$

are good approximations for the Pauli blocking factors.

Once the cross sections have been calculated, the local mean free path is given by

$$\lambda_{\nu_i}(E) = \left(\sum_r n_r \sigma_r(E)\right)^{-1} \equiv (E^2 \zeta_{\nu_i})^{-1}, \tag{2.23}$$

where the n_r denote the target number densities, the index r runs over the reactions given above with cross-sections σ_r and E is the neutrino energy. The dependence of the cross-sections on the squared neutrino energies has been separated out in the definition of ζ_{ν_i}. The optical depth, τ, along a specified path is then given as

$$\tau_{\nu_i}(E) = \int_{x1}^{x2} \frac{dx}{\lambda_{\nu_i}(E)}. \tag{2.24}$$

In this original scheme, the optical depths are evaluated in axisymmetry, using a local ray-by-ray approach, i.e. along three directions from each grid point: in Z-direction ($\tau^1_{\nu_i}$), i.e. parallel to the rotational axis, along the outgoing diagonal ($\tau^2_{\nu_i}$) and along the ingoing diagonal ($\tau^3_{\nu_i}$). The finally used optical depth, (τ_{ν_i}), is the minimum of the three, $\tau_{\nu_i} = \min(\tau^1_{\nu_i}, \tau^2_{\nu_i}, \tau^3_{\nu_i})$. Note that the quantity χ is independent of the neutrino energy and the (energy dependent) optical depth is given by

$$\tau_{\nu_i}(E) = E^2 \mathrm{min}_d(\chi^d_{j,\nu_i}) \equiv E^2 \chi_{j,\nu_i}. \tag{2.25}$$

The diffusion rate depends on the optical depth τ_{ν_i}. We base our estimates on a very simple, one-dimensional diffusion model. Along one propagation direction, we assume equal probabilities for forward and backward scattering and impose strict flux conservation in a stationary state situation. This leads to the following relationship between the neutrino density $J(E)$ and the neutrino number flux $H(E)$,

$$\frac{H_{\nu_i}(E)}{cJ_{\nu_i}(E)} = \frac{1}{2\tau_{\nu_i}(E)+1}. \tag{2.26}$$

This relationship was tested against a complete numerical solution of the diffusion equation (e.g., in a supernova environment where all relevant opacities are included) and an agreement to about a factor of two was found. If the thermodynamical conditions and the neutrino densities along the propagation direction are set, relation (2.26) defines a local neutrino number flux $H_{\nu_i}(E)$ which in general no longer obeys flux conservation in a stationary state situation. Assuming that we still have a stationary state situation and that the fluxes are locally well represented, we can use the balance of fluxes across a infinitesimally thin layer perpendicular to the propagation direction to obtain an estimate of the rate R_{ν_i} of neutrinos produced in this layer. Denoting the propagation direction with x, we express the rate in terms of the prevailing neutrino density and a diffusion time scale $t_{\mathrm{diff},\nu_i,x}$ with

$$R_{\mathrm{diff},\nu_i}(E) = \frac{\partial H_{\nu_i}(E)}{\partial x} = \frac{J_{\nu_i}(E)}{t_{\mathrm{diff}\nu_i}(E)}. \tag{2.27}$$

The substitution of eq. (2.26) for H_{ν_i} leads to spatial derivatives of the neutrino density $J_{\nu_i}(E)$ and the optical depth τ_{ν_i}. As the latter is given by the negative inverse mean free path, $-1/\lambda_{\nu_i}(E)$, eq. (2.27) can be solved for the diffusion time scale according to

$$t_{\mathrm{diff},\nu_i}(E) = \frac{2\tau_{\nu_i}(E)+1}{c}\left(\frac{\partial \ln J_{\nu_i}(E)}{\partial x} + \frac{2}{(2\tau_{\nu_i}(E)+1)\,\lambda_{\nu_i}(E)}\right)^{-1}. \tag{2.28}$$

This estimate can be re-written with a distance parameter, $\Delta x(E)$, to obtain

$$t_{\mathrm{diff},\nu_i}(E) = \frac{\Delta x_{\nu_i}(E)}{c}\left(2\tau_{\nu_i}(E)+1\right), \tag{2.29}$$

$$\Delta x_{\nu_i}(E) = \left(\frac{\partial \ln J_{\nu_i}(E)}{\partial x} + \frac{2}{(2\tau_{\nu_i}(E)+1)\,\lambda_{\nu_i}(E)}\right)^{-1}. \tag{2.30}$$

In our scheme Δx defines the effective width of a layer drained by the diffusive flux, i.e. provides the conversion between a net emitted neutrino flux (number/s/cm^2) and

a production rate (number/s/cm^3). The spatial derivative of the neutrino density in eq. (2.30) is quite inconvenient, one would prefer a diffusion timescale that does not depend on neutrino densities. Hence, this term has been neglected. In physical terms this means that neutrino sources keep the neutrino density close to constant over a spatial interval where the mean free path changes significantly. The expression for the distance parameter, however, greatly simplifies to

$$\Delta x_{\nu_i}(E) = \left(\tau_{\nu_i}(E) + \frac{1}{2}\right)\lambda_{\nu_i}. \tag{2.31}$$

If we go back and use $\tau_{\nu_i} \sim 1$ for the "last interaction region" to simplify eq. (2.26) further by the approximation

$$\frac{H_{\nu_i}(E)}{cJ_{\nu_i}(E)} = \frac{1}{3\tau_{\nu_i}(E)},$$

we obtain

$$t_{\mathrm{diff},\nu_i}(E) = 3\frac{\Delta x_{\nu_i}(E)}{c}\tau_{\nu_i}(E) \tag{2.32}$$

by the same analysis used to derive eq. (2.29). However, the distance parameter is then given by

$$\Delta x_{\nu_i}(E) = \tau_{\nu_i}(E)\lambda_{\nu_i}(E). \tag{2.33}$$

The equations (2.32) and (2.33) have been chosen as final expressions because the linear dependence in τ_{ν_i} allows the extraction of the energy dependence as in eq. (2.25).

Approximating the neutrino distribution function in the high-density regime with a thermal equilibrium distribution, the application of the diffusion timescale leads to an estimation of the diffusion rates

$$R_{\mathrm{diff},\nu_i} = \int_0^\infty \frac{\tilde{n}_{\nu_i}(E)}{t_{\mathrm{diff},\nu_i}(E)}dE = \frac{4\pi c g_{\nu_i}}{(hc)^3}\frac{\zeta_{\nu_i}}{3\chi_{\nu_i}^2}TF_0(\eta_{\nu_i}) \tag{2.34}$$

$$Q_{\mathrm{diff},\nu_i} = \int_0^\infty \frac{E\tilde{n}_{\nu_i}(E)}{t_{\mathrm{diff},\nu_i}(E)}dE = \frac{4\pi c g_{\nu_i}}{(hc)^3}\frac{\zeta_{\nu_i}}{3\chi_{\nu_i}^2}T^2F_1(\eta_{\nu_i}) \tag{2.35}$$

with

$$\langle E_{\mathrm{diff},\nu_i}\rangle = \frac{Q_{\mathrm{diff},\nu_i}}{R_{\mathrm{diff},\nu_i}} = T\frac{F_1(\eta_{\nu_i})}{F_0(\eta_{\nu_i})}. \tag{2.36}$$

Here $\tilde{n}_{\nu_i}(E)$ is related to the number density by $n_{\nu_i} = \int_0^\infty \tilde{n}_{\nu_i}(E)dE$. The statistical weights g_{ν_i} are 1 for ν_e and $\bar{\nu}_e$ and 4 for ν_x. After the second equals sign in eqs. (2.34) and (2.35) we have inserted the explicit estimate (2.32) for the diffusion time scale and (2.33) for the distance parameter.

2.2.3 Application: a grey leakage scheme for $\nu_{\mu,\tau}$ and $\bar{\nu}_{\mu,\tau}$ neutrinos

The leakage scheme which was presented in the previous section, has been implemented for the $\nu_{\mu,\tau}$ neutrinos and their antiparticles $\bar{\nu}_{\mu,\tau}$, in the context of core collapsing supernovae. The goal was the implementation of a local cooling term, which could take into

account the important release of energy, due these neutrinos species, in three dimensional CCSN simulations, performed with the ELEPHANT supernova model. This model is built from different codes: the outer stellar layers are evolved in spherical symmetry by the implicit general relativistic hydrodynamics code AGILE [87] . The innermost part of the simulation, extending to about 500 km radius, is covered by an equidistant three-dimensional Cartesian mesh. The state vector in this inner 3D computational domain is evolved by our code FISH [63], which solves the MHD equations. FISH implements a Riemann-solver-free central method, where the magnetic field is guaranteed to be solenoidal by a dimensionally split constrained transport method. The algorithm is second order accurate in both, space and time. A newly developed general method for the treatment of the gravitationally induced source terms near steady states reduces the dissipation of the advection scheme in the PNS to a minimum. A more extended description of this code will be provide in Chapter 4. FISH includes a spherical approximation to the solution of the Poisson equation for self-gravity. Full 3D solution algorithms are currently being implemented. For all variants, general relativistic effects are approximated by an effective potential [89], that takes the dominant monopole term into account. Spectral neutrino transport for the electron flavor neutrinos is treated by the IDSA [88]. The IDSA features 3D advection, diffusion and compressional heating of trapped neutrinos, and it retains the spectral information of outstreaming neutrinos. The advection of the trapped neutrinos is evolved together with the hydrodynamics, while the diffusion of neutrinos and the evolution of the magnetic field is operator split. The outstreaming neutrinos provide a spherically symmetric background flux from which neutrinos are absorbed in the semi-transparent and optically thin regime. A consistent solution between the split diffusion and outstreaming/absorption updates is found by iterations within each time step. In the spirit of investigating the delayed neutrino-driven explosion mechanism, the emission and the absorption of electron neutrinos and antineutrinos have to be modeled with great care. On the other hand, $\nu_{\mu,\tau}$ and $\bar{\nu}_{\mu,\tau}$ interact only via neutral current reactions with matter in CCSNe. Then, their role is mainly to cool the protoneutron star, without interacting further with the accreting layers, once they have been emitted from the neutrino surface. This is the reason why we decided to implement a leakage scheme to model them.

The scheme estimates the energy released by each fluid elements, interpolating the production and the diffusion rates, according to Eq.(2.4). Because of the neutral current reactions, the lepton number is assumed to be always 0 (i.e., the amount of emitted neutrinos and antineutrinos always balance). For these reason, we just focus on the energy rates, and we neglect the number rates. The reaction which is considered as the main source of neutrinos is the pair production:

$$e^+ + e^- \rightarrow \nu_{\mu,\tau} + \bar{\nu}_{\mu,\tau}$$

The associated production rates are calculated using the interpolating formulae provided by [57], which give directly the production rate, once the thermodynamical conditions are specified:

$$(\rho, T, Y_e) \rightarrow R_{\text{prod}}$$

where ρ is the matter density, T the temperature and Y_e is the electron fraction. Other processes are relevant for the production of those neutrinos in the centre of CCSNe,

mainly the neutrino bremsstrahlung and the pair production from electron neutrino-antineutrino annihilation,

$$\begin{aligned} N + N &\rightarrow N + N + \nu_{\mu,\tau} + \bar{\nu}_{\mu,\tau} \\ \nu_e + \bar{\nu}_e &\rightarrow \nu_{\mu,\tau} + \bar{\nu}_{\mu,\tau} \end{aligned}$$

It has been shown that these processes have even larger rates, compared with electron-positron annihilation, [15] and [162]. But these processes are dominant deep inside the neutrinosphere. There, we do not need to model the production rates correctly: they just need to be higher than the diffusive rates. Outside the neutrinosphere, in the transparent region, electron-positron annihilation is the most relevant source of neutrinos. This is why we included only that reaction. To model the diffusive process, we need the most relevant opacity sources. Neglecting any distinction between thermalization and elastic scattering processes, we include the scattering on nucleons and on nuclei, as the major opacity source. The diffusion timescale is calculated according to the prescription 2.32, but we write it in this form:

$$t_{\mathrm{diff},\nu_i}(E) = \alpha_{\mathrm{diff}} \frac{\Delta x_{\nu_i}(E)}{c} \tau_{\nu_i}(E) \tag{2.37}$$

keeping α_{diff} as a free parameter ($\alpha_{\mathrm{diff}} \sim 1$), whose value has to be defined by comparison with detailed simulations. From the diffusion timescale, the diffusion rates are calculated according to 2.35, where

$$n_{\nu_{\mu,\tau}}(E) = \frac{4\pi}{(hc)^3} \frac{1}{1 + \exp(E/T)} E^2$$

(the chemical potential is assumed to be 0 for $\nu_{\mu,\tau}$ and $\bar{\nu}_{\mu,\tau}$).

As a first step, the scheme was implemented in the spherically symmetric CCSN model `AGILE-BOLZTRAN` [87]. `BOLZTRAN` is a multiflavor spectral neutrino transport code, which solves the Boltzmann equation for ν_e, $\bar{\nu}_e$, $\nu_{\mu,\tau}$ and $\bar{\nu}_{\mu,\tau}$, assuming spherically symmetric hydrodynamics. `BOLZTRAN` solves the transport equation using finite differences, on a grid with is centered in the zones evolved (at the edges) by the AGILE code [98, 85, 87, 84, 81]. The energy spectrum is usually discretized with 20 energy bins, which cover the interval $3\mathrm{MeV} \leq E_\nu \leq 300\,\mathrm{MeV}$; the local neutrino direction is discretized by N_θ propagation angles θ, which are the angles between the possible neutrino momenta and the local radial direction. Typical values for N_θ go from 2, in the case of test runs, to 4 or 6 in the case of production runs. We added the grey leakage scheme, as an alternative to the `BOLZTRAN` treatment for $\nu_{\mu,\tau}$ and $\bar{\nu}_{\mu,\tau}$, while we kept the ν_e and $\bar{\nu}_e$ `BOLZTRAN` treatment untouched. The scheme calculated the effective energy rates for a single neutrino species; the result is, then, multiplied by four (because of the four species); then it is added to the energy variation due to ν_e and $\bar{\nu}_e$, and passed to the hydrodynamical code.
We performed simulations using Lattimer-Swesty equation of state, with nuclear compressibility $K = 180\mathrm{MeV}$; as initial profile, we took a $15M_\odot$ progenitor model from Woosley and Weaver (1995). We performed two simulations with the full `AGILE-BOLZTRAN` code: the first one with all neutrino species included and with all the implemented reactions (in particular, neutrino pair production, neutrino bremsstrahlung and neutrino electron scattering for $\nu_{\mu,\tau}$ and $\bar{\nu}_{\mu,\tau}$). The second one, only with ν_e and $\bar{\nu}_e$, without any

treatment for the heavy flavor neutrinos.
The first simulation was assumed to be our calibration model. The second one is a useful comparison model, to see when and how much $\nu_{\mu,\tau}$ and $\bar{\nu}_{\mu,\tau}$ neutrinos affect the evolution of the model. Then, we re-started the first simulation just after bounce, and we performed several different runs with `AGILE-BOLZTRAN` for the electron flavor neutrinos, and the leakage scheme to take into account heavy flavor neutrino emission. We varied the $\alpha_{\rm diff}$ parameter, to find the closest agreement. We report here some snapshots, taken at different time after bounce. To compare different models, we decided to compare directly the different radial profiles of four relevant hydrodynamical quantities: the fluid radial velocity, the matter density, the fluid entropy and the electron fraction. We plot on the same graphs four different models: the two full `AGILE-BOLZTRAN` calculations, and two models with the leakage scheme for $\nu_{\mu,\tau}$ and $\bar{\nu}_{\mu,\tau}$, one with $\alpha_{\rm diff} = 3$ and the other with $\alpha_{\rm diff} = 6$. We consider four different times after bounce, representing different moments and conditions in the system evolution: $t$pb $= 50$ ms, which is still close to bounce and which is for sure located at the end of the prompt shock expansion phase; $t_{\rm pb} = 100$ ms, which is at the beginning of the ν_e and $\bar{\nu}_e$ heating phase;$t_{\rm pb} = 250$ ms, which is located at the end of the ν_e and $\bar{\nu}_e$ heating phase; and, finally, $t_{\rm pb} = 500$ ms, which represents the late cooling phase.

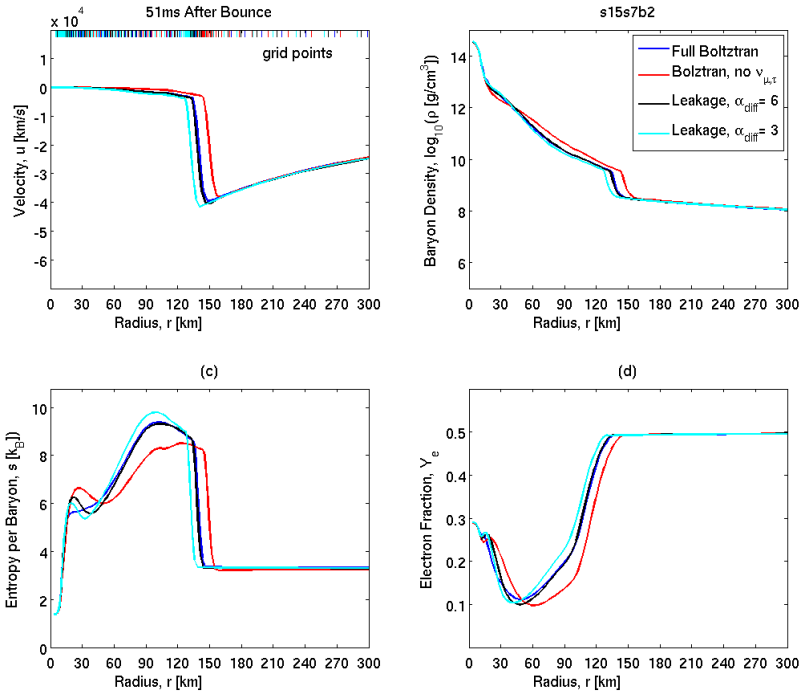

Figure 2.1: Comparison between our reference case (full `AGILE-BOLZTRAN` run, blue lines), a test case without $\nu_{\mu,\tau}$ and $\bar{\nu}_{\mu,\tau}$ (red lines), and two runs with the leakage scheme for heavy flavor neutrinos presented in the text, with two different parameters diffusion parameter, $\alpha_{\rm diff} = 6$ (black lines) and $\alpha_{\rm diff} = 3$ (cyan lines), at $t_{\rm pb} = 50$ ms. The plotted quantities in the panels are radial profiles of the radial velocity (top left), of the baryon density (top right), of the entropy (bottom left) and of the electron fraction (bottom right).

Up to $t_{\rm pb} = 50\,$ms the impact of $\nu_{\mu,\tau}$ and $\bar{\nu}_{\mu,\tau}$ cooling is still sub-dominant: the neutrino gas of heavy flavor neutrinos has already formed due to the high temperatures reached in the shock, but their luminosity is still smaller compared with the one of ν_e and $\bar{\nu}_e$. This is visible in the small distance in the shock position between the two reference simulations in Fig. 2.1. In the next 50 ms, neutrino cooling due to $\nu_{\mu,\tau}$ and $\bar{\nu}_{\mu,\tau}$ becomes more and more relevant, so that the model without them has a shock position which is displaced by more than 30km from the reference run Fig. 2.2. Differences between the two leakage runs arise: the $\alpha_{\rm diff} = 3$ case looks more pessimistic, because it leads to higher luminosities. Due to the higher cooling rate, the protoneutron star shrinks more rapidly, with larger entropy (and larger temperature). At $t_{\rm pb} = 250\,$ms, all the differences previously introduced, have increased dramatically, highlighting the importance of having a good estimation for $\nu_{\mu,\tau}$ and $\bar{\nu}_{\mu,\tau}$ cooling, Fig. 2.3. Finally, we use the profiles at $t_{\rm pb} = 500\,$ms to test that the good agreement we have found for the $\alpha_{\rm diff} = 6$ case, is not a transient feature, but it is preserved also on long timescales and in late cooling phases, Fig. 2.4.

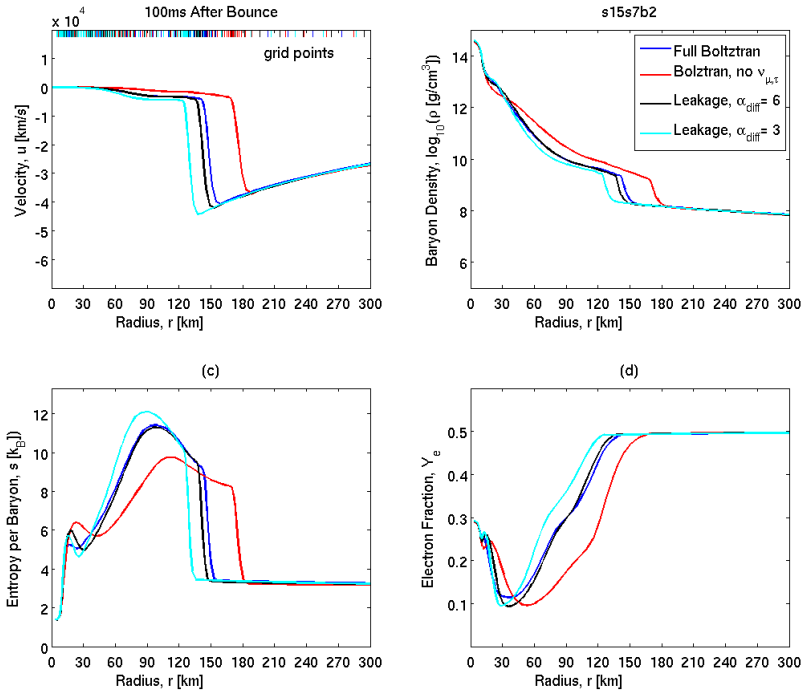

Figure 2.2: Same as figure 2.1, but at $t_{\rm pb} = 100$ms.

Overall, we can say that both the models with the leakage treatment show a good qualitative agreement; especially the one with $\alpha_{\rm diff} = 6$ is also quantitatively very close to the reference model. The larger discrepancies arise around $t_{\rm pb} \sim 250$ms, but they reduce later. Different attempts to include more physical processes and details have been made, but without increasing the agreement. In particular, an attempt to include neutrino bremsstrahlung in the non-degenerate limits was performed (using formulas taken from [124]), but the run looked too pessimistic on long timescales. Nevertheless, the assumption of thermal equilibrium inside the neutrinosphere implicitly assumes the presence of many possible equilibrium reactions (like the bremsstrahlung emission or

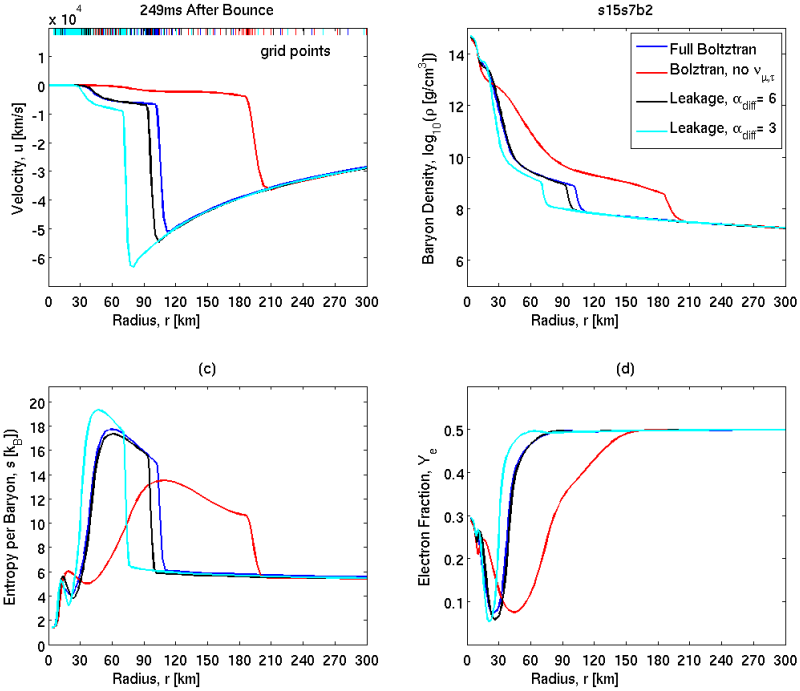

Figure 2.3: Same as figure 2.1, but at $t_{\rm pb} = 250$ms.

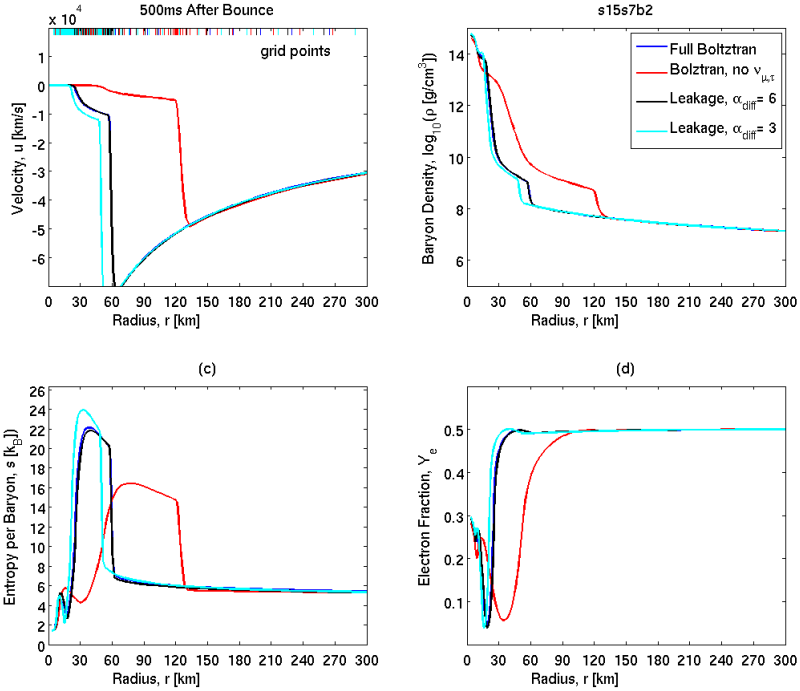

Figure 2.4: Same as figure 2.1, but at $t_{\rm pb} = 500$ms.

the neutrino-electron scattering), even without modeling explicitly the reaction rates. After this encouraging test, the leakage treatment of the emission of $\nu_{\mu,\tau}$ and $\bar{\nu}_{\mu,\tau}$

was included as a module in the ELEPHANT supernova model by Matthias Liebendörfer and Stuart Whitehouse, and also in the spherically symmetric publicly available code AGILE-IDSA, at http://www.physik.unibas.ch/∼liebend/download/index.html .

2.3 The new ASL treatment

The successful implementation of a minimal leakage scheme to treat the emission of $\nu_{\mu,\tau}$ and $\bar{\nu}_{\mu,\tau}$ in core collapse supernova models, motivated us to develop a more general neutrino treatment. We named this new scheme Advanced Spectral Leakage (ASL) treatment. The goals of the new scheme were mainly 1) to include all neutrino flavors in a consistent way; 2) to be suitable for large multidimensional simulations, in very general symmetry configurations; 3) to show a reasonable agreement with reference models, if applied to radiation transport problems of which accurate numerical solutions are available. Concerning the point 3), we decided to use spherically symmetric core collapse supernova models, obtained with the code AGILE-BOLZTRAN, as calibration models.

The first attempt in this direction was simply made by implementing the scheme presented in section (2.2) for all the three neutrino species (ν_e, $\bar{\nu}_e$ and $\nu_{\mu,\tau}$). The treatment for $\nu_{\mu,\tau}$ and $\bar{\nu}_{\mu,\tau}$ was kept the same as the one presented in 2.2.3. The implementation for the electron flavor was done using rates taken from [166] for the electron caption of protons and for the positron capture on neutrons, as reported in Sec.(2.2.1). For the opacity, we considered the inverse reactions (capture on neutrons and on protons, respectively) and the scattering on nucleons and nuclei; for their numerical values, we followed the prescription reported in 2.2.2. The new treatment was implemented in AGILE, completely parallel to BOLZTRAN. It shared with BOLZTRAN the interface with AGILE and the passed quantities were the variations of internal energy, $\dot{e}$, and electron fraction, $\dot{Y}_e$, due to neutrinos.
The scheme was tested in the core collapse supernovae scenario. We took a configuration identical to the one used to test the $\nu_{\mu,\tau}$ and $\bar{\nu}_{\mu,\tau}$ leakage scheme: a $15M_\odot$ progenitor model with Solar metallicity, from Woosley and Weaver (1995), and we used Lattimer-Swesty EOS. The collapse proceeded up to bounce, but the physical properties of the system were different from what we expected from the reference model. In particular, the electron fraction in the center was quite large ($Y_e(R=0) \approx 0.37$) and it didn't decrease any more after neutrino trapping ($\rho \gtrsim 10^{12}\mathrm{g/cm}^3$). We analyzed the results and we found these possible sources of discrepancy:

- the leakage scheme presented in the previous section estimates, with the calculation of the effective rates R_{eff}, the amount of neutrinos that leave the fluid element; they are assumed to be *instantly* emitted to infinity. But the scheme does not take into account the possibility that, in the very opaque area, electrons and positrons are converted into neutrinos, due to weak interactions, without leaving the system instantly, but forming a gas of neutrinos. Actually, the scheme, as it is, evolves the total lepton number, Y_l, which is conserved after neutrino trapping, but not the electron and the neutrino numbers individually, Y_e, Y_{ν_e}, $Y_{\bar{\nu}_e}$ and $Y_{\nu_{\mu,\tau}}$.

- the scheme is a grey scheme, i.e. it performs energy integrations of the rates to find an average behavior. While this approximation can be good for an almost steady, emitting source of neutrinos (like a protoneutron star in the late post

bounce phase), its validity can be challenged in more dynamical phases (like the collapse or the early post bounce phase, with the propagation of the shock wave in the iron core): in these phases, the local properties of matter change rapidly and detailed information about the neutrinos and their energy are required to model, for example, which neutrinos are emitted and which are trapped. For example, in Fig. 2.5, we plot the total optical depth for ν_e (left panel) and $\nu_{\mu,\tau}$ (right panel), for different values of the neutrino energy, calculated along radial rays of our reference core collapse model, at bounce. There are several notable aspects in those figures. The main ones are the broad range of optical depths that occur inside the domain (more than 10 orders of magnitude); and the large gap in τ that, at the same radius, distinguishes between low energy and high energy neutrinos. The latter difference depends on the quadratic energy dependence of neutrino cross section (in particular, at relatively low energies).

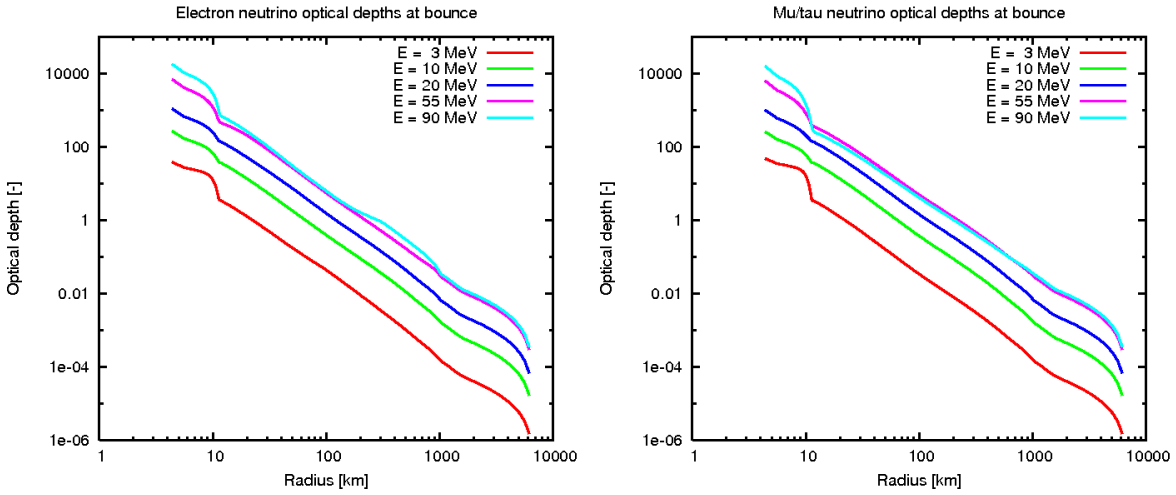

Figure 2.5: Radial profiles of the ν_e (left panel) and $\nu_{\mu,\tau}$ (right panel) optical depth, at bounce, calculated along radial paths, from opacities obtained in our CCSN reference model (see the text for details). We choose different values for the neutrino energy, ranging between 3 MeV and 90 MeV. The position of the shock wave at $R \sim 12$ km is clearly visible.

These considerations motivated us to extend the previous grey scheme to a new spectral treatment, in which, if necessary, the trapped components of the neutrinos and their temporal evolutions are also modeled.

Recently, a new approximated neutrino transport scheme was developed by Matthias Liebendörfer in Basel (the Isotropic Diffusion Source Approximation, IDSA, [88]). This transport scheme was implemented in the general relativistic, spherically symmetric hydrodynamics code `AGILE`, and tested against `AGILE-BOLZTRAN` models of CCSNe. We followed a very similar approach: we decided to implement the scheme in `AGILE`, using an interface between the hydrodynamics and the neutrino treatment which is almost identical to the one of IDSA. Then, we tested our results against `AGILE-BOLZTRAN` solutions of the same problem. Even more, `AGILE-IDSA` has been a continous source of inspiration and comparison, as well as a source of useful subroutines for the calculation of some of the neutrino rates.

The goal of this approach is also to provide a tool in which it is possible to switch between different neutrino treatments, and different levels of accuracy (for example, from a more accurate `AGILE-IDSA` ν_e,$\bar{\nu}_e$-ALS $\nu_{\mu,\tau}$, $\bar{\nu}_{\mu,\tau}$ to a less accurate `AGILE`-ASL ν_e, $\bar{\nu}_e$).

2.3.1 The coupling with the hydrodynamics and the role of the Equation of State

In the following, we will consider a hydrodynamical system at time t, which is evolving in time with a step dt. The system is described by its density $\rho(\mathbf{x}, t)$, temperature $T(\mathbf{x}, t)$ and electron fraction $Y_e(\mathbf{x}, t)$, and by its velocity field $\mathbf{v}(\mathbf{x}, t)$. To be more general, we will consider a three dimensional problem; if not explicitly stated, no symmetries are assumed. To keep the equations as simple as possible, we assume Newtonian gravity and, if not explicitly mentioned, we will consider a fix time t (so, all the temporal dependences are drop out).
The neutrinos present in the system can be fully described by their distribution functions, $f(\mathbf{x}, \mathbf{p})$. Depending on the local opacity of matter and on the local interaction rates, the behavior of these neutrinos moves between two extreme cases: they can be considered as trapped particles, when they interact locally with the fluid and on timescales shorter than any other dynamical or diffusive timescale; in this limit, they can be collectively thought of as a neutrino gas, which is almost in thermodynamical equilibrium with the fluid. On the other hand, when matter is locally transparent to them and, once they are produced, they can just stream away, at the speed of light, they can be considered as free streaming particles. When they are present, trapped neutrinos can be described isolating their contribution to the total distribution functions: this contribution is called $f^t(\mathbf{x}, \mathbf{p})$. We assume that the trapped component of f has no explicit angular dependence in the momentum space, so that its dependences become $f^t(\mathbf{x}, E)$. Integration over the neutrino phase space gives information about the particle and the energy fractions (Y_ν and z_ν, respectively) of the neutrino gas, which is embedded in the fluid and, actually, behaves like a fluid component:

$$Y^t(\mathbf{x}) = \frac{4\pi}{(hc)^3} \frac{m_b}{\rho(\mathbf{x})} \int f^t(\mathbf{x}, E) E^2 dE \tag{2.38}$$

$$Z^t(\mathbf{x}) = \frac{4\pi}{(hc)^3} \frac{m_b}{\rho(\mathbf{x})} \int f^t(\mathbf{x}, E) E\, E^2 dE \tag{2.39}$$

The dynamics of a system with matter and trapped neutrinos is given by the conservation laws of hydrodynamics:

$$\frac{\partial}{\partial t} U + \nabla \cdot F = g \tag{2.40}$$

where U is the vector of primitive variables, F the vector of fluxes and g is the source term. A possible set of primitive variables and of the related fluxed are:

$$U = \begin{pmatrix} \rho \\ \rho \mathbf{v} \\ \rho(e + \frac{1}{2}v^2) \\ \rho Y_{\mathrm{e}} \\ \rho Y^t_{\nu,\bar{\nu}} \\ \left(\rho Z^t_{\nu,\bar{\nu}}\right)^{3/4} \end{pmatrix} \qquad F = \begin{pmatrix} \mathbf{v}\rho \\ \mathbf{v}\rho\mathbf{v} + \mathbb{I}p \\ \mathbf{v}\rho\left(e + \frac{1}{2}v^2 + \frac{p}{\rho}\right) \\ \mathbf{v}\rho Y_{\mathrm{e}} \\ \mathbf{v}\rho Y^t_{\nu,\bar{\nu}} \\ \mathbf{v}\rho Z^t_{\nu,\bar{\nu}} \end{pmatrix}. \tag{2.41}$$

where e is the specific internal energy, p the fluid pressure and v is the modulus of the fluid velocity. The momentum equation and the energy equation have source terms which are related to the gravitational field, ϕ:

$$g_{\mathrm{grav}} = \begin{pmatrix} 0 \\ -\rho\,\nabla\phi \\ -\rho\mathbf{v}\cdot\nabla\phi \\ 0 \\ 0 \\ 0 \end{pmatrix} \tag{2.42}$$

which can be obtained from the Poisson equation:

$$\nabla^2\phi = 4\pi G\rho. \tag{2.43}$$

Also the interaction between neutrinos and matter provides contributions to the source term. These terms are related to the energy and particles emission in form of neutrinos, to the conversion between neutrinos and electron/positrons, and to the pressure provided by the neutrino gas in its trapped component:

$$g_\nu = \begin{pmatrix} 0 \\ \rho\dot{\mathbf{v}} \\ \rho\dot{e} \\ \rho\dot{Y}_{\mathrm{e}} \\ \rho\dot{Y}^t_{\nu,\bar{\nu}} \\ \left(\rho\dot{Z}^t_{\nu,\bar{\nu}}\right)^{3/4} \end{pmatrix}. \tag{2.44}$$

The goal of the ASL scheme is the estimation of the neutrino source term, g_ν from the actual values of the thermodynamical state U of the system.
The hydrodynamics equations (2.40) need a closure relation to be solved; this relation is provided by the Equation of State (EOS). More explicitly, the EOS can be seen as a known function, whose arguments are a set of three independent thermodynamical parameters, which specifies univocally the thermodynamical state of the system; they can be, for example, density, temperature and electron fraction:

$$(\rho \quad T \quad Y_{\mathrm{e}})_{\mathrm{EOS\,in}}. \tag{2.45}$$

The EOS provides the specific internal energy of matter $e\,[\mathrm{erg/g}]$, and the pressure $p\,[\mathrm{erg/cm^3}]$, which are directly needed for the hydrodynamics equations; but also several

other quantities can be obtained from the EOS and some of them will be important for the neutrino treatment: the abundances of all considered particle species (protons $Y_{\rm p}$, neutrons $Y_{\rm n}$, alpha particles Y_α and heavy nuclei $Y_{\rm h}$), the electron chemical potential μ_e[MeV], the difference between the proton and neutron chemical potential $\hat{\mu}$[MeV] and the entropy per baryon $s_{\rm b}$ [$k_{\rm B}$/baryon]. So, we indicate the EOS output as

$$(e \quad p \quad Y_{\rm p} \quad Y_{\rm n} \quad Y_\alpha \quad Y_{\rm h} \quad \mu_{\rm e} \quad \hat{\mu} \quad s_{\rm b})_{\rm EOS\,out}. \tag{2.46}$$

Summarizing the interplay between the hydrodynamics and the neutrino treatment, we can conclude that the quantities which are needed as input are:

$$\big(\rho(\mathbf{x}) \quad Y_{\rm e}(\mathbf{x}) \quad T(\mathbf{x}) \quad Y_\nu^t(\mathbf{x}) \quad Z_\nu^t(\mathbf{x})\big)_{\rm leaklage\,in} \tag{2.47}$$

where

- ρ[g/cm^3] is the matter local density;
- $Y_{\rm e}$[particels/baryon] is the local electron abundance;
- T[MeV] is the local matter temperature;
- Y_ν^t[particles/baryon] is the local trapped neutrino fraction;
- Z_ν^t[MeV/baryon] is the energy per baryon stored in the local trapped neutrinos.

And the quantities which are determined by the neutrino treatment and which are given back to the hydrodynamics are:

$$\Big(\dot{e}(\mathbf{x},t) \quad \dot{Y}_{\rm e}(\mathbf{x},t) \quad \dot{\mathbf{v}}(\mathbf{x},t) \quad \dot{Y}_\nu^t(\mathbf{x},t) \quad \dot{Z}_\nu^t(\mathbf{x},t)\Big)_{\rm leakage\,out}. \tag{2.48}$$

More explicitly,

- $\dot{e}$ [erg/g/s] is the rate of variation of internal energy, due to neutrino emission, absorption and diffusion;
- $\dot{Y}_e$ [particles/g/s] is the rate of variation of electron fraction due to neutrino processes;
- $\dot{\mathbf{v}}$ [cm/s^2] is the stress given by the trapped neutrinos and by the outgoing neutrino flux;
- $\dot{Y}_\nu^t$ [particles/baryon/s] is the variation of the trapped neutrino fraction;
- $\dot{Z}_\nu^t$ [MeV/baryon/s] is the variation of the energy per baryon stored in the trapped neutrinos.

2.3.2 Overview of the scheme

In this section, we present an overview on the neutrino treatment contained. A more detailed description of some part of it will be done in the next paragraphs.
The scheme is designed for ν_e, $\bar{\nu}_e$ and $\nu_{\mu,\tau}$ and $\bar{\nu}_{\mu,\tau}$. μ and τ neutrinos, as well as their antiparticles, are treated in the same way. So, for compactness, we will refer to them simply as $\nu_{\mu,\tau}$. For each neutrino species, we perform a spectral treatment, i.e. we distinguish between particles of different energies and we express all the main quantities as a function of the particle energy.
The initial hydrodynamical state is characterized by the set of quantities (2.47):

$$\Big(\rho(\mathbf{x}) \quad Y_{\mathrm{e}}(\mathbf{x}) \quad T(\mathbf{x}) \quad Y^t_{\nu_e,\bar{\nu}_e,\nu_{\mu,\tau}}(\mathbf{x}) \quad Z^t_{\nu,\bar{\nu},\nu_{\mu,\tau}}(\mathbf{x})\Big)_{\text{leaklage in}}, \tag{2.49}$$

Starting from this set, it is possible to compute two new quantities which will be, finally, the ones affected by the net loss of neutrinos, according to the leakage prescription: the total electron lepton number Y_l[particles/baryon],

$$Y_l(\mathbf{x},t) = Y_e(\mathbf{x}) + Y_{\nu_e}(\mathbf{x}) - Y_{\bar{\nu}_e}(\mathbf{x}) \tag{2.50}$$

and the total specific internal energy, u[erg/g]

$$u(\mathbf{x},t) = e(\mathbf{x},t) + \frac{1}{m_{\mathrm{b}}}(Z_{\nu_e}(\mathbf{x}) + Z_{\bar{\nu}_e}(\mathbf{x}) + 4Z_{\nu_{\mu,\tau}}(\mathbf{x})). \tag{2.51}$$

We notice that the contributions to Y_l given by $\nu_{\mu,\tau}$ and $\bar{\nu}_{\mu,\tau}$ cancel in our approach.

The interaction between matter and neutrinos is provided by both neutral and charged weak interaction processes. Among all the possible processes, we focus on a reduced set of reactions, choosing the ones which are expected to be dominant. For each production/absorption reaction, we need to compute the spectral emissivity and absorptivity,

$$j_\nu(E,\mathbf{x})\,[\text{particle/s}] \qquad \chi_{\nu,\mathrm{ab}}(E,\mathbf{x})\,[\text{particle/s}] \tag{2.52}$$

as they are defined in the Boltzmann equation. For the scattering reaction, we compute a scattering absorptivity,

$$\chi_{\nu,\mathrm{sc}}\,[\text{particle/s}], \tag{2.53}$$

which is not related to any physical absorption, but it is linked to the scattering mean free path, $\lambda_{\nu,\mathrm{sc}} = c/\chi_{\nu,\mathrm{sc}}$. The total emissivity and the total absorptivity are computed as the sum over all considered processes of each single emissivity. While the emissivity provides the local rates of neutrino production, the absorptivity and the scattering rates are the sources of the local neutrino opacity. The opacity can be expressed by the total neutrino mean free path,

$$\lambda_\nu = \frac{c}{\sum\limits_r \chi_{\mathrm{ab},\nu,\mathrm{r}} + \sum\limits_s \chi_{\mathrm{sc},\nu,\mathrm{s}}} \tag{2.54}$$

where the indices r (s) run over all the considered absorption (scattering) reactions, and λ_ν represents the average distance between two consecutive neutrino interactions. Its inverse, $1/\lambda_\nu$, is the necessary quantity to compute the optical depth, according to Eq.(2.1). The search for a suitable neutrino path in a more general context, will be the topic of next chapter. In the following, we assume that, assuming some *ad hoc* paths or

applying some more general algorithm, the local optical depth can be calculated from the inverse mean free paths:

$$\lambda_\nu(E,\mathbf{x}) \rightarrow \tau_\nu(E,\mathbf{x}) \tag{2.55}$$

When the neutrino trapping conditions are fulfilled, we reconstruct the trapped component of the distribution functions, f^t, from the values of Y^t_ν and Z^t_ν,

$$Y_{\nu_i}(\mathbf{x},t) \longrightarrow f^t_{\nu_i}(\mathbf{x},t,E) \qquad \text{for} \quad \nu_i = \nu_e, \bar{\nu}_e, \nu_{\mu,\tau}. \tag{2.56}$$

To this end, we assume that the distribution functions tend to the equilibrium values, represented by the Fermi-Dirac distribution functions of a neutrino gas in thermal and weak equilibrium with matter

$$(f_{\nu_i})_{\rm eq} = \frac{1}{e^{(E/T-\eta_{\nu_i})}+1} \qquad \text{for} \quad \nu_i = \nu_e, \bar{\nu}_e, \nu_{\mu,\tau} \tag{2.57}$$

where η_{ν_i} is the neutrino degeneracy parameter. The degeneracy parameter used in these expressions is always 0 for $\nu_{\mu,\tau}$. For ν_e and $\bar{\nu}_e$, it is not always the standard equilibrium degeneracy parameter; in particular, we correct its expression so that $\eta_\nu = (\eta_\nu)_{\rm eq}$ when (anti-)neutrinos are in equilibrium with matter (i.e. when $\tau_\nu \gg 1$), and $\eta_\nu \approx 0$ in the transparent regime (i.e., when $\tau_\nu \sim 0$).
As Y^t_ν and Z^t_ν are advected, f^t changes accordingly; but this is not the only possible way to evolve the distributions functions: the local conversion of electron and positrons into ν_e and $\bar{\nu}_e$, the conversion of fluid energy into neutrino pairs (and the opposite absorption processes), together with diffusion process, allow an "internal degree of freedom" for the trapped components of the neutrino distribution functions:

$$f^t(\mathbf{x},t+{\rm d}t,E) = f^t(\mathbf{x},t,E) + \dot{f}^t(\mathbf{x},t,E)\,dt \tag{2.58}$$

where $\dot{f}^t$ is the distribution function rate due to neutrino production and diffusion. Once the new, time evolved distributions functions are known, the evolved neutrino fractions $Y^t_\nu(\mathbf{x},t+{\rm d}t)$ and $Z^t_\nu(\mathbf{x},t+{\rm d}t)$ can be calculated according to Eq.(2.38) and Eq.(2.39), and the related rates are:

$$\dot{Y}^t_\nu(\mathbf{x},t) = \frac{Y^t_\nu(\mathbf{x},t+{\rm d}t) - Y^t_\nu(\mathbf{x},t)}{{\rm d}t} \tag{2.59}$$

and

$$\dot{Z}^t_\nu(\mathbf{x},t) = \frac{Z^t_\nu(\mathbf{x},t+{\rm d}t) - Z^t_\nu(\mathbf{x},t)}{{\rm d}t}\,. \tag{2.60}$$

Neutrinos do not appear only as trapped fluid components; they can diffuse out of the system, or just stream freely at the speed of light, according to their local mean free path and optical depth. This is actually the main aspect to catch for a leakage scheme; in our treatment, we calculate the emission rates directly from the emissivity

$$j(E,\mathbf{x}) \rightarrow r_{\nu,{\rm em}}(E,\mathbf{x}). \tag{2.61}$$

where the specific rates $r_{\nu,{\rm em}}(E,\mathbf{x})$ are linked with the total rate $R_{\nu,{\rm em}}(\mathbf{x})$ by

$$R_{\nu,{\rm em}}(\mathbf{x}) = \frac{4\pi}{(hc)^3}\int r_{\nu,{\rm em}}(E,\mathbf{x})E^2\,dE. \tag{2.62}$$

From the optical depth and the mean free path, we calculate the diffusion timescale according to 2.37, and the specific diffusion rates according to a definition derived directly from 2.34:

$$\left(f^t(E,\mathbf{x}), \lambda(E,\mathbf{x}), \tau(E,\mathbf{x})\right) \rightarrow r_{\nu,\mathrm{diff}(E,\mathbf{x})} \tag{2.63}$$

where

$$R_{\nu,\mathrm{diff}}(\mathbf{x}) = \frac{4\pi}{(hc)^3} \int r_{\nu,\mathrm{diff}}(E,\mathbf{x}) E^2 \, dE \tag{2.64}$$

Finally, the effected rates are obtained by a smooth interpolation between the spectral production rates and the spectral diffusion rates, directly derived from 2.3:

$$(r_{\nu,\mathrm{prod}}(E,\mathbf{x}), r_{\nu,\mathrm{diff}}(E,\mathbf{x})) \rightarrow r_{\nu,\mathrm{eff}}(E,\mathbf{x}). \tag{2.65}$$

Differently from the previous grey scheme, the particles and the energy rates are not independent, because a specific energy rate can be immediately calculated as

$$q_\nu(E,\mathbf{x}) = E\, r_\nu(E,\mathbf{x}). \tag{2.66}$$

In the end, the local energy and particle rates emitted in form of neutrinos, from each point of the system, are determined:

$$Q_{\nu,\mathrm{eff}}(\mathbf{x})\ [\mathrm{erg/g/s}] \qquad R_{\nu,\mathrm{eff}}(\mathbf{x})\ [\mathrm{particles/g/s}] \tag{2.67}$$

Neutrinos are mainly emitted from the region close to the semitransparent area. Outside the last interaction surface (which is usually called neutrinosphere in CCSNe models; we will call it, more generally, neutrino surface), huge neutrino fluxes are expected. This very high neutrino luminosity goes through layers of matter with decreasing density and temperature (i.e., less and less opaque). However, due to the large incoming flux, there is a non-negligible probability for ν_e and $\bar{\nu}_e$ to be re-absorbed there. In this new scheme, we included an estimation of the local absorption rates, $h_\nu(\mathbf{x})$. Also for these rates, the spectral rates are the calculated, so that the total rate is obtained as

$$H_\nu(\mathbf{x}) = \frac{4\pi}{(hc)^3} \int_0^{+\infty} h_\nu(E,\mathbf{x}) E^2 \, dE \tag{2.68}$$

$$G_\nu(\mathbf{x}) = \frac{4\pi}{(hc)^3} \int_0^{+\infty} E\, h_\nu(E,\mathbf{x}) E^2 \, dE \tag{2.69}$$

A simple approach to the heating term calculation would be to use directly, as spectral luminosities, the ones obtained from the cooling part of the scheme (i.e, the ones obtained by the integration of $r_{\nu,\mathrm{eff}}$). A direct test showed that this solution overestimates the heating effect. This is due to a too hard neutrino spectrum in the spectral neutrino luminosity. This is somehow expected from the scheme: the locally emitted neutrinos retain information about the thermal properties of matter where their are produced or diffused. But the spectrum of the neutrinos emitted at the last scattering surface will be different, and it will be affected by the thermalization processes which occur during the diffusion (at least, where thermalization reactions occur). We do not model the diffusion with accuracy, so we can not model the thermalization either. However, we can mimic its effect on the outgoing neutrino spectrum. This is done in a very simple way, reducing the high energy tail of the energy luminosity, using an exponential cut based on the

optical depth. Using this prescription, we define a new "spectrum-corrected" effective rate,

$$(r_{\nu,\text{eff}}(E,\mathbf{x}),\tau_\nu(E,\mathbf{x})) \to \tilde{r}_{\nu,\text{eff}}(E,\mathbf{x}) \tag{2.70}$$

Condition 2.70 is not enough to define the new rates; we have to fix another constraint. Two different approaches have been explored:

- we assume that the neutrino number luminosity is the same, before and after the correction. Then, the redefinition of the effective rates leads to a lower energy luminosity;
- we assume that the neutrino luminosity has to be conserved, before and after the correction. In this case, after the redefinition of the effective rates, the neutrino number luminosity would be higher.

In both cases, the definition of the $\tilde{r}_{\nu,\text{eff}}$ introduces an ambiguity in the scheme. Which are the rates that have to be used for the cooling contribution in the opaque area? The thermalization process is a transport process which does not happen where neutrinos are at first released, but during their path towards the optically thin region. Thus, we decided to keep the original $r_{\nu,\text{eff}}$ rates for the cooling term. From the $\tilde{r}_{\nu,\text{eff}}$ rates, it is possible to calculate the neutrino luminosities outside the neutrino surfaces and use it as input flux for the absorption rates. This calculation requires to model the emission from the last interaction surface, and the conversion from particle flux to particle density:

$$(\tilde{r}_{\nu,\text{eff}},\dots) \to (L_\nu,\rho_\nu) \tag{2.71}$$

We do not provide a general recipe to calculate the neutrino luminosity and the density; it will be specified case by case, because it can depend very much on the geometry and on the symmetry of the system.
In the end, once the local neutrino density has been computed, the absorption rates h_ν are obtained combing it with the local absorptivity:

$$(\rho_\nu,\chi_{\nu,\text{ab}}) \to h_\nu \tag{2.72}$$

The net balance between the effective rates and the absorption rates is the net amount of particles and energy released from the fluid out of the system: these quantities are the variation rates of the total lepton number and of the total specific energy, defined in equations (2.50) and (2.51):

$$\dot{Y}_l(\mathbf{x}) = -\frac{1}{m_b}\left((R_{\nu_e,\text{eff}}(\mathbf{x}) - R_{\bar{\nu}_e,\text{eff}}(\mathbf{x})) - (H_{\nu_e}(\mathbf{x}) - H_{\bar{\nu}_e}(\mathbf{x}))\right) \tag{2.73}$$

and

$$\begin{aligned} \dot{u}(\mathbf{x}) = \; & -\left(\left(Q_{\nu_e,\text{eff}}(\mathbf{x}) + Q_{\bar{\nu}_e,\text{eff}}(\mathbf{x}) + 4Q_{\nu_{\mu,\tau},\text{eff}}(\mathbf{x})\right) - \right. && (2.74)\\ & \left.\left(G_{\nu_e}(\mathbf{x}) + G_{\bar{\nu}_e}(\mathbf{x}) + 4G_{\nu_{\mu,\tau}}(\mathbf{x})\right)\right). && (2.75) \end{aligned}$$

At this point, the leakage scheme can be finally applied. Once we know the final values of the lepton number and of the total specific energy,

$$Y_l(\mathbf{x},t+\mathrm{d}t) \approx Y_l(\mathbf{x},t) + \dot{Y}_l(\mathbf{x},t)\,dt \tag{2.76}$$

and

$$u(\mathbf{x}, t + \mathrm{d}t) = u(\mathbf{x}, t) + \dot{u}(\mathbf{x}, t)\, dt \ , \tag{2.77}$$

we can invert equations (2.50) and (2.51) to get the final values of the electron fraction $Y_{\mathrm{e}}(\mathbf{x}, t + \mathrm{d}t)$ and of the fluid internal energy $e(\mathbf{x}, t + \mathrm{d}t)$. Thanks to these results, two more output quantities can be calculated: first, the rate of variation of the electron fraction,

$$\dot{Y}_e(\mathbf{x}, t) = \frac{(Y_e(\mathbf{x}, t + \mathrm{d}t) - Y_e(\mathbf{x}, t))}{dt} \tag{2.78}$$

and, second, the rate of variation of the internal energy of matter,

$$\dot{e}(\mathbf{x}, t) = \frac{(e(\mathbf{x}, t + \mathrm{d}t) - e(\mathbf{x}, t))}{dt} \ . \tag{2.79}$$

Finally, the neutrinos provide a source of stress for the fluid. When neutrinos are trapped (optically thick regime), the stress is determined by the gradient of the pressure of the neutrino gas,

$$\left(\frac{d\mathbf{v}}{dt}\right)_{\tau \gg 1} (r, t) = -\frac{1}{\rho} \left(\nabla P_\nu\right)_r \tag{2.80}$$

The neutrino pressure is simply evaluated based on the energy content of the neutrino gas,

$$P_\nu(\mathbf{x}) = \frac{1}{3} \frac{\rho(\mathbf{x})}{m_b} (Z^t_{\nu_e}(\mathbf{x}) + Z^t_{\bar{\nu}_e}(\mathbf{x}) + 4\, Z^t_{\nu_{\mu,\tau}}(\mathbf{x})) \tag{2.81}$$

and this contribution is always considered. In the optically thin regime, neutrino stress is related to the neutrino number luminosity, $L_{\mathrm{n},\nu}$. In spherically symmetric core collapse simulation, this term has been implemented, according the prescription given in [81], but only during the collapse phase, while it is neglected after bounce.

2.3.3 Reactions and rates

- for electron neutrino and antineutrino absorption and emission, we include charged current reactions on nucleons and on nuclei:

$$e^- + p \ \leftrightarrow \ n + \nu_e \tag{2.82}$$
$$e^- + (A, Z) \ \leftrightarrow \ (A, Z - 1) + \nu_e \tag{2.83}$$
$$e^+ + n \ \leftrightarrow \ p + \bar{\nu}_e \tag{2.84}$$

  Following [12], we calculate the associated emissivity j [particles/s]:

$$j_{\nu_i}(\mathbf{x}, E) \qquad \text{for} \quad \nu_i = \nu_e, \bar{\nu}_e \tag{2.85}$$

  and absorptivity χ_{ab} [particles/s],

$$\chi_{\mathrm{ab},\nu_i}(\mathbf{x}, E) \qquad \text{for} \quad \nu_i = \nu_e, \bar{\nu}_e \tag{2.86}$$

  for both ν_e and $\bar{\nu}_e$. We took the publicaly available subroutines from the spherically symmetric `AGILE-IDSA` CCSN model.

- We consider also the production of all kind of neutrinos from pair processes, like pair production from electron-positron annihilation, and neutrino bremsstrahlung from nucleons,

$$e^- + e^+ \quad \leftrightarrow \quad \nu + \bar{\nu} \tag{2.87}$$
$$N + N \quad \leftrightarrow \quad N + N + \nu + \bar{\nu} \tag{2.88}$$
$$\tag{2.89}$$

  Following [12], [98] and [51], we calculate the associated emissivity

$$j_{\nu_i,\mathrm{PAIR}}(\mathbf{x}, E)\,[\text{particles/s}] \qquad \text{for} \quad \nu_i = \nu_e, \bar{\nu}_e, \nu_{\mu,\tau} \tag{2.90}$$

  and absorptivity,

$$\chi_{\mathrm{ab},\nu_i,\mathrm{PAIR}}(\mathbf{x}, E) \qquad \text{for} \quad \nu_i = \nu_e, \bar{\nu}_e, \nu_{\mu,\tau}. \tag{2.91}$$

  Remembering that we are considering pair processes, the collision integral in the Bolztmann equation looks like:

$$\dot{f}_\nu(\mathbf{k}_\nu)\Big|_{\mathrm{coll}} = \mathcal{C} \int \tfrac{\mathrm{d}^3\mathbf{k}_{\bar{\nu}}}{(2\pi)^3} \left[(1 - f_\nu(\mathbf{k}_\nu)(1 - f_{\bar{\nu}}(\mathbf{k}_{\bar{\nu}}))S(E_\nu + E_{\bar{\nu}}, \mathbf{k}_\nu + \mathbf{k}_{\bar{\nu}}) \right. \tag{2.92}$$
$$\left. + f_\nu(\mathbf{k}_\nu) f_{\bar{\nu}}(\mathbf{k}_{\bar{\nu}}) S(-(E_\nu + E_{\bar{\nu}}), -(\mathbf{k}_\nu + \mathbf{k}_{\bar{\nu}}))\right] \tag{2.93}$$

  where the spatial dependence has been omitted and S represent the scattering kernel, with $\mathcal{C}$ a related constant. We calculate the emissivity taking the first term in the integral, integrating over the whole phase space of the second neutrino and averaging over the angular part of the phase space of the first one (ν), and neglecting Pauli blocking factors:

$$j_{\nu,\mathrm{PAIR}}(\mathbf{x}, E) = \frac{\mathcal{C}}{4\pi} \int_{\Omega_{\bar{\nu}}} \mathrm{d}\Omega_\nu \int \frac{\mathrm{d}^3\mathbf{k}_{\bar{\nu}}}{(2\pi)^3} S(E_\nu + E_{\bar{\nu}}, \mathbf{k}_\nu + \mathbf{k}_{\bar{\nu}}) \tag{2.94}$$

  For the absorptivity, we do the same for the second integral, assuming Fermi-Dirac distribution functions and zero chemical potentials for $f_{\bar{\nu}}$,

$$\chi_{\mathrm{ab},\nu,\mathrm{PAIR}}(\mathbf{x}, E) = \frac{\mathcal{C}}{4\pi} \int_{\Omega_{\bar{\nu}}} \mathrm{d}\Omega_\nu \int \frac{\mathrm{d}^3\mathbf{k}_{\bar{\nu}}}{(2\pi)^3} f_{\bar{\nu}}(\mathbf{k}_{\bar{\nu}}) S(-(E_\nu + E_{\bar{\nu}}), -(\mathbf{k}_\nu + \mathbf{k}_{\bar{\nu}})). \tag{2.95}$$

  The calculation during runtime of the integrals 2.94 and 2.95 would be by far the most expensive part of the computation. Then, we decide to tabulate all these rates and to interpolate them during the program execution.

- For the neutrino scattering reactions, we consider scattering off nucleons and off nuclei, which are due to both charged current and neutral current processes:

$$n/p + \nu \quad \rightarrow \quad n/p + \nu \tag{2.96}$$
$$(A, Z) + \nu \quad \rightarrow \quad (A, Z) + \nu \tag{2.97}$$

  Also for these reactions, it is possible to compute the associated scattering rates χ_{sc} [1/s], using expressions derived from [12]:

$$\chi_{\mathrm{sc},\nu_i}(\mathbf{x}, E) \qquad \text{for} \quad \nu_i = \nu_e, \bar{\nu}_e, \nu_{\mu,\tau} \tag{2.98}$$

  To compute them, we took the publicly available subroutines from the spherically symmetric `AGILE-IDSA` CCSN model.

2.3.4 Opacities

The total mean free path $\lambda_{\rm tot}$ [cm] can, then, be calculated from the previously estimated rates:

$$\lambda_{{\rm tot},\nu_i}(E,\mathbf{x}) = \frac{c}{\chi_{{\rm ab},\nu_i} + \chi_{{\rm sc},\nu_i}} \qquad \text{for} \quad \nu_i = \nu_e, \bar{\nu}_e, \nu_{\mu,\tau} \tag{2.99}$$

Besides the total mean free path, we can also define an effective mean free path for absorption (and, eventually, scattering processes which are very effective in exchanging energy between radiation and fluid) [150], $\lambda_{\rm eff}$ [cm]:

$$\lambda_{{\rm eff},\nu_i}(E,\mathbf{x}) = \frac{c}{\sqrt{\chi_{{\rm ab},\nu_i}(\chi_{{\rm ab},\nu_i} + \chi_{{\rm sc},\nu_i})}} \qquad \text{for} \quad \nu_i = \nu_e, \bar{\nu}_e, \nu_{\mu,\tau} \tag{2.100}$$

The mean free path can be directly used to compute the neutrino optical depth, $\tau_\nu(E,\mathbf{x})$. In the case of spherically symmetric models, $\tau_\nu(E,R)$ can be simply calculated on along radial paths:

$$\tau(E,R) = \int_R^{+\infty} \frac{1}{\lambda_\nu(E,r)}\,{\rm d}r. \tag{2.101}$$

Otherwise, suitable paths have to be defined.
The presence of two different mean free paths gives two different optical depths, a *total* optical depth, $\tau_{{\rm tot},\nu}(E,\mathbf{x})$, and an *effective* absorption optical depth, $\tau_{{\rm eff},\nu}(E,\mathbf{x})$. The different meaning of these two quantities becomes more clear when the concept of neutrino surface is considered. In general, the neutrino surface can be defined as the surface where the optical depth becomes 2/3; in spherical symmetry, this corresponds to a radius R_ν, so that:

$$\tau(E,R_\nu) = \int_{R_\nu}^{+\infty} \frac{1}{\lambda_\nu(E,r)}\,{\rm d}r = \frac{2}{3} \tag{2.102}$$

R_ν (the one related to the total optical depth) can be thought of as the radius where neutrinos interact with matter for the last time (whatever kind of interaction is concerned), before streaming out of the system. On the other hand, the $R_{\nu,{\rm eff}}$ (the one related to the effective optical depth) is the radius where neutrinos are absorbed and emitted for the last time, during their diffusion out of the star; this does not imply that neutrinos can not further be scattered by matter. The scattering of neutrinos on nuclei or nucleons is, in first approximation, an elastic scattering, which does not change significantly the energy of the interacting neutrino; on the other hand, absorption and emission are among the most effective process for neutrino thermalization. This intrinsic difference has an impact on the energy of the neutrino coming out of the spheres: ν's and $\bar{\nu}$'s passing through the effective neutrinosphere will be in thermal equilibrium with the local matter; after that, neutrinos could, in principle, continue to diffuse out, via scattering processes; in this case, they will leave the neutrinosphere without being in thermal equilibrium with matter, but keeping memory of the matter temperature at the last absorption/emission radius. Keeping in mind this physical difference between the two optical depths, we will use $\tau_{{\rm tot},\nu}$ whenever the total diffusion effect is considered; otherwise, where thermodynamical properties and energy spectra of the neutrinos will come into play, we will refer to $\tau_{{\rm eff},\nu}$.

2.3.5 Timescales and neutrino fractions' evolution

Information about neutrino abundances are provided, at the beginning of each time step, by the neutrino fractions, Y_ν and Z_ν. The storage of the energy-dependent distribution functions would be too memory consuming, in particular in multidimensional simulations. Then, we designed a very simple procedure to reconstruct the distribution function from the neutrino fraction. We assume that the actual distribution function value is proportional to the Fermi-Dirac equilibrium one, multiplied by an exponential cut, which ensures the fact that the considered neutrinos (of a specific kind ν_i and with a certain energy E) are actually trapped:

$$f^t_{\nu_i}(E,\mathbf{x}) \propto \left(f_{\nu_i}(E,\mathbf{x})\right)_{\rm eq}\left(1-\exp\left(-\frac{\tau_{\nu_i}(E,\mathbf{x})}{\beta_{\rm rec}}\right)\right) \tag{2.103}$$

The proportionality constant is fixed by Eq.(2.38); the constant $\beta_{\rm rec}$ is fixed from direct comparison with the calibration model. Once the distribution functions have been computed, they have to be temporally evolved during the timestep $\mathrm{d}t$. This evolution is based on some important timescales, associated with the neutrino production, absorption and diffusion. The *production* timescale, $t_{\rm prod}$ [s], can be simply viewed as the timescale needed to produce enough neutrinos to reach the equilibrium configuration (assuming that the diffusion timescale is much longer, in order to allow equilibrium setting); clearly, it depends on how large is their production rates:

$$t_{\nu_i,{\rm prod}}(\mathbf{x},t,E) = \frac{1}{j_{\nu_i}(\mathbf{x},t,E)} \qquad \text{for} \quad \nu_i = \nu_e, \bar\nu_e, \nu_{\mu,\tau} \tag{2.104}$$

Similarly, the absorption rate suggests an *absorption* timescale, $t_{\rm ab}$ [s], defined as

$$t_{\nu_i,{\rm ab}}(\mathbf{x},t,E) = \frac{1}{(f^t_{\nu_i})_{\rm eq}(\mathbf{x},t,E)\chi_{{\rm ab},\nu_i}(\mathbf{x},t,E)} \qquad \text{for} \quad \nu_i = \nu_e, \bar\nu_e, \nu_{\mu,\tau} \tag{2.105}$$

which estimates the typical timescale after that a neutrino can be absorbed by matter. Finally, the *diffusion* timescale is the timescale which characterizes the diffusion of neutrinos from the optically thick to the optically thin regions. In the new scheme, we keep the definition already used for the previous grey scheme, Eq.(2.37). The update of f^t is performed in two step; the first one considers the production of neutrinos: if we consider a particular position in space $\mathbf{x}$, and a particular value for the neutrino energy E,

$$f^t_{\nu_i,1}(t+\mathrm{d}t) \approx f^t_{\nu_i}(t) + \dot f^t_{\nu_i,{\rm prod}}(t)\,\mathrm{d}t \qquad \text{for} \quad \nu_i = \nu_e, \bar\nu_e, \nu_{\mu,\tau} \tag{2.106}$$

with

$$\dot f^t_{\nu_i,{\rm prod}} = \frac{((f^t_{\nu_i})_{\rm eq} - f^t_{\nu_i})}{\max((f^t_{\nu_i})_{\rm eq}\, t_{\nu_i,{\rm prod}}, \mathrm{d}t)}\,\exp\left(-\frac{t_{\nu_i,{\rm prod}}}{t_{\nu_i,{\rm diff}}}\right) \tag{2.107}$$

where all the quantities are evaluated at time t. The first part ensures that, whenever the production timescale is small enough compared with the timestep $\mathrm{d}t$, the distribution function reaches the equilibrium value. The second term is a sort of switch between the diffusive and the trapped regime: as long as $t_{\nu_i,{\rm prod}}$ is large compared with $t_{\nu_i,{\rm prod}}$, equilibrium cannot set it, just because diffusion prevent it (i.e. the second term goes to

0); in the opposite limit, equilibrium can set in, because the term goes to 1. The second step is similar to the first one and considers the diffusion of the neutrinos:

$$f^t_{\nu_i,2}(t+dt) = f^t_{\nu_i,1}(t+\mathrm{d}t) + \dot{f}^t_{\nu_i,\mathrm{diff}}(t)\,\mathrm{d}t \qquad \text{for} \quad \nu_i = \nu_e, \bar{\nu}_e, \nu_{\mu,\tau} \tag{2.108}$$

with

$$\dot{f}^t_{\nu_i,\mathrm{diff}} = -\frac{(f^t_{\nu_i,1})(t+\mathrm{d}t)}{\max(t_{\nu_i,\mathrm{diff}}, \mathrm{d}t)} \exp\left(-\frac{t_{\nu_i,\mathrm{diff}}}{t_{\nu_i,\mathrm{prod}}}\right) \tag{2.109}$$

Again, the first part provides the expected behavior of the distribution functions when the diffusion timescale is smaller then the timestep, while the exponential term distinguishes between the production-dominated and the diffusion-dominated regime. Finally, $f^t_{\nu_i,2}$ is considered as the updated value of the distribution function, $f^t_{\nu_i}(t+\mathrm{d}t)$.

2.3.6 Rates and interpolation

The production specific rates can be defined simply as the properly normalized neutrino emissivity,

$$r_{\nu_i,\mathrm{prod}}(E,\mathbf{x}) = \frac{j_{\nu_i,\mathrm{em}}(E,\mathbf{x})}{\rho(\mathbf{x})} \quad \text{for}\, \nu_i = \nu_e, \bar{\nu}_e. \tag{2.110}$$

On the other hand, the diffusion rate is derived directly from Eq.(2.34):

$$r_{\nu_i,\mathrm{diff}}(E,\mathbf{x}) = \frac{1}{\rho(\mathbf{x})} \frac{(f^t_{\nu_i})_{\mathrm{eq}}(E,\mathbf{x})}{t_{\nu_i,\mathrm{diff}(E,\mathbf{x})}} \qquad \text{for} \quad \nu_i = \nu_e, \bar{\nu}_e. \tag{2.111}$$

The interpolation between the two rates is done, for each different neutrino species, at each point $\mathbf{x}$ and for each energy, according to the prescription directly derived from 2.3:

$$r_{\nu_i,\mathrm{eff}}(E,\mathbf{x}) = \frac{r_{\nu_i,\mathrm{prod}}(E,\mathbf{x}) \cdot r_{\nu_i,\mathrm{diff}}(E,\mathbf{x})}{r_{\nu_i,\mathrm{prod}}(E,\mathbf{x}) + r_{\nu_i,\mathrm{diff}}(E,\mathbf{x})} \qquad \text{for} \quad \nu_i = \nu_e, \bar{\nu}_e, \nu_{\mu,\tau}. \tag{2.112}$$

For each single spectral component, the meaning of the interpolation is assumed to be the same as it was for the integrated rates:

- in the transparent regime, neutrinos are expected to stream out freely from the sysyem. This limit is reproduced correctly if emission rates are relatively low, compared with diffusion rates;

- in the opaque regime, neutrinos diffuse out of the star, because they interact with matter. The diffusive limit is correctly taken if the production rates are much higher than the diffusion rates.

While the second condition seems to be more easily fulfilled (because, in our case high opacity regions typically corresponds also to high production regions), the first one is not. The problem is that the equilibrium distribution functions at low temperature and high energy are also very small. So, it is unclear which of the two rates dominates. Then,

we solved the problem just modifying the previous expression, in order to enforce the use of $r_{\nu,\mathrm{prod}}$ at low optical depth:

$$r_{\nu_i,\mathrm{eff}}(E,\mathbf{x}) = \frac{r_{\nu_i,\mathrm{prod}}(E,\mathbf{x})\cdot r_{\nu_i,\mathrm{diff}}(E,\mathbf{x})}{r_{\nu_i,\mathrm{prod}}(E,\mathbf{x}) + r_{\nu_i,\mathrm{diff}}(E,\mathbf{x})}\left(1-\exp\left(-\frac{\tau_{\nu_i}(E,\mathbf{x})}{\alpha_{\mathrm{int}}}\right)\right) + r_{\nu_i,\mathrm{prod}}(E,\mathbf{x})\exp\left(-\frac{\tau_{\nu_i}(E,\mathbf{x})}{\alpha_{\mathrm{int}}}\right) \qquad \text{for} \quad \nu_i = \nu_e, \bar{\nu}_e, \nu_{\mu,\tau} \tag{2.113}$$

with $\alpha_{\mathrm{int}} \gtrsim 3$.
Once the interpolation has been done, the specific rates can be properly integrated over the energy to give the total emission rates

$$R_{\nu_i,\mathrm{eff}}(\mathbf{x}) = \frac{4\pi}{(hc)^3}\int r_{\nu_i,\mathrm{eff}}(E,\mathbf{x})\,E^2\,dE \qquad \text{for} \quad \nu_i = \nu_e, \bar{\nu}_e, \nu_{\mu,\tau}, \tag{2.114}$$

and

$$Q_{\nu_i,\mathrm{eff}}(\mathbf{x}) = \frac{4\pi}{(hc)^3}\int E\,r_{\nu_i,\mathrm{eff}}(E,\mathbf{x})\,E^2\,dE \qquad \text{for} \quad \nu_i = \nu_e, \bar{\nu}_e, \nu_{\mu,\tau}. \tag{2.115}$$

2.3.7 The heating term: spherically symmetric case

In this section, we describe how we implemented the calculation of the heating terms, $h(E,R)$, in the context of spherically symmetric CCSN models.

The rates obtained as $r_{\nu,\mathrm{eff}}(E,R)$ do not correspond to the rates measured outside the neutrinospheres, because during the diffusion from the opaque region the mean neutrino energy usually decreases, due to the interaction with matter at lower temperature (compared with the hotter matter at the emission point). We take this effect into account in a very simple, effective way, defining new "corrected" rates, based on the original one and on the effective optical depth, $\tau_{\nu,\mathrm{eff}}$. We assume that the new rates can be obtained from the original ones with an exponential cut,

$$\tilde{r}_{\mathrm{eff}}(R,E) = \beta_{\mathrm{cut}}(R)\,r_{\mathrm{eff}}(E,R)\exp\left(-\frac{\tau_{\mathrm{eff}}(R,E)}{\alpha_{\mathrm{cut}}}\right). \tag{2.116}$$

The local constant β_{cut} is set by imposing the conservation of the number of emitted neutrinos:

$$\int_0^\infty r_{\mathrm{eff}}(R,E)E^2\,\mathrm{d}E = \int_0^\infty \tilde{r}_{\mathrm{eff}}(R,E)E^2\,\mathrm{d}E; \tag{2.117}$$

or the total emitted energy:

$$\int_0^\infty r_{\mathrm{eff}}(R,E)E^3\,\mathrm{d}E = \int_0^\infty \tilde{r}_{\mathrm{eff}}(R,E)E^3\,\mathrm{d}E. \tag{2.118}$$

α_{cut} is a positive constant, the value of which is set by comparing the resulting spectrum with expected values from a reference solution. We introduce the local spectral quantity $\Delta_{\mathrm{eff}}(R,E)$, to quantify the energy difference introduced by the corrected rates:

$$\Delta_{\mathrm{eff}}(R,E) \equiv \tilde{r}_{\mathrm{eff}}(R,E) - r_{\mathrm{eff}}(R,E). \tag{2.119}$$

If the effect of the cut Eq.(2.116) is to soften the spectrum, we expect that, inside the neutrinosphere, for large value of E, $\Delta_{\text{eff}}(E,R) < 0$; while for small E, $\Delta_{\text{eff}}(E,R) > 0$. This variation is intended as a down scattering in energy of neutrinos or as an absorption of energetic neutrinos and the re-emission of low energy ones; in any case, we do not model this process in detail, and this has to be intended as an effective explanation.

Once the radial effective rates $\tilde{r}_{\text{eff}}(E,R)$ have been calculated, the spectral number luminosity, $\mathrm{d}L_{N,\nu}/\mathrm{d}E$, and the spectral luminosity, $\mathrm{d}L_{\nu}/\mathrm{d}E$, outside the neutrinosphere can be calculated as:

$$\frac{\mathrm{d}L_{N,\nu}}{\mathrm{d}E}(E,R) = \frac{4\pi E^2}{(hc)^3}\int_0^R 4\pi r^2 \rho(r)\tilde{r}_{\text{eff}}(E,r)\mathrm{d}r, \quad R > R_{\nu}(E), \tag{2.120}$$

$$\frac{\mathrm{d}L_{\nu}}{\mathrm{d}E}(E,R) = \frac{4\pi E^3}{(hc)^3}\int_0^R 4\pi r^2 \rho(r)\tilde{r}_{\text{eff}}(E,r)\mathrm{d}r, \quad R > R_{\nu}(E). \tag{2.121}$$

This spectral luminosity becomes the necessary ingredient to calculate the heating rate outside the neutrinosphere. Roughly speaking, the absorption rate is proportional to the local neutrino density (provided by the flux of the free streaming particles) and to the local absorptivity:

$$H_{\nu_i} \propto \rho_{\nu_i}\chi_{\nu_i,\text{ab}} \qquad \nu_i = \nu_e, \bar{\nu}_e \tag{2.122}$$

Considering the spectral approach and the use of the spectral specific rates, we get

$$h_{\nu_i}(E,R) = \frac{(hc)^3}{4\pi E^2}\frac{1}{\rho(R)}\frac{\mathrm{d}\rho_{\nu}}{\mathrm{d}E}(E,R)\,\chi_{\nu_i,\text{ab}}(E,R) \qquad \nu_i = \nu_e, \bar{\nu}_e \tag{2.123}$$

For this heating term, we neglect the absorptivity due to $\nu_{\mu,\tau}$: its contribution can be safely considered negligible. The conversion between the neutrino flux and the neutrino density is one of the major problems in modeling heating from a radiating source. It involves a quantity called (spectral) flux factor $\mu_{\nu_i}(E,R)$, which can be understood as the ratio between the neutrino flux and the neutrino energy density times c. Assuming to have spherical symmetry, the neutrino distribution function depends locally on the neutrino energy, E, on the radius, R, and on the cosine of local propagation angle (with respect to the radial direction) θ, $\mu = \cos\theta$: $f_{\nu_i}(E,R,\mu)$. The flux factor is the average propagation angle:

$$\mu_{\nu_i}(E,R) \equiv \frac{\int_{-1}^{+1}\mu f_{\nu}(E,R,\mu)\,\mathrm{d}\mu}{\int_{-1}^{+1} f_{\nu}(E,R,\mu)\,\mathrm{d}\mu} \tag{2.124}$$

Usually, far from the neutrinosphere, the distribution functions are expected to peak in the forward direction, which leads to $\mu_{\nu_i}(R \gg R_{\nu_i}) \sim 1$. Close to the neutrinosphere, radiation is emitted in an almost isotropic way above the plane tangential to the neutrinosphere, and $\mu_{\nu_i}(R \sim R_{\nu_i}) \sim 1/2$. A useful approximation to this factor can be found in [88], based on a suggestion of S. Bruenn:

$$\mu_{\nu_i}(E,R) \approx \frac{1}{2}\left(1 + \sqrt{1 - \left(\frac{R_{\nu_i}(E)}{\max(R, R_{\nu_i}(E))}\right)^2}\right). \tag{2.125}$$

Then, the spectral neutrino density can be calculated as

$$\frac{\mathrm{d}\rho_{\nu_i}}{\mathrm{d}E}(E,R) = \frac{1}{4\pi R^2 c\,\mu_{\nu_i}(E,R)}\frac{\mathrm{d}L_{N,\nu_i}}{\mathrm{d}E}(E,R) \tag{2.126}$$

In order to have a smooth transition from inside and outside the neutrinosphere, the calculation of the luminosities is performed also inside it. Then, the calculation of the heating term, according to 2.123, is completed by an exponential term:

$$h_{\nu_i,\mathrm{out}}(E,R) = \frac{(hc)^3}{4\pi E^2}\frac{1}{\rho(R)}\frac{\mathrm{d}\rho_\nu}{\mathrm{d}E}(E,R)\,\chi_{\nu_i,\mathrm{ab}}(E,R)\,\exp(-\alpha_{\mathrm{heat}}\,\tau(E,R)) \qquad \nu_i = \nu_e, \bar{\nu}_e \tag{2.127}$$

with $\alpha_{\mathrm{heat}} \sim 2$.

2.4 Tests and validation: results from 1D core collapse simulations

To test and to refine the new scheme, we follow the same strategy we used for the grey $\nu_{\mu,\tau}$ leakage scheme: we set up a spherically symmetric, general relativistic model, and we run it with both `AGILE-BOLZTRAN` and with `AGILE`-ASL. Results obtained with the `AGILE-BOLZTRAN` model are considered as the calibration solution for the `AGILE`-ASL model. This means that results from the two simulations are systematically compared, in order to develop the ALS scheme and fix its free parameters.
We choose a $15M_\odot$ progenitor model from Woosley and Weaver (1995); we use the Lattimer-Swesty nuclear equation of state, with nuclear compressibility $K = 180$MeV.

2.4.1 First test: electron flavor and minimal reaction set

We start with the electron flavor, taking into account only ν_e and $\bar{\nu}_e$ in the model. In both models, we include a first minimal set of relevant reactions concerning ν_e and $\bar{\nu}_e$, as reported in table 2.2. The implementation of the ASL scheme in spherical symmetry

Reactions	Currents	Main Role	Reference
$e^- + p \rightarrow n + \nu_e$	CC	P, T, O	[12]
$e^+ + n \rightarrow p + \bar{\nu}_e$	CC	P, T, O	[12]
$e^- + (A,Z) \rightarrow \nu_e + (A, Z-1)$	CC	P, T, O	[12]
$N + \nu_e/\bar{\nu}_e \rightarrow N + \nu_e/\bar{\nu}_e$	NC	O	[12]
$(A,Z) + \nu_e/\bar{\nu}_e \rightarrow (A,Z) + \nu_e/\bar{\nu}_e$	NC	O	[12]

Table 2.2: Table with the relevant ν_e and $\bar{\nu}_e$ reactions included in models to test the ASL scheme for the electron flavor. In the reactions column, N represents nucleons. In the current column, NC stands for neutral current, while CC for charged current reactions. In the Main Role column, P stands for production, T for thermalization and O for opacity.

follows closely the description provided in section 2.3. The discretization of the neutrino energy is provided by 20 energy bins, spanning the range $3\,\mathrm{MeV} \leq E \leq 300\,\mathrm{MeV}$, with an increasing gap spacing (according to an algorithm suggested by S. Bruenn). We tested the definition of the effective rates using both the possible prescriptions: in run I, we use the conservation of the number luminosity, Eq.(2.117), while in run II the conservation of the energy luminosity, Eq.(2.117). In table 2.3 we report the values of all the free parameters necessary to set the ASL treatment.

Name of the parameter	Run I	Run II
α_{diff}	3.00	3.00
β_{rec}	2.00	2.00
α_{int}	3.00	3.00
$\alpha_{\nu_e,\mathrm{cut}}$	15.0	15.0
$\alpha_{\bar{\nu}_e,\mathrm{cut}}$	15.0	15.0
α_{heat}	1.00	1.00
β_{cut}	$L_{\nu,\mathrm{N}}$	L_{ν}

Table 2.3: Table with the values of all the free parameters of the ASL scheme, used in the first test case.

Collapse phase

We begin with the collapse phase. In Figures 2.6, 2.7, 2.8 and 2.9, we draw the evolution of the last 10 ms of the collapse, before core bounce. We plot, as a function of the enclosed mass, the radial profiles of velocity, density, entropy and electron fraction. At

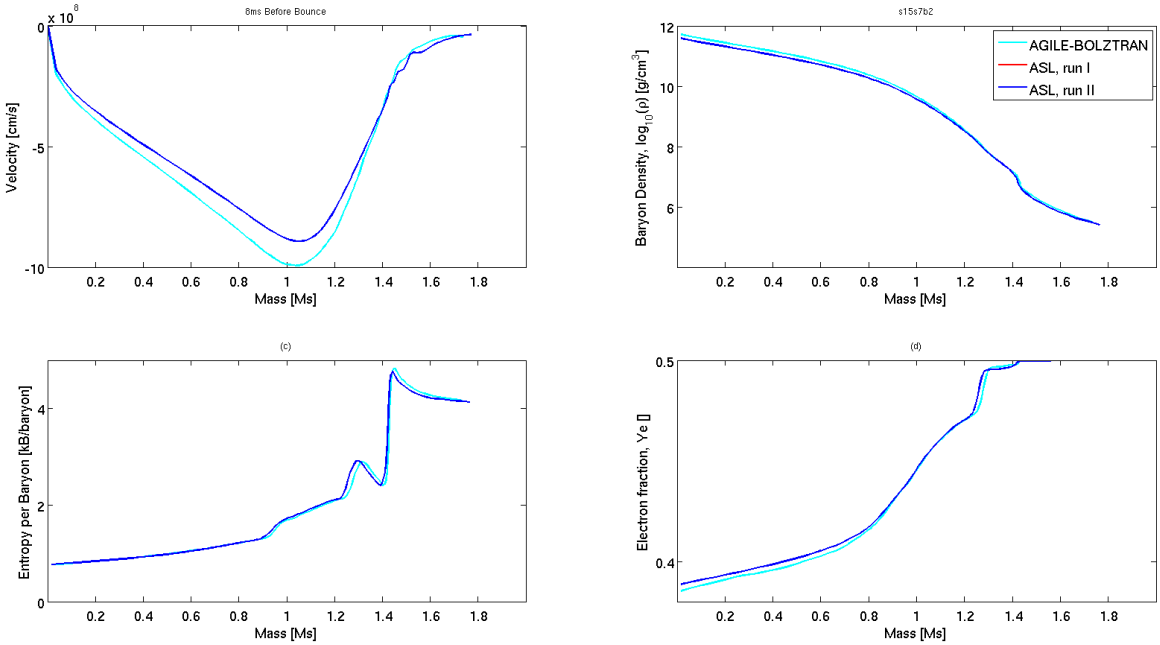

Figure 2.6: Comparison between the radial profiles of the velocity (upper left), baryon density (upper right), entropy (lower left) and electron fraction (lower right), at $t \approx 10$ ms before bounce, for three different models: an `AGILE-BOLZTRAN` run (cyan line) and two different ASL runs (blue and red lines). The difference between the two ASL runs consists in a different normalization of the emitted neutrino luminosity outside the neutrinosphere. Being in the collapse phase, this difference does not play any significant role.

ten milliseconds from bounce, the core has started deleptonizing and its central part is collapsing homologously. The ASL models are very close to the reference simulation; small differences come mainly from a slightly different output time. The two ASL runs

are indistinguishable. We will see that this will be a common feature during all the collapse, because the difference among them is associated with the heating process, which is completely negligible during collapse. At 5 ms before bounce, the central density

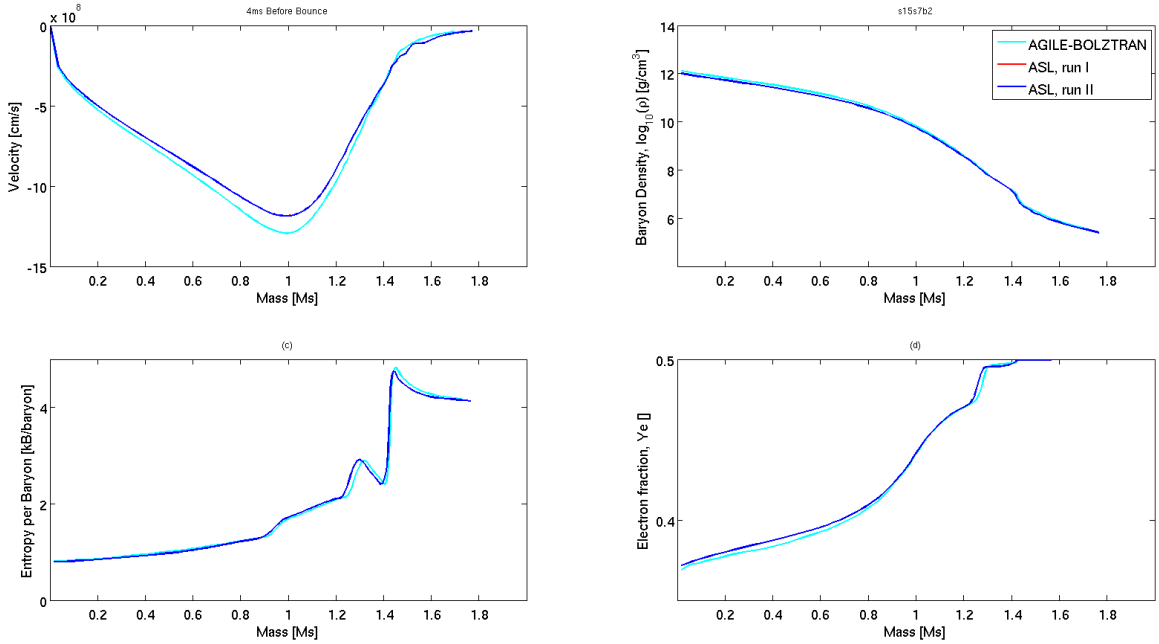

Figure 2.7: The same as 2.6, but at $t = 5\,\mathrm{ms}$ before bounce.

has reached $\sim 10^{12}\mathrm{g/cm}^3$ and neutrino trapping sets in. The lepton number decreases no more; any further decrease in Y_e is due to the conversion of electrons into electron neutrinos. Also at this time, the ASL models show a very close agreement with the reference solution. Very close to bounce, the first differences rise. The electron fraction in the center has reached the same value ($Y_e \approx 0.32$), but the profiles in the innermost part are slightly different, also in the entropy profiles. Actually, the difference is due to a small increase in entropy in the reference solution, which is not present in the ASL model. Finally, at bounce the different models show again a very good agreement among them. Also the point at which the shock forms is very close, at an enclosed mass of about $0.65 M_\odot$. The differences we have noticed in the previous snapshot are still there (and even amplified) in front of the shock, but they have been erased inside it, because of the sudden increase in entropy and reaction rates, which favor the fast achievement of equilibrium conditions. This consideration is in favor of the idea that the difference seen before (and now present in front of the shock) comes from a non-equilibrium feature, probably linked with the interaction between free streaming neutrinos and matter. [1]

In Figure 2.10 we compare the ν_e fraction, Y_{ν_e}, for three different times, $t = 5, 1, 0\,\mathrm{ms}$, before bounce. Solid lines correspond to the Run I, while dashed lines with our reference solution obtained by the `AGILE-BOLZTRAN` model. The comparison shows that the ASL treatment is able to reproduce quite well the growth and the shape of the neutrino trapped component; the right part of the graph, which is present in the `AGILE-BOLZTRAN`

[1] Actually, once the feature after bounce has been reproduced by the ASL scheme, imposing a strong thermalization of the emitted ν_e and $\bar{\nu}_e$, and allowing these low energy particles to be (partially) re-absorbed, deep in the core.

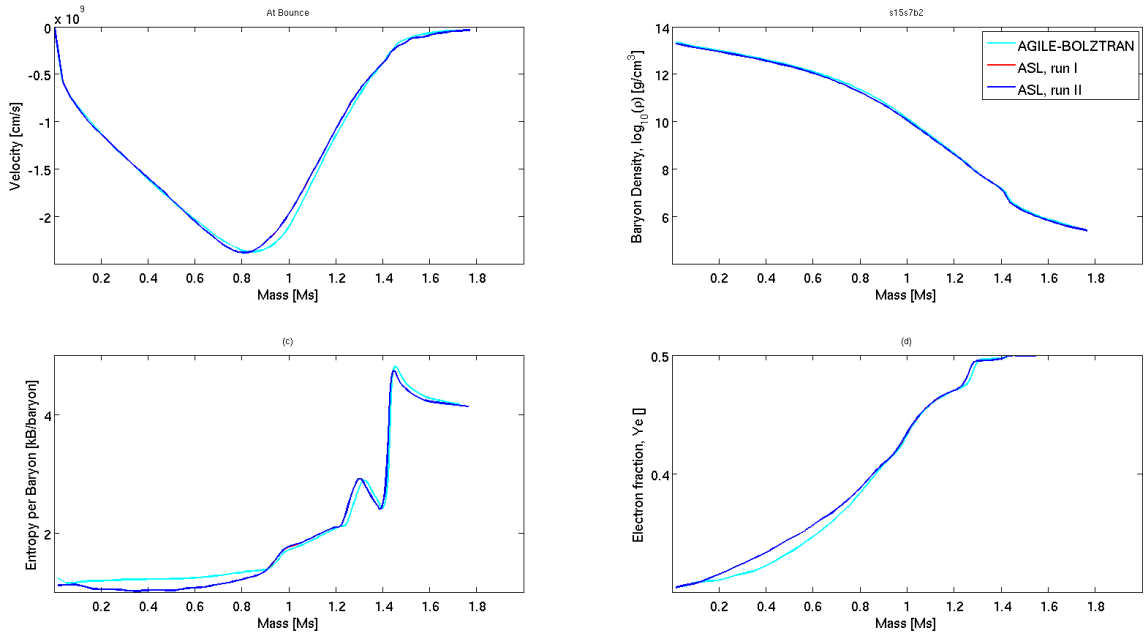

Figure 2.8: The same as 2.6, but at $t = 1\,\mathrm{ms}$ before bounce.

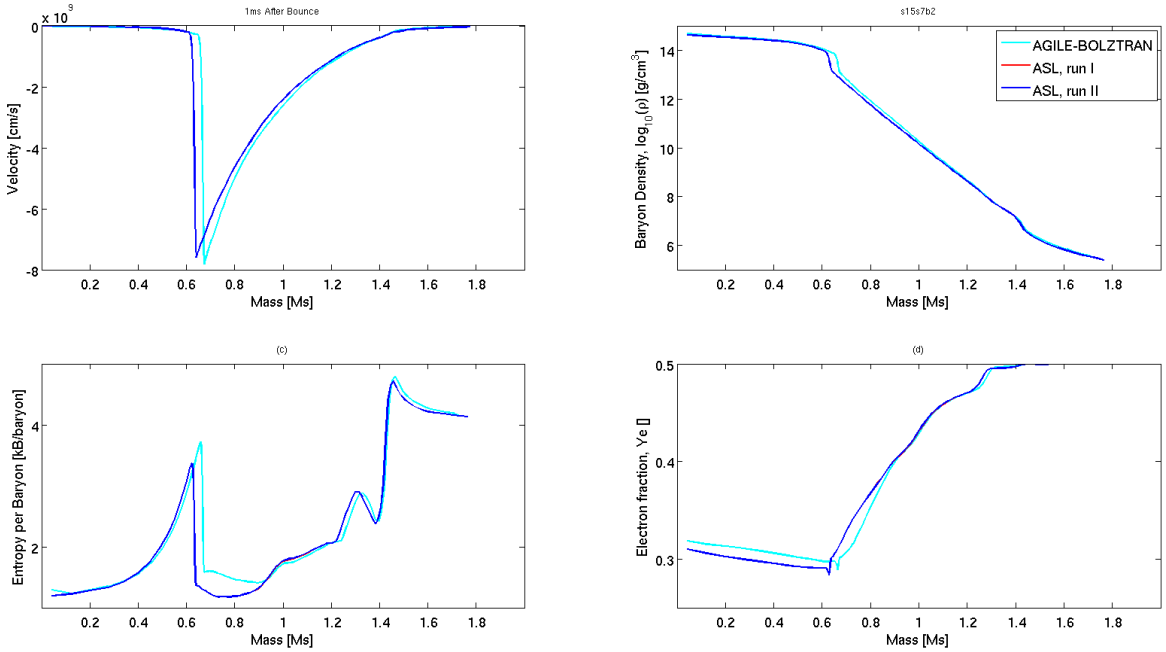

Figure 2.9: The same as 2.6, but at bounce.

results, but not in the Run I, corresponds to the free streaming component, which has not been included in the ASL treatment. We notice that the difference between the two models here is opposite to the one seen in the electron fraction: for example, the excess of electrons in the ASL model at $t = 1\,\mathrm{ms}$ before bounce corresponds to a lower electron neutrino fraction. This suggests that the differences in Y_e before the shock formation can be induced by a slightly delayed neutrino gas growth.

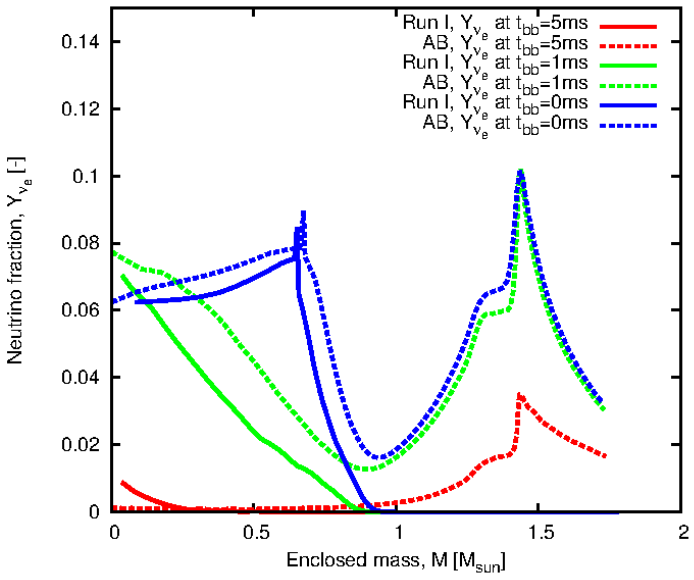

Figure 2.10: Comparison between the ASL Run I (solid lines) and the `AGILE-BOLZTRAN` solution (AB, dashed lines), of the ν_e fraction, at three different times before bounce. The ASL Run I lines represent only the trapped component, without the free streaming one. Good agreement can be seen in the shape and in the temporal evolution of the trapped neutrino gas in the stellar core.

After bounce phase

A good agreement between the ASL model and the reference `AGILE-BOLZTRAN` solution is the necessary point to start with, for the comparison of the after bounce phase.
In Figures 2.11-2.14 we show the comparison between the reference `AGILE-BOLZTRAN` solution and the two ASL model runs, during the first 350 ms after core bounce, from the expansion of the prompt-shock, to the shock stalling and, finally, to the cooling phase.

In Figure 2.11, we show the profiles (still as function of the enclosed mass) in the very early shock expansion phase, corresponding to the first 5 ms, during which neutrino burst happens. Overall, the agreement between the reference solution and the ASL model persists; the two different normalization choices (Run I and Run II) are still very similar. In the region around $1M_{\odot}$ we can see some differences, especially in the entropy and in the Y_e profiles. These differences are probably due to the transport of the large neutrino flux, which will be soon emitted as neutrino burst: a fraction of this radiation can be absorbed just in front of the shock, resulting in a local peak in the electron fraction. Later, the passage of the shock wave erases this feature. However, even this effect is slightly different in the two models.
Comparison between the radial profiles, in the innermost radial portion, at 10 and 50 ms after bounce are shown in Figure 2.12. There, we can finally see that the two different version of the ASL models start to differ, even if they present very similar behaviors. After the prompt shock expansion, the shock wave stalls and converts into an accreting shock front, clearly visible from the velocity profile. In this first phase, the ASL model seems to be a bit more pessimistic, probably due to a large deleptonization inside the

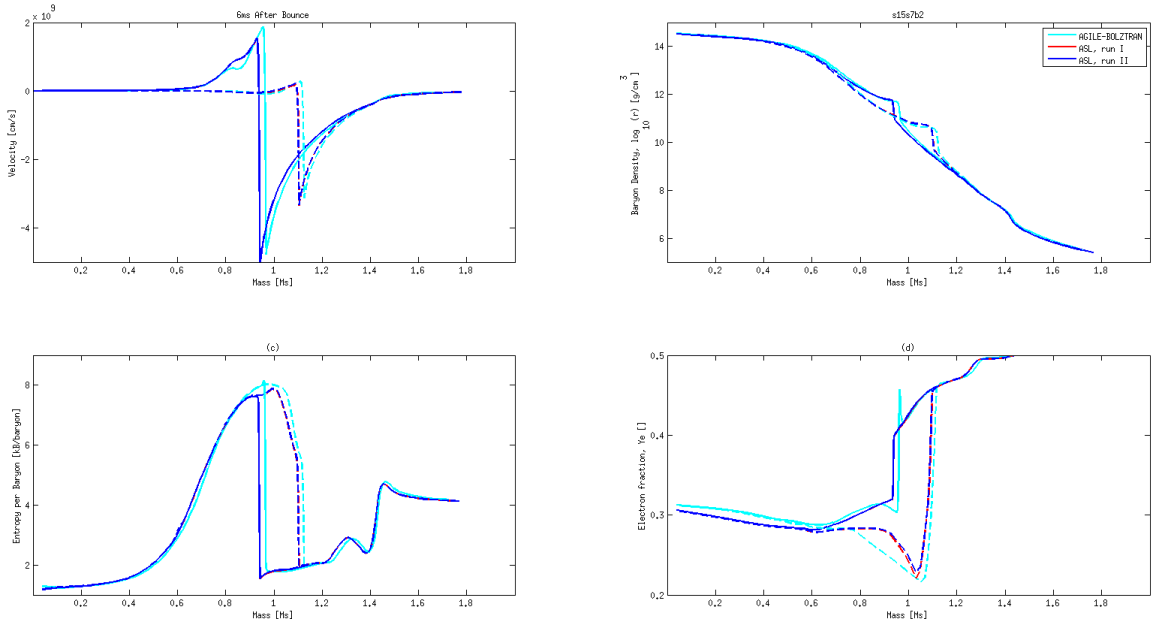

Figure 2.11: Comparison between the radial profiles of the velocity (upper left), baryon density (upper right), entropy (lower left) and electron fraction (lower right), at $t \approx 1\,\mathrm{ms}$ (solid lines) and at $t \approx 5\,\mathrm{ms}$ (dashed lines) after bounce, for three different models: an `AGILE-BOLZTRAN` run (cyan line) and two different ASL runs (blue and red lines).

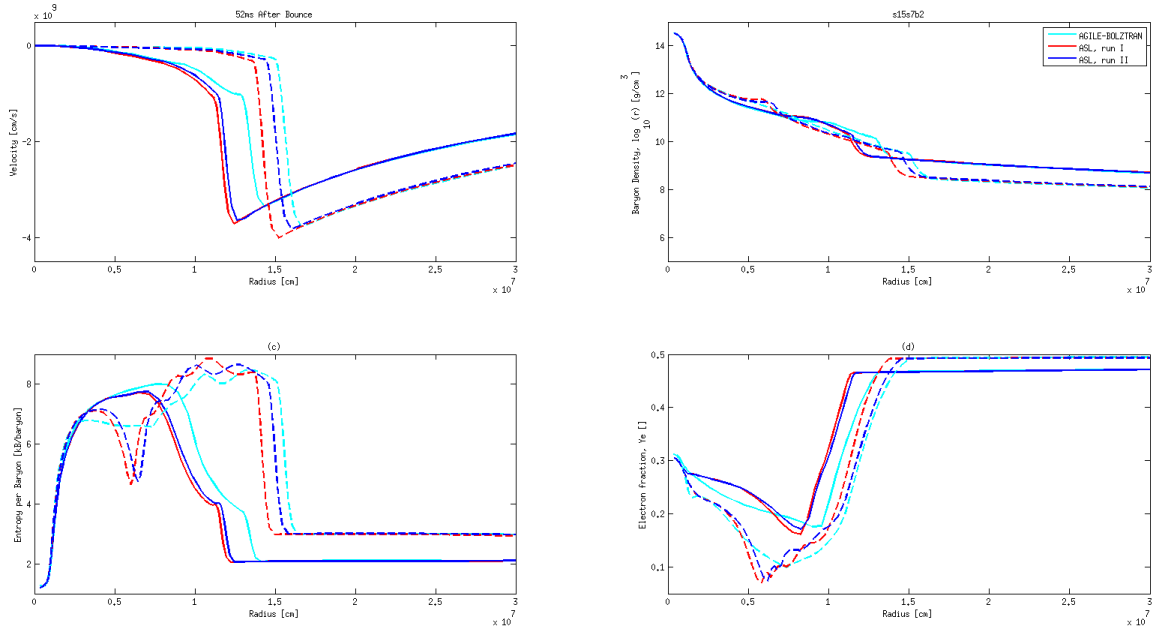

Figure 2.12: Same as Figure 2.11, but at $t \approx 10\,\mathrm{ms}$ (solid lines) and at $t \approx 50\,\mathrm{ms}$ (dashed lines) after bounce, for three different models: an `AGILE-BOLZTRAN` run (cyan line) and two different ASL runs (blue and red lines).

shock. The lower value of the of electron fraction translates in a more visible valley in

the entropy profile, which is not present in the reference solution.

Around 50ms after bounce the stalling shock wave starts to feel the heating effect of

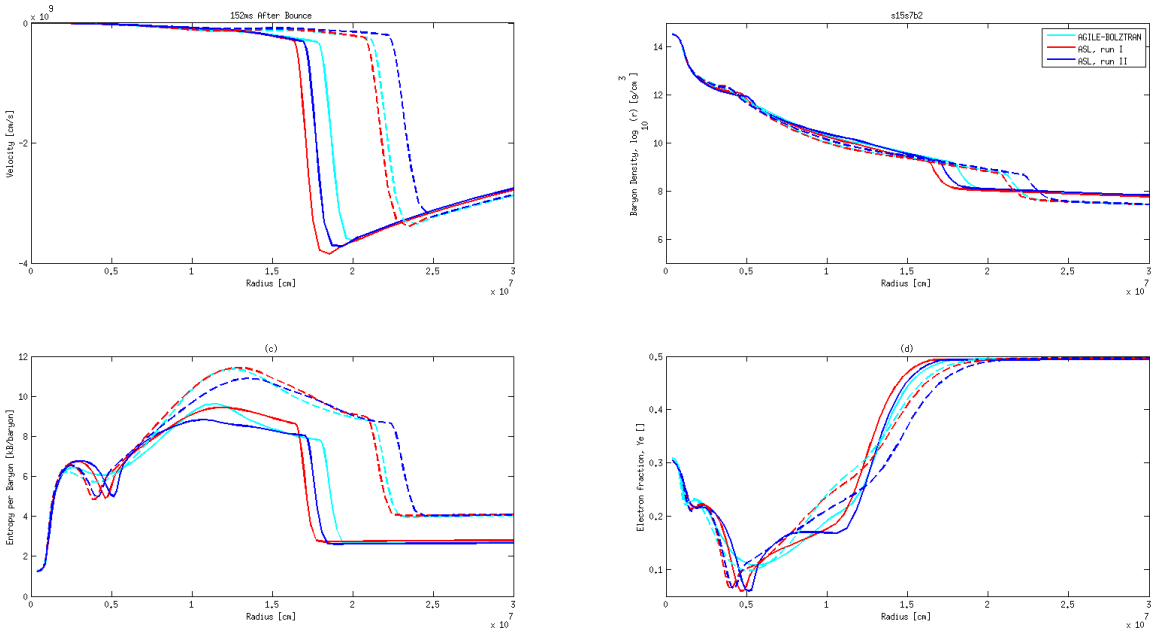

Figure 2.13: Same as Figure 2.11, but at $t \approx 100\,\text{ms}$ (solid lines) and at $t \approx 150\,\text{ms}$ (dashed lines) after bounce, for three different models: an `AGILE-BOLZTRAN` run (cyan line) and two different ASL runs (blue and red lines).

neutrinos emitted at the neutrinosphere and reabsorbed below the shock front. As a result, the shock expands again, up to $\sim 250\,\text{km}$ from the center at 150 ms. All the three models show a similar behavior and a similar expansion. Apart from the variable discrepancy in the shock position, small differences persist or arise, mainly in the Y_e profile. Remarkably, the entropy profiles of the ASL models present the typical shape and slope change, which characterize the heating phase. Finally, due to the not enough effective heating effect, the shock stops expanding and start to contract and cool, because of the pre-existing neutrino emission, as we can see in Figures 2.14. Also in this phase, our approximated treatment reproduces qualitatively, and partially quantitatively, the reference solution. Run I seems to be closer to the `AGILE-BOLZTRAN` model, not only in the shock position, but also in the Y_e profile. We notice that all the plotted quantities show a good agreement in the innermost 30 km, corresponding to the newly born protoneutron star. This means that the diffusion rates from this region are well calibrated with the reference solution.

Similarly to what we have done for the collapse phase, we compare the radial profiles of the trapped component of the electron neutrinos and antineutrinos with the (total) neutrino fraction obtained by the `AGILE-BOLZTRAN` model, in three snapshots taken from the first 50 ms after bounce, Figure 2.15. Compared to the (relatively) cold collapsing phase, the hot expanding phase seems to be more difficult to model, probably because of the presence of more relevant transport phenomena. Nevertheless, the qualitative shape and temporal evolution of the trapped components are reproduced. Moreover, the differences we have seen in the Y_e profiles translate in a different electron chemical potential and, finally, in a different equilibrium chemical potential for ν_e (and, consequently, for

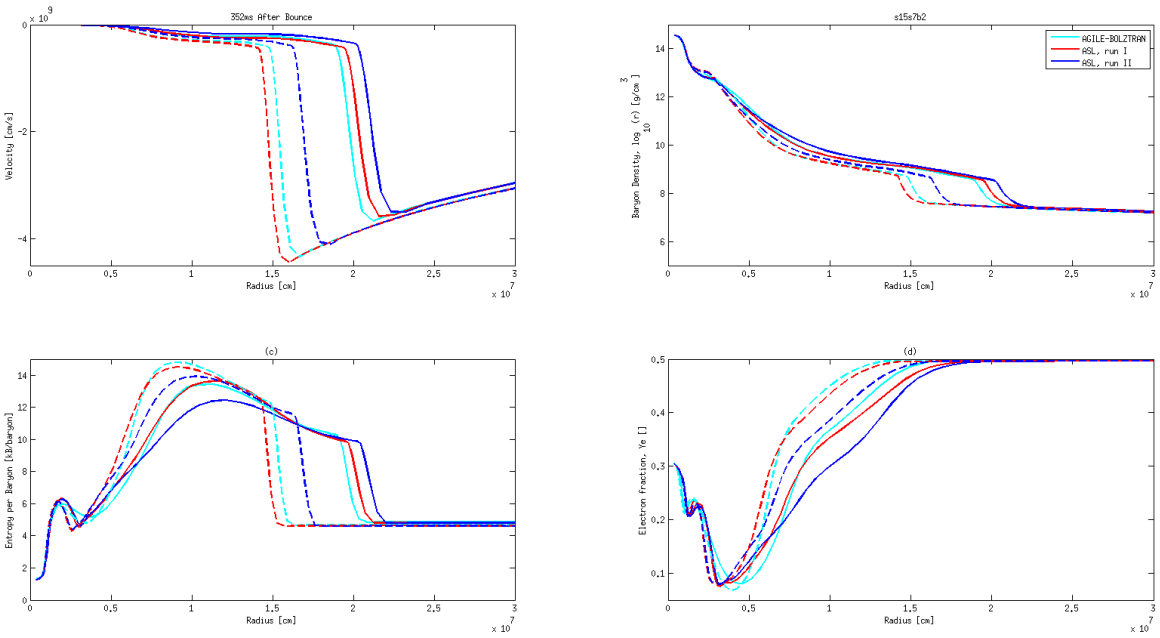

Figure 2.14: Same as Figure 2.11, but at $t \approx 250\,\mathrm{ms}$ (solid lines) and at $t \approx 350\,\mathrm{ms}$ (dashed lines) after bounce, for three different models: an `AGILE-BOLZTRAN` run (cyan line) and two different ASL runs (blue and red lines).

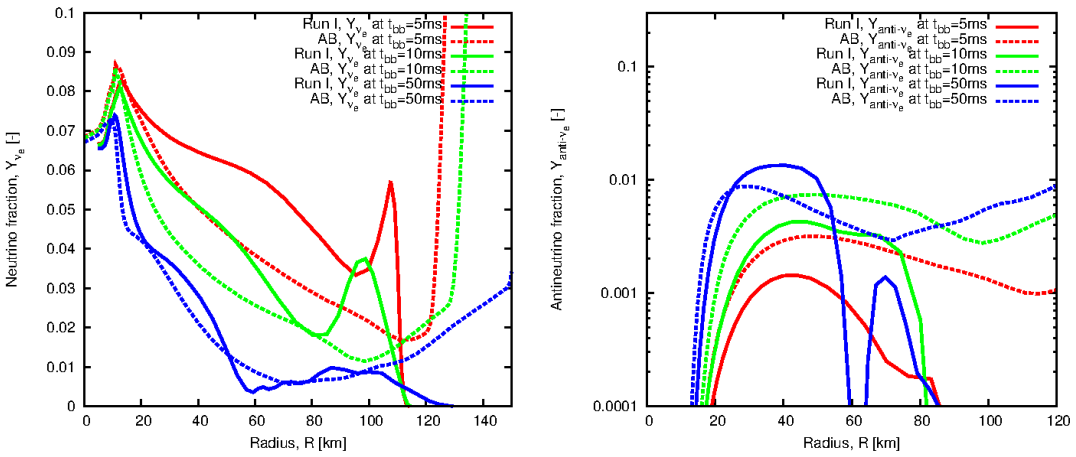

Figure 2.15: Comparison between the radial profiles of the electron neutrino (left) and electron antineutrino (right) fraction, at three different times after bounce, of the `AGILE-BOLZTRAN` (AB) solution and the ASL model (Run I).

$\bar{\nu}_e$), which has a direct impact on the equilibrium distribution functions and, by them, on the neutrino fractions.

Luminosity

The amount of energy released by neutrinos during the collapse and the post bounce phase can be directly measured by the neutrino luminosity. In Figure 2.16 we compare

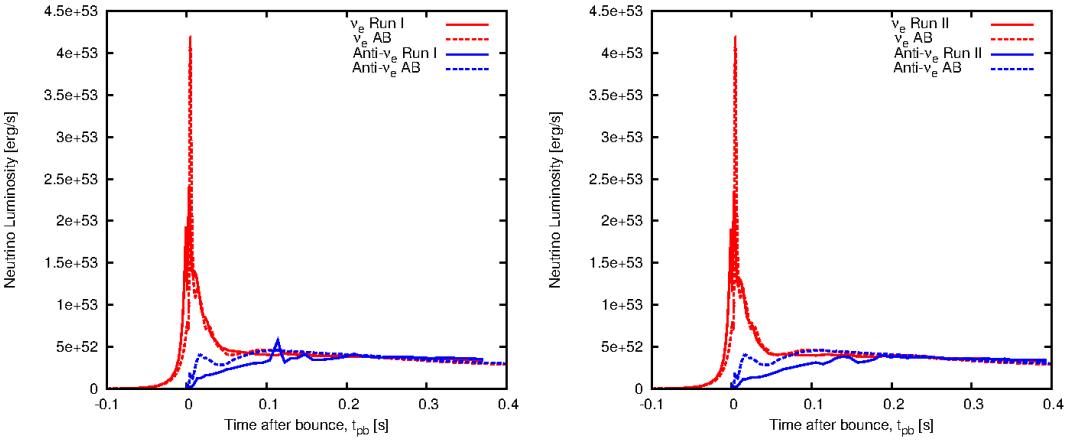

Figure 2.16: Comparison between the temporal evolution of the electron neutrino (red lines) and electron antineutrino (blue lines) luminosities obtained by the `AGILE-BOLZTRAN` model (dashed lines) and the ASL models (solid lines). On the left panel, Run I is considered; on the right panel, Run II.

the luminosities obtained by the reference `AGILE-BOLZTRAN` solution and the two ALS models. As expected from the very similar profiles obtained during the simulated time, also the luminosities show a similar behavior: we recognize the increase in ν_e luminosity during the collapse, followed by the decrease due to neutrino trapping. After bounce, neutrino burst occurs and the ν_e luminosity reaches its peak, before settling to a slowly decreasing luminosity during the accreting and cooling phase, where the energy emitted in form of neutrino is the gravitational energy lost by matter falling on the compact central object (the protoneutron star). The $\bar{\nu}_e$ luminosity rises after bounce, on a timescale of a few tens of milliseconds, when the temperature in the shocked material is high enough to reduce the $\bar{\nu}_e$ suppression, due to their large negative chemical potential. After $\sim 100\,\mathrm{ms}$, the two luminosities are almost equal and they stay very close during the accretion phase. In both cases (Run I and II), the ASL model is able to reproduce the qualitative behavior of the two luminosities, and also their asymptotic value for $t_{\mathrm{pb}} \gtrsim 0.1\mathrm{s}$.

However, some important differences can be pointed out:

- the rise of the $\bar{\nu}_e$ luminosity is faster in the reference solution;
- the luminosity peaks at neutrino trapping and at neutrino burst are different: as we can see from a deep inspection of the luminosity profile in the bounce region, Figure 2.17, in the `AGILE-BOLZTRAN` model, neutrino trapping is more effective in reducing the luminosity at the end of the collapse, while the burst has a much larger peak luminosity (almost a factor of 2);
- the shape and the timescales of the neutrino trapping and neutrino burst are different. In the ASL model, the trapping and the burst appear earlier, and the burst peak is wider (i.e less sharp).

The different value of the luminosity at neutrino trapping indicates that the diffusion rates are too high there. Nevertheless, the value 3 for the parameter α_{diff} is good in the

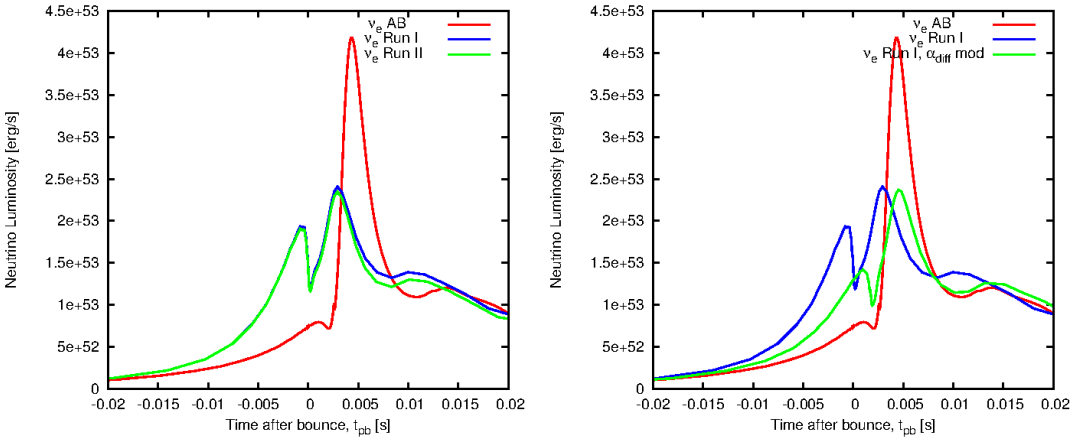

Figure 2.17: Details of the temporal evolution of the electron neutrino luminosity around bounce. On the left panel, red lines correspond to the `AGILE-BOLZTRAN` model; blue and green lines respectively to Run I and Run II. On the right panel, red lines correspond to the `AGILE-BOLZTRAN` model; blue lines to the Run I and green lines to Run II with the modified diffusion rate constant (see the text for details). respectively to Run I and Run II.

after bounce phase. Then, we decided to modify it to distinguish between before and after bounce, and we use the fraction of heavy nuclei (X_h) to do it:

$$\alpha_{\rm diff} = 3 \rightarrow \alpha_{\rm diff} = 3 + 3 \cdot X_h, \tag{2.128}$$

so that before bounce we obtain a value close to the one obtained in the grey scheme for $\nu_{\mu,\tau}$, and after bounce a value which gives a good deleptonization rate for the protoneutron star. We perform a run (Run III) with this new diffusion coefficient and we check the differences with the previous Run I model. The profiles at bounce are actually identical to the previous one. They are different just after bounce (in the first $10-20$ ms after bounce), showing a better agreement with the reference solution, as it can be seen in Figure 2.18. Later they become again identical to the previous Run I model. The better results translate also in an improvement on the luminosity curves. In the right panel of Figure 2.17 we plot ν_e luminosity at bounce for the reference solution, for Run I and for Run III, and shifted in time by $\delta t = +1.75$ms, so that the minima at bounce coincide. With the new diffusive parameter, the first maximum has significantly improved. The meaning of the time shift we have introduced can be understood remembering that `BOLZTRAN` is a transport scheme, while the ASL is an effective treatment: in the former, neutrinos travel from the production site to a distant place, where the luminosity is measured, and the travel and the amount of time needed for it is consistently taken into account. In the ASL treatment, neutrinos are assumed to leave the system when they simply leave the fluid cell where they have been produced. Obviously, the time needed to travel is not taken into account. If neutrino production happens in a (almost) transparent area (like when the shock breaks through the neutrinosphere and neutrino burst occurs), the position of the corresponding peak is simply shifted by the free streaming timescale to reach the surface where luminosity is measured. But, when neutrinos are diffusing, the complicated diffusion motion can not be described by a simple time shift, but probably by a superposition of different shifts, occurring for different neutrino

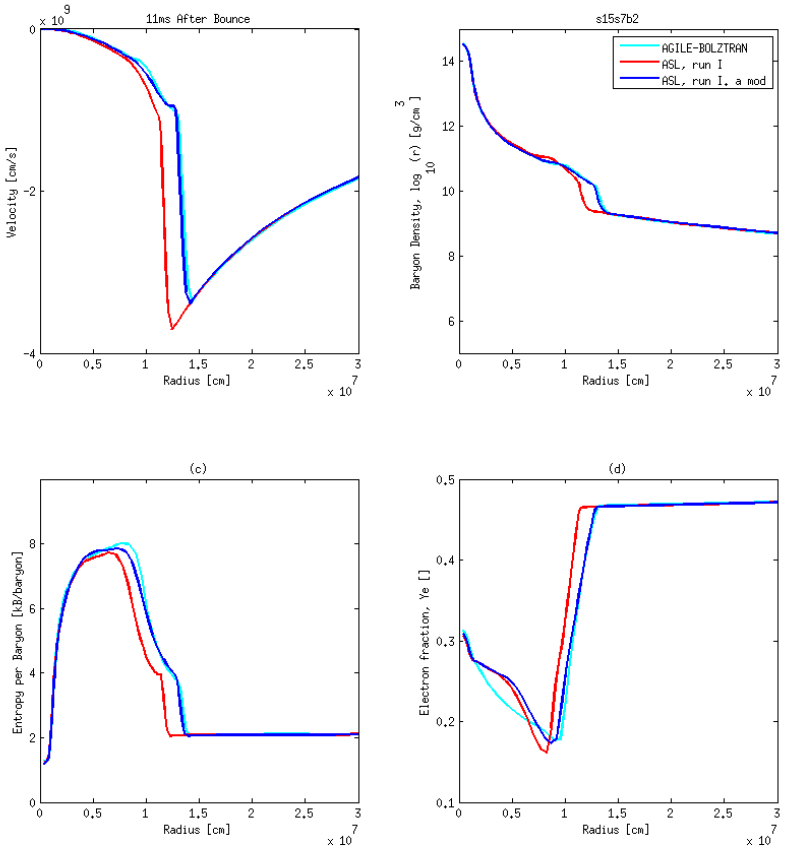

Figure 2.18: Comparison between the radial profiles of the velocity (upper left), baryon density (upper right), entropy (lower left) and electron fraction (lower right), at $t \approx 10\,\mathrm{ms}$ after bounce, for three different models: an `AGILE-BOLZTRAN` run (cyan line), the Run I and the Run III models (Run III is defined as Run I model, with α_{diff} modified according to Eq.(2.128)).

energies. Then, in the `AGILE-BOLZTRAN` model we expect most of the neutrinos to be produced deep in the optical thick region, to diffuse in the expanding shock wave and, finally, to be released mainly at neutrino burst, when they all enter the optically thin regime. On the other hand, in the ASL scheme, they are assumed to leave the system as soon as they cool locally the fluid. This should explain why the peak at neutrino burst is lower and wider in the ASL scheme, and the peak at neutrino trapping is again wider, but higher. As a counter-proof of this argument, we calculate the integrals below the luminosity curves (i.e. the total emitted energy) for all the four models, :

$$\Delta E = \int_{t_1+\delta t}^{t_2+\delta t} L_{\nu_e}\, \mathrm{d}t. \tag{2.129}$$

first in an interval close to bounce ($t_1 = -0.02\,\mathrm{ms}$ and $t_2 = 0.015\,\mathrm{ms}$); results are reported in Table 2.4. It is clear that all ASL runs have a total emitted energy close to bounce quite consistent with the reference model one, with a maximum discrepancy of 17% in model Run II, and a very close result (discrepancy on only 3%) with the

Model	Flavor	δt [ms]	t_1 [ms]	t_2 [ms]	$\Delta E[10^{51}\text{erg}]$	$\epsilon_{\Delta E}$
AB	ν_e	0.0	- 20	15	3.0357	0
Run I	ν_e	1.75	- 20	15	3.2920	0.0844
Run II	ν_e	1.75	- 20	15	3.4963	0.152
Run III	ν_e	1.75	- 20	15	2.9495	-0.028
AB	ν_e	0.0	- 100	350	17.756	0
Run I	ν_e	1.75	- 100	350	18.488	0.0412
Run II	ν_e	1.75	- 100	350	18.078	0.0181
Run III	ν_e	1.75	- 100	350	18.190	0.0244
AB	$\bar{\nu}_e$	0.0	- 100	350	13.735	0
Run I	$\bar{\nu}_e$	1.75	- 100	350	12.225	-0.110
Run II	$\bar{\nu}_e$	1.75	- 100	350	11.494	-0.163
Run III	$\bar{\nu}_e$	1.75	- 100	350	12.317	-0.103

Table 2.4: Table with the time integral of the total luminosity. We explore different models and different time intervals: close to bounce for L_{ν_e}; over the whole simulation for both L_{ν_e} and $L_{\bar{\nu}_e}$. In the last column, we report the discrepancy of each model x, with respect to the `AGILE-BOLZTRAN` model, $\epsilon_{\Delta E,x} = (\Delta E_x - \Delta E_{AB})/\Delta E_{AB}$

model Run III, with the modified α_{diff}. In the same table, we report also the integral of the luminosity over the whole simulation period, for both ν_e and $\bar{\nu}_e$. Results are better for ν_e than for $\bar{\nu}_e$. Overall, the model Run III expresses the better agreement with the reference model.

Mean energies

In Figure 2.19, we plot the temporal evolution of the mean energy measured far from the shock (around 400 km) for the Run III model presented in the previous section. For the ASL scheme, we draw both the original values obtained by the scheme (i.e. the values directly obtained by the spectral effective rates, $\tilde{r}_{\text{eff}}$,) and the values obtained by the corrected effective rates, $\tilde{r}_{\text{eff}}$, with the exponential cut, as expressed by equation 2.70, assuming to keep the number of emitted neutrinos constant. It is clear that the original spectral rates are too hard outside the neutrinosphere, while the cut ones are much more consistent in that area, crucial for the heating process.

2.4.2 Second test: electron flavor and extended reaction set

As second test, we perform simulations very similar to the first test, but we include more reactions regarding the electron flavor neutrinos. In particular, the pair production due to electron-positron annihilation and the neutrino bremsstrahlung due to strong interaction between nucleons. To summarize, in both models (`AGILE-BOLZTRAN` and `AGILE`-ASL), we include the reactions reported in table 2.5. The included pair reactions are interpolated from tables previously calculated, in order to save time during the execution. Results from the `AGILE-BOLZTRAN` simulation of this second test are very close to the one we have obtained in the first test: this is a confirmation of the fact that the new pair reactions play a sub-dominant role for this flavor, compared to the

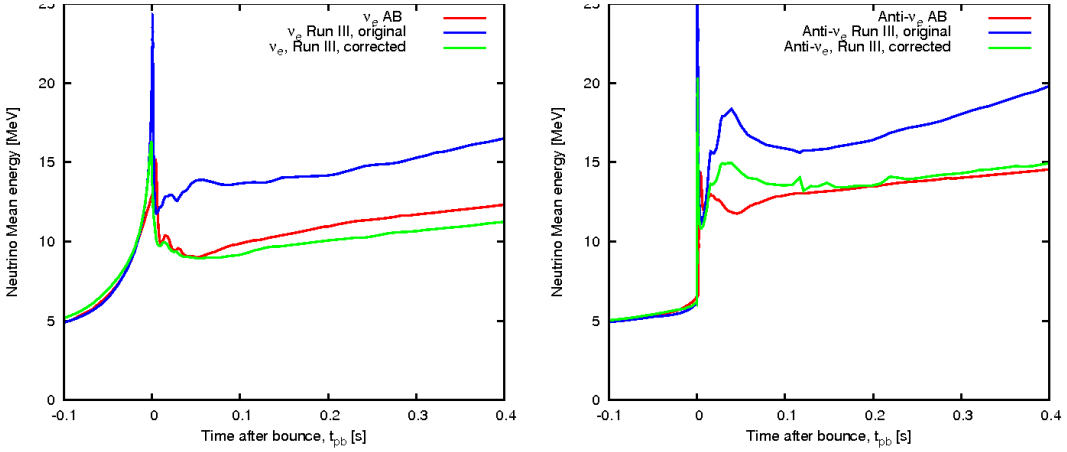

Figure 2.19: Temporal evolution of the electron neutrino (left panel) and electron antineutrino (right panel) mean energies. Red lines corresponds to the results obtained with the AGILE-BOLZTRAN model; blue lines are the results obtained in Run III, without applying the cut at the spectrum; green lines are the results obtained with the Run III model, and taking into account the spectrum cut (with $\alpha_{\rm cut} = 15$).

Reactions	Currents	Main Role	Reference
$e^- + p \rightarrow n + \nu_e$	CC	P, T, O	[12]
$e^+ + n \rightarrow p + \bar{\nu}_e$	CC	P, T, O	[12]
$e^- + (A, Z) \rightarrow \nu_e + (A, Z-1)$	CC	P, T, O	[12]
$e^+ + e^- \rightarrow \nu_e + \bar{\nu}_e$	NC & NC	P, T	[12], [102]
$N + N \rightarrow N + N + \nu_e + \bar{\nu}_e$	NC	P, T	[51]
$N + \nu_e/\bar{\nu}_e \rightarrow N + \nu_e/\bar{\nu}_e$	NC	O	[12]
$(A, Z) + \nu_e/\bar{\nu}_e \rightarrow (A, Z) + \nu_e/\bar{\nu}_e$	NC	O	[12]

Table 2.5: Table with the relevant ν_e and $\bar{\nu}_e$ reactions included in models to test the ASL scheme for the electron flavor. In the reactions column, N represents nucleons. In the current column, NC stands for neutral current, while CC for charged current reactions. In the Main Role column, P stands for production, T for thermalization and O for opacity.

essential reactions we have already explored. In Table 2.6, we summarize the parameter we have used for the ASL models. We choose two different models, changing the values of the $\alpha_{\rm cut}$ parameter: in Run IV, ν_e and $\bar{\nu}_e$ have different parameters, and the cut for antineutrinos is more pronounced than the one for neutrinos; in Run V, we choose the same parameter, but larger compared with first tests. Compared to the previous cases, we choose different values for the $\alpha_{\rm cut}$ parameter, in order to have a slightly harder spectrum. In Figure 2.20 - 2.22 we can see comparisons between the reference model and the two ASL tested models, at different times between bounce and ~ 300 ms after bounce. Direct comparison between the AGILE-BOLZTRAN results here and in the first test shows that the inclusion of the new reactions has not a relevant impact on the general dynamics. The heating mechanism is slightly enhanced and the shock is a bit more extended around 150 km. The agreement between the ASL model and the reference solution is still quite good, even if the problems we found before can be seen

Name of the parameter	ASL Run IV	ASL Run V
α_{diff}	$3.00 + 3.00X_h$	$3.00 + 3.00X_h$
β_{rec}	2.00	2.00
α_{int}	3.00	3.00
$\alpha_{\nu_e,\mathrm{cut}}$	25.0	20.0
$\alpha_{\bar{\nu}_e,\mathrm{cut}}$	15.0	20.0
α_{heat}	1.00	1.00
β_{cut}	$L_{\nu,\mathrm{N}}$	$L_{\nu,\mathrm{N}}$

Table 2.6: Table with the values of all the free parameters of the ASL scheme, used in the second test case.

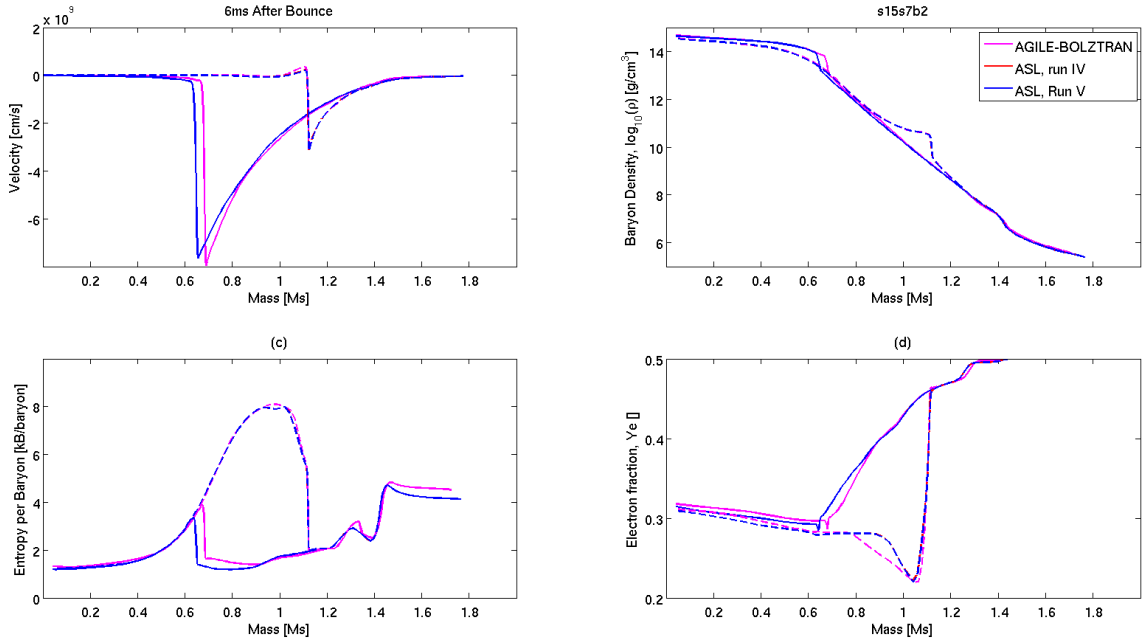

Figure 2.20: Comparison between the velocity (upper left), baryon density (upper right), entropy (lower left) and electron fraction (lower right), at $t \approx 0\,\mathrm{ms}$ (solid lines) and at $t \approx 5\,\mathrm{ms}$ (dashed lines) after bounce, for three different models: an `AGILE-BOLZTRAN` run (magenta line) and two different ASL runs (blue and red lines). The profiles are expressed as function of the enclosed mass.

also here, and the difference on the shock position is, on average, slightly increased. We also notice that the variation induced by the different choice of the α_{cut} parameter (in the explored range) are minimal and smaller than the differences with the reference solution. In Figures 2.23 and 2.24, we compared, similarly to what we have done in the first test, the luminosities and the mean neutrino energies produced by the ASL scheme and the reference ones, for both ν_e and $\bar{\nu}_e$. As in the previous case, they all show a good agreement with the expected behavior and also with the actual values, with errors similar to the ones we have already discussed in the previous paragraph.

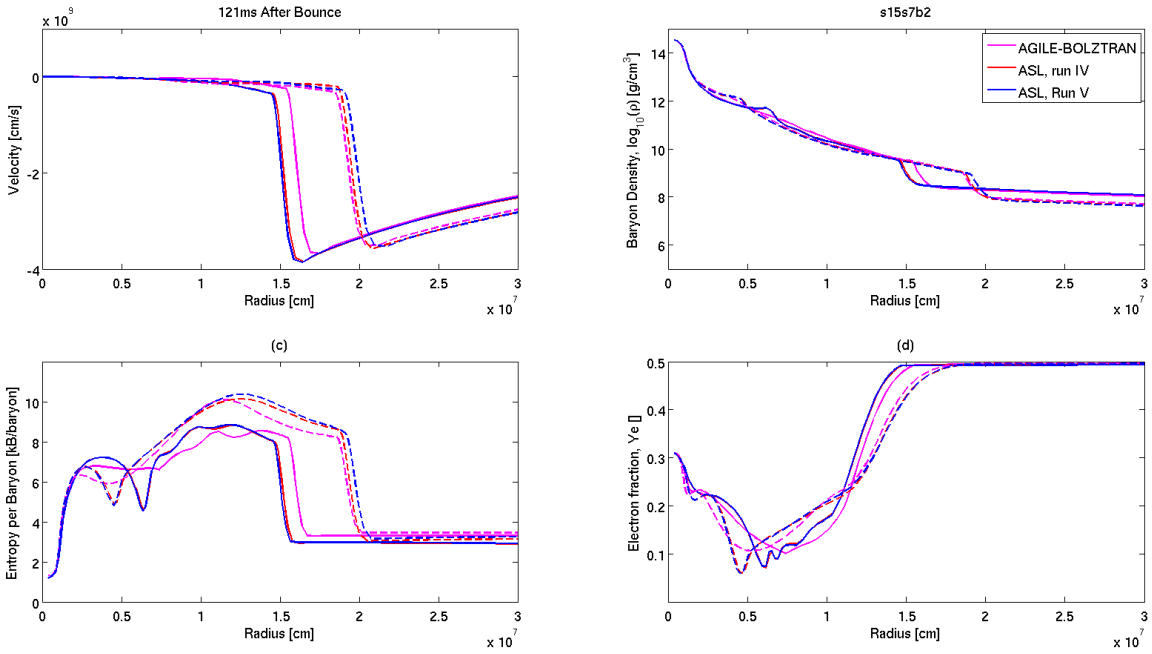

Figure 2.21: Same as Figure 2.20, but at $t \approx 50\,\mathrm{ms}$ (solid lines) and at $t \approx 120\,\mathrm{ms}$ (dashed lines) after bounce, for three different models: an `AGILE-BOLZTRAN` run (magenta line) and two different ASL runs (blue and red lines). Here the profiles are represented as function of the radius.

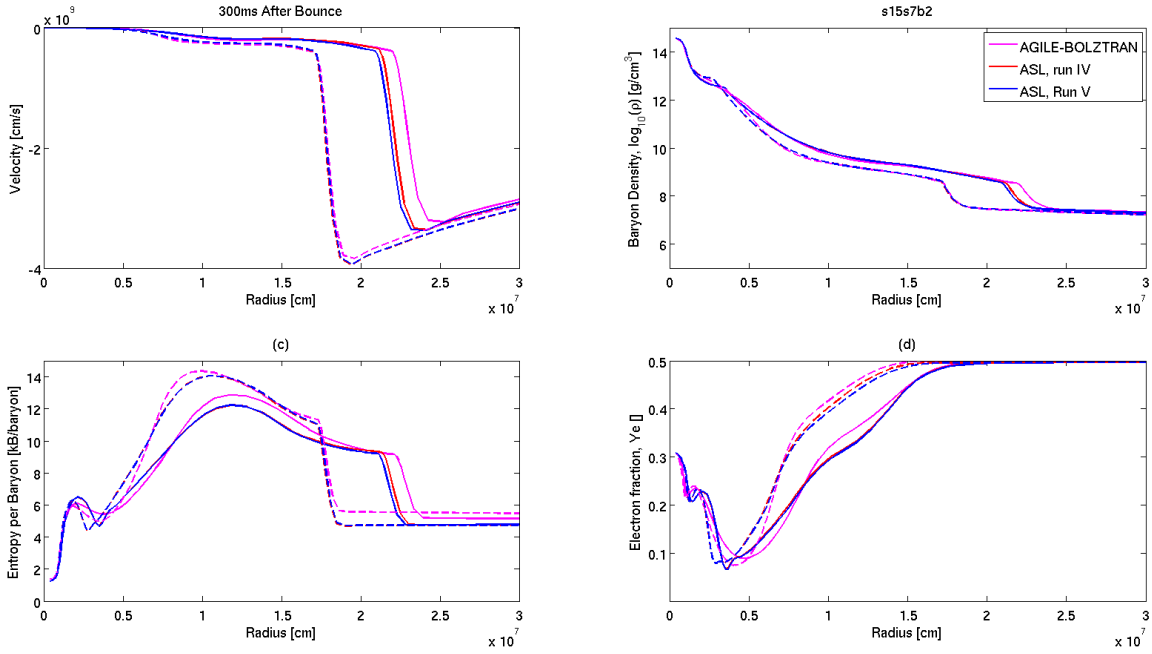

Figure 2.22: Same as Figure 2.20, but at $t \approx 200\,\mathrm{ms}$ (solid lines) and at $t \approx 300\,\mathrm{ms}$ (dashed lines) after bounce, for three different models: an `AGILE-BOLZTRAN` run (magenta line) and two different ASL runs (blue and red lines). Here the profiles are represented as function of the radius.

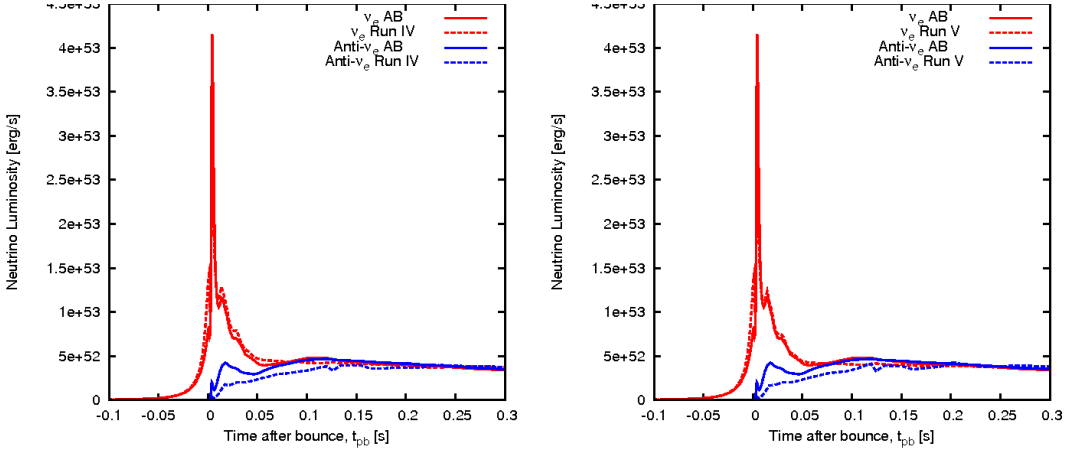

Figure 2.23: Comparison between the temporal evolution of the electron neutrino (red lines) and electron antineutrino (blue lines) luminosities obtained by the `AGILE-BOLZTRAN` model (dashed lines) and the ASL models (solid lines). On the left panel, Run IV is considered; on the right panel, Run V.

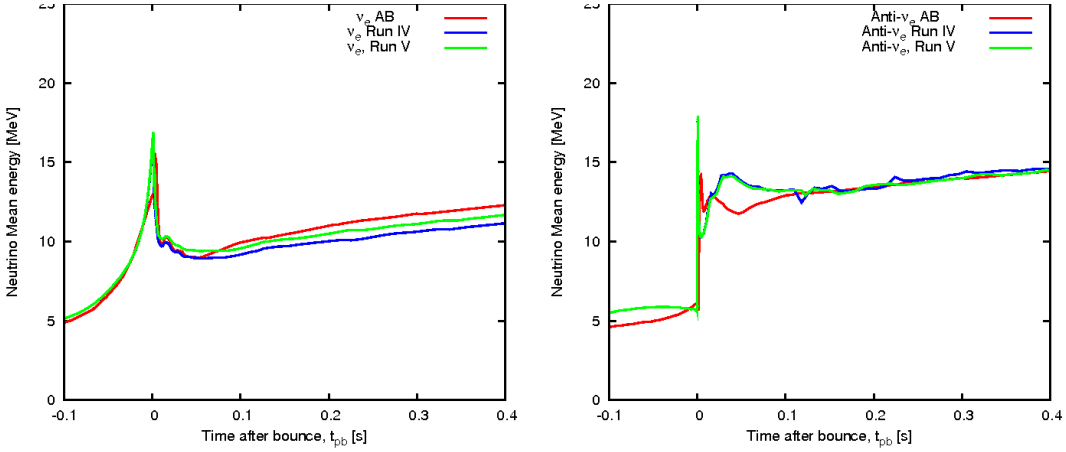

Figure 2.24: Temporal evolution of the electron neutrino (left panel) and electron antineutrino (right panel) mean energies. Red lines corresponds to the results obtained with the `AGILE-BOLZTRAN` model; blue lines are the results obtained in Run IV, green lines are the results obtained with the Run V model. For the latter two models, we are taking into account the spectrum cut.

2.4.3 Third test: μ and τ flavors

For the third test, we consider the model V of the previous test and we add $\nu_{\mu,\tau}$ and $\bar{\nu}_{\mu,\tau}$ to it. We compare the results obtained with an `AGILE-BOLZTRAN` simulation, setting similar input neutrino physics. In Table 2.7 we summarize the reaction used in the new simulations. Similarly to the previous case, in this one pair reactions are interpolated from a table. In Table 2.8, we summarize the parameters we have used for the ASL model, regarding all flavors:

In Figures (2.25) - (2.27) we show the comparison between the ASL model and the `AGILE-BOLZTRAN` reference solution. Unfortunately, the reference model could run only up to ~ 200 ms before it stopped running, due to numerical problems in the protoneutron

Reactions	Currents	Main Role	Reference
$e^- + p \rightarrow n + \nu_e$	CC	P, T, O	[12]
$e^+ + n \rightarrow p + \bar{\nu}_e$	CC	P, T, O	[12]
$e^- + (A, Z) \rightarrow \nu_e + (A, Z-1)$	CC	P, T, O	[12]
$e^+ + e^- \rightarrow \nu + \bar{\nu}$	NC & NC	P, T	[12], [102]
$N + N \rightarrow N + N + \nu + \bar{\nu}$	NC	P, T	[21]
$N + \nu \rightarrow N + \nu$	NC	O	[12]
$(A, Z) + \nu \rightarrow (A, Z) + \nu$	NC	O	[12]

Table 2.7: Table with the relevant ν_e, $\bar{\nu}_e$, $\nu_{\mu,\tau}$ and $\bar{\nu}_{\mu,\tau}$ reactions included in models to test the ASL scheme for μ and τ flavors. In the reactions column, N represents nucleons. In the current column, NC stands for neutral current, while CC for charged current reactions. In the Main Role column, P stands for production, T for thermalization and O for opacity. ν stays for a generic neutrino kind, and $\bar{\nu}$ for its antiparticles.

Name of the parameter	ASL Run VI
$\alpha_{\nu_e,\bar{\nu}_e\text{diff}}$	$3.00 + 3.00X_h$
$\alpha_{\nu_{\mu,\tau},\text{diff}}$	6.00
β_{rec}	2.00
α_{int}	3.00
$\alpha_{\nu_e,\text{cut}}$	25.0
$\alpha_{\bar{\nu}_e,\text{cut}}$	15.0
$\alpha_{\nu_{\mu,\tau},\text{cut}}$	15.0
α_{heat}	1.00
β_{cut}	$L_{\nu,\text{N}}$

Table 2.8: Table with the values of all the free parameters of the ASL scheme, used in the second test case.

star. Then, we can compare the ASL model only up to 200ms; nevertheless, when we developed the grey scheme for $\nu_{\mu,\tau}$, we already saw that important effects from the new cooling sources can be seen already a few tens of milliseconds after bounce. So, this problem should not affect dramatically our analysis. From these figures we can say that, also in this case, there is a good qualitative agreement between the model and the reference solution. Comparing the new profiles with the old one, we can also say that we catch the essential aspect introduced by $\nu_{\mu,\tau}$ cooling, limiting the expansion of the shock wave. Also from a quantitative point of view, many aspects can be considered satisfactory. For example, the mean energies of $\nu_{\mu,\tau}$, at $\sim 100\,\text{ms}$ after bounce and at a large radius, should be $\sim 22.7\,\text{MeV}$, according to the `AGILE-BOLZTRAN` reference solution. The value that we obtained in the ASL model, considering the spectral cut, is $\sim 21.2\,\text{MeV}$, very close to what we expect. However, a more detailed inspection of the new results shows that more differences arose in this last test (see, for example, the differences in the electron fraction profiles at late times). We think that these differences could derive from the less extended expansion of the shock wave, and from the different thermodynamical conditions in which the shocked material can be found here, compared with the previous tests. A more detailed analysis and an attempt to fix this discrepancies

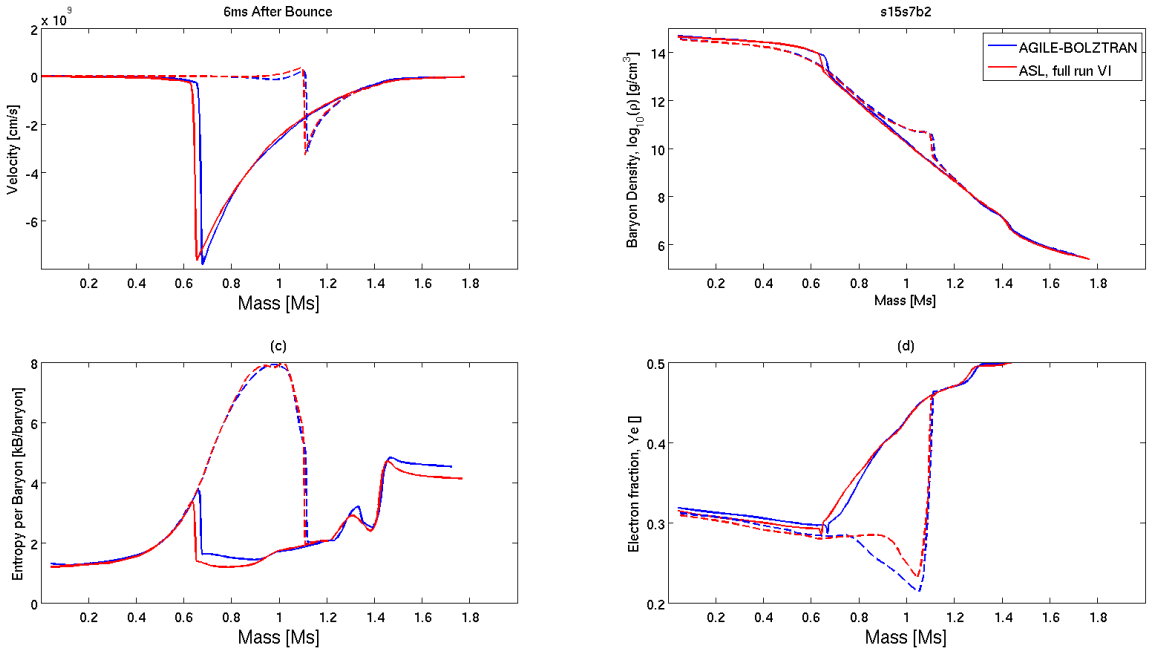

Figure 2.25: Comparison between the velocity (upper left), baryon density (upper right), entropy (lower left) and electron fraction (lower right), at $t \approx 0\,\mathrm{ms}$ (solid lines) and at $t \approx 5\,\mathrm{ms}$ (dashed lines) after bounce, for two different models: an `AGILE-BOLZTRAN` run (blue line) and an ASL runs (red lines). The profiles are expressed as function of the enclosed mass.

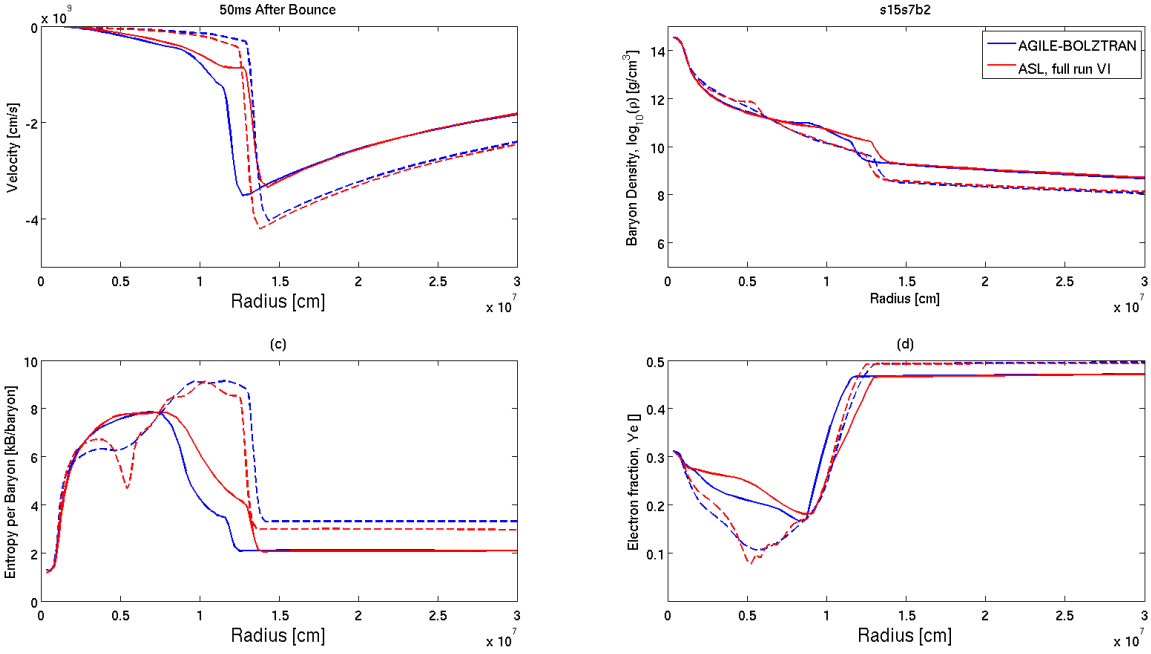

Figure 2.26: The same as 2.25, but at $t = 10\,\mathrm{ms}$ (solid lines) and $t = 50\,\mathrm{ms}$ (dashed lines) after core bounce. Here the profiles are expressed as function of radius.

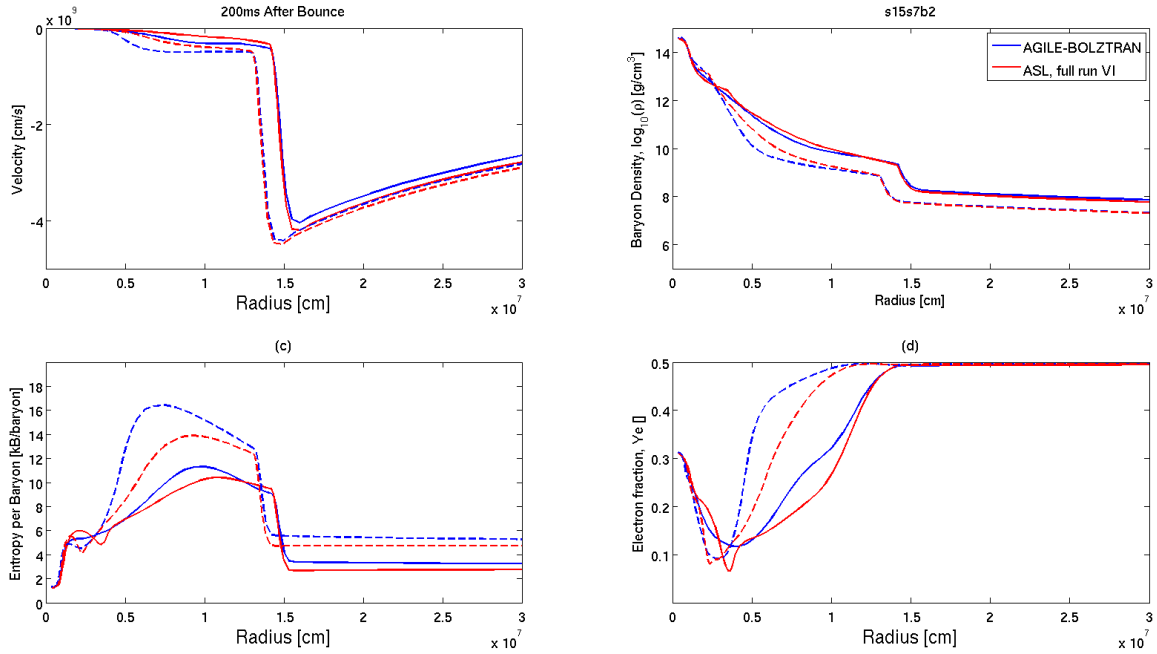

Figure 2.27: The same as 2.25, but at $t = 100\,\mathrm{ms}$ (solid lines) and $t = 200\,\mathrm{ms}$ (dashed lines) after core bounce. Here the profiles are expressed as function of radius.

will be the next step in the further development of the ASL scheme.

Chapter 3

MODA, multi-dimensional optical depth algorithm

The neutrino optical depth is one of the crucial ingredient of the ASL scheme: it defines the limit between different optical regimes and it enters directly the calculation of the diffusion rates. The major difficult to compute it, in particular in multidimensional simulations, resides in its intrinsically non-local nature: counting the average amount of interactions that a radiation particles experiences from it production site to the limits of the domain, it requires the knowledge of the geometry and of the local properties of matter-radiation interaction in the whole computational domain, at the same time. Symmetries have provided powerful arguments to suggest radiation paths along which the optical depth can be calculated. For example, in a spherically symmetric cases, radial paths are the most natural choice, compatible with the symmetry of the system. For other symmetries (like axial symmetry) or for systems that do not present any evident or even approximated invariance, there are no natural and univoque path choices. The calculation of the optical depth in these cases has been traditionally done choosing a set of (usually straight) paths, along which the optical depth path integral can be easily computed. If more than one path could be associated with the same point in the domain, then the actual optical depth is usually the minimal among the different possibilities.
For example, in systems with an almost spherically symmetry (like CCSN in multi-dimensions), multidimensional radiation transport problems can be treated using the *ray-by-ray* approximation: the multidimensional problem is approximated by a set of (eventually coupled) one-dimensional problems, each of which models a sector of the solid angle. In other cases, when rays from the center do not describe typical radiation paths (like in accretion disk), each point of the domain has it own set of straight paths. We call this approach as *local* ray-by-ray.

In this following, we discuss a new algorithm to calculate optical depths in two or in three spatial dimensions. Unlike most commonly used algorithms, we do not make any *a priori* assumptions about symmetries in the system or the radiation direction. Instead, we calculate both, a path out of a given matter distribution and the corresponding optical depth, without such restrictive assumptions.

3.1 Definitions and main hypotheses

The optical depth along a path γ from A to B is defined as

$$\tau_{A\to B}\left[\gamma\right] = \int_{\gamma:A\to B} \frac{ds}{\lambda}, \tag{3.1}$$

where λ is the local mean free path and ds an infinitesimal displacement along the radiation direction. Obviously, λ is a function of position, and the optical depth depends on the exact path between A and B. Eq. (3.1) also contains the physical interpretation of τ: being related to the inverse of the mean free path, it counts the average number of interactions between radiation and matter along the path γ.
In many approximative radiation treatments, the required information is the number of radiation-matter interactions from a given position out to the edge of the computational domain, from which the radiation can escape freely. If we denote by $\mathbf{x}_e$ any point of the edge from which a given radiation parcel can leave the domain, the optical depth at a point $\mathbf{x}$ inside the computational domain, calculated along $\gamma : \mathbf{x} \to \mathbf{x}_e$, is given by

$$\tau_{\mathbf{x}\to\mathbf{x}_e}[\gamma] = \int_{\gamma:\mathbf{x}\to\mathbf{x}_e} \frac{ds}{\lambda}. \tag{3.2}$$

Even though each radiation particle travels and interacts in its own way and along its own path, we are interested in an average behavior, that characterizes how opaque or transparent the matter is to radiation. If we consider that each interaction causes the radiation to be absorbed (and, eventually, emitted again) or scattered, changing its original direction, we can say that the path which minimizes τ corresponds to the most likely way for the radiation to leave the system. Following this prescription, more emphasis is usually devoted to the path that minimizes the optical depth,

$$\tau(\mathbf{x}) = \min_{\{\gamma|\,\gamma:\mathbf{x}\to\mathbf{x}_e\}} \int_\gamma \frac{ds}{\lambda}. \tag{3.3}$$

With the exception of very few cases, where the strong degree of symmetry of the system simplifies the calculation, the detection of the path which minimizes the optical depth is not obvious and computationally too expensive to be calculated. For this reason, we have searched for a different prescription that can be applied to more general cases, where no evident symmetries are present, and that can be related to the physical behavior of the radiation traveling inside an opaque medium; but still using the minimization of the path integral as a guide line. This prescription is presented in the next section.

Before proceeding, we indicate a few hypotheses concerning the computational domain and the behavior of the mean free path λ in it. 1) Each point in our matter distribution is –apart from its physical properties– also characterized by a local, numerical resolution length that we denote by h. 2) Once the density and the other thermodynamical quantities are known, the local mean free path λ can be calculated. 3) We assume that λ is a smooth function of the spatial variables, and, of course, is large in transparent and small in opaque regions. 4) We assume that the most opaque areas are located well inside the domain, far from the edge. Then, the mean free path decreases (globally) and it has its minima at the edge of the computational domain, from where the radiation can escape on sufficiently long timescales.

3.2 The algorithm

In what follows, we present our prescription for selecting the path that enters into Eq. (3.2). The local opacity value of a medium is determined by both, scattering off other particles and absorption, and it is quantified by the local mean free path λ. From a microscopic point of view[1], the production occurs isotropically, i.e., radiation can be emitted in any direction; on the macroscopic scale, the properties of matter influence the behavior of radiation, and break the symmetry of the emission: if a radiation particle is emitted towards a region of decreasing mean free path, it will likely interact again with matter, changing its original propagation direction; on the contrary, if it is emitted towards a direction of increasing mean free path, it will probably move away freely from the production site. This simple consideration suggests that, even if radiation is emitted locally in an isotropic way, it moves macroscopically preferentially towards regions of larger mean free path. For convenience, we introduce σ as inverse of the mean free path

$$\sigma(\mathbf{x}) = \frac{1}{\lambda(\mathbf{x})}. \tag{3.4}$$

Under the hypotheses presented in the previous section, σ has its largest values well inside the computational domain, and reaches its absolute minimum at the edge of the domain. Note that we do not assume σ to decrease monotonically, it is allowed to have local maxima and minima. One could calculate the local gradient of σ and proceed in the direction of its minimum, but this does not necessarily correspond to the direction that globally minimizes the optical depth. To avoid getting "trapped" in local minima, we proceed in the following way. First, we define a sphere with radius R, comparable to the local resolution length $R \sim h$, around a given point $\mathbf{x}$. On this sphere, we search for a point $\mathbf{z}$ that satisfies

$$\sigma(\mathbf{z}) < f_{\text{dec}}\sigma(\mathbf{x}), \tag{3.5}$$

where $f_{\text{dec}} < 1$. If found, R is stored as the local decreasing length , $l_{\text{dec}}(\mathbf{x}) = R$. If no such point can be found, we increase the radius of the sphere (for example, by taking increasing integer multiples of h) and repeat the search until we find an acceptable decreasing lenghtscale.

Typical values of f_{dec} that we have tested (see section 4 for more details) lie in the interval $0.1 - 0.5$. Larger values, closer to unity, can be less effective on avoiding local extremes, while smaller values require more computational effort, and are prone to push the decreasing lengthscale search too early at the edge of the computational domain, introducing boundary conditions effects. In any case, we recommend a preventive study of $\sigma(\mathbf{x})$ and its typical spatial and temporal variations, in order to choose a meaningful values of f_{dec}.

Once we know the lengthscale at which σ has certainly decreased down to the chosen limit $\sigma_{\text{dec}}(\mathbf{x})$, we also obtain the direction towards the minimum of $\sigma(\mathbf{x})$, $\mathbf{v}_{\text{min}}(\mathbf{x})$. Nevertheless, using $\mathbf{v}_{\text{min}}(\mathbf{x})$ systematically for the calculation of $\tau(\mathbf{x})$, can lead to abrupt and unrealistic discontinuities in the optical depth, that are basically the outcome of the interplay between the local resolution and the geometrical complexity of the simulated

[1]With macro-/microscopic we mean large/small in comparison to the local mean free path λ.

system. To avoid this, it is better to devise a smoothed definition of the path direction. To that end, we consider again the sphere centered on $\mathbf{x}$, with radius $R = l_{\mathrm{dec}}(\mathbf{x})$. We denote the corresponding spherical surface by S_{dec}. For points $\mathbf{y}$ on this surface, we define unit vectors $\hat{e}_{\mathbf{y}} = (\mathbf{y} - \mathbf{x})/|\mathbf{y} - \mathbf{x}|$, which –when properly weighted– yield an "average" direction where *sigma* becomes minimal on S_{dec}

$$\mathbf{v}_{\mathrm{dec}}(\mathbf{x}) = \left(\int_{S_{\mathrm{dec}}} \frac{\hat{e}_{\mathbf{y}}}{\sigma(\mathbf{y})}\, ds \right) \Big/ \left| \int_{S_{\mathrm{dec}}} \frac{\hat{e}_{\mathbf{y}}}{\sigma(\mathbf{y})}\, ds \right| . \tag{3.6}$$

This average favors the directions where σ is minimum on the spherical surface, but it also takes globally into account the behavior of σ at the scale of $l_{\mathrm{dec}}(\mathbf{x})$, smoothing the evolution of the direction in case of sharp, local variations. In order to avoid a compensation effect due to the average calculation (for example, when a system has a strong symmetry with respect to a plane, on the plane itself the average calculation can partially cancel the contributions from two symmetric points of minimum), we calculate the cosine between $\mathbf{v}_{\mathrm{dec}}(\mathbf{x})$ and $\mathbf{v}_{\mathrm{min}}(\mathbf{x})$. If the two directions are too different (the cosine exceeds, for example, 0.9), we reject $\mathbf{v}_{\mathrm{dec}}(\mathbf{x})$, calculated with Eq. (3.6), and we use $\mathbf{v}_{\mathrm{dec}}(\mathbf{x}) = \mathbf{v}_{\mathrm{min}}(\mathbf{x})$ instead.

Once $\mathbf{v}_{\mathrm{dec}}(\mathbf{x})$ is known, we proceed by one resolution lenghtscale h in its direction and denote the corresponding end point by $\mathbf{x}'$. It is noteworthy that although the search for the integration direction $\mathbf{v}_{\mathrm{dec}}(\mathbf{x})$ is made by "looking ahead" to whatever distance is necessary in order to find an acceptable σ, the integration itself is done in as small increments as possible. Therefore, $\mathbf{x}'$ will *always be the closest point* to $\mathbf{x}$ in the direction $\mathbf{v}_{\mathrm{dec}}(\mathbf{x})$.

Starting from a point $\mathbf{x}$, this procedure is repeated until the edge of the computational domain is reached: $\mathbf{x}^{(0)} = \mathbf{x}$, $\mathbf{x}^{(1)} = \mathbf{x}'$, $\mathbf{x}^{(2)}$, $\mathbf{x}^{(3)}$, …, $\mathbf{x}_{\mathrm{e}}^{(n)}$. Along this path, the optical depth $\tau(\mathbf{x})$ is calculated as

$$\tau(\mathbf{x}) = \int_{\gamma:\mathbf{x}\to\mathbf{x}_{\mathrm{e}}} \frac{ds}{\lambda} = \sum_{i=1,n} \left(\int_{\gamma^{(i)}:\mathbf{x}^{(i-1)}\to\mathbf{x}^{(i)}} \frac{ds}{\lambda} \right) . \tag{3.7}$$

3.3 Tests performed

MODA has been implemented and tested in both, grid-based and SPH codes. We present results from the grid-based version in the following sections; The description, tests and results of the SPH implementation can be found on the master thesis of Emanuel Gafton (Master student at Jacobs University, Bremen; private communication).

A grid-based version of MODA has been implemented on 2D and 3D Cartesian grids. A description of the implementation is reported in the Section 3.4. First, we present illustrative results for some test cases where the mean free path is expressed as an analytical function of the Cartesian coordinates; we compare the results obtained with our algorithm with those of more conventional methods. The latter usually employ a fixed path (or a set of possible fixed paths), eventually suggested by the symmetries of the system. We compare also the computational performances of the different methods for the 3D case and we discuss possible parallelization strategies. Finally, we show other

illustrative results for neutrino radiation in a core-collapse supernova and a neutron star merger contexts, where the neutrino mean free path is calculated from data taken from multi-dimensional hydrodynamics simulations.

2D tests

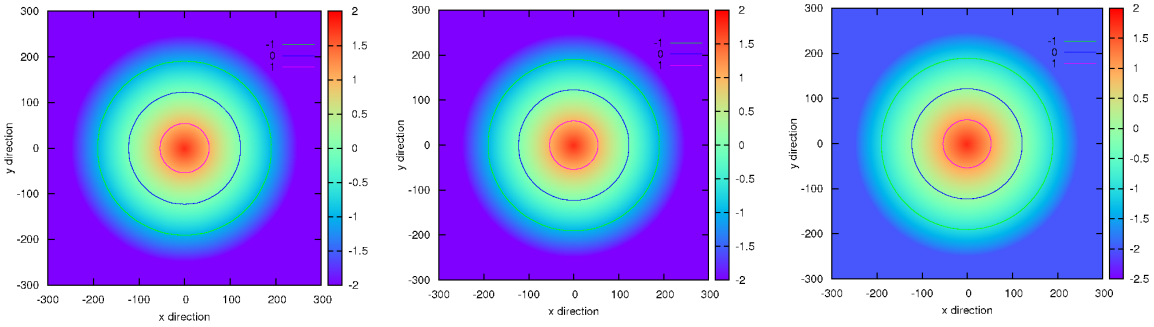

Figure 3.1: Logarithm of the optical depth for the first spherically symmetric test on a 2D Cartesian grid. The colored circumferences correspond to lines of constant optical depth. Left: MODA. Center: Local ray-by-ray. Right: Global ray-by-ray.

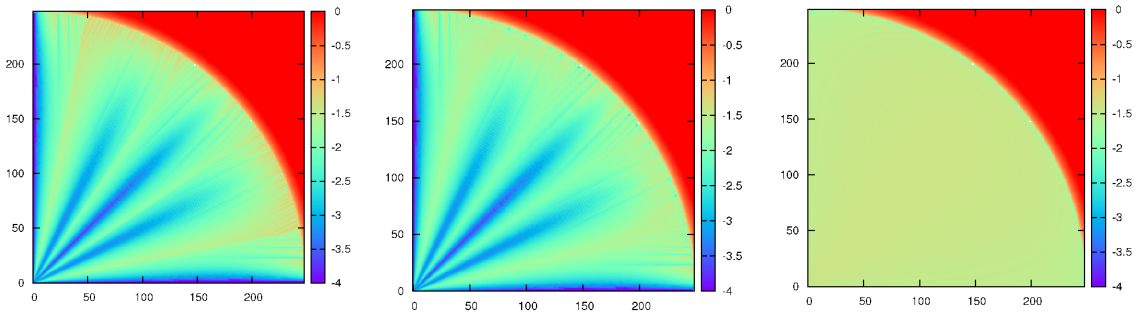

Figure 3.2: Logarithm of the modulus of the difference between the calculated optical depth and the analytical result given by Eq. (3.9). The three different panels corresponds to the same three methods represented in Fig. 3.1.

We present here the results for two different tests, with an increasing level of complexity. In all cases the computational domain is represented by an equally spaced Cartesian grid of 600×600 zones, where each zone has a unitary width. In each test, we compare three different methods to compute the optical depth starting from the same theoretical mean free path. 1) Our MODA algorithm. 2) A local ray-by-ray method: from each point of the grid, we integrated the inverse mean free path along a set of predefined straight paths (rays); then, the local optical depth is defined as the minimum value among those integrals. In order to guarantee a good resolution, we use 16 rays. 3) A global ray-by-ray method: we interpolate the mean free path from the Cartesian mesh on a spherical one; then, we calculate the local optical depth in each point of the spherical grid by the integration of the inverse mean free path along the radial path; finally, τ is interpolated back on the Cartesian mesh. As the resolution of this method depends on the resolution

of the spherical grid, we keep the same (constant) resolution of the Cartesian grid in the radial direction, while we divide the planar angle into 32 bins for the angular coordinate.

In the first test, we define a monotonically decreasing spherically symmetric inverse mean free path

$$\sigma(x_1, x_2) = \sigma_0 \exp\left(-\frac{\sqrt{x_1^2 + x_2^2}}{d_0}\right), \tag{3.8}$$

with $\sigma_0 = 5$ and $d_0 = 30$; here, x_1 and x_2 represent the coordinates with respect to the center of the computational domain. According to the symmetry of the system, the path which minimizes the optical depth is always radial. Then, assuming spherical boundary condition at $R_{\text{out}} = 249$, $\tau(R \geq R_{\text{out}}) = \tau_{\text{boundary}} = 10^{-2}$, the optical depth can be calculated analytically in each point of the domain,

$$\tau(x_1, x_2) = d_0\sigma_0 \left(\exp\left(-\frac{\sqrt{x_1^2 + x_2^2}}{d_0}\right) - \exp\left(-\frac{R_{\text{out}}}{d_0}\right)\right) + \tau_{\text{boundary}}. \tag{3.9}$$

In Fig. 3.1, we present the calculated optical depth resulting from the three algorithms. The fact that the lines of constant τ are almost perfect circumferences shows that all three algorithms reproduce accurately the original spherical symmetry of the input data. While this result is obvious for the global ray-by-ray method (third panel), where the spherical symmetry is directly encoded in the algorithm, it is less obvious for the other two, especially for MODA, where no symmetry and no predefined path is assumed. In Fig. (3.2) we compare the results of all three methods with the analytic solution given by Eq. (3.9); to do that, we calculate the quantity

$$\epsilon_{\text{numeric}}(x_1, x_2) = \log\left|\frac{\tau_{\text{numeric}}(x_1, x_2) - \tau_{\text{analytic}}(x_1, x_2)}{\tau_{\text{analytic}}(x_1, x_2)}\right|, \tag{3.10}$$

and we plot it in the first quadrant of the computational domain. All the three methods look consistent with the analytic solution, but with some interesting differences. The first two methods show a similar pattern that is caused by the Cartesian grid and by the step (our method) or by the direction (local ray-by-ray method) discretization: the results are better when the paths on the Cartesian grid have the very precise radial direction. Otherwise, when a path differs from the radial direction, the error increases, but being typically only a few percents, always below $\sim 10\%$. In this test, MODA looks slightly less accurate than the local ray-by-ray, in particular closer to the external boundary radius, where the more complicated boundary treatment can introduce a larger error. However, when we compare it with the third method, we see an homogeneous error which is related to the double interpolation between the Cartesian and the spherical grids.

In the second test, we keep the same grid configuration, but we relax the spherical symmetry of the input data defining a different analytic inverse mean free path as a superposition of two off-centered, elliptical Gaussian distributions

$$\sigma(x_1, x_2) = \sum_{n=1,2} \sigma_n \exp\left(-\left(\left(\frac{x_1 - \tilde{x}_{1,n}}{s_{1,n}}\right)^2 + \left(\frac{x_2 - \tilde{x}_{2,n}}{s_{2,n}}\right)^2\right)\right), \tag{3.11}$$

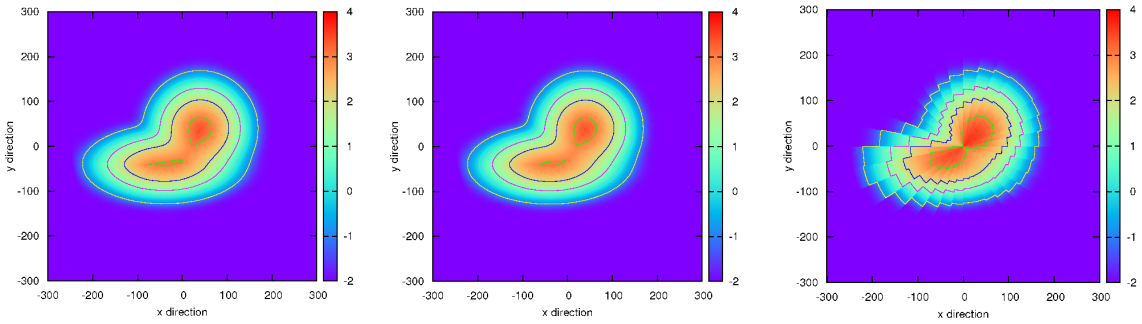

Figure 3.3: Logarithm of the optical depth for the first spherically symmetric test on a 2D Cartesian grid. The colored contours correspond to lines of constant optical depth. Left: MODA. Center: Local ray-by-ray. Right: Global ray-by-ray.

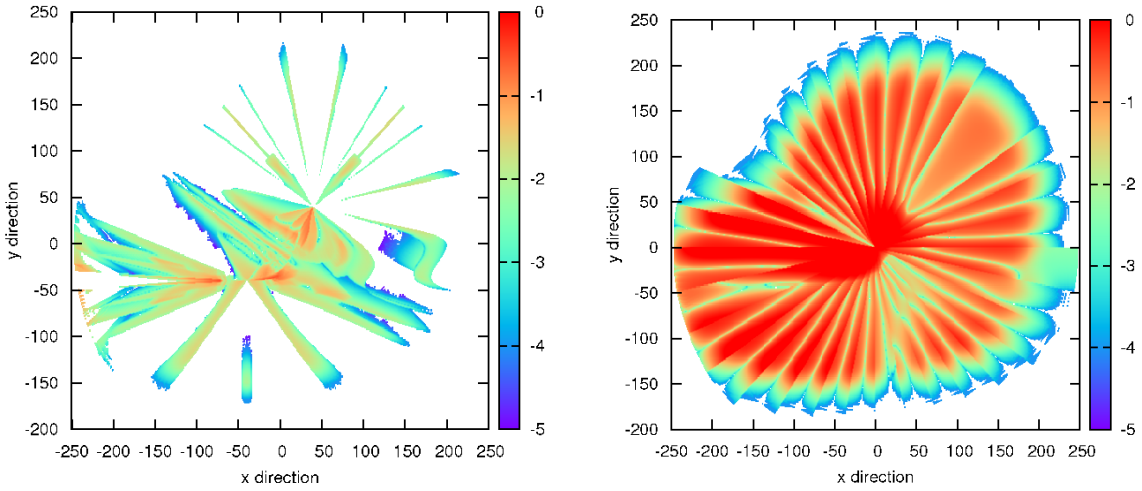

Figure 3.4: Logarithm of the modulus of the relative difference between the optical depth calculated using the local ray-by-ray method (taken as a reference) and the other two methods. Left: MODA. Right: Global ray-by-ray.

with $\sigma_1 = 60$, $\sigma_2 = 40$, $s_{1,1} = s_{2,1} = 14\sqrt{14}$, $s_{1,2} = 20\sqrt{10}$, $s_{2,2} = 10\sqrt{10}$, $\tilde{x}_{1,1} = \tilde{x}_{2,1} = 40$ and $\tilde{x}_{1,2} = \tilde{x}_{2,2} = -40$; here, x_1 and x_2 represent the Cartesian coordinates with respect to the center of the computational domain. For the boundary conditions, we assume again constant spherical boundary conditions at radius $R_{\rm out} = 249$, $\tau(R \geq R_{\rm out}) = \tau_{\rm boundary} = 10^{-2}$.

We present in Fig. 3.3, for the new inverse mean free path, the calculated optical depth resulting from all three algorithms. In this case, there is no simple analytic solution for the optical depth, hence we decide to use the local ray-by-ray method as the referential case, and we compare the results of the other two methods with it. In particular, we use this referential optical depth in the expression for ϵ, Eq. (3.10), after the substitution $\tau_{\rm analytic} \to \tau_{\rm local\,ray-by-ray}$. The lack of a clear spherical symmetry in the input data introduces large discrepancies in the global ray-by-ray method, as it can be seen from the shape of the constant optical depth lines in Fig. (3.3) or, more explicitly, in the right panel of Fig. (3.4). MODA also shows some differences with the referential model, but the agreement is considerably better than the global ray-by-ray method (as

it can be seen from the left panel of Fig. (3.3)), and the relative difference is typically orders of magnitude lower (left panel of Fig. (3.4)).

3D tests

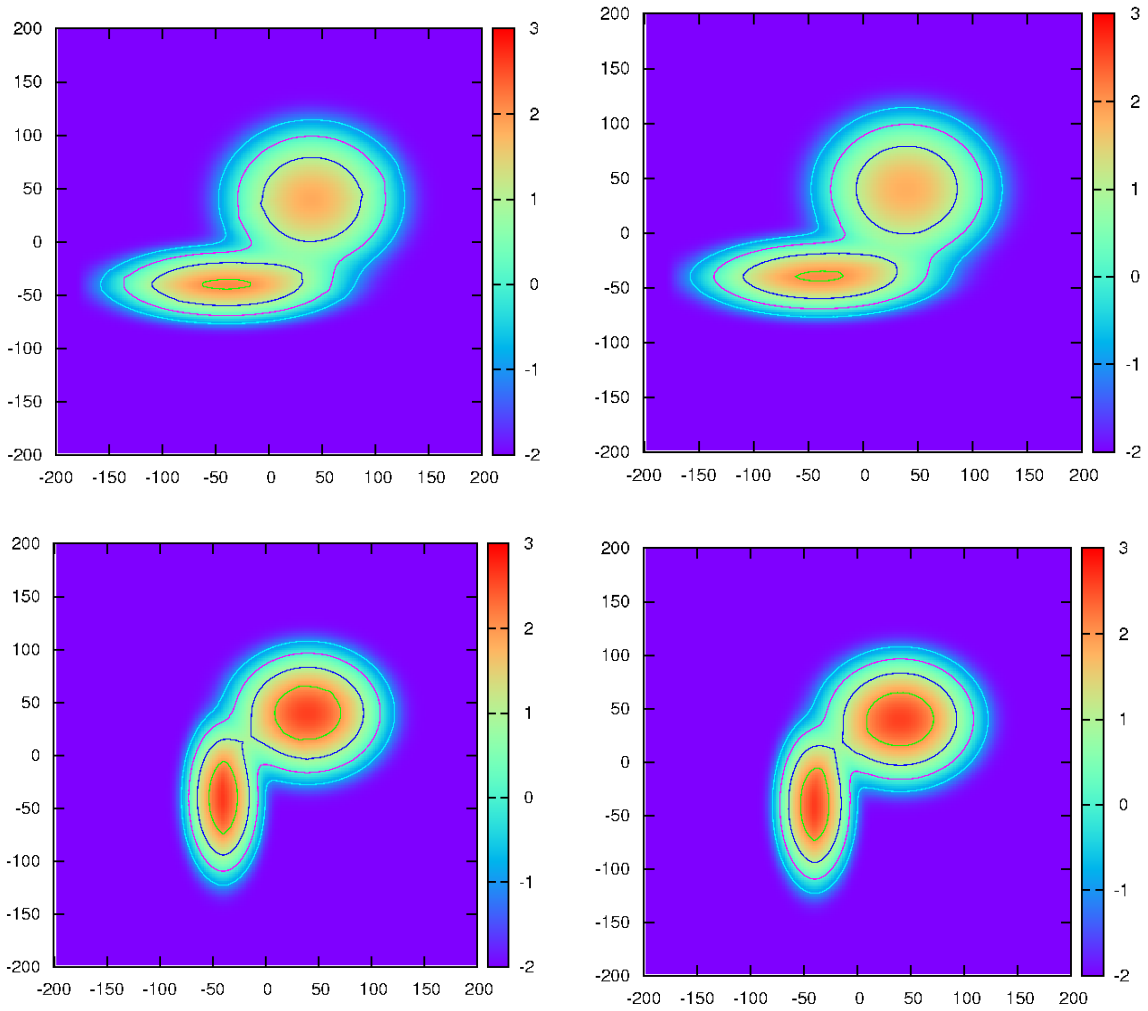

Figure 3.5: Logarithm of the optical depth for the asymmetric test on a 3D Cartesian grid. Left: MODA. Right: local ray-by-ray. Upper (lower) row shows a xy plane (yz plane) centered slice of the 3D domain. The colored contours correspond to lines of constant optical depth.

MODA can be easily extended to 3D. In the following, we present the results of a completely 3D asymmetric case, where we compare the optical depths obtained with the new algorithm and the ones obtained with a classical local ray-by-ray.

We consider a Cartesian grid of 400 x 400 x 400 cells, with unitary width. In order to guarantee a high directional resolution in the path construction, we consider 98 possible directions from each cell, corresponding to the first and second cubes concentric with the cell itself. In order to have a comparable resolution in the local ray-by-ray method, we calculate the optical depth using the same 98 possible directions/paths from each cell.

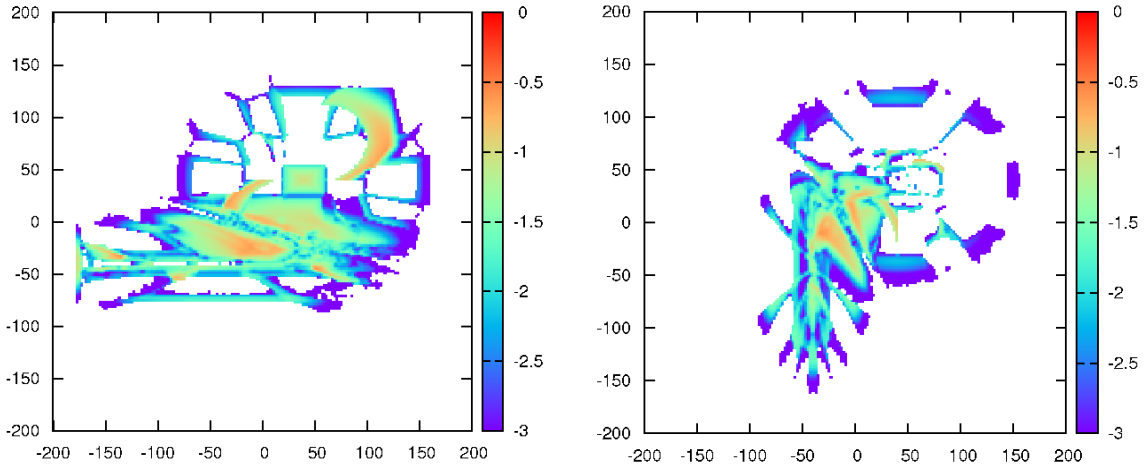

Figure 3.6: Logarithm of the modulus of the relative difference between the optical depth calculated using the local ray-by-ray method (taken as a reference) and MODA. Left: xy plane. Right: yz plane.

We define an analytical inverse mean free path as a superposition of two ellipsoidal, off-centered Gaussian distributions

$$\sigma(x_1, x_2, x_3) = \sum_{n=1,2} \sigma_n \exp\left(-\left(\left(\frac{x_1 - \tilde{x}_{1,n}}{s_{1,n}}\right)^2 + \left(\frac{x_2 - \tilde{x}_{2,n}}{s_{2,n}}\right)^2 + \left(\frac{x_3 - \tilde{x}_{3,n}}{s_{3,n}}\right)^2\right)\right), \tag{3.12}$$

with $\sigma_1 = 120$, $\sigma_2 = 80$, $s_{1,1} = 35$, $s_{2,1} = 30$, $s_{3,1} = 25$, $s_{1,2} = 45$, $s_{2,2} = 15$,$s_{3,2} = 30$, $\tilde{x}_{1,1} = \tilde{x}_{2,1} = \tilde{x}_{3,1} = 40$ and $\tilde{x}_{1,2} = \tilde{x}_{2,2} = \tilde{x}_{3,2} = -40$. For the boundary conditions, we assume again constant spherical boundary conditions at radius $R_{\text{out}} = 249$, $\tau(R \geq R_{\text{out}}) = \tau_{\text{boundary}} = 10^{-2}$.

In Fig. (3.5) we plot the logarithm of the optical depth for our method (left panel) and for the ray-by-ray (right panel). We choose the x_1x_2 plane, $x_3 = 0$, (upper panel) and the x_2x_3 plane, $x_1 = 0$, (lower panel) to show two slices of the 3D domain. As in the previous 2D tests, also in this 3D test the results obtained with the two different methods are qualitatively consistent and show a remarkable agreement and similar resolution. In Fig. (3.6), we plot the logarithm of the relative difference between the two methods, calculated according to Eq. (3.10) and taking the ray-by-ray method as a reference. From this more quantitative analysis, we can see that, on average, the difference is below 10%. In some areas, the discrepancy rises up to $\sim 30\%$, in particular at the intersection between the two Gaussian distributions, where the trend of σ deviates mostly from a monotonic distribution and the search for an optimal radiation path is less obvious. Nevertheless, two important points have to be taken into account. First, the optical depth is a magnitude with a wide range of values (five orders of magnitude in our calculations), therefore a high error in a limited amount of zones in does not imply a noticeable effect on the overall calculation of τ, as can be seen in Fig. (3.5). The agreement is good because the number of zones with high deviation from the referential value is low and not dominant. Second, we obtain a precise result at a considerably lower computational cost.

Performance analysis and parallelization issues

In this paragraph, we compare the performances of both methods in multi-dimensional applications and we discuss the impact that parallelization has on them. We decided to focus on 3D simulations, where the computational effort is higher and, consequently, the impact of the optical depth calculation is larger. In principle, both methods require the knowledge of the local mean free path over the whole computational domain to calculate the optical depth in each point. Then, the most natural parallelization strategy is the OpenMP parallelization, which has been applied to both codes.
In the first test, we vary the size of the computational domain $N = N^{1/3} \times N^{1/3} \times N^{1/3}$, and we consider two cases, one without using any parallelization and one using the OpenMP parallelization with $N_{\text{threads}} = 8$. In order to keep the input data constant, but avoiding resolution or boundary conditions problems, we choose a simple spherically symmetric inverse mean free path

$$\sigma(x_1, x_2, x_3) = \sigma_0 \exp\left(-\frac{x_1^2 + x_2^2 + x_3^2}{s^2}\right), \tag{3.13}$$

with $\sigma_0 = 30$ and $s = 50$. Taking into account the increasing computational time, we consider a version of both methods with a lower direction resolution: instead of 98 possible directions available from each cell, we consider 26 possible directions (i.e. the smallest cube around each cell). We repeat the calculations for different dimensions of the domain, spanning from $N^{1/3} = 200$ to $N^{1/3} = 400$ in the first (not parallelized) case, and up to $N^{1/3} = 600$ in the second (parallelized) case, for both methods. In these tests we have implemented squared boundary conditions (see Section 3.4 for details). In Fig. 3.7, left panel, we plot the computational time as a function of the number of cells N. In both cases, we clearly see that MODA is always faster than the ray-by-ray for each explored size, and the performance difference increases for larger domains. In particular, fitting the four curves as a function of N, we find that MODA scales with $\log t\,[\text{s}] \sim \log N$ while the ray-by-ray scales as $\log t\,[\text{s}] \sim \log N^{3/2}$. As expected, the parallelized versions are significantly faster than the serial ones. In the second test, we want to study more systematically the efficiency of the parallelization approach. In order to do this, we fix the dimensions of the computational domain to $N^{1/3} = 400$ and we vary the number of OpenMP threads from 1 to 48. In Fig. 3.7, central panel, we plot the computational time, normalized to the serial case ($N_{\text{threads}} = 1$), as a function of the number of OpenMP threads for the two methods. Both methods show a reduction of the computational time due to the OpenMP parallelization; but the efficiency of the parallelization and its trend appear quite different: MODA has larger benefits from the parallelization compared with the ray-by-ray. Moreover, the speed-up of MODA increases up to the maximum number we have tested (48 threads), while in the ray-by-ray saturates around 16 threads and the parallelization becomes even inefficient for a larger number of CPUs involved.

Astrophysical examples

In the following we present results for more realistic cases; in particular, we consider the calculation of the neutrino optical depth in relevant multi-dimensional astrophysical contexts, like core-collapse supernova and double neutron star mergers. In these scenarios, matter density and matter temperature become so large that a large amount

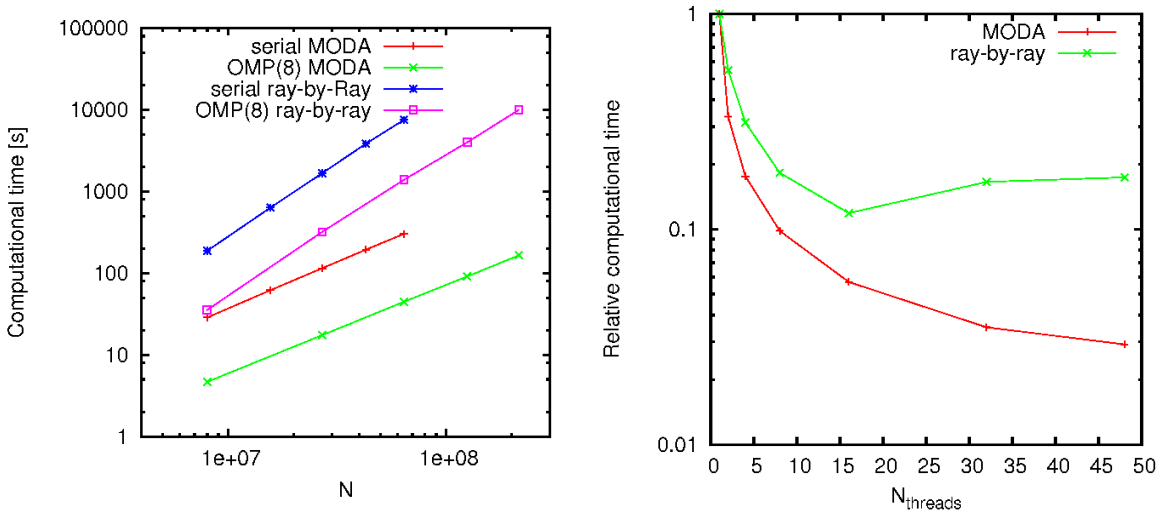

Figure 3.7: Performance comparisons between MODA (red lines) and the ray-by-ray algorithm (green lines). Left: computational time as a function of the effective number of cells, $N3$, in a serial code and in an OMP parallelized version with 8 threads. Right: computational time (normalized to the serial case) as a function of the number of OpenMP threads ($N_{\rm threads}$) used in the parallelization of the codes. In all cases, the dimension of the computational domain is fixed to $N = 400$.

of neutrinos (with energy of the order $\sim 1 - 100$ MeV) is produced. In such extreme conditions, neutrinos interact with matter, so that the neutrino local mean free path can become smaller than other typical lengthscales. Therefore, these systems are a suitable scenario for the calculation of a multi-dimensional neutrino optical depth.

In order to test our algorithm, we consider thermodynamical conditions extracted from 3D simulations and, based on them, we calculate the local mean free path for electron neutrinos with a typical energy of 54 MeV. Then, we use these data as input for the neutrino optical depth calculation.

In the first test, we take a 2D Cartesian slice of data (density, temperature and electron fraction), from a 3D core collapse supernova simulation performed with the ELEPHANT code [175], with a spatial resolution of 2 km. Considering that the system is, in first approximation, spherically symmetric, we calculate the electron neutrino optical depth using MODA (2D version) and the global ray-by-ray method (2D version, with 64 rays). Both results are shown in Fig. 3.8. We find similar results with both methods: inside a radius of about 60 km (that includes the proto-neutron star and the inner part of the shocked material), the optical depth contours are spherically symmetric, as expected. Above that radius, matter is convective and multi-dimensional effects come into play. The contour lines start to show multi-dimensional features, which are related to inhomogeneities in density, temperature and electron fraction. The main difference between both methods is the spatial resolution of the results. While the ray-by-ray approach decreases its resolution moving outwards, the new algorithm maintains a constant resolution. As a result, the outer optical depth contours are smoother that those found by the global ray-by-ray method.

As a 3D test case we take the matter distribution (density, temperature and electron fraction) from the remnant of a double neutron star merger simulation [121], performed

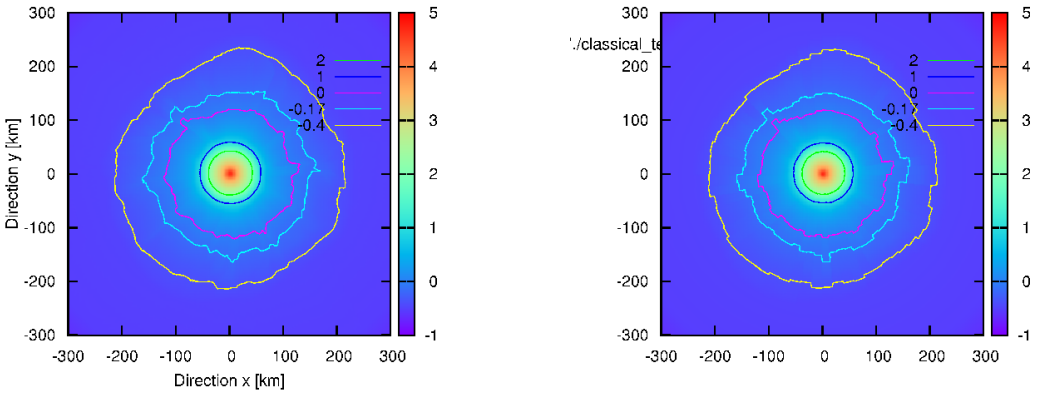

Figure 3.8: Logarithm of the optical depth for electron neutrinos of 54 MeV of energy, for a 2D Cartesian slice, obtained from a full 3D core-collapse supernova simulation, in the post-bounce phase. Left: MODA. Right: global ray-by-ray, using 64 different radial rays. The contours correspond to lines of constant optical depth. The cyan line refers to the so called neutrinosphere ($\tau = 2/3$).

with the SPH code MAGMA [140]. We map the particles onto a 3D Cartesian, equidistant grid (spatial resolution of 2 km) and calculate the neutrino mean free path for electron neutrinos with 54 MeV of energy. Then, we use MODA to calculate the neutrino optical depth, τ. The results of this calculation are shown in Fig. 3.9 (left panel), where we compare them with the optical depth calculated with a local ray-by-ray method (right panel). As it can be seen from Fig. 3.9, the two methods show good agreement. Again, fine-structure differences appear, due to the fact that our method is based on a purely local exploration of the suitable radiation path, that does not invoke any special global symmetry or predefined direction. In this sense, our 3D method provides an optical depth calculation which is more general and automatically adapts to the geometry of the matter distribution. The local ray-by-ray method is, also in this case, prohibitively expensive from the computational point of view, and the resolution shown in this test is never achieved with this method in actual hydrodynamical calculations.

3.4 Details of the implementation for the grid code

The implementation of the new method to compute the radiation optical depth in arbitrary, multi-dimensional configurations, follows closely the description of the algorithm we gave in Sect. 3.2. In this section, we discuss in more details some more technical aspects of the implementation for an equally-spaced Cartesian grid code.

As the method requires at each point the exploration of the neighboring areas to find $l_{\rm dec}(\mathbf{x})$, we need to set a boundary layer, of thickness $N_{\rm boundary}$, at the edge of the computational domain. This layer has to be large enough to allow the search for $l_{\rm dec}(\mathbf{x})$, but it should be not too large, because otherwise it would reduce the actual computational size. For example, in our tests, when we defined squared boundary conditions, we set $N_{\rm boundary} = 20$, for an original computational dimension which

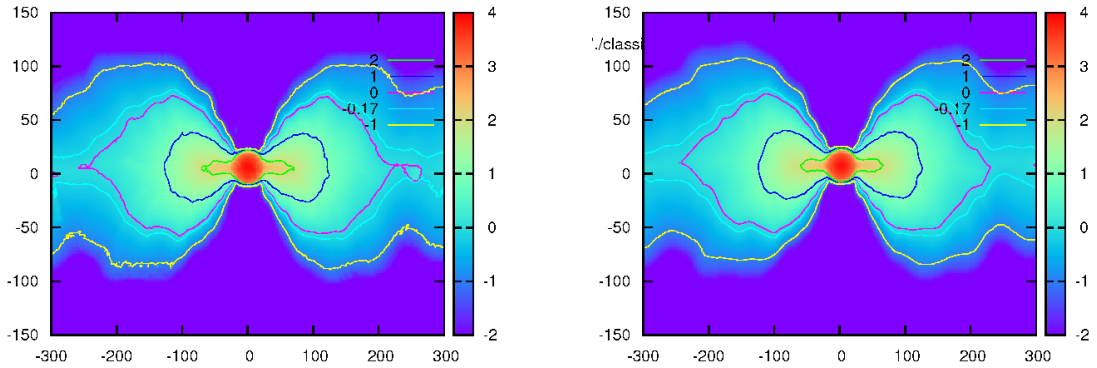

Figure 3.9: Logarithm of the optical depth for electron neutrinos of 54 MeV of energy, for the aftermath of a double neutron star merger simulation. Left: slice of the 3D calculation performed with MODA. Right: results of the 2D calculation, obtained along a set of selected paths (see the main text for more details). The colored lines correspond to lines of constant optical depth. The cyan line refers to the so called neutrinosphere ($\tau = 2/3$).

ranges from 200 to 600, and we define the actual computational domain in the range $N_{\rm boundary} \leq x_i \leq N^{1/3} - N_{\rm boundary}$, for each Cartesian coordinate. When we used spherically boundary conditions, we defined a boundary radius inside our Cartesian domain (for example, $R_{\rm boundary} = 249$ for a linear dimension $N^{1/3} = 600$), using the portion outside it as a boundary layer. In the boundary layer, the optical depth has to be analytically defined as a normal boundary conditions.

The search of $l_{\rm dec}(\mathbf{x})$ is performed sampling the inverse mean free path, σ, at a certain distance from $\mathbf{x}$. In the 2D case, we consider 8 points separated by an angle $\pi/4$; in the 3D case, we use solutions of the Thompson problem (reference) with 64 (32) points in the high (low) resolution case. To calculate the direction according to Eq. 3.6, we replace the integral average by a discrete average at a distance $l_{\rm dec}(\mathbf{x})$ from $\mathbf{x}$: in the 2D case, we used 16 points, separated by an angle $\pi/8$, while in the 3D case we used again the 64 (or 32 in the lower resolved case) points, solution of the Thompson problem, and later we mapped the calculated vector on 98 (26) possible directions, defined on the Cartesian grid by the cube of side 5 (3), built around the considered cell.
Starting from any point of the domain, the radiation path is built following the local radiation direction, and it stops when it reaches the boundary layer. There, the corresponding boundary value of the optical depth is summed to the result of the path integral.

Chapter 4

3D simulations of the aftermath of neutron star mergers

A binary neutron star merger (hereafter, BNS merger) forms initially a central, hypermassive neutron star (HMNS) surrounded by a thick accretion torus. During the merger process a small fraction of the total mass becomes ejected via gravitational torques and hydrodynamic processes ("dynamic ejecta"). The decompression of this initially cold and extremely neutron-rich nuclear matter had long been suspected to provide favorable conditions for the formation of heavy elements through the rapid neutron capture process (the "r-process") [75, 76, 72, 157, 32, 96, 26]. While initially only considered as an "exotic" or second-best model behind core-collapse supernovae, there is nowadays a large literature that –based on hydrodynamical and nucleosynthetic calculations– consistently finds that the dynamic ejecta of a neutron star merger is an extremely promising site for the formation of the heaviest elements with $A > 130$ [see, e.g., 138, 42, 130, 66]. Core-collapse supernovae, on the contrary, seem seriously challenged in generating the conditions that are needed to produce elements with $A > 90$ [2, 132, 37]. A possible exception, though, may be magnetically driven explosions of rapidly rotating stars [176]. Such explosions, however, require a combination of rather extreme properties of the pre-explosion star and are therefore likely rare.

There are at least two more channels, apart from the dynamic ejecta, by which a compact binary merger releases matter into space, and both of them are potentially interesting for nucleosynthesis and –if enough long-lived radioactive material is produced– they may also power additional electromagnetic transients. The first channel is the post-merger accretion disc. As it evolves viscously, expands and cools, the initially completely dissociated matter recombines into alpha-particles and –together with viscous heating– releases enough energy to unbind an amount of material that is comparable to the dynamic ejecta [95, 6, 78].

The second additional channel is related to neutrino-driven winds, the basic mechanisms of which are sketched in Fig.(4.1). This wind is, in several respects, similar to the one that emerges from proto-neutron stars. In particular, in both cases a similar amount of gravitational binding energy is released over a comparable (neutrino diffusion) time scale, which results in a luminosity of $L_\nu \sim \Delta E_{\rm grav}/\tau_{\rm diff} \sim 10^{53}$ erg/s and neutrinos with energies $\sim 10 - 15$ MeV. Under these conditions, energy deposition due to neutrino absorption is likely to unbind a fraction of the merger remnant. In contrast to proto-neutron stars, however, the starting point is extremely neutron-rich nuclear matter, rather than

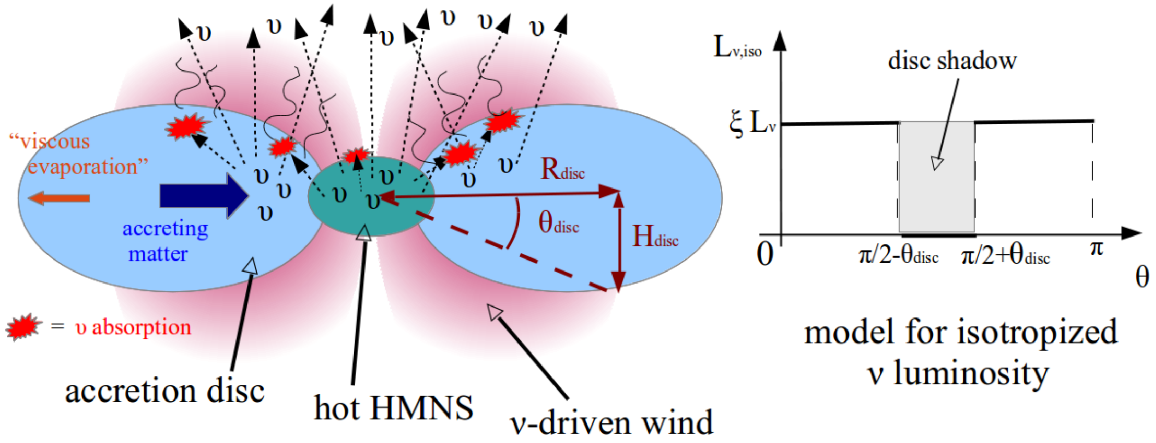

Figure 4.1: Left: sketch of the neutrino-driven wind from the remnant of a BNS merger. The hot hypermassive neutron star (HMNS) and the accretion disc emit neutrinos, preferentially along the polar direction and at intermediate latitudes. A fraction of the neutrinos is absorbed by the disc and can lift matter out of its gravitational potential. On the viscous time scale, matter is also ejected along the equatorial direction. Right: sketch of the isotropized ν luminosity we are using for our analytical estimates (see the main text for details).

a deleptonizing stellar core. At remnant temperatures of several MeV electron antineutrinos therefore dominate over electron neutrinos, contrary to the proto-neutron star case. Based on scaling relations from the proto-neutron star context [31, 123], early investigations discussed neutrino-driven winds from merger remnants either in an order-of-magnitude sense or via parametrized models [144, 137, 90, 155, 156, 95, 170, 22]. To date, only one neutrino-hydrodynamics calculation for merger remnants has been published [29]. This study was performed in two dimensions with the code VULCAN/2D and drew its initial conditions from 3D SPH calculations with similar input physics, but without modelling the heating due to neutrinos [121]. These calculations confirmed indeed that a neutrino-driven wind develops (with $\dot{M} \sim 10^{-3} M_{\odot}/s$), blown out into the funnel along the binary rotation axis that was previously thought to be practically baryon-free. By baryon-loading the suspected launch path, this wind could potentially threaten the emergence of the ultra-relativistic outflow that is needed for a short GRB. [29] therefore concluded that the launch of a sGRB was unlikely to happen in the presence of the HMNS, but could possibly occur after the collapse to a black hole.
The aim of this study is to explore further neutrino-driven winds from compact binary mergers remnants. We focus here on the phase where a HMNS is present in the centre and we assume that it does not collapse during the time frame of our simulation, as in [29]. Given the various stabilizing mechanism such as thermal support, possibly magnetic fields and in particular the strong differential rotation of the HMNS together with a lower limit on the maximum mass in excess of $2.0 M_{\odot}$ [27], we consider this as a very plausible assumption. We are mainly interested to see how robust the previous 2D results are with respect to a transition to three spatial dimensions. The questions about the understanding of the heavy element nucleosynthesis that occurs in compact binary mergers, the prediction of observable electromagnetic counterparts for the different

outflows, and the emergence of sGRBs and of are main drivers behind this work.

4.1 Analytical estimates

The properties of the remnant of a BNS merger can vary significantly, depending on the binary parameters (mass, mass ratio, eccentricity, spins etc.) and on the nuclear equation of state (hereafter, EoS). For our estimates and scaling relations, we use numerical values that characterize our initial model, see Sec.(4.2.3) for more details.
We consider a central HMNS of mass $M_{\rm ns} \approx 2.5 M_\odot$, radius $R_{\rm ns} \approx 25\,{\rm km}$ and temperature $k_{\rm B} T_{\rm ns} \approx 15\,{\rm MeV}$. Inside of it, neutrinos are assumed to be in thermal equilibrium with matter. Under these conditions the typical neutrino energy can be estimated as $E_{\nu,{\rm ns}} \sim (F_3(0)/F_2(0))\; k_{\rm B} T_{\rm ns} \approx 3.15\, k_{\rm B} T_{\rm ns} \approx 50\,{\rm MeV}$, where $F_n(0)$ is the Fermi integral of order n, evaluated for a vanishing degeneracy parameter. The central object is surrounded by a geometrically thick disc of mass $M_{\rm disc} \approx 0.2 M_\odot$, radius $R_{\rm disc} \approx 100\,{\rm km}$ and height $H_{\rm disc} \approx 33\,{\rm km}$. The aspect ratio of the disc is then $H/R \approx 1/3$. We assume a neutrino energy in the disc of $E_{\nu,{\rm disc}} \sim 15\,{\rm MeV}$, comparable with the mean energy of the ultimately emitted neutrinos.
Representative density values in the HMNS and in the disc are $\rho_{\rm ns} \sim 10^{14} {\rm g\,cm^{-3}}$ and $\rho_{\rm disc} \sim 5 \cdot 10^{11} {\rm g\,cm^{-3}}$, respectively.
The *dynamical time scale* $t_{\rm dyn}$ of the torus is set by the orbital Keplerian motion around the HMNS,

$$t_{\rm dyn} \sim \frac{2\pi}{\Omega_K} \approx 0.011\,{\rm s} \left(\frac{M_{\rm ns}}{2.5 M_\odot}\right)^{-1/2} \left(\frac{R_{\rm disc}}{100\,{\rm km}}\right)^{3/2}, \tag{4.1}$$

where Ω_K is the Keplerian angular velocity.
On a longer time scale, $t_{\rm dyn}$, viscosity drives radial motion. Assuming it can be described by an α-parameter model [149], we estimate the *lifetime of the accretion disc* $t_{\rm disc}$ as

$$t_{\rm disc} \sim \alpha^{-1} \left(\frac{H}{R}\right)^{-2} \Omega_K^{-1} \approx 0.3\,{\rm s} \left(\frac{\alpha}{0.05}\right)^{-1} \left(\frac{H/R}{1/3}\right)^{-2} \left(\frac{M_{\rm ns}}{2.5 M_\odot}\right)^{-1/2} \left(\frac{R_{\rm disc}}{100\,{\rm km}}\right)^{3/2}. \tag{4.2}$$

The *accretion rate* on the HMNS $\dot{M}$ is then of order

$$\dot{M} \sim \frac{M_{\rm disc}}{t_{\rm disc}} \approx 0.64\, \frac{M_\odot}{\rm s} \left(\frac{M_{\rm disc}}{0.2\, M_\odot}\right) \left(\frac{\alpha}{0.05}\right) \left(\frac{H/R}{1/3}\right)^2 \left(\frac{M_{\rm ns}}{2.5 M_\odot}\right)^{1/2} \left(\frac{R_{\rm disc}}{100\,{\rm km}}\right)^{-3/2}. \tag{4.3}$$

Neutrinos are the major cooling agent of the remnant. Neutrino scattering off nucleons is one of the major sources of *opacity* for all neutrino species[1] and the corresponding mean free path can be estimated as

$$\lambda_{N\nu} \approx 7.44 \cdot 10^3\,{\rm cm} \left(\frac{\rho}{10^{14}\,{\rm g/cm^3}}\right)^{-1} \left(\frac{E_\nu}{10\,{\rm MeV}}\right)^{-2}, \tag{4.4}$$

[1] In the case of ν_e's, the opacity related with absorption by neutrons is even larger. Nevertheless, it is still comparable to the scattering off nucleons.

where ρ is the matter density and E_ν is the typical neutrino energy. The large variation in density between the HMNS and the disc suggests to treat these two regions separately. For the central compact object, the *cooling time scale* $t_{\rm cool,ns}$ is governed by neutrino diffusion (see, for example, [137]). If $\tau_{\nu,\rm ns}$ is the neutrino *optical depth* inside the HMNS, then

$$t_{\rm cool,ns} \sim 3\,\frac{\tau_{\nu,\rm ns}\,R_{\rm ns}}{c}. \tag{4.5}$$

If we assume $\tau_{\nu,\rm ns} \sim R_{\rm ns}/\lambda_{N\nu}$,

$$t_{\rm cool,ns} \sim 1.88\,{\rm s}\left(\frac{R_{\rm ns}}{25\,{\rm km}}\right)^2\left(\frac{\rho_{\rm ns}}{10^{14}{\rm g/cm^3}}\right)\left(\frac{k_{\rm B}T_{\rm ns}}{15\,{\rm MeV}}\right)^2. \tag{4.6}$$

The neutrino luminosity coming from the HMNS is powered by an internal energy reservoir $\Delta E_{\rm ns}$. We estimate it as the difference between the internal energy of a hot and of a cold HMNS. For the first one, we consider typical profiles of a HMNS obtained from a BNS merger simulation. For the second one, we set $T = 0$ everywhere inside it. Under these assumptions, $\Delta E_{\rm ns} \approx 0.30\,E_{\rm int,HMNS} \approx 3.4\cdot 10^{52}$erg, and the associated HMNS neutrino luminosity (integrated over all neutrino species) is approximately

$$L_{\nu,\rm ns} \sim \frac{\Delta E_{\rm ns}}{t_{\rm diff,ns}} \approx 1.86\cdot 10^{52}\,{\rm erg/s}\left(\frac{\Delta E_{\rm ns}}{3.5\cdot 10^{52}{\rm erg}}\right)$$
$$\left(\frac{R_{\rm ns}}{25\,{\rm km}}\right)^{-2}\left(\frac{\rho_{\rm ns}}{10^{14}{\rm g/cm^3}}\right)^{-1}\left(\frac{k_{\rm B}T_{\rm ns}}{15\,{\rm MeV}}\right)^{-2}. \tag{4.7}$$

The disc diffusion time scale can be estimated using Eq.(4.5):

$$t_{\rm cool,disc} \sim 1.68\,{\rm ms}\left(\frac{H_{\rm disc}}{33\,{\rm km}}\right)^2\left(\frac{\rho_{\rm disc}}{5\cdot 10^{11}{\rm g/cm^3}}\right)\left(\frac{E_{\nu,\rm disc}}{15\,{\rm MeV}}\right)^2. \tag{4.8}$$

Due to this fast cooling time scale, a persistent neutrino luminosity from the disc requires a constant supply of internal energy. In an accretion disc, this is provided by the *accretion mechanism*: while matter falls into deeper Keplerian orbits, the released gravitational energy is partially ($\sim 50\%$) converted into internal energy. If $R_{\rm disc} \sim 100\,{\rm km}$ denotes the typical initial distance inside the disc, and the radius of the HMNS is assumed to be the final one, then $\Delta E_{\rm grav} \sim (GM_{\rm ns}M_{\rm disc}/R_{\rm ns})$, where we have used $R_{\rm ns}^{-1} \gg R_{\rm disc}^{-1}$. The neutrino luminosity for the accretion process is approximately

$$L_{\nu,\rm disc} \sim 0.5\,\frac{\Delta E_{\rm grav}}{t_{\rm disc}} \approx 8.35\cdot 10^{52}\,{\rm erg/s}\left(\frac{M_{\rm ns}}{2.5\,M_\odot}\right)^{3/2}\left(\frac{\alpha}{0.05}\right)$$
$$\left(\frac{M_{\rm disc}}{0.2\,M_\odot}\right)\left(\frac{H/R}{1/3}\right)^2\left(\frac{R_{\rm disc}}{100\,{\rm km}}\right)^{-3/2}\left(\frac{R_{\rm ns}}{25\,{\rm km}}\right)^{-1}. \tag{4.9}$$

Note that during the disc accretion phase $L_{\nu,\rm disc}$ is larger than $L_{\nu,\rm ns}$. Together, the HMNS and the disk release neutrinos at a luminosity of $\sim 10^{53}$ erg/s, consistent with the simple estimate from the introduction.
Due to the density (opacity) structure of the disc, the neutrino emission is expected

to be anisotropic, with a larger luminosity in the polar directions ($\theta = 0$ and $\theta = \pi$), compared to the one along the equator ($\theta = \pi/2$), see also [142, 29]. For a simple model of this effect, we assume that the disc creates an axisymmetric shadow area across the equator, while the emission is uniform outside this area. The amplitude of the shadow is $2\,\theta_{\rm disc}$, where $\tan\theta_{\rm disc} = (H/R)$. Then, we define an isotropised axisymmetric luminosity $L_{\nu,\rm iso}(\theta)$ as (see the right sketch in Fig.(4.1)):

$$L_{\nu,\rm iso}(\theta) = \begin{cases} \xi\, L_\nu & \text{for } |\theta - \pi/2| > \theta_{\rm disc} \\ 0 & \text{for } |\theta - \pi/2| \leq \theta_{\rm disc}. \end{cases} \tag{4.10}$$

The value of ξ is set by the normalization of $L_{\nu,\rm iso}$ over the whole solid angle Ω, $\int_\Omega L_{\nu,\rm iso}\,{\rm d}\Omega = L_\nu$:

$$\xi = \frac{1}{1 - \sin\theta_{\rm disc}}. \tag{4.11}$$

For $(H/R) \approx 1/3$, one finds $\theta_{\rm disc} \approx \pi/10$ and $\xi \approx 1.5$.

After having determined approximate expressions for the neutrino luminosities, we are ready to estimate the relevant time scale for the formation of the ν-driven wind. We define the *wind time scale* $t_{\rm wind}$ as the time necessary for the matter to absorb enough energy to overcome the gravitational well generated by the HMNS. This energy deposition happens inside the disc and it is due to the re-absorption of neutrinos emitted at their last interaction surface. Thus,

$$t_{\rm wind} \sim e_{\rm grav}/\dot{e}_{\rm heat}, \tag{4.12}$$

where $e_{\rm grav} \approx GM_{\rm ns}/R$ is the specific gravitational energy, and $\dot{e}_{\rm heat}$ is the specific heating rate provided by neutrino absorption at a radial distance R from the centre:

$$\dot{e}_{\rm heat} \sim k\,\frac{L_{\nu_e,\rm iso}(|\theta - \pi/2| > \theta_{\rm disc})}{4\,\pi\,R^2}. \tag{4.13}$$

In the equation above we have assumed that $L_{\nu_e} \approx L_{\bar\nu_e} \sim (L_{\nu,\rm ns} + L_{\nu,\rm disc})/3$. If $k \approx 5.65 \cdot 10^{-20}\,{\rm cm^2\,g^{-1}\,MeV^{-2}}\,E_\nu^2$ is the typical absorptivity on nucleons [12], the heating rate can be re-expressed as

$$\dot{e}_{\rm heat} \sim 4.6 \cdot 10^{20} {\rm erg\,g^{-1}\,s^{-1}} \left(\frac{R}{100\,{\rm km}}\right)^{-2} \left(\frac{L_{\nu_e}}{3 \cdot 10^{52}\,{\rm erg/s}}\right) \left(\frac{\xi}{1.5}\right) \left(\frac{E_{\nu,\rm disc}}{15\,{\rm MeV}}\right)^2. \tag{4.14}$$

Finally, the wind time scale, Eq.(4.12), becomes

$$t_{\rm wind} \sim 0.07\,{\rm s} \left(\frac{M_{\rm ns}}{2.5\,M_\odot}\right) \left(\frac{R}{100\,{\rm km}}\right) \left(\frac{L_{\nu_e}}{3 \cdot 10^{52}\,{\rm erg/s}}\right)^{-1} \left(\frac{\xi}{1.5}\right)^{-1} \left(\frac{E_{\nu,\rm disc}}{15\,{\rm MeV}}\right)^{-2}. \tag{4.15}$$

Since $t_{\rm wind} < t_{\rm disc}$, neutrino heating can drive a wind within the lifetime of the disc. Moreover, since the disc provides a substantial fraction of the total neutrino luminosity, a wind can form also in the absence of the HMNS.

Of course, the neutrino emission processes are much more complicated than what can be captured by these simple estimates. Nevertheless, they provide a reasonable first guidance for the qualitative understanding of the remnant evolution.

4.2 Numerical model for the remnant evolution

4.2.1 Hydrodynamics

We perform our simulations with the FISH code [62]. FISH is a parallel grid code that solves the equations of ideal, Newtonian hydrodynamics (HD) [2]:

$$\frac{\partial \rho}{\partial t} + \nabla \cdot (\rho \mathbf{v}) = 0 \tag{4.16}$$

$$\frac{\partial \rho \mathbf{v}}{\partial t} + \nabla \cdot (\rho \mathbf{v} \otimes \mathbf{v}) + \nabla p = -\rho \nabla \phi + \rho \left(\frac{\mathrm{d}\mathbf{v}}{\mathrm{d}t} \right)_\nu \tag{4.17}$$

$$\frac{\partial E}{\partial t} + \nabla \cdot [(E + p)\, \mathbf{v}] = -\rho \mathbf{v} \nabla \phi + \rho \left(\frac{\mathrm{d}e}{\mathrm{d}t} \right)_\nu \tag{4.18}$$

$$\frac{\partial \rho Y_e}{\partial t} + \nabla \cdot (\rho Y_e \mathbf{v}) = \rho \left(\frac{\mathrm{d}Y_e}{\mathrm{d}t} \right)_\nu \tag{4.19}$$

Here ρ is the mass density, $\mathbf{v}$ the velocity, $E = \rho e + \rho v^2/2$ the total energy density (i.e., the sum of internal and kinetic energy density), e the specific internal energy, p the matter pressure and Y_e the electron fraction. The code solves the HD equations with a second-order accurate finite volume scheme on a uniform Cartesian grid. The source terms on the right hand side stem from gravity and from neutrino-matter interaction. We notice that the viscosity of our code is of numerical nature, while no physical viscosity is explicitly included. The neutrino source terms will be discussed in detail in Sec.(4.2.2). The gravitational potential ϕ obeys the Poisson equation

$$\nabla^2 \phi = 4\pi G \rho, \tag{4.20}$$

where G is the gravitational constant. The merger of two neutron stars with equal masses is expected to form a highly axisymmetric remnant. We exploit this approximate invariance by solving the Poisson equation in cylindrical symmetry. This approximation results in a high gain in computational efficiency, given the elliptic (and hence global) nature of Eq.(4.20). To this end, we *conservatively* average the three-dimensional density distribution onto an axisymmetric grid, having the HMNS rotational axis as the symmetry axis. The Poisson equation is then solved with a fast multigrid algorithm [120], and the resulting potential is interpolated back on the three-dimensional grid.

The HD equations are closed by an EoS relating the internal energy to the pressure. In our model, we use the TM1 EoS description of nuclear matter supplemented with electron-positron and photon contributions, in tabulated form [165, 53]. This description is equivalent to one provided by the Shen et al. EoS [151] in the high density part.

4.2.2 Neutrino treatment

To model neutrino radiation, we emply the ASL scheme presented in this work.
The neutrino energy is discretized in 12 geometrically increasing energy bins, chosen in

[2] FISH can actually solve the equations of ideal magnetohydrodynamics. However, we have not included magnetic fields in our current setup.

Reaction	Roles	Ref.
$e^- + p \leftrightarrow n + \nu_e$	O,T,P	a
$e^+ + n \leftrightarrow p + \bar{\nu}_e$	O,T,P	a
$e^- + (A, Z) \leftrightarrow \nu_e + (A, Z-1)$	T,P	a
$N + \nu \leftrightarrow N + \nu$	O	a
$(A, Z) + \nu \leftrightarrow (A, Z) + \nu$	O	a
$e^+ + e^- \leftrightarrow \nu + \bar{\nu}$	T,P	a,b
$N + N \leftrightarrow N + N + \nu + \bar{\nu}$	T,P	c

Table 4.1: List of the neutrino reactions included in the simulation (left column; $\nu \equiv \nu_e, \bar{\nu}_e, \nu_{\mu,\tau}$), of their major effects (central column; O stands for opacity, P for neutrino production, T for neutrino thermalization), and of the references for the implementation (right column): "a" corresponds to [12], "b" to [102], and "c" to [51].

the range $2\,\mathrm{MeV} \leq E_\nu \leq 200\,\mathrm{MeV}$. The ASL scheme includes the reactions listed in Tab.(4.1). They correspond to the reactions that we expect to be more relevant in hot and dense matter. Due to the geometry of the emission, neutrino pair annihilation is also supposed to be important in optically thin conditions (see, for example, [58, 18]. For the application to the BNS merger scenario, see [29] and references therein). Therefore, our numbers concerning the mass loss $\dot{M}$ need to be considered as lower limits on the true value. The inclusion of this process in our model will be performed in a future step.

As a consequence of the distinction between emission and absorption processes, and between different neutrino species, the source terms in Eq.(4.17)-(4.19) can be split into different contributions. For the electron fraction,

$$\left(\frac{\mathrm{d}Y_e}{\mathrm{d}t}\right)_\nu = -m_b \left[\left(R^0_{\nu_e} - R^0_{\bar{\nu}_e}\right) + \left(H^0_{\nu_e} - H^0_{\bar{\nu}_e}\right)\right], \tag{4.21}$$

where R^0_ν and H^0_ν denote the specific particle emission and absorption rates for a neutrino type ν respectively, and m_b is the baryon mass (with $m_b c^2 = 939.021\,\mathrm{MeV}$). For the specific internal energy of the fluid,

$$\left(\frac{\mathrm{d}e}{\mathrm{d}t}\right)_\nu = -\left(R^1_{\nu_e} + R^1_{\bar{\nu}_e} + 4\,R^1_{\nu_{\mu,\tau}}\right) + H^1_{\nu_e} + H^1_{\bar{\nu}_e}, \tag{4.22}$$

where R^1_ν and H^1_ν indicate the specific energy emission and absorption rates, respectively. The factor 4 in front of $R^1_{\nu_{\mu,\tau}}$ accounts for the four different species modelled collectively as $\nu_{\mu,\tau}$. And, finally, for the fluid velocity,

$$\left(\frac{\mathrm{d}\mathbf{v}}{\mathrm{d}t}\right)_\nu = \left(\frac{\mathrm{d}\mathbf{v}}{\mathrm{d}t}\right)_{\nu_e} + \left(\frac{\mathrm{d}\mathbf{v}}{\mathrm{d}t}\right)_{\bar{\nu}_e}. \tag{4.23}$$

is the acceleration provided by the momentum transferred by the absorption of ν_e's and $\bar{\nu}_e$'s in the optically thin region. Since the trapped neutrino component is not dynamically modelled, we neglect the related neutrino stress in optically thick conditions. As a consequence, $\nu_{\mu,\tau}$'s do not contribute to the acceleration term.

For each neutrino ν species, the *luminosity* (L_ν) and *number luminosity* ($L_{N,\nu}$) are calculated as:

$$L_\nu = \int_V \rho \left(R^1_\nu - H^1_\nu\right) \mathrm{d}V \tag{4.24}$$

and

$$L_{N,\nu} = \int_V \rho \left(R^0_\nu - H^0_\nu\right) \mathrm{d}V. \tag{4.25}$$

where V is the volume of the domain. The explicit distinction between the emission and the absorption contributions, as well as their dependence on the spatial position, allows the introduction of two supplementary luminosities:
1) The *cooling luminosities*, $L_{\nu,\mathrm{cool}}$ and $L_{\mathrm{N},\nu,\mathrm{cool}}$, obtained by neglecting the heating rates H^1_ν and H^0_ν in eq.(4.24) and Eq.(4.25), respectively.
2) The *HMNS luminosities*, $L_{\nu,\mathrm{HMNS}}$ and $L_{\mathrm{N},\nu,\mathrm{HMNS}}$, obtained by restricting the volume integral in Eq.(4.24) and Eq.(4.25) to V_{HMNS}, the volume of the central object. Due to the continous transition between the HMNS and the disc, the definition of V_{HMNS} is somewhat arbitrary. We decide to include also the innermost part of the disc, delimited by a density contour of $5 \times 10^{11} \mathrm{g\,cm^{-3}}$. This corresponds to the characteristic density close to the innermost stable orbit for a torus accreting on stellar black holes. It is also comparable with the surface density of a cooling proto-neutron star. For each luminosity we associate a *neutrino mean energy*, defined as $\langle E_\nu \rangle \equiv L_\nu / L_{N,\nu}$.
Since the scheme is spectral, all the terms on the right hand side of Eq.(4.21), Eq.(4.22) and Eq.(4.23) are energy-integrated values of spectral emission (r_ν), absorption (h_ν) and stress ($\mathbf{a}_\nu$) rates:

$$R^n_\nu = \int_0^{+\infty} r_\nu \, E^{n+2} \, dE, \tag{4.26}$$

$$H^n_\nu = \int_0^{+\infty} h_\nu \, E^{n+2} \, dE, \tag{4.27}$$

$$\left(\frac{\mathrm{d}\mathbf{v}}{\mathrm{d}t}\right)_\nu = \int_0^{+\infty} \mathbf{a}_\nu \, E^2 \, \mathrm{d}E. \tag{4.28}$$

The calculation of r_ν, h_ν and $\mathbf{a}_\nu$ is the ultimate purpose of the ASL scheme.

The neutrino optical depths τ_ν's play a central role in our scheme. We distinguish between the scattering ($\tau_{\nu,\mathrm{sc}}$) and the energy ($\tau_{\nu,\mathrm{en}}$) spectral optical depth. The first one is obtained by summing all the relevant neutrino processes:

$$\mathrm{d}\tau_{\nu,\mathrm{sc}} = \rho \left(k_{\mathrm{sc}} + k_{\mathrm{ab}}\right) \mathrm{d}s \tag{4.29}$$

where k_{ab} and k_{sc} are the neutrino opacities for absorption and scattering, respectively. For the second, more emphasis is put on those inelastic processes, that are effective in keeping neutrinos in thermal equilibrium with matter. In this case, we have

$$\mathrm{d}\tau_{\nu,\mathrm{en}} = \rho \sqrt{k_{\mathrm{ab}} \left(k_{\mathrm{sc}} + k_{\mathrm{ab}}\right)} \, \mathrm{d}s, \tag{4.30}$$

where we have considered absorption processes as inelastic, and scattering processes as elastic[3]. The values of the two τ_ν's at each point are calculated using a local ray-by-ray method. It consists of integrating Eq.(4.29) and Eq.(4.30) along several predefined

[3]This is not true in general. However, it applies to the set of reactions we have chosen for our model. See Tab.(4.1).

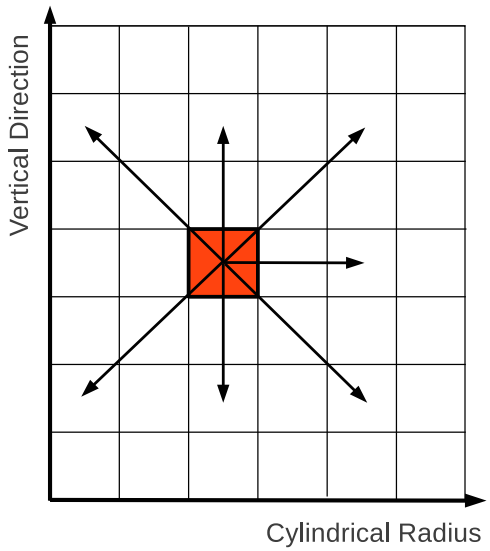

Figure 4.2: Schematic plot of the seven directions (paths) used to compute the optical depth at each point of the cylindrical domain.

paths and taking the minimum values among them. These paths are straight oriented segments, connecting the considered point with the edge of the computational domain. Due to the intrinsically global character of these integrations, we decided to exploit also here the expected symmetry of the remnant, and to calculate τ_ν in axial symmetry. The seven different paths we explore in the $(R_{\rm cyl} - z)$ plane are shown in Fig.(4.2). The optical depths vary largely and they decrease, following the density profile, proceeding from the HMNS to the edge of the remnant. To characterize this behaviour, we define the unit vector

$$\hat{\mathbf{n}}_\tau \equiv -\nabla\tau_{\nu,\rm sc} / \left|\nabla\tau_{\nu,\rm sc}\right| , \tag{4.31}$$

computed at each point of the domain from finite differences on the grid. This vector will be crucial later to model the diffusion and the final emission of the neutrinos.
The surfaces where τ_ν equals 2/3 are defined as *neutrino surfaces*. The neutrino surfaces obtained from $\tau_{\nu,\rm sc}$ can be understood as the *last scattering surfaces*; the ones derived from $\tau_{\nu,\rm en}$ correspond to the surfaces where neutrinos decouple thermally from matter, and they are often called *energy surfaces* [see, for example, 125]. According to the value of $\tau_{\nu,\rm sc}$, we distinguish between three disjoint volumes: 1) $V_{\rm thin}$, for the optically thin region ($\tau_{\nu,\rm sc} \ll 2/3$); 2) $V_{\rm surf}$, for the neutrino surface region[4] ($\tau_{\nu,\rm sc} \sim 2/3$); 3) $V_{\rm thick}$, for the optically thick region ($\tau_{\nu,\rm sc} \gg 2/3$). Obviously, $V = V_{\rm thick} \cup V_{\rm surf} \cup V_{\rm thin}$.

After having introduced τ_ν, we can now explain in which way the neutrino rates are

[4]In principle, the neutrino surfaces should have no volume. However, due to the discretization on the (axisymmetric) grid we adopted to calculate τ, every neutrino surface is replaced by a shell of width $\sim \Delta x$. This thin layer is formed by the cells $\mathbf{x}$ inside which τ is expected to become equal to 2/3.

Quantity	Definition	Related quantities
$j_{\rm em}$	emissivity	$r_{\nu,\rm prod}$
$k_{\rm ab}$	absorption opacity	λ_ν, τ_ν, h_ν, $\mathbf{a}_\nu$
$k_{\rm sc}$	scattering opacity	λ_ν, τ_ν
λ_ν	mean free path	$r_{\nu,\rm diff}$
τ_ν	optical depth	$\hat{\mathbf{n}}_\tau$, $\hat{\mathbf{n}}_{\rm path}$, $r_{\nu,\rm diff}$, $r_{\nu,\rm ult}$, h_ν, $\mathbf{a}_\nu$
$\hat{\mathbf{n}}_\tau$	opposite τ gradient	$\hat{\mathbf{n}}_{\rm path}$, n_ν, $\mathbf{s}_\nu$
$\hat{\mathbf{n}}_{\rm path}$	diffusion direction	$r_{\nu,\rm ult}$
$r_{\nu,\rm prod}$	production rate	r_ν
$r_{\nu,\rm diff}$	diffusion rate	r_ν
r_ν	emission rates	$r_{\nu,\rm ult}$, $(\mathrm{d}Y_e/\mathrm{d}t)_\nu$, $(\mathrm{d}e/\mathrm{d}t)_\nu$
$r_{\nu,\rm ult}$	ultimate emission rates	n_ν, $\mathbf{s}_\nu$
n_ν	particle density	h_ν
$\mathbf{s}_\nu$	momentum density	$\mathbf{a}_\nu$
h_ν	absorption rate	$(\mathrm{d}Y_e/\mathrm{d}t)_\nu$, $(\mathrm{d}e/\mathrm{d}t)_\nu$
$\mathbf{a}_\nu$	stress	$(\mathrm{d}\mathbf{v}/\mathrm{d}t)_\nu$

Table 4.2: List of the most important spectral quantities appearing in the ASL scheme (left column) and their definition (central column). In the right column, we list the relevant quantities (spectral quantities and source terms) that depend directly on each table entry. See the text for more details.

calculated within the ASL scheme. In Tab.(4.2) we have summarized the most important quantities, their definitions and relations in the context of the ASL scheme.
The spectral emission rates r_ν are calculated as smooth interpolation between diffusion ($r_{\nu,\rm diff}$) and production ($r_{\nu,\rm prod}$) spectral rates: the first ones are the relevant rates in the optically thick regime, the latter in the optically transparent region.
We compute $r_{\nu,\rm prod}$ and $r_{\nu,\rm diff}$ as

$$r_{\nu,\rm prod} = \frac{4\pi}{(hc)^3}\frac{j_{\rm em}}{\rho}, \tag{4.32}$$

$$r_{\nu,\rm diff} = \frac{4\pi}{(hc)^3}\frac{f_\nu^{\rm FD}}{\rho\, t_{\nu,\rm diff}}. \tag{4.33}$$

$j_{\rm em}$ is the neutrino spectral emissivity, while $f_\nu^{\rm FD}$ is the Fermi-Dirac distribution function for a neutrino gas in thermal and weak equilibrium with matter. $t_{\nu,\rm diff}$ is the local diffusion time scale, calculated as

$$t_{\nu,\rm diff} = \alpha_{\rm diff}\frac{\tau_{\nu,\rm sc}^2\,\lambda_{\nu,\rm sc}}{c} \tag{4.34}$$

where $\lambda_{\nu,\rm sc} = (\rho\,(k_{\nu,\rm ab}+k_{\nu,\rm sc}))^{-1}$ is the scattering mean free path. $\alpha_{\rm diff}$ is a constant set to 3. The interpolation formula for r_ν is provided by half of the harmonic mean between the production and diffusion rates.
We compute the spectral heating rate as the properly normalized product of the absorp-

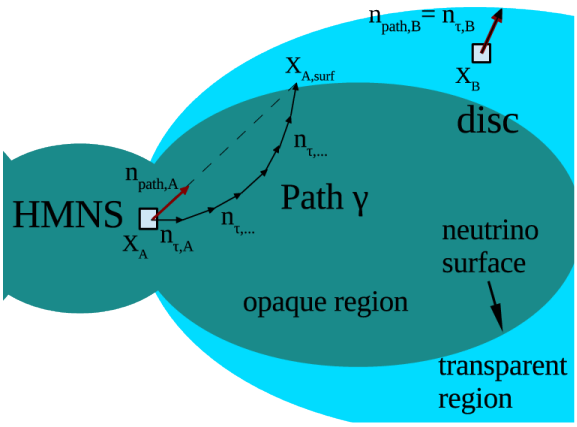

Figure 4.3: Schematic representation of the procedure to calculate the ultimate emission rates at the neutrino surface and in the optically thin region, $r_{\nu,\mathrm{ult}}$, from the emission rates, r_ν. The thin black arrows represent the inverse of the gradient of τ_{sc} ($\hat{\mathbf{n}}_\tau$), while the thick red arrow is $\hat{\mathbf{n}}_{\mathrm{path}}$. x_A refers to a point inside the neutrino surface (opaque region), while x_B is a point inside the disc, but in the optically thin zone, for which $\hat{\mathbf{n}}_{\mathrm{tau}} = \hat{\mathbf{n}}_{\mathrm{path}}$. See the text for more details.

tion opacity $k_{\nu,\mathrm{ab}}$ and of the spectral neutrino density n_ν:

$$h_\nu = c\, k_{\nu,\mathrm{ab}}\, n_\nu\, \mathcal{F}_{e,\nu}\, \mathcal{H}. \tag{4.35}$$

$\mathcal{H} \equiv \exp(-\tau_{\nu,\mathrm{sc}})$ is an exponential cut off that ensures the application of the heating term only outside the neutrino surface, and $\mathcal{F}_{e,\nu}$ is the Pauli blocking factor for electrons or positrons in the final state. n_ν is defined so that the energy-integrated particle density N_ν is given by:

$$N_\nu = \int_0^{+\infty} n_\nu\, E^2\, \mathrm{d}E. \tag{4.36}$$

The stress term is calculated similarly to the neutrino heating rate:

$$\mathbf{a}_\nu = c\, k_{\nu,\mathrm{ab}}\, \mathbf{s}_\nu\, \mathcal{F}_{e,\nu}\, \mathcal{H}, \tag{4.37}$$

where $\mathbf{s}_\nu$ is the spectral density of linear momentum associated with the streaming neutrinos, while $\mathcal{H}$ and $\mathcal{F}_{e,\nu}$ are defined as in Eq.(4.35).

The quantities n_ν and $\mathbf{s}_\nu$ are computed using a multidimensional ray-tracing algorithm. This algorithm assumes that neutrinos (possibly, after having diffused from the optically thick region) are *ultimately* emitted isotropically at the neutrino surface and in the optically transparent region. If we define $l_\nu(\mathbf{x}', \hat{\mathbf{n}})$ as the specific rate per unit solid angle of the radiation emitted from a point $\mathbf{x}' \in (V_{\mathrm{surf}} \cup V_{\mathrm{thin}})$, in the direction $\hat{\mathbf{n}}$, then

$$n_\nu(\mathbf{x}) = \int_{V_{\mathrm{surf}} \cup V_{\mathrm{thin}}} \rho\, \frac{l_\nu\left(\mathbf{x}', \hat{\mathbf{n}}(\mathbf{x}, \mathbf{x}')\right)}{c\, |\mathbf{x}' - \mathbf{x}|^2} \mathrm{d}^3\mathbf{x}' \tag{4.38}$$

and

$$\mathbf{s}_\nu(\mathbf{x}) = \int_{V_{\mathrm{surf}} \cup V_{\mathrm{thin}}} \rho\, \frac{l_\nu\left(\mathbf{x}', \hat{\mathbf{n}}(\mathbf{x}, \mathbf{x}')\right)}{c\, |\mathbf{x}' - \mathbf{x}|^2}\, \frac{E}{c}\, \hat{\mathbf{n}}(\mathbf{x}, \mathbf{x}')\, \mathrm{d}^3\mathbf{x}'. \tag{4.39}$$

where $\hat{\mathbf{n}}(\mathbf{x},\mathbf{x}') = (\mathbf{x}'-\mathbf{x})/(|\mathbf{x}'-\mathbf{x}|)$. The isotropic character of the emission allows us to introduce the angle-integrated *ultimate emission rates* $r_{\nu,\mathrm{ult}}$ as:

$$l_\nu(\hat{\mathbf{n}}) = \begin{cases} r_{\nu,\mathrm{ult}}/(2\pi) & \text{if } \hat{\mathbf{n}}\cdot\hat{\mathbf{n}}_\tau \geq 0 \\ 0 & \text{otherwise.} \end{cases} \tag{4.40}$$

$r_{\nu,\mathrm{ult}}$ and r_ν can differ locally, but they have to provide the same cooling (spectral) luminosity:

$$\int_V \rho\, r_\nu \,\mathrm{d}V = \int_V \rho\, r_{\nu,\mathrm{ult}} \,\mathrm{d}V. \tag{4.41}$$

Since $r_{\nu,\mathrm{ult}}$ represents the ultimate emission rate, *after* the diffusion process has drained neutrinos from the opaque region to the neutrino surface, $r_{\nu,\mathrm{ult}} = 0$ inside V_{thick}. On the other hand, inside V_{thin} diffusion does not take place and $r_{\nu,\mathrm{ult}} = r_\nu$. In light of this, Eq.(4.41) becomes

$$\int_{V_{\mathrm{thick}}\cup V_{\mathrm{surf}}} \rho\, r_\nu \,\mathrm{d}^3\mathbf{x} = \int_{V_{\mathrm{surf}}} \rho\, r_{\nu,\mathrm{ult}} \,\mathrm{d}^3\mathbf{x}. \tag{4.42}$$

Eq.(4.42) has a clear physical interpretation: inside V_{surf}, $r_{\nu,\mathrm{ult}}$ is obtained 1) from the emission rate, r_ν, at the neutrino surface and 2) from the re-mapping of the emission rates obtained in the opaque region onto the neutrino surface, as a consequence of the diffusion process. A careful answer to this re-mapping problem would rely on the solution of the diffusion equation in the optically thick regime and of the Boltzmann equation in the semi-transparent region. The ASL algorithm calculates the amount of neutrinos diffusing from a certain volume element. But it does not provide information about the angular dependence of their flux, neither about the point of the neutrino surface where they are ultimately emitted. Thus, a phenomenological model is required. When the properties of the system under investigation change on a time scale larger than (or comparable to) the relevant diffusion time scale (see Sec.(4.1)), the neutrino fluxes can be considered as quasi-stationary. Under these conditions, the statistical interpretation of the optical depth, as the average number of interactions experienced by a neutrino before escaping, suggests to consider $\hat{\mathbf{n}}_\tau$ as the local preferential direction for neutrino fluxes. While in the (semi-)transparent regime, this unitary vector provides already the final emission direction, in the diffusion regime we have to take into account the spatial variation of $\hat{\mathbf{n}}_\tau$. To this end, at each point $\mathbf{x}$ in V_{thick}, we associate a point $\mathbf{x}_{\mathrm{surf}}(\mathbf{x})$ in V_{surf} and a related preferential direction

$$\hat{\mathbf{n}}_{\mathrm{path}}(\mathbf{x}) = \frac{\mathbf{x}_{\mathrm{surf}}(\mathbf{x})-\mathbf{x}}{|\mathbf{x}_{\mathrm{surf}}(\mathbf{x})-\mathbf{x}|}, \tag{4.43}$$

according to the following prescription: the points $\mathbf{x}$ and $\mathbf{x}_{\mathrm{surf}}$ are connected by a non-straight path γ that has $\hat{\mathbf{n}}_\tau$ as local gradient: $\gamma(s) : [0,1] \to [\mathbf{x},\mathbf{x}_{\mathrm{surf}}]$, $\mathbf{x} \in V_{\mathrm{thick}}$, $\mathbf{x}_{\mathrm{surf}} \in V_{\mathrm{surf}}$, and $\mathrm{d}\gamma/\mathrm{d}s = \mathbf{n}_\tau$. This procedure is sketched in Fig.(4.3).
Once $\hat{\mathbf{n}}_{\mathrm{path}}$ has been calculated everywhere inside V_{thick}, we can re-distribute the neutrinos coming from the optically thick region on the neutrino surface. This is done assuming that neutrinos coming from a point $\mathbf{x}$ are emitted preferentially from points of the neutrino surface located around $\mathbf{x}_{\mathrm{surf}}(\mathbf{x})$. More specifically, from points $\mathbf{x}'$ for which 1) $\mathbf{x}' \in V_{\mathrm{surf}}$; and 2) $\mu(\mathbf{x},\mathbf{x}') \equiv \hat{\mathbf{n}}(\mathbf{x},\mathbf{x}')\cdot\hat{\mathbf{n}}_{\mathrm{path}}(\mathbf{x}) > 0$, where $\hat{\mathbf{n}}(\mathbf{x},\mathbf{x}') \equiv (\mathbf{x}'-\mathbf{x})/|\mathbf{x}'-\mathbf{x}|$. If $\hat{\mathbf{n}}$ and $\hat{\mathbf{n}}_{\mathrm{path}}$ are close to the parallel condition (i.e. $\mu \approx 1$) we expect more neutrinos

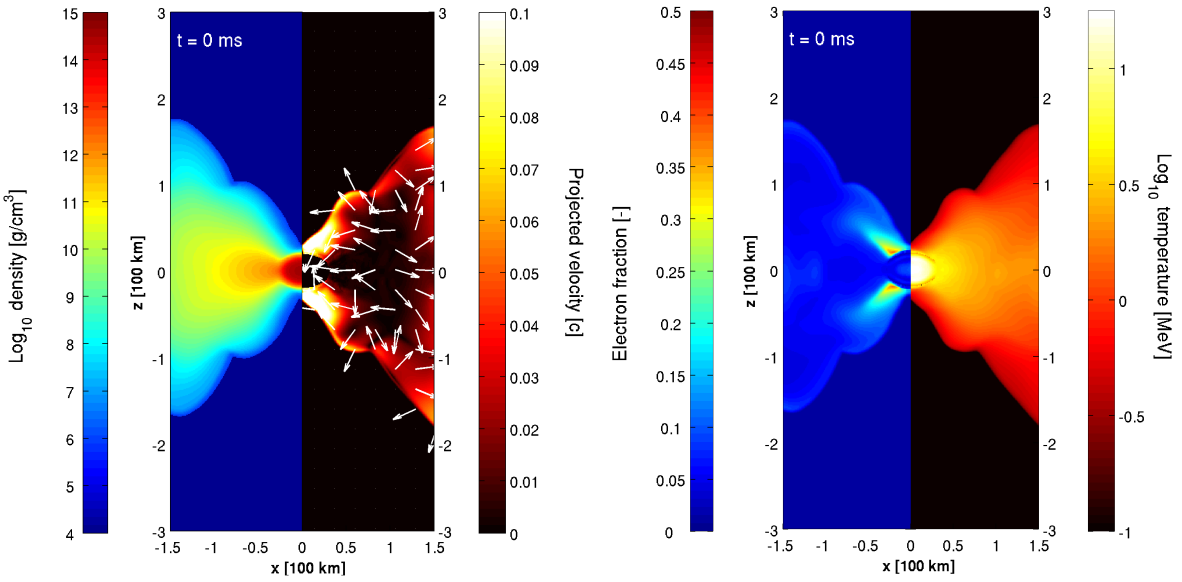

Figure 4.4: Vertical slices of the three dimensional domain (corresponding to the $y = 0$ plane), recorded at the beginning of the simulation. In the left panel, we color coded the logarithm of the matter density (in g/cm^3, left side) and the projected fluid velocity (in units of c, on the right side); the arrows indicate the direction of the projected velocity in the plane). On the right panel, we represent the electron fraction (left side) and the logarithm of the matter temperature (in unit of MeV, right side).

than in the case of perpendicular directions (i.e. $\mu \approx 0$). We smoothly model this effect assuming a μ^2 dependence.
The global character of this re-mapping procedure represents a severe computational limitation for our large, three dimensional, MPI-parallelized Cartesian simulation. In order to make the calculation feasible, we take again advantage of the expected high degree of axial symmetry of remnant (especially in the innermost part of it, where the diffusion takes place and most of the neutrino are emitted), and we compute $r_{\nu,\mathrm{ult}}$ in axisymmetry.

4.2.3 Initial Conditions

The current study is based on previous, 3D hydrodynamic studies of the merger of two non-spinning $1.4M_\odot$ neutron stars. This simulation was performed with a 3D Smoothed Particle Hydrodynamics (SPH) code, the implementation details of which can be found in the literature [136, 137, 134, 141]. The neutron star matter is modeled with the Shen et al. EoS [151]. During the merger process the debris can cool via neutrino emission, and electron/positron captures can change the electron fraction. These processes are included via the opacity-dependent, multi-flavor leakage scheme of [137]. Note, however, that no heating via neutrino absorption is included. Their effect are the main topic of this study.
As the starting point of our neutrino-radiation hydrodynamics study, we consider the matter distribution of the 3D SPH simulation with 10^6 particles, at 15 ms after the first contact (corresponding to 18 ms after the simulation start). Not accounting for

the neutrino absorption during this short time, should only have a small effect, since, according to the estimates from Sec. (4.1), the remnant hardly had time to change.
We map the 3D SPH matter distributions of density, temperature, electron fraction and fluid velocity on the Cartesian, equally spaced grid of `FISH`, with a resolution of 1 km. The initial extension of the grid is (800km × 800km × 640km). During the simulation, we increase the domain in all directions to follow the wind expansion, keeping the HMNS always in the centre. At the end, the computational box is (2240km × 2240km × 3360km) wide.
The initial data cover a density range of $10^8 \mathrm{g\,cm^{-3}} - 3.5 \times 10^{14} \mathrm{g\,cm^{-3}}$. Surrounding the remnant, we place an inert atmosphere, characterized by the following stationary properties: $\rho_{\mathrm{atm}} = 5 \cdot 10^3\,\mathrm{g/cm^3}$, $T_{\mathrm{atm}} = 0.1\,\mathrm{MeV}$, $Y_{e,\mathrm{atm}} = 0.01$ and $\mathbf{v}_{\mathrm{atm}} = \mathbf{0}$. The neutrino source terms are set to 0 in this atmosphere. With this treatment, we minimize the influence of the atmosphere on the disc and on the wind dynamics.

Even though in our model we try to stay as close as possible to the choices adopted in the SPH simulation, initial transients appear at the start of the simulation. One of the causes is the difference in the spatial resolutions between the two models. The resolution we are adopting in `FISH` is significantly lower than the one provided by the initial SPH model inside the HMNS, $\sim 0.125\,\mathrm{km}$, (which is necessary to model consistently the central object), while it is comparable or better inside the disc. Due to this lack of resolution, we decide to treat the HMNS as a stationary rotating object. To implement this, we perform axisymmetric averages of all the hydrodynamical quantities at the beginning of the simulation. At the end of each hydrodynamical time step, we re-map these profiles in cells contained inside an ellipsoid, with $a_x = a_y = 30\,\mathrm{km}$ and $a_z = 23\,\mathrm{km}$, and for which $\rho > 2 \cdot 10^{11}\mathrm{g/cm^3}$. For the velocity vector, we consider only the azimuthal component, since 1) the HMNS is rotating fast around its polar axis (with a period $P \approx 1.4\,\mathrm{ms}$) and 2) the non-azimuthal motion inside it is characterized by much smaller velocities (for example, $|v_R| \sim 10^{-3}\,|v_\phi|$, where v_R and v_ϕ are the radial and the azimuthal velocity components). Concerning the density and the rotational velocity profiles, our treatment is consistent with the results obtained by [29] (Fig. 4), who showed that $\sim 100\,\mathrm{ms}$ after the neutron star have collided those quantities have changed only slightly inside the HMNS. We expect the electron fraction and the temperature also to stay close to their initial values, since the most relevant neutrino surfaces for ν_e and $\bar{\nu}_e$ are placed outside the stationary region and the diffusion time scale is much longer than the simulated time (see, for example, Sec.(4.1)).

To give the opportunity to the system to adjust to a more stable configuration on the new grid, we consider the first 10 ms of the simulation as a "relaxation phase". During this phase, we evolve the system considering only neutrino emission. Its duration is chosen so that the initial transients arrive at the disc edge, and the profiles inside the disc reach new quasi-stationary conditions. The "relaxed" conditions are visible in Fig.(4.4). They are considered as the new initial conditions and we evolved them for $\sim 90\,\mathrm{ms}$, including the effect of neutrino absorption. In the following, the time t will be measured with respect to this second re-start. During the relaxation phase, we notice an increase of the electron fraction, from 0.05 up to 0.1-0.35, for a tiny amount of matter ($\lesssim 10^{-5} M_\odot$) in the low density region ($\rho \lesssim 10^9\mathrm{g/cm^3}$) situated above the innermost, densest part of the disc ($R_{\mathrm{cyl}} \lesssim 50\,\mathrm{km}$, $|z| \gtrsim 20\,\mathrm{km}$). Here, the presence of neutron-rich, hot matter in optically thin conditions favours the emission of $\bar{\nu}_e$, via positron absorption

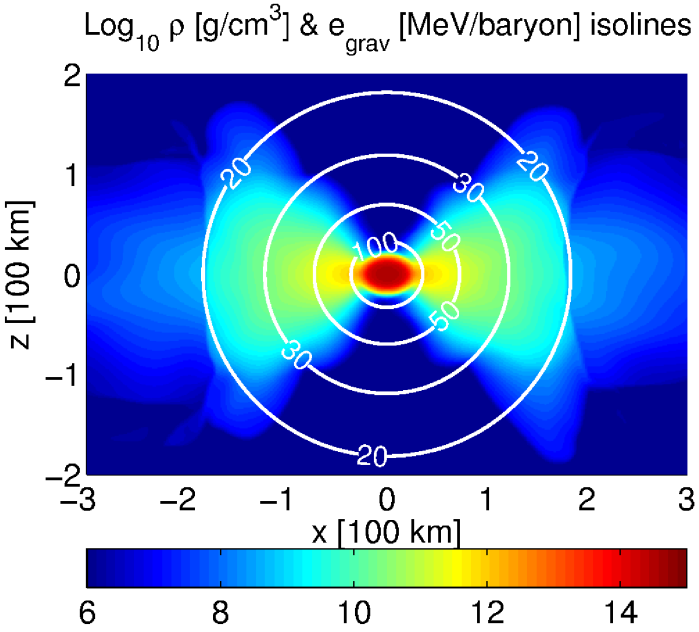

Figure 4.5: Logarithm of the matter density (color coded, in $\mathrm{g\,cm^{-3}}$) and isocontours of the gravitational energy (white lines, in $\mathrm{MeV\,baryon^{-1}}$), on a vertical slice of the three dimensional domain, at $t = 0$.

on neutrons. A similar increase of Y_e is also visible in the original SPH simulations, for times longer than 15 ms after the first collision.
In Fig.(4.5) we show isocontours of the absolute value of gravitational specific energy, drawn against the colour-coded matter density, at the beginning of our simulation. The gravitational energy provides an estimate of the energy that neutrinos have to deposit to unbound matter, at different locations inside the disc (see Sec.(4.1)).

4.3 Simulation results

4.3.1 Disc evolution and matter accretion

After the highly dynamical merger phase the remnant is still dynamically evolving and not yet in a perfectly stationary state.
In Fig.(4.6), we show the radial component of the fluid velocity on the $y = 0$ plane, at 41 ms after the beginning of the simulation. The central part of the disc, corresponding to a density coutour of $\sim 5 \cdot 10^9\,\mathrm{g\,cm^{-3}}$, is slowly being accreted onto the HMNS ($v_R \sim$ a few $10^{-3}c$), while the outer edge is gradually expanding along the equatorial direction. The velocity profile shows interesting asymmetries and deviations from an axisymmetric behaviour. The surface of the HMNS and the innermost part of the disc are characterized by steep gradients of density and temperature, and they behave like a pressure wall for the infalling matter. Outgoing sound waves are then produced and move outwards inside the disc, transporting energy, linear and angular momentum. At a cylindrical radius of $R_{\mathrm{cyl}} \lesssim 80\,\mathrm{km}$, they induce small scale perturbations in the velocity field, visible as bubbles of slightly positive radial velocity. These perturbations dissolve at larger radii, releasing their momentum and energy inside the disc, and favouring its equatorial

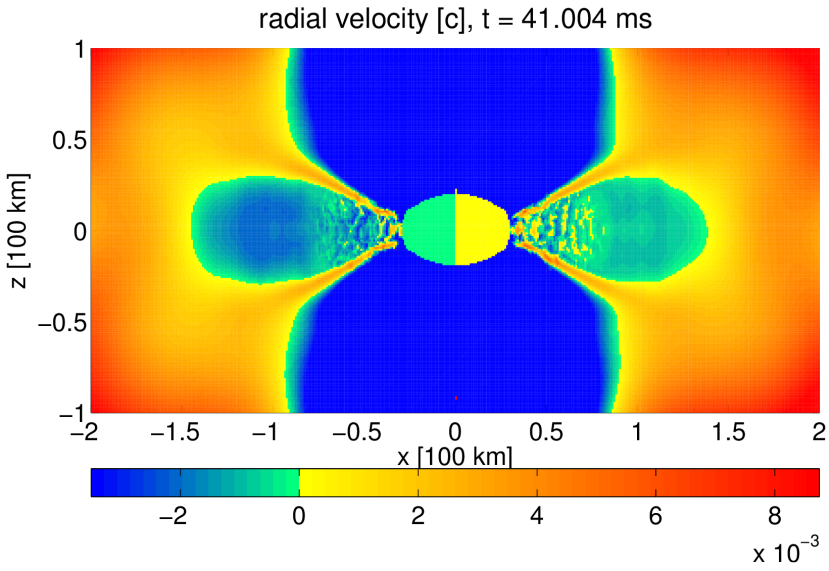

Figure 4.6: Vertical slice of the inner part of the three dimensional domain ($y = 0$ plane), taken at 41 ms after the beginning of the simulations. Color coded is the radial component of the fluid velocity. The two coloured hemispheres in the centre represent the stationary central object for which $v_r \approx 0$ (the two actual colors are very small numbers).

expansion.

The temporal evolution of the accretion rate $\dot{M}$, computed as the net flux of matter crossing a cylindrical surface of radius $R_{\rm cyl} = 35\,$km and axis corresponding to the rotational axis of the disc, is plotted in Fig.(4.7). This accretion rate is compatible with the estimate performed in Sec.(4.1) using an α-viscosity disc model. A direct comparison with Eq.(4.3) suggests an effective parameter $\alpha \approx 0.05$ for our disc. We stress again that no physical viscosity is included in our model: the accretion is driven by unbalanced pressure gradients, neutrino cooling (see Sec.(4.3.2)) and dissipation of numerical origin. However, the previous estimate is useful to compare our disc with purely Keplerian discs, in which a physical α-viscosity has been included (usually, with $0.01 \lesssim \alpha \lesssim 0.1$). Our value of $\alpha \approx 0.05$ is close to what is usually assumed for such disks (~ 0.1). Higher viscosities would enhance the neutrino emission and probably the mass loss.

On a timescale of a few tens of milliseconds, the profiles inside the disc change, as consequence of the accretion process and of the outer edge expansion. These effects are visible in the upper row of Fig.(4.8), where radial profiles of temperature and density are drawn, at different times and heights inside the disc. We notice, in particular, that the density decreases in the internal part of the disc ($50\,{\rm km} \lesssim R_{\rm cyl} \lesssim 200\,{\rm km}$), as result of the accretion. In the same region, the balance between the increase of internal energy and the efficient cooling provided by neutrino emission keeps the temperature almost stationary. At larger radial distances ($R_{\rm cyl} \gtrsim 200\,{\rm km}$), the initial accretion of a cold, thin layer of matter (visible in the $t = 2\,$ms profiles) is followed by the continous expansion of the outer margin of the hot internal disc.

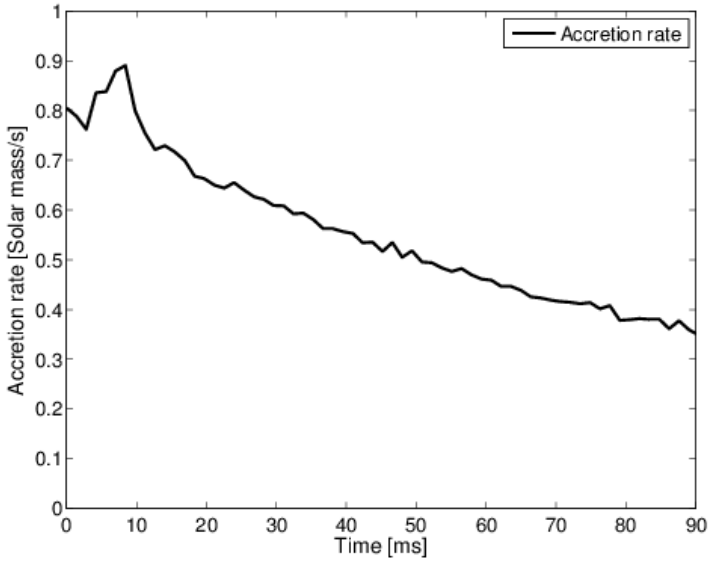

Figure 4.7: Temporal evolution of the accretion rate on the HMNS, $\dot{M}$, calculated as the net flux of matter crossing a cylindrical surface of radius $R_{\rm cyl} = 35\,$km and axis corresponding to the rotational axis of the disc.

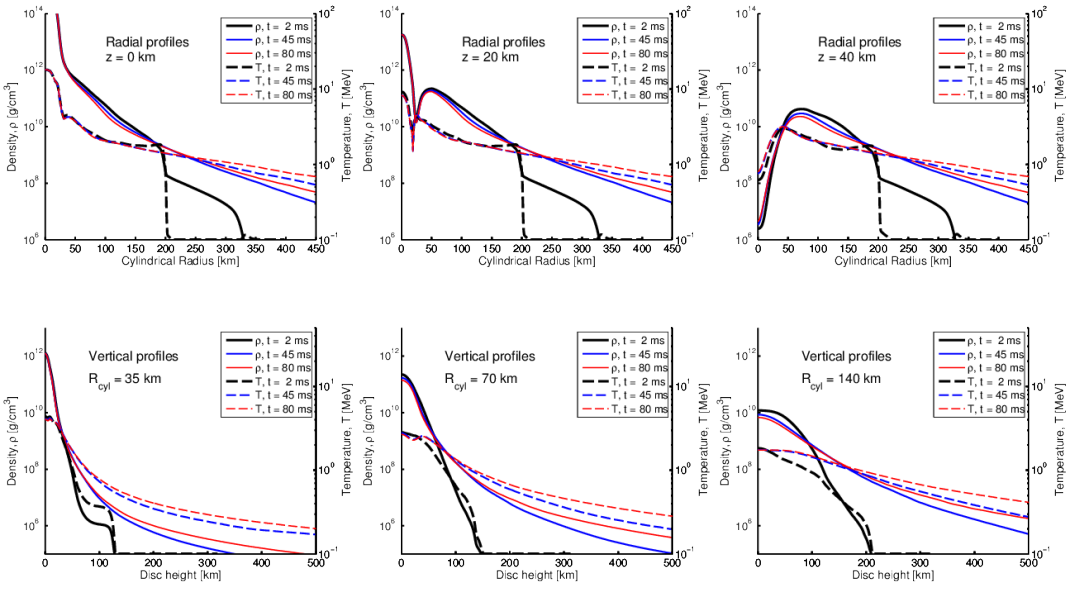

Figure 4.8: Radial (upper row) and vertical (lower row) profiles of the axisymmetric density (solid lines) and temperature (dashed lines) inside the disc, recorded at different times during the simulation ($t \approx 2\,$ms (black-thick lines), $t \approx 45\,$ms (blue-normal lines), $t \approx 80\,$ms (red-thin lines)). The different columns correspond to different values of the section coordinates: from left to right, $z = 0\,$km, $20\,$km, $40\,$km for the radial profiles; $R_{\rm cyl} = 35\,$km, $70\,$km, $140\,$km for the vertical ones.

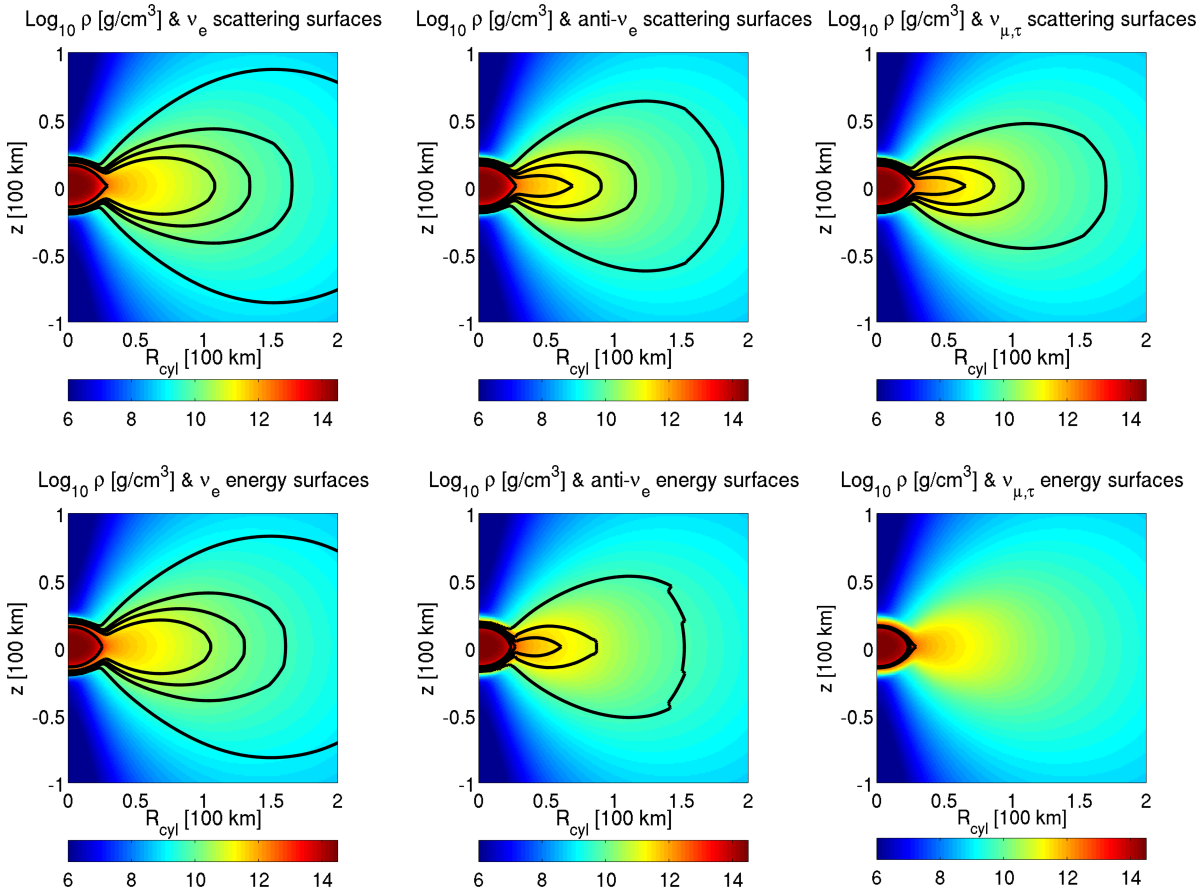

Figure 4.9: Location of the neutrino surfaces for ν_e (left column), $\bar{\nu}_e$ (central column) and $\nu_{\mu,\tau}$ (right column), for the scattering optical depth (upper row) and for the energy optical depth (bottom row), 40 ms after the beginning of the simulation. Color coded is the logarithm of cylindrically averaged matter density, $\rho\,[\mathrm{g/cm^3}]$. The different lines correspond to the neutrino surfaces for different values of the neutrino energy: from the innermost line to the outermost one, E_ν = 4.62 MeV, 10.63MeV, 16.22MeV, 24.65MeV, 56.96MeV.

4.3.2 Neutrino emission

In Fig.(4.9), we show the neutrino surfaces obtained by the calculation of the spectral neutrino optical depths, together with the matter density distribution (axisymmetric, color coded). Different lines correspond to different energy bins. In the upper panels, we represent the scattering neutrino surfaces, while in the lower panels the energy ones. Their shapes follow closely the matter density distribution, due to the explicit dependence appearing in Eq.(4.29) and Eq.(4.30). The last scattering surfaces for the energies that are expected to be more relevant for the neutrino emission ($10\,\mathrm{MeV} \lesssim E_\nu \lesssim 25\,\mathrm{MeV}$, corresponding to the expected range for the mean energies, as we will discuss below) extend far outside in the disc, compared with the radius of the central object. ν_e's have the largest opacities, due to the extremely neutron rich environment that favours processes like neutrino absorption on neutrons. Since the former reaction is also very efficient in thermalizing neutrinos, the scattering and the energy

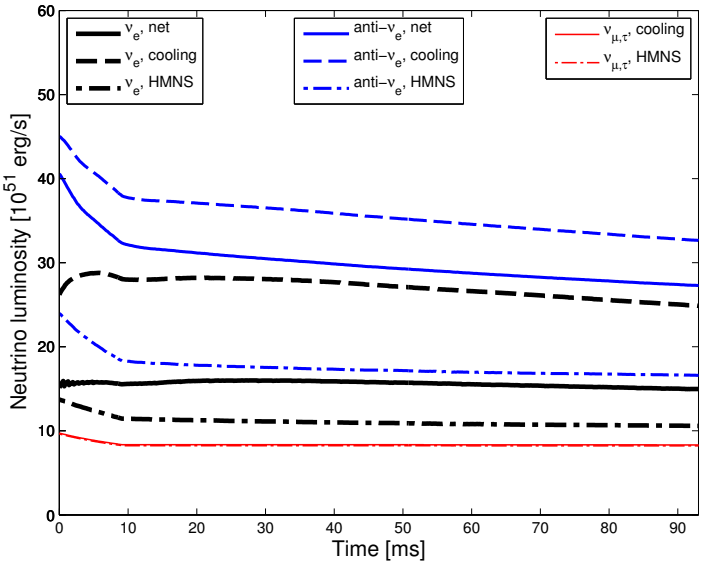

Figure 4.10: Time evolution of the net (solid) and cooling (dashed) luminosities obtained by the ASL scheme for ν_e (black-thick), $\bar{\nu}_e$ (blue-normal) and $\nu_{\mu,\tau}$ (red-thin) neutrino species. The difference between the cooling and the net luminosities is represented by the re-absorbed luminosity. The contributions to the cooling luminosities coming from the HMNS, defined as the volume characterized by $\rho > 5 \cdot 10^{11} \mathrm{g\,cm^{-3}}$, is also plotted (dot-dashed lines). Note that for $\nu_{\mu,\tau}$, the net and the cooling luminosities coincide, and they are almost equal to the HMNS contribution.

neutrino surfaces are almost identical for ν_e's. In the case of $\bar{\nu}_e$'s, the relatively low density of free protons determines the reduction of the scattering and, even more, of the energy optical depth. For $\nu_{\mu,\tau}$'s, neutrino bremsstrahlung and $e^+ - e^-$ annihilation freeze out at relatively high densities and temperatures ($\rho \sim 10^{13}\,\mathrm{g/cm^3}$ and $k_\mathrm{B}T \sim 8\,\mathrm{MeV}$), reducing further the energy neutrino surfaces, while elastic scattering on nucleons still provides a scattering opacity comparable to the one of $\bar{\nu}_e$'s.

The energy- and volume-integrated luminosities obtained during the simulation are presented in Fig.(4.10). The cooling luminosities for ν_e's and $\bar{\nu}_e$'s (dashed lines) decrease weakly and almost linearly with time. This behaviour reflects the continuous supply of hot accreting matter. The faster decrease of $\dot{M}$ (cf. Fig.(4.7)) would imply a similar decrease in the luminosities, if the neutrino radiative efficiency of the disc were constant. However, the latter increases with time due to the decrease of density and the constancy of temperature characterizing the innermost part of the disc (see Sec.(4.3.1)). Also the luminosity for the $\nu_{\mu,\tau}$ species is almost constant. This is a consequence of the stationarity of the central object, since most of the $\nu_{\mu,\tau}$'s come from there. However, this result is compatible with the long cooling time scale of the HMNS, Eq.(4.6). We specify here that the plotted lines for $\nu_{\mu,\tau}$ correspond to one single species. Thus, the *total* luminosity coming from heavy flavour neutrinos is four times the plotted one, see also Eq.(4.22).
In the case of ν_e's and $\bar{\nu}_e$'s, the luminosity provided by V_HMNS (defined in Sec.(4.2.2) and represented by dot-dashed lines in Fig.(4.10)) and the luminosity of the accreting disc are comparable. This result is compatible with what is observed in core collapse super-

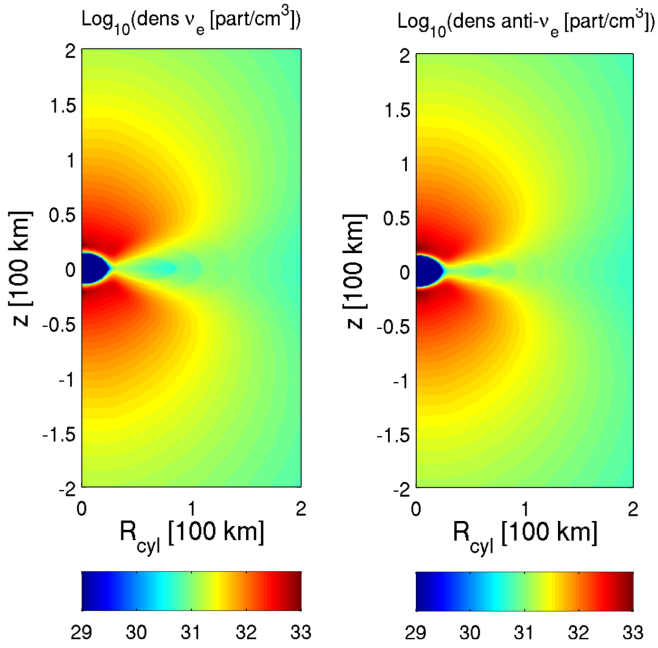

Figure 4.11: Energy-integrated (axisymmetric) neutrino density of the free-streaming neutrinos, N_ν, for ν_e (left panel) and $\bar{\nu}_e$ (right panel), calculated outside the innermost neutrino surface (corresponding to $E_\nu = 3\,\mathrm{MeV}$), at $t \approx 40\,\mathrm{ms}$ after the beginning of the simulation.

nova simulations [see, for example, Fig. 6 of 86], a few tens of milliseconds after bounce: assuming a density cut of $5 \times 10^{11} \mathrm{g\,cm^{-3}}$ for the proto-neutron star, its contribution is roughly half of the total emitted luminosity, for both ν_e and $\bar{\nu}_e$. Instead, if we further restrict V_{HMNS} only to the central ellipsoid (see Sec.(4.2.3) for more details), we notice that the related luminosity reduces to $\lesssim 10 \times 10^{51} \mathrm{erg\,s^{-1}}$ for all neutrino species. This is consistent with our preliminary estimate, Eq.(4.7).
The inclusion of neutrino absorption processes in the optically thin region reduces the cooling luminosities to the net luminosities (solid lines in Fig.(4.10)). For ν_e's, the neutron rich environment reduces the number luminosity by $\sim$ 37%, while for $\bar{\nu}_e$'s this fraction drops to $\sim$ 14%.

The values of the neutrino mean energies are practically stationary during the simulation: from the net luminosities at $t \approx 40\mathrm{ms}$, $\langle E_{\nu_e} \rangle \approx 10.6\,\mathrm{MeV}$, $\langle E_{\bar{\nu}_e} \rangle \approx 15.3\,\mathrm{MeV}$ and $\langle E_{\nu_{\mu,\tau}} \rangle \approx 17.3\,\mathrm{MeV}$. The mean neutrino energies show the expected hierarchy, $\langle E_{\nu_e} \rangle < \langle E_{\bar{\nu}_e} \rangle < \langle E_{\nu_{\mu,\tau}} \rangle$, reflecting the different locations of the thermal decoupling surfaces. While the values obtained for ν_e's and $\bar{\nu}_e$'s are consistent with previous calculations, $\langle E_{\nu_{\mu,\tau}} \rangle$ is smaller than expected. This is due to the lack of resolution at the HMNS surface, where most of the energy neutrino surfaces for $\nu_{\mu,\tau}$ are located. This discrepancy has no dynamical effects for us, since most of $\nu_{\mu,\tau}$ come from the stationary central object.

The ray-tracing algorithm, see Sec.(4.2.2), allows us to compute 1) the neutrino densities outside the neutrino surfaces; 2) the angular distribution of the isotropised neutrino cooling luminosities and mean neutrino energies, as seen by a far observer. In Fig.(4.11), we represent the energy-integrated axisymmetric neutrino densities N_ν,

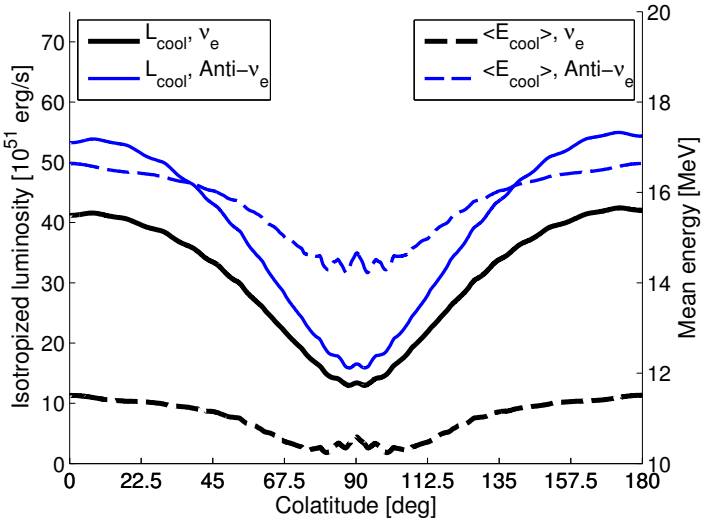

Figure 4.12: Angular dependence of the isotropised neutrino cooling luminosities (solid line) and of the neutrino mean energies (dashed lines), as a function of the colatitude. The black-thick lines correspond to ν_e, while the blue-thin lines to $\bar{\nu}_e$. As a representative time, we consider $t \approx 40$ms after the beginning of the simulation.

Eq.(4.38), for ν_e (left) and $\bar{\nu}_e$ (right). These densities reach their maximum in the funnel above the HMNS, due to the geometry of the emission and to the short distance from the most emitting regions. At distances much larger than the dimension of the neutrino surfaces, N_ν shows the expected R^{-2} dependence.
The disc geometry introduces a clear anisotropy in the neutrino emission, visible in Fig.(4.12). Due to the larger opacity along the equatorial direction, the isotropic luminosity along the poles is $\sim 3 - 3.5$ more intense than the one along the equator. The different temperatures at which neutrinos decouple from matter at different polar angles determine the angular dependence of the mean energies.

4.3.3 Neutrino-driven wind

The evolution of the disc and the formation of a neutrino-driven wind depend crucially on the competition between neutrino emission and absorption. In Fig.(4.13), we show axisymmetric averages of the net specific energy rate (left), of the net electron fraction rate (centre), and of the acceleration due to neutrino absorption(right), at $t = 40\,\mathrm{ms}$.
Inside the most relevant neutrino surfaces and a few kilometers outside them, neutrino cooling dominates. Above this region, neutrino heating is always dominant. The largest neutrino heating rate happens in the funnel, where the neutrino densities are also larger. However, these regions are characterized by matter with low density ($\rho \lesssim 10^7 \mathrm{g\,cm^{-3}}$) and small specific angular momentum. Thus, this energy deposition has a minor dynamical impact on this rapidly accreting matter. On the other hand, at larger radii ($80\,\mathrm{km} \lesssim R_{\mathrm{cyl}} \lesssim 120\,\mathrm{km}$) net neutrino heating affects denser matter ($\rho \lesssim 10^{10} \mathrm{g\,cm^{-3}}$), rotating inside the disc around the HMNS. This combination provides an efficient net energy deposition.
Neutrino diffusion from the optically thick region determines small variations around the

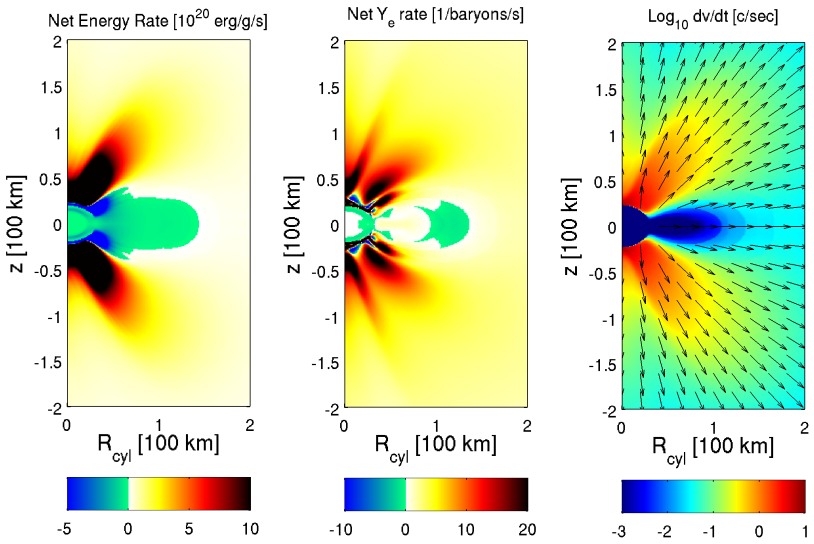

Figure 4.13: Energy- and species-integrated axisymmetric ν net rates for energy (left panel, in units of 10^{20} erg/g/s) and Y_e (central panel, in units of 1/baryon/s), and of the fluid velocity variation provided by neutrino absorption in the optically thin regions (right panel, in units of c/s). As a representative time, we consider $t \approx 40\,\mathrm{ms}$ after the beginning of the simulation. The complex structure of the net Y_e rate in the funnel, above the HMNS poles, originates from the variety of conditions of Y_e, ρ and $\mathbf{v}$ at that specific moment.

initial weak equilibrium value in the electron fraction. On the contrary, in optically thin conditions, the initial very low electron fraction favours reactions like the absorption of e^+ and ν_e on free neutrons. Both processes lead to a positive and large $(\mathrm{d}Y_e/\mathrm{d}t)_\nu$, in association with efficient energy deposition.
Due to the geometry of the emission and to the shadow effect provided by the disc, the direction of the acceleration provided by neutrino absorption is approximately radial, but its intensity is much larger in the funnel, where the energy deposition is also more intense.

As a consequence of the continous neutrino energy and momentum deposition, the outer layers of the disc start to expand a few milliseconds after the beginning of the simulation, and they reach an almost stable configuration in a few tens of milliseconds. Around $t \sim 10\,\mathrm{ms}$, also the neutrino-driven wind starts to develop from the expanding disc. Wind matter moves initially almost vertically (i.e., with velocities parallel to the rotational axis of the disc), decreasing its density and temperature during the expansion. We show the corresponding vertical profiles inside the disc in the bottom panels of Fig.(4.8), at different times and for three cylindrical radii. Both the disc and the wind expansions are visible in the rise of the density and temperature profiles, expecially at cylindrical radii of 70 km or 140 km.
Among the energy and the momentum contributions, the former is the most important one for the formation of the wind. To prove this, we repeat our simulation in two cases, starting from the same intial configuration and relaxation procedure. In a first case, we set the heating rate h_ν appearing in Eq.(4.27) and Eq.(4.28) to 0. Under this assumption, we observe neither the disc expansion nor the wind formation. In a second test, we

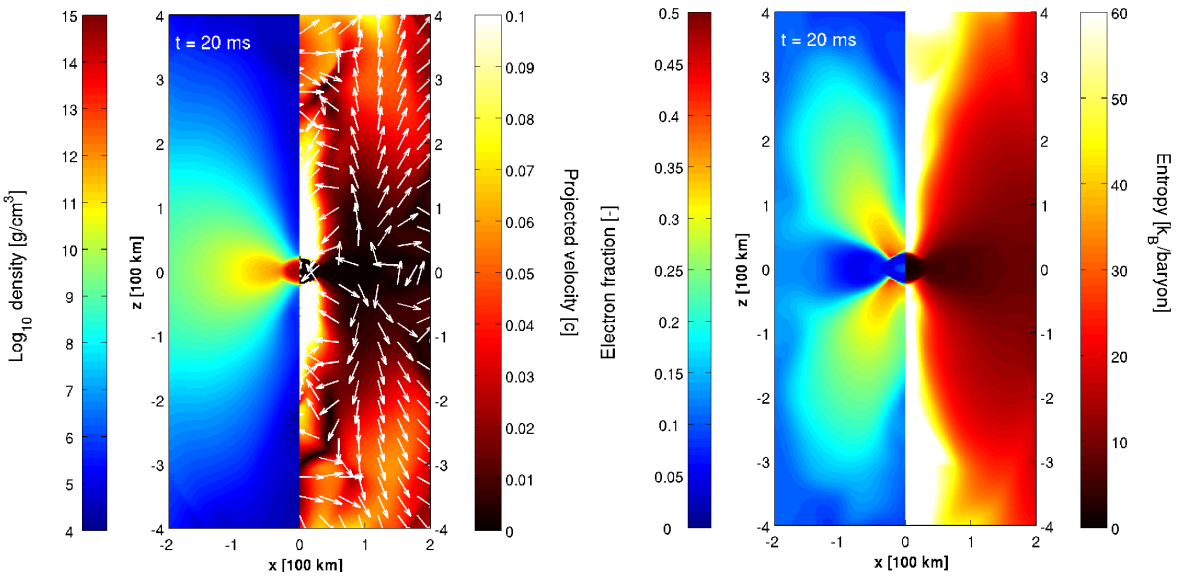

Figure 4.14: Vertical slices of the three dimensional domain (corresponding to the $y = 0$ plane), recorded 20 ms after the beginning of the simulation. In the left panel, we represent the logarithm of the matter density (in g/cm^3, left side) and the projected fluid velocity (in units of c, on the right side); the arrows indicate the direction of the projected velocity in the plane). On the right panel, we represent the electron fraction (left side) and the matter entropy (in unit of $k_{\rm B}$/baryon, right side).

include the effect of neutrino absorption only in the energy and Y_e equations, but not in the momentum equation. In this case, the wind still develops and its properties are qualitatively very similar to our reference simulation.

In Fig. 4.14, 4.15 and 4.16 we present three different times of the wind expansion, $t = 20, 40, 85$ ms. To characterize them, we have chosen vertical slices of the three dimensional domain, for the density and the projected velocity (left picture), and for the electron fraction and the matter entropy (right picture).
The development of the wind is clearly associated with the progressive increase of the electron fraction. The resulting Y_e distribution is not uniform, due to the competition between the wind expansion time scale (Eq.(4.12)) and the time scale for weak equilibrium to establish. The latter can be estimated as $t_{\rm weak} \sim Y_{e,\rm eq}/\left({\rm d}Y_e/{\rm d}t\right)_\nu$. Using the values of the neutrino luminosities, mean energies and net rates for the wind region, we expect $Y_{e,\rm eq} \approx 0.42$ [see, for example, eq. (77) of 123] and $0.042\,{\rm s} \lesssim t_{\rm weak} \lesssim 0.090\,{\rm s}$. If we keep in mind that the absorption of neutrinos becomes less efficient as the distance from the neutrino surfaces increases, we understand the presence of both radial and vertical gradients for Y_e inside the wind: the early expanding matter has not enough time to reach $Y_{e,\rm eq}$, especially if it is initially located at large distances from the relevant neutrino surfaces ($R_{\rm cyl} \gtrsim 100\,{\rm km}$). On the other hand, matter expanding from the innermost part of the disc and moving in the funnel (within a polar angle of $\lesssim 40^o$), as well as matter that orbits several times around the HMNS before being accelerated in the wind, increases its Y_e close to the equilibrim value, but on a longer time scale.
Also the matter entropy in the wind rises due to neutrino absorption. Typical initial val-

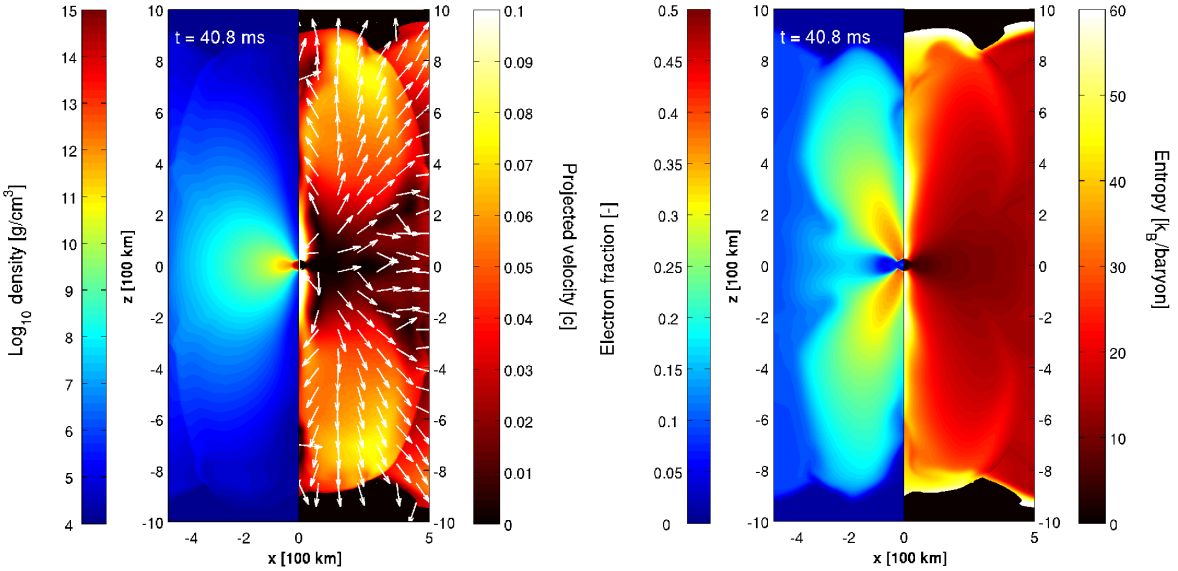

Figure 4.15: Same as in Fig.(4.14), but at $\approx 40\,\mathrm{ms}$ after the beginning of the simulation.

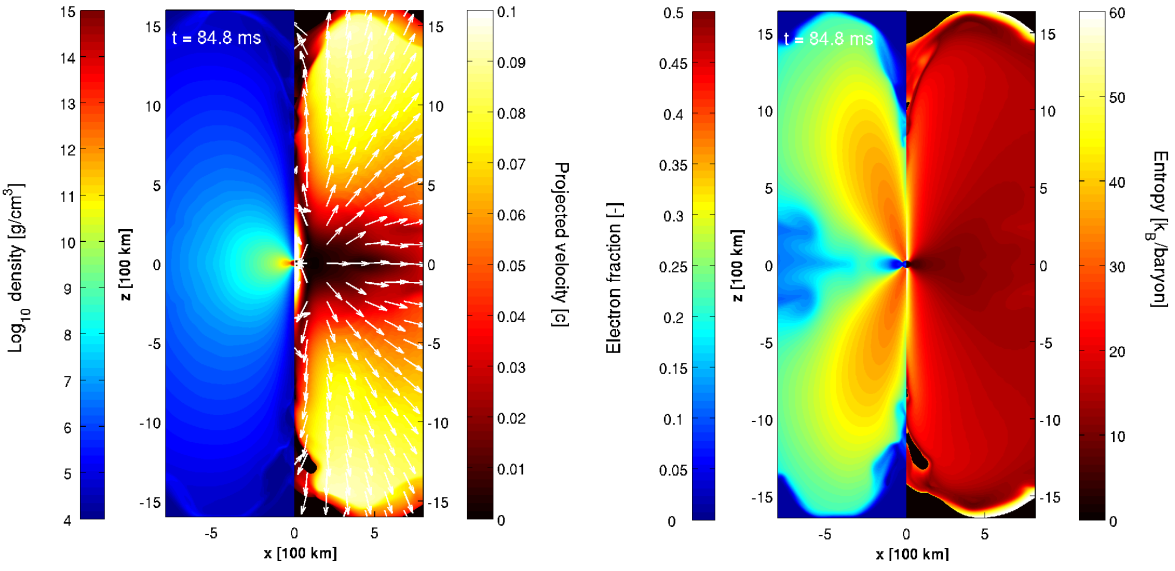

Figure 4.16: Same as in Fig.(4.14), but at $\approx 85\,\mathrm{ms}$ after the beginning of the simulation.

ues in the disc are $s \sim 5-10\,k_{\rm B}$ baryon^{-1}, while later we observe $s \sim 15-20\,k_{\rm B}$ baryon^{-1}. The entropy is usually larger where the absorption is more intense and Y_e has increased more. However, differently from Y_e, its spatial distribution is more uniform. Once the distance from the HMNS and the disc has increased above ~ 400 km, neutrino absorption becomes negligible and the entropy and the electron fraction are simply advected inside the wind.
The radial velocity in the wind increases from a few times $10^{-2}\,c$, just above the disc, to a typical asymptotic expansion velocity of $0.08 - 0.09c$. This acceleration is caused by the continous pressure gradient provided by newly expanding layers of matter.

To characterize the matter properties, we plot in Fig.(4.17) *occurrence diagrams* for couples of quantities, namely $\rho - Y_e$ (top row), $\rho - s$ (central row) and $Y_e - s$ (bottom row), at three different times ($t = 0, 40, 85$ ms). Colour coded is a measure of the amount of matter experiencing specific thermodynamical conditions inside the whole system, at a certain time [5].
We notice that most of the matter is extremely dense ($\rho > 10^{11}\,{\rm g\,cm^{-3}}$), neutron rich ($Y_e < 0.1$) and, despite the large temperatures ($T > 1$ MeV), at relatively low entropy ($s < 7\,k_B$ baryon^{-1}). This matter correspond to the HMNS and to the innermost part of the disc, where matter conditions change only on the long neutrino diffusion timescale, Eq.(4.6), or on the disc lifetime, Eq.(4.2). In the low density part of the diagrams ($\rho < 10^{11}\,{\rm g\,cm^{-3}}$), the expansion of the disc and the development of the wind can be traced.

In Fig.(4.18) (a-d), we represent the mass fractions of the nuclear species provided by the nuclear EoS inside the disc and the wind, at 40 ms after the beginning of the simulation. Close to the equatorial plane ($|z| < 100$ km), the composition is dominated by free neutrons. In the wind, the increase of the electron fraction corresponds to the conversion of neutrons into protons due to ν_e absorption. In the early expansion phase, the relatively high temperature ($T \gg 0.6$ MeV) favours the presence of free protons. When the decrease of temperature allows the formation of nuclei, protons cluster into α particles and, later, into neutron-rich nuclei. Then, the composition in the wind, at large distances from the disc, is distributed between free neutrons ($0.4 \lesssim X_n \lesssim 0.6$) and heavy nuclei ($0.6 \gtrsim X_h \gtrsim 0.4$, respectively). The heavy nuclei component is described in the EoS by a representative average nucleus, assuming Nuclear Statistical Equilibrium (NSE) everywhere. In Fig.(4.18) (e-f), we have represented the values of its mass and charge number. The most representative nucleus in the wind corresponds often to ^{78}Ni. The black line defines the surface across which the freeze-out from NSE is expected to occur ($T = 0.5$ MeV). Outside it the actual composition will differ from the NSE prediction.

4.3.4 Ejecta

Matter in the wind can gain enough energy from the neutrino absorption and from the subsequent disc dynamics to become unbound. The amount of ejected matter is calculated as volume integral of the density and fulfills three criteria: 1) has positive radial velocity; 2) has positive specific total energy; 3) lies inside one of the two cones of

[5] A formal definition of the plotted quantity can be found in Sec. 2 of [5]. However, in this work we don't calculate the time average.

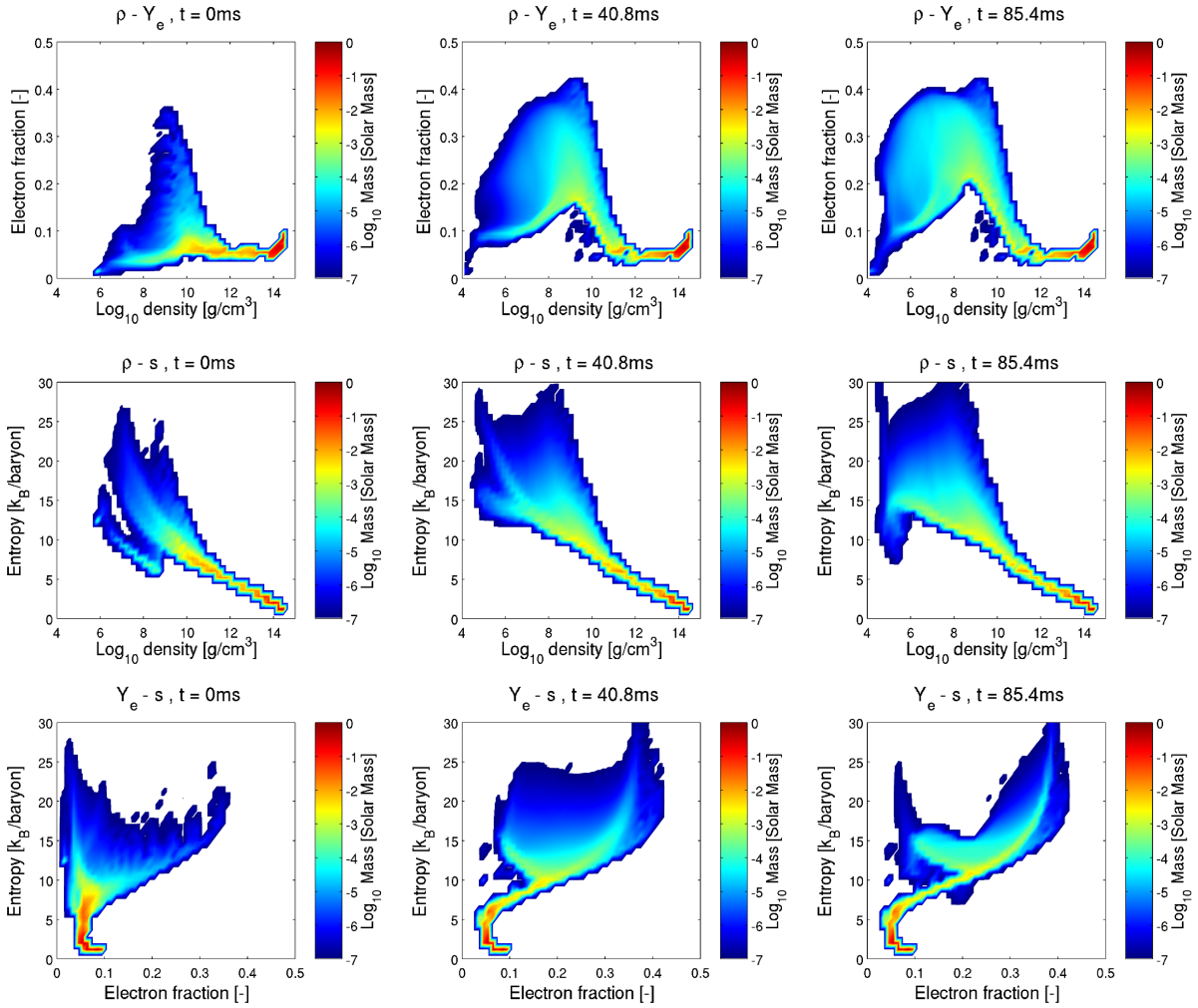

Figure 4.17: Occurrence diagrams for (ρ, Y_e) (top panel), (ρ, s) (middle panels) and (Y_e, s) (bottom panels), for the thermodynamical properties of matter in the whole system, at $t \approx 0\,\mathrm{ms}$ (left column), $t \approx 40\,\mathrm{ms}$ (central column) and $t \approx 85\,\mathrm{ms}$ (right column) after the beginning of the simulation. Colour coded is a measure of the amount of matter experiencing specific thermodynamical conditions inside the whole system. Occurrence smaller than $10^{-7} M_\odot$ have been omitted from the plot.

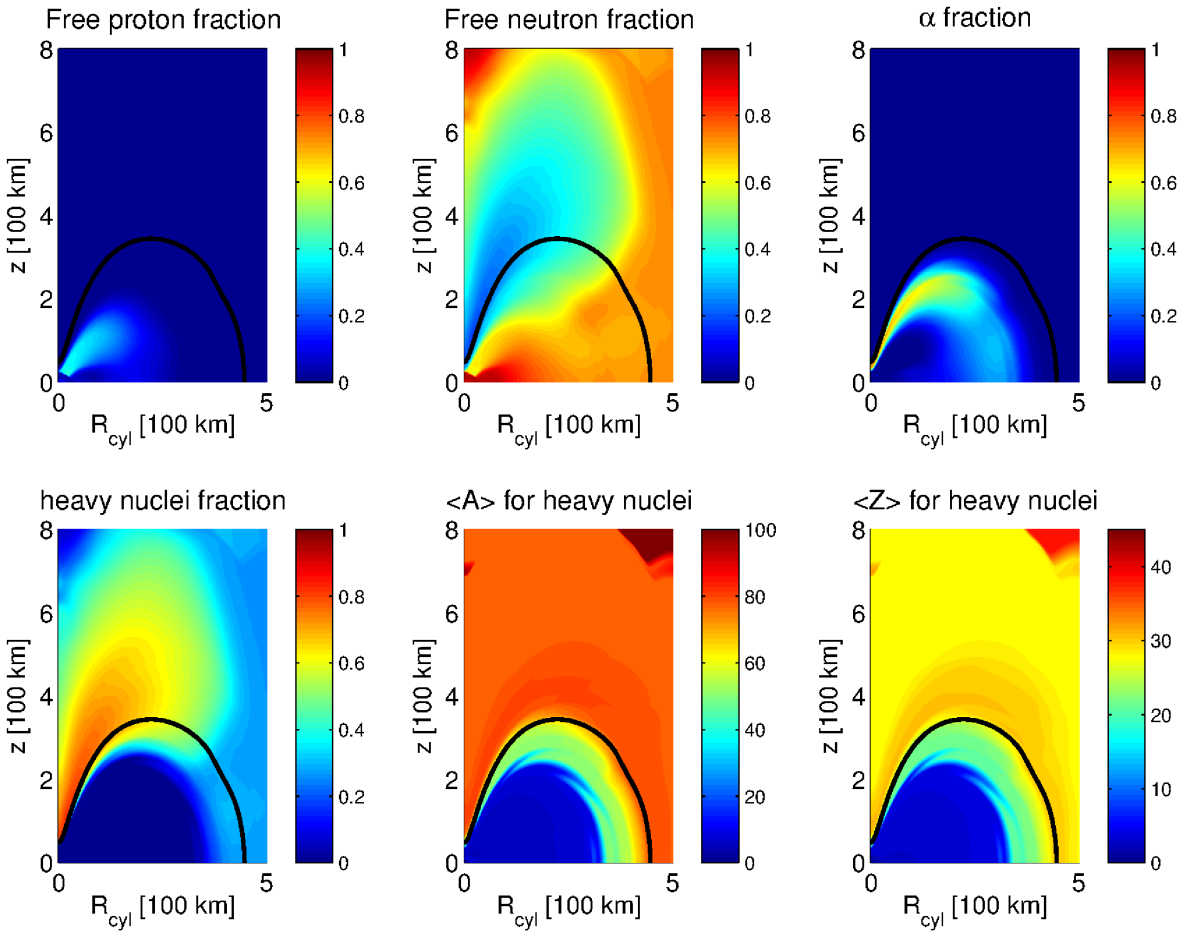

Figure 4.18: Nuclear composition provided by the EoS (assuming everywhere NSE) in the disc and in the wind, at $t \approx 40\,\mathrm{ms}$. On the top row, free proton (left), free neutron (centre) and α particles (right) mass fractions. On the bottom row, heavy nuclei mass fraction (left), and mass number (centre) and atomic number (right) of the representative heavy nucleus. The black line represents the $T = 0.5\,\mathrm{MeV}$ surface.

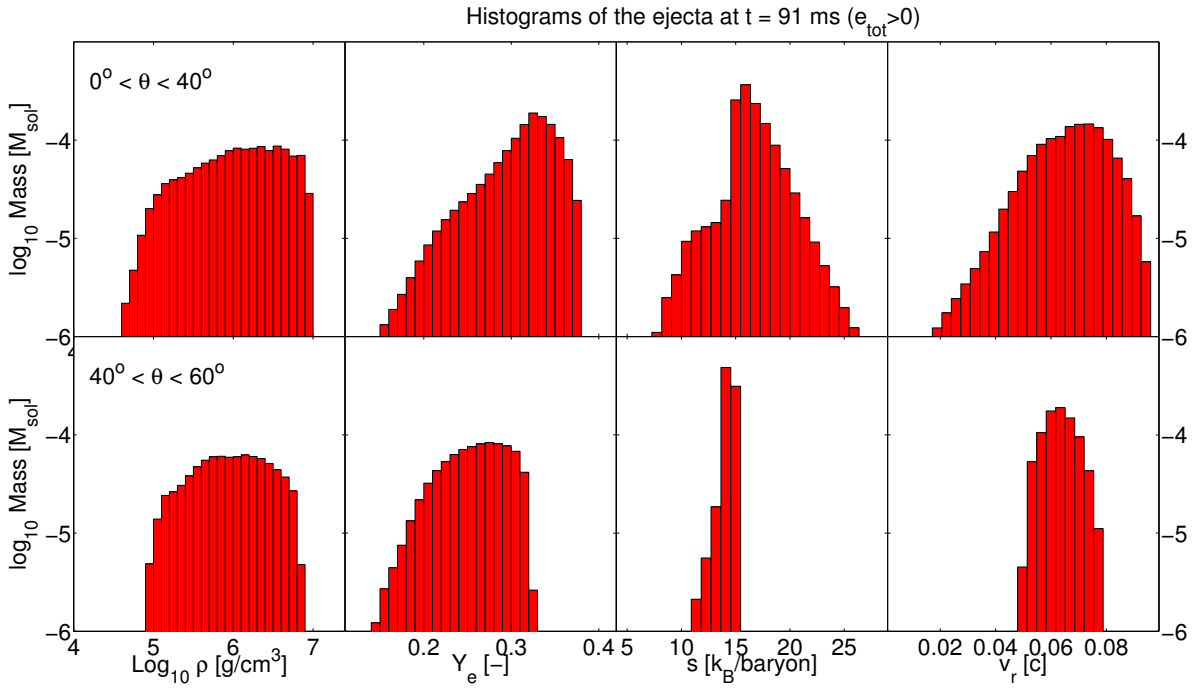

Figure 4.19: Distributions in the ν-driven wind ejecta binned by different physical properties. The different columns refer to density (ρ, left), electron fraction (Y_e, central-left), entropy per baryon (s, central-right) and radial velocity (v_r, right). The top (bottom) panels refer to high (low) latitudes.

opening angle 60°, vertex in the centre of the HMNS and axes coincident with the disc rotation axes. The latter geometrical constrain excludes possible contributions coming from equatorial ejecta, which have not been followed properly during their expansion. The profile of Y_e at the end of the simulation (see, for example, Fig.(4.16)) suggests to further distinguish between two zones inside each cone, one at high (H: $0° \leq \theta < 40°$) and one at low (L: $40° \leq \theta < 60°$) latitudes.
The specific total internal energy is calculated as:

$$e_{\rm tot} = e_{\rm int} + e_{\rm grav} + e_{\rm kin}. \tag{4.44}$$

$e_{\rm grav}$ is the Newtonian gravitational potential, and $e_{\rm kin}$ is the specific kinetic energy. The specific internal energy $e_{\rm int}$ takes into account the nuclear recombination energy and, to compute it, we use the composition provided by the EoS. For the nuclear binding energy of the representative heavy nucleus, we use the semi-empirical nuclear mass formula [see, for example, the fitting to experimental nuclei masses reported by 133]: in the wind, for $\langle A \rangle \approx 78$ and $\langle Z \rangle \approx 28$, the nuclear binding energy is $\sim 8.1\,{\rm MeV\,baryon^{-1}}$.

At the end of the simulation, $M_{\rm ej}(t = 91\,{\rm ms}) \approx 2.12 \times 10^{-3} M_\odot$, corresponding to $\sim 1.2\%$ of the initial disc mass ($M_{\rm disc} \approx 0.17 M_\odot$). This mass is distributed between $M_{\rm ej,H}(t = 91\,{\rm ms}) \approx 1.3 \times 10^{-3} M_\odot$ at high latitudes and $M_{\rm ej,L}(t = 91\,{\rm ms}) \approx 0.8 \times 10^{-3} M_\odot$ at low latitudes. In Fig.(4.19), we represent the mass distributions of density, electron fraction, entropy and radial velocity, for the ejecta at the end of our simulation. At high latitude, the larger ν_e absorption enhanches the electron fraction and the entropy more than at lower latitudes. The corresponding mass distributions are broader, with peaks

at $Y_e \sim 0.31 - 0.35$ and $s \sim 15 - 20 k_{\rm B}$/baryon. At lower latitudes, the electron fraction presents a relatively uniform distribution between 0.23 and 0.31, while the entropy has a very narrow peak around 14-15 $k_{\rm B}$/baryon. The larger energy and momentum depositions produce a faster expansion of the wind close to the poles. This effect is visible in the larger average value and in the broader distribution of the radial velocity that characterizes the high latitude ejecta.
To quantify the uncertainties in the determination of the ejecta mass, we repeat the previous calculation assuming an error of 0.5 MeV in the estimate of the nuclear recombination energy. For $M_{\rm ej,H}$ this translates in an uncertainty of $\approx 7\%$, while in the case of $M_{\rm ej,L}$ the potential error is much larger ($\sim 50\%$). This is a consequence of the different ejecta properties. At high latitudes, most of the free neutrons have been incorporated into heavy nuclei, releasing the corresponding binding energy. Moreover, the large radial velocities ($v_r \sim 0.08 - 0.09\, c$) provides most of the energy needed to overcome the gravitational potential. At lower latitudes, the more abundant free neutrons and the lower radial velocities ($v_r \sim 0.06 - 0.07\, c$) translate into a smaller ejecta amount, with a larger dependence on the nuclear recombination energy.

Chapter 5

Other applications of the ASL treatment

In this chapter we want to present some other results, which have been obtained using the ASL treatment for neutrinos, in different astrophysical contexts and simulations. The goal of this section is not only to show interesting results, but, at the same time, to prove that the scheme we have developed is plastic enough to be included into one- or multi-dimensional simulations, in grid, as well as in SPH code, always keeping most of its original features untouched. The applications that we want to show are:

- a three dimensional Newtonian CCSN model, with strong rotation and high magnetic field, which develops quickly after bounce a jet-like explosion. The magneto-hydrodynamics evolution is provided by the grid code `FISH`. The ASL treatment takes into account the important deleptonization process during the collapse, and the mean neutrino cooling features during the post-bounce phase, due to ν_e and $\bar{\nu}_e$. Being a early version of the treatment, it slightly differ from the one presented in Chapter 2; and it does not include any neutrino thermalization or heating features. As electron neutrino and electron antineutrino absorption plays a major role in the definition of the electron fraction of ejected matter, this effect has been estimated in a post-processing way; the resulting trajectories have been post-processed by a nuclear network, to asses the abundances of heavy elements (in particular, r-process elements). This project is part of a close collaboration between Roger Käppeli, Christian Winteler and my-self, at the University of Basel. The results have been well documented also in their PhD thesis and in [176].

- A three-dimensional Newtonian CCSN model, with no rotation and no magnetic field, which undergoes core collapse, bounce and then shock stalling. In this case, the hydrodynamics evolution is provided by the SPH code `SPHYNX`. As in the previous case, the ASL treatment takes into account the important deleptonization process during the collapse, and the mean neutrino cooling features during the post-bounce phase. The used version is the one presented in Chapter 2; but, at the moment, it does not include the neutrino thermalization and the heating process. This project is done in close collaboration with Ruben Cabezon, at the University of Basel.

- Spherically symmetric CCSN models, evolved by the relativistic hydrodynamics

code AGILE. The transport of electron neutrinos and antineutrinos is provided by the Isotropic Diffusion Source Approximation (IDSA); the ASL treatment provides a spectral treatment for the emission of $\nu_{\mu,\tau}$ and $\bar{\nu}_{\mu,\tau}$. The model proposes a new way to induce the explosion of the star in spherical symmetry, which uses the μ and τ spectral neutrino luminosity. This combination of codes, together with a new consistent treatment of the EOS at low densities and the inclusion of a simplified treatment to follow the nuclear burning out of NSE, allows 1) to follow the long term evolution of the newly born neutron star in a relatively inexpensive way; 2) to test the impact of the nucleon potential inside the NSE treatment for the ejected matter, for different EOS. This work is currently under development, in collaboration with Matthias Hempel and Kevin Ebinger at the University of Basel, and with Carla Fröhlich and Jordi Casanova Bustamante at North Carolina State University.

5.1 3D MHD core collapse supernova simulations with FISH & ASL

5.1.1 Background and motivation

As it has been pointed out in Chapter 1, CCSN mechanism, explaining how massive stars end in a central collapse, producing a neutron star (or a black hole) and explosive ejection of the outer layers of the star, is still debated. Neutrino emission from the hot collapsed core plays a major role in this scenario; the re-absoprtion of a fraction of this huge luminosity by the shocked matter in the gain region (a region located just below the shock radius and well above the neutrinosphere) has been proposed as a possible explosion mechanism (delayed neutrino-driven explosion). Recent multi-D hydrodynamic approaches, including improved spectral neutrino transport, seems to confirm the validity of this mechanism, at least for some tested progenitor models and standard hadronic EOS [e.g. 107, 79, 82, 20].
The equation of state (EOS) caused explosion scenario has found some recent revival, based on the quark-hadron phase transition at super-nuclear densities [145]. Nevertheless, the viability of this mechanism depends on specific choices of EOS properties in a very narrow parameter range.
Another interesting option is the magneto-rotationally driven mechanism, related to stellar rotation and magnetic fields; this topic has been discussed for more than 30 years, but required three-dimensional (3D) modeling and had, therefore, only been addressed with limited success in the early days. The major outcome was that high rotation rates and (possibly unrealistically high) magnetic fields were required to launch explosions. The central question concerning it, is whether such magnetic fields can be attained during collapse with rotation and on which timescale after collapse [77, 91, 9, 106, and references therein]. This topic has recently been re-addressed by [103], [158] and [17]. We tackled this problem using our 3D magneto-hydrodynamics grid code FISH [63], the same one which has been used to study the aftermath of double neutron star mergers.

The magneto-rotationally driven explosion are, for sure, intrinsically interesting, first of all as a possible (maybe, not very frequent) explosion mechanism for CCSNe. But there is another reason of interest: the search for the site of a (full) r-process early in galactic

evolution. The initially postulated neutrino wind in regular (neutrino-driven) supernovae [54, 97, 35] (a) did not result in having sufficiently high entropies [163, 169, 2], and (b) in addition, the innermost ejecta turned out to be proton-rich instead of neutron-rich [122, 43], a situation which has now also been shown in long-term simulations [37, 55]. Electron-capture supernovae, which explode without a long phase of accretion onto the proto-neutron star (PNS), apparently provide more favorable conditions [171]. However, also the proton to nucleon ratios obtained under such conditions do not support a strong r-process, which successfully reproduces the platinum peak of r-elements around $A = 195$. A similar result was recently obtained for core-collapse supernova (CCSN) explosions triggered by a quark-hadron phase transition during the early post-bounce phase when investigating their detailed nucleosynthesis [110]. Both types of events might support a weak but not a full r-process.

Neutron star mergers have been shown to be powerful sources of r-process matter, in fact ejecting a factor of 100 to 1000 more r-process material than required on average from CCSNe, if those would have to explain solar r-process element abundances. This would actually support the large scatter of Eu/Fe found in very metal-poor stars. The only problem is that it might be hard to explain the early appearance of r-process matter for metallicity at and below [Fe/H] $= -3$ [4]. Some recent studies, which include the fact that our Galaxy is possibly the result from smaller merging subsystems (with different star formation rates) have been expected to show a way out of this dilemma. If this cannot be solved, we need another strong r-process source already at low metallicities, and possibly jets from rotating core collapses with strong magnetic fields could be the solution [23, 111, 46].

5.1.2 3D MHD-CCSN model

The calculation was performed with the computational setup similar to previous investigations, which have been documented in [86, 147]. The initially innermost (600 km)^3 of the massive star are covered by a 3D Cartesian domain uniformly discretized with a resolution of 1 km. The resulting cube of 600^3 cells is embedded in a spherically symmetric domain, encompassing the iron core and parts of the silicon shell. The magnetic fluid is evolved with the `FISH` code [63], solving the ideal MHD equations, as explained in Chapter 4. The spherically symmetric domain is evolved with the `AGILE` code [87], and it provides boundary condition values for the infalling matter, at the interface with the three dimensional domain. The gravitational potential is approximated by an effective axisymmetric mass distribution that includes general relativistic monopole corrections [89]. We use the Lattimer-Swesty EOS [71], with nuclear compressibility 180 MeV. We have included a Lagrangian component in the form of tracer particles, which are passively advected with the flow. They record the thermodynamic conditions of a particular fluid element and serve as input to the post-processing nucleosynthesis calculations.

The transport of the electron neutrinos and antineutrinos is approximated by the ASL treatment. The neutrino energy is discretized with 12 geometrically increasing energy groups, spanning the range $2\text{MeV} \leq E_\nu \leq 200\,\text{MeV}$. The scheme has been implemented in three dimensions, combining a purely local approach with a ray-by-ray axisymmetric one. The reason for such a combination is that the treatment requires, as fundamental quantity, the neutrino optical depth, τ_ν. Its values depend on the distribution of matter in the full domain; but this detailed information is very difficult and

expensive to access for a MPI parallelized, three-dimensional domain. Considering that the star has an intrinsically quasi-spherical symmetry, broken in a quasi-axisymmetric one by the rotation and the magnetic field, we decided for an axisymmetric ray-by-ray approximation. The latter is realized on a uniform polar grid: we set a constant resolution of 1 km for the radial spacing, and we introduced 30 angular rays, covering the whole $[0, \pi]$ polar angle extension. Along each ray, the axisymmetric values of the basic code quantities (i.e., matter density, internal energy, electron density, velocity components, trapped neutrino densities and energy) are interpolated. Starting from these values, it is possible to apply the ASL treatment along each ray. The calculation will provide, among other things, the value of the neutrino stress, and of the optical depth, integrated along the ray itself. These two central ray-by-ray quantities can be, finally, re-mapped locally on the three dimensional domain. Having all the local quantities (i.e., matter density, internal energy, electron density, velocity components, trapped neutrino densities and energy) and the interpolated optical depths and neutrino stress, it is possible to apply the ASL locally, to calculate the effective neutrino rates, and, consequently, the local variations of the internal energy, electron fraction, trapped neutrino fraction and energy, and fluid velocity.
All fundamental ν_e and $\bar{\nu}_e$ reactions have been included:

Reactions	Currents	Main Role	Reference
$e^- + p \rightarrow n + \nu_e$	CC	P, T, O	[12]
$e^+ + n \rightarrow p + \bar{\nu}_e$	CC	P, T, O	[12]
$e^- + (A, Z) \rightarrow \nu_e + (A, Z-1)$	CC	P, T, O	[12]
$N + \nu \rightarrow N + \nu$	NC	O	[12]
$(A, Z) + \nu \rightarrow (A, Z) + \nu$	NC	O	[12]

Table 5.1: Table with the relevant reactions included in the MHD CCSN model. In the reactions column, N represents nucleons; ν and $\bar{\nu}$ both electron neutrinos and anti-neutrinos. In the current column, NC stands for neutral current, while CC for charged current reactions. In the Main Role column, P stands for production, T for thermalization and O for opacity.

Inside the neutrinosphere, weak equilibrium is assumed and trapped neutrinos are modeled accordingly; outside of it, no explicit absorption is considered. Thus we can only follow neutrino emission and the associated neutronization of matter. However, the up to now microphysically most complete two-dimensional axisymmetric study of MHD-CCSN with multi-group flux-limited diffusion neutrino transport performed by [19] has shown, that neutrino heating contributes only $10\% - 25\%$ to the explosion energy and is therefore subdominant. This justifies at first our pragmatic approach.
$\nu_{\mu,\tau}$ and $\bar{\nu}_{\mu,\tau}$ were not included in this simulation. This is due to the fact that the implemented ASL version (differently from the last one) contained only the electron flavor neutrinos. Due to the quick development of the jet, the importance of the additional cooling provided by $\nu_{\mu,\tau}$ and $\bar{\nu}_{\mu,\tau}$ can be considered negligible for our purposes. Nevertheless, a future inclusion is already planned.

We employed the pre-collapse $15M_\odot$ model of [52]. Although the model provides profiles for rotation and magnetic fields, we use an analytic prescription for their dis-

tributions, in order to verify good conditions for the developing of the jet. The initial rotation law was assumed to be shellular with $\Omega(r) = \Omega_0 R_0^2/(r^2 + R_0^2)$, $\Omega_0 = \pi$ s^{-1} and $R_0 = 1000$ km corresponding to an initial ratio of rotational energy to gravitational binding energy $T_{\rm rot}/|W| = 7.63 \times 10^{-3}$. For the magnetic field we have assumed a homogeneous distribution of a purely poloidal field throughout the computational domain of strength 5×10^{12} G corresponding to an initial ratio of magnetic energy to gravitational binding energy $T_{\rm mag}/|W| = 2.63 \times 10^{-8}$.

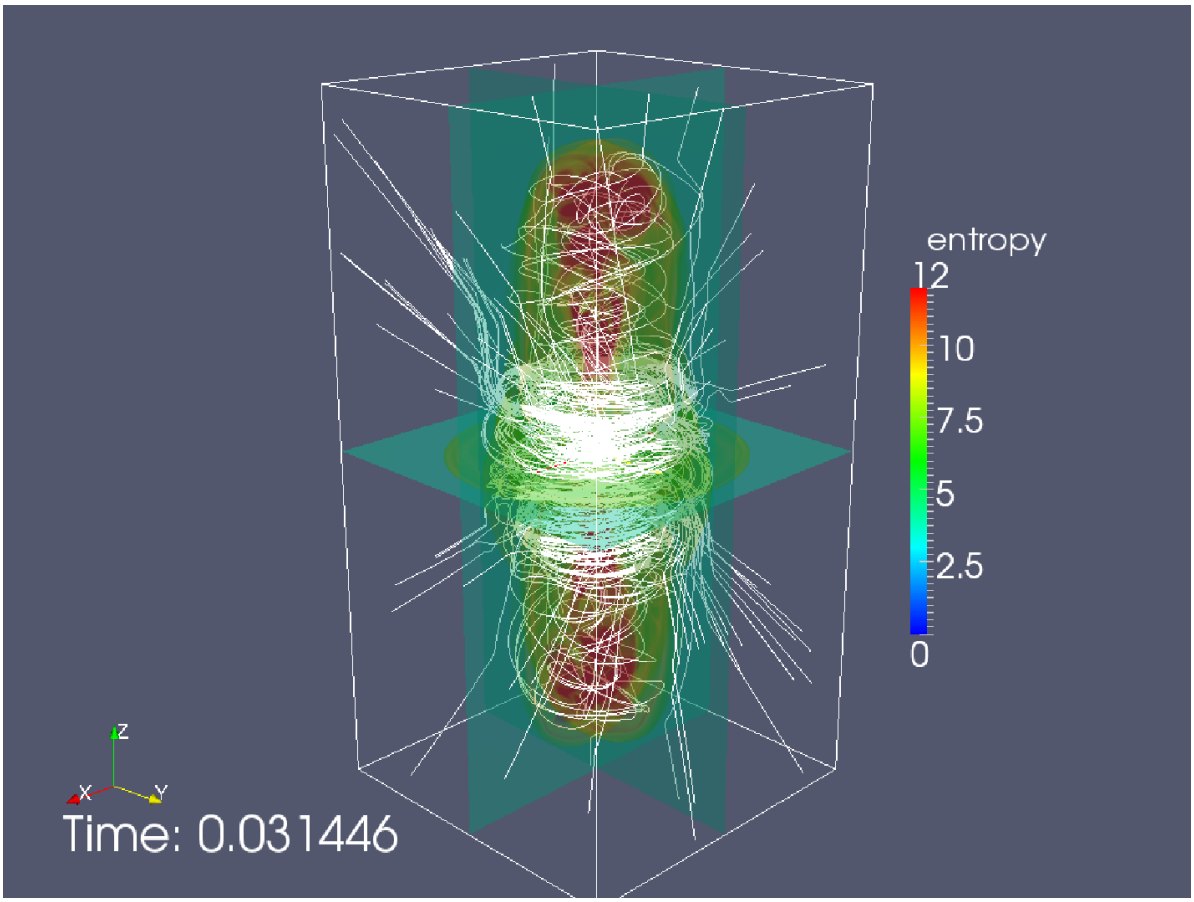

Figure 5.1: 3D entropy contours spanning the coordinates planes with magnetic field lines (white lines) of the MHD-CCSN simulation ~ 31 ms after bounce. The 3D domain size is $700 \times 700 \times 1400$ km (Courtesy of R. Käppeli).

The computed model then undergoes gravitational collapse and experiences core-bounce due to the stiffening of the EOS above nuclear saturation density. Conservation of angular momentum in combination with the collapse leads to a massive spin-up of the core, reaching $T_{\rm rot}/|W| = 6.81 \times 10^{-2}$ at bounce, and significant rotationally induced deformations. During the collapse the magnetic field is amplified by magnetic flux conservation reaching a central strength of $\sim 5 \times 10^{15}$ G and $T_{\rm mag}/|W| = 3.02 \times 10^{-4}$ at bounce. After bounce, differential rotation winds up the poloidal field very quickly into a very strong toroidal field increasing the magnetic energy/pressure at the expense of rotational energy. Consequently, strongly magnetized regions appear near the rotational axis with an associated magnetic pressure quickly reaching and exceeding that of the local gas pressure. The Lorentz force then becomes dynamically important and matter

near the rotational axis is lifted from the PNS and drives a bipolar outflow, i.e., jets are launched. The jets rapidly propagate along the rotational axis and quickly reach the boundary of the initial 3D domain. In order to follow the jet propagation further, we have continuously extended the 3D domain to a final size of $700 \times 700 \times 1400$ km at ~ 31 ms after bounce. Figure 5.1 displays a snapshot at the final time.

The quickly expanding bipolar jets transport energy and neutron rich material outward against the gravitational attraction of the PNS. We have estimated the ejected mass $M_{\rm ej} = 6.72 \times 10^{-3} M_\odot$ and explosion energy $E_{\rm exp} = 8.45 \times 10^{49}$ erg by summing over the fluid cells that are gravitationally unbound. We defined a fluid cell as unbound if its total specific energy (internal+kinetic+magnetic+potential) is positive and if the radial velocity is pointing outward. These are admittedly crude lower bound estimates and these numbers were still growing at the end of the simulation.

5.1.3 Electron fraction and neutrino quantities

The collapse proceeds as a standard core collapse. Electron neutrino luminosity rises, as the central density and temperature increase, up to neutrino trapping (when the central density reaches $\sim 10^{11}\,{\rm g/cm^3}$), just a few milliseconds before core bounce. Due to electron capture on protons and nuclei, the electron fraction in the core decreases, leading to the characteristic Y_e radial profile at bounce, with a central value of $Y_e(R=0) \approx 0.325$. Once the (almost spherical) shock wave has formed at the surface of the protoneutron star, it travels through the iron core, photodissociating and neutronizing matter. When the shock reaches the average neutrinosphere, a strong neutrino burst happens and the characteristic peak in ν_e luminosity appears. A few milliseconds after bounce, due to the large amount of energy dissipated, the shock stalls around ~ 120km. Already at this

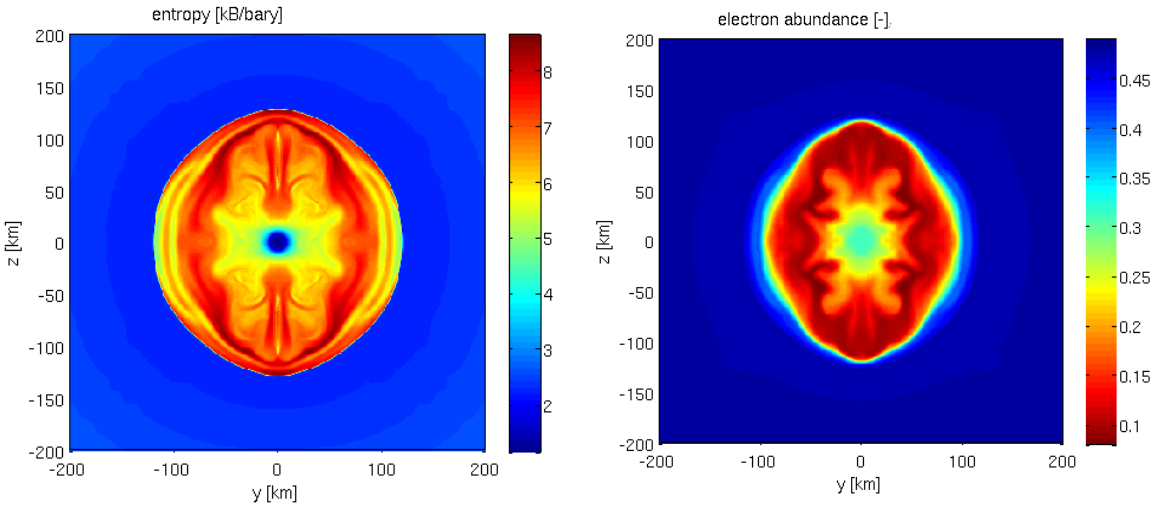

Figure 5.2: Vertical slices of the entropy (left panel) and of the electron fraction (right panel), 10 millisecond after bounce. The shock position can be recognized in the entropy panel, as well as the growth of instabilities and effects due to rotation and magnetic field. On the electron fraction picture, the neutronization inside the shock is visible, as well as the effect of multi-dimensional instability on it (Courtesy of R. Käppeli).

time, instabilities due to the strong rotation and to the intense magnetic fields introduce

some multi-dimensional effects. They can be seen, for example, in Figure 5.2. The shock position is easily recognized in the entropy graph (left panel); the strong rotation has already broken the spherical symmetry of the shock (which looks slightly oblated), and inside it instabilities and convection appear and grow. In the electron fraction plot (right panel), we can see the effect of the shock on the neutronization degree of matter, as well as the effect on it of multi-dimensional instabilities.

On longer timescale, the amplification and the winding of the magnetic field lines pro-

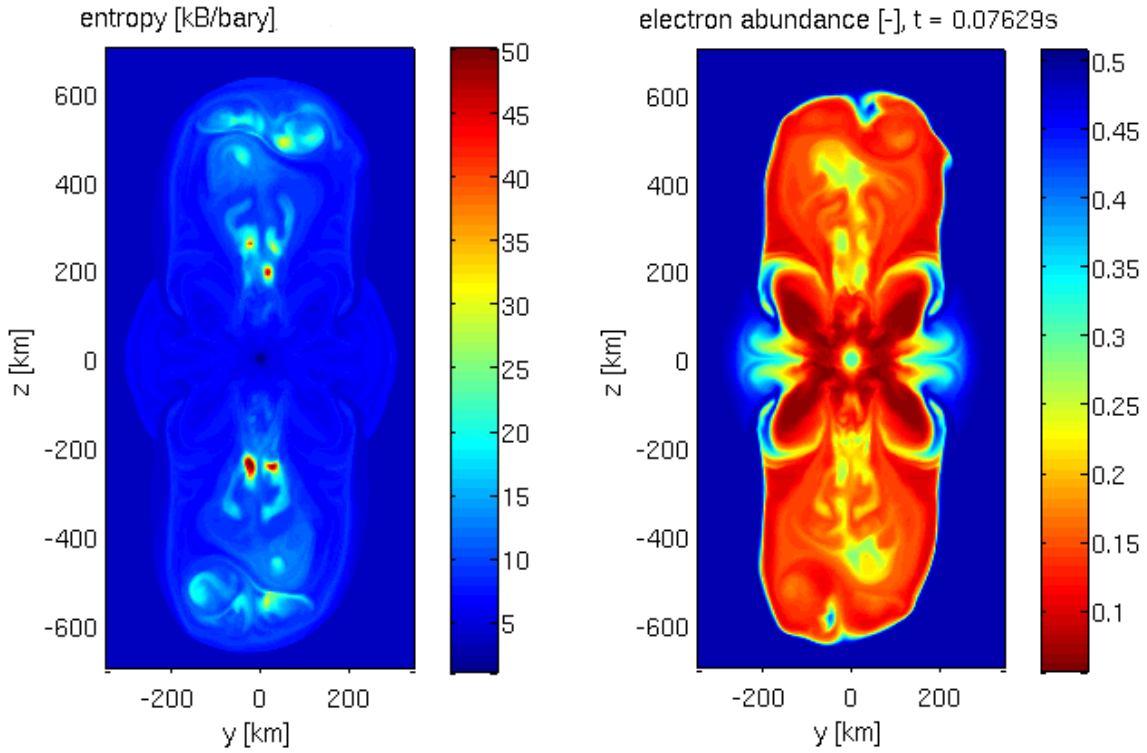

Figure 5.3: Same as in Figure 5.2, but 33 millisecond after bounce. The explosion has been launched by the formation of two strong magnetically driven jets. Matter in the jets keeps a relatively low entropy and electron fraction, provided by the initial shock expansion. Multi-dimensional effect are visible both on large and small scales (Courtesy of R. Käppeli).

duce two strong polar jets, which form inside the shock and break through it. In Figure 5.3, we present a vertical slice ($x = 0$) of the three dimensional data at $t \approx 33$ms, when the polar jets have formed and the explosion has been launched. Both in the entropy and in the Y_e profile, multi-dimensional effects due to the jet formation and expansion, as well as instabilities can be seen. Remarkably, the electron fraction of the matter expanding at the top of the jets has a very low, $Y_e \sim 0.17$, and a relatively low entropy $s \sim 12 k_{\rm B}$/baryon, which are very similar to the values obtained inside the shock by its first expansion. This is linked with the fact that the jets forms deep inside the shocked region, and matter expansion happens very fast (i.e, on very short timescales). We note also that all the scales (the spatial ones and the color coded ones) differ in the two plots.

In Figure 5.4, we plot the isotropized neutrino number luminosity (left panel) and the luminosity (right panel), for both electron neutrinos (solid lines) and electron antineutrinos (dashed lines), as a function of time. We choose three different rays (the magenta

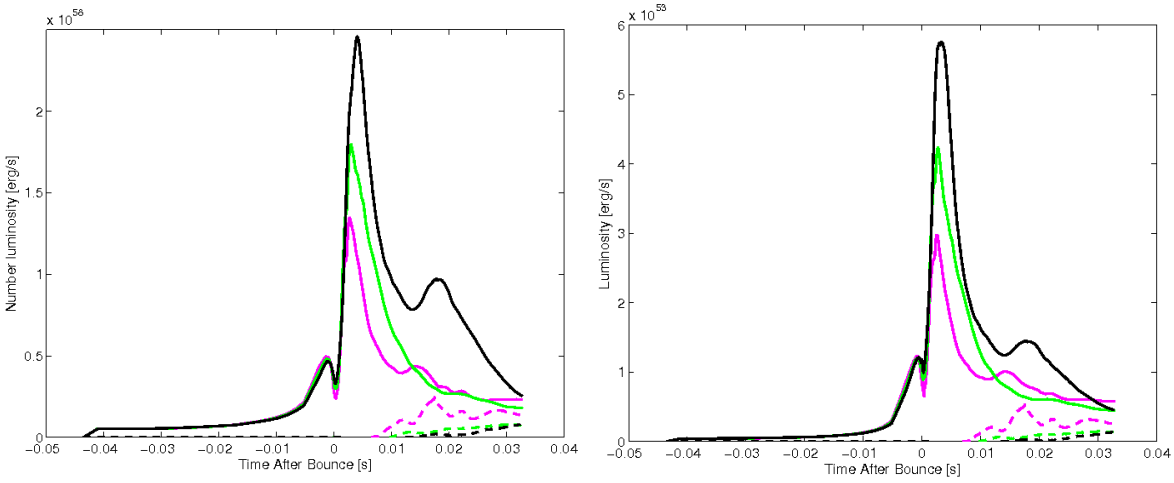

Figure 5.4: Temporal evolution of the ν_e (solid lines) and $\bar{\nu}_e$ (dashed lines) isotropized neutrino number luminosity (left panel) and luminosity (right panel), along three representative rays. The magenta lines correspond to $\theta = 0$ (i.e. along the pole), the black lines to $\theta = \pi/2$ (i.e. along the equator), while the green one is the middle ray, $\theta = \pi/4$ (Courtesy of R. Käppeli).

lines are along the polar direction,$\theta_i = 0$; the black lines along the equatorial direction, $\theta_i = \pi/2$, and the green lines in between, $\theta = \pi/4$), and we normalized them, in order to compare them (because different solid angles correspond to different rays):

$$L_{\rm norm}(\theta_i - \Delta\theta/2 < \theta < \theta_i + \Delta\theta/2) = \frac{L(\theta_i - \Delta\theta/2 < \theta < \theta_i + \Delta\theta/2)}{\cos(\theta_i - \Delta\theta/2) - \cos(\theta_i + \Delta\theta/2)}. \tag{5.1}$$

Overall, the three luminosity profiles look qualitatively similar, and consistent with what we expect from a typical CCSN model. We notice that the collapse proceeds in an almost symmetric way, because the different curves before bounce are very similar. Then, the luminosity decreases, due to neutrino trapping, and explodes in the neutrino burst a few milliseconds after it. The ν_e luminosity, integrated over the whole solid angle, shows a peak of $L_{\nu_e,\rm peak} \sim 5 \cdot 10^{53}$erg/s. A more detailed analysis reveals interesting differences between the different rays. For example, the shift in the neutrino burst moment, which happens earlier along the poles than along the equator. This is probably linked with the oblated density profile, due to the fast rotation of the core, which induces an oblated shape also in the shock position, in the neutrinospheres and, consequently, in the moment in which the shock breaks through them. The luminosity is also more intense in the equatorial region, up to the onset on the explosion. This is related with a much higher accretion rate along the equatorial direction, while along the poles matter accretion is partially halted by the faster rotation and by the formation of the jets. This hypothesis is confirmed by Figure 5.5, where it is possible to see how matter is preferentially accreted along the equator, due to the expanding jets. Matter passing polarity through the shock is redistributed at lower latitudines. The final decrease in luminosity (more pronounced in the equatorial plane) is due to the sudden decrease in the accretion rate, which happens when the explosion sets in and the shock expands in all directions. This is visible in Figure 5.6.

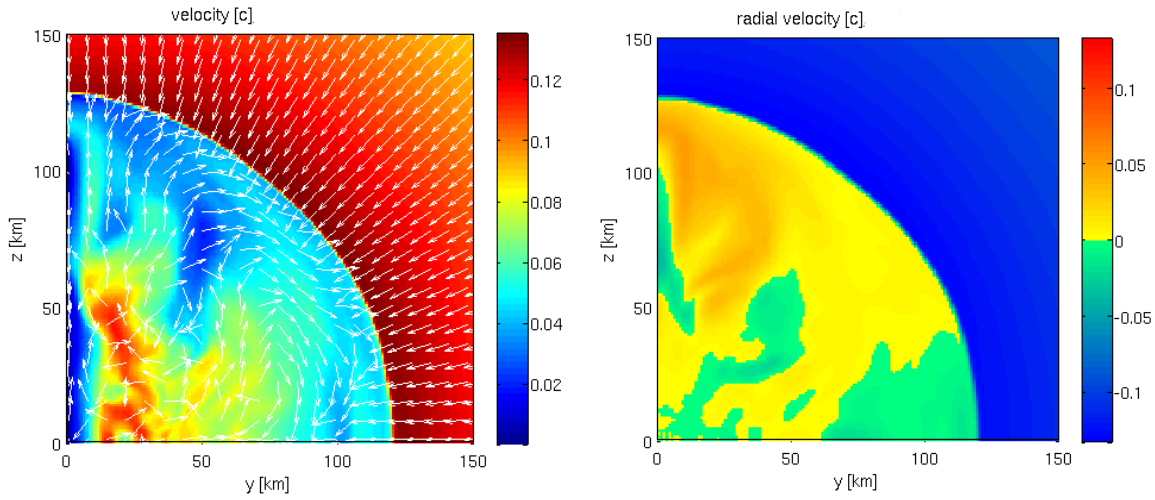

Figure 5.5: Vertical slices of the modulus and projected direction of the velocity (left panel), and of the radial velocity (right panel), 10 millisecond after bounce. It is possible to see the forming jets along the polar directions, and the consequent pattern in velocity, which trigger a larger accretion along the equatorial plane (Courtesy of R. Käppeli).

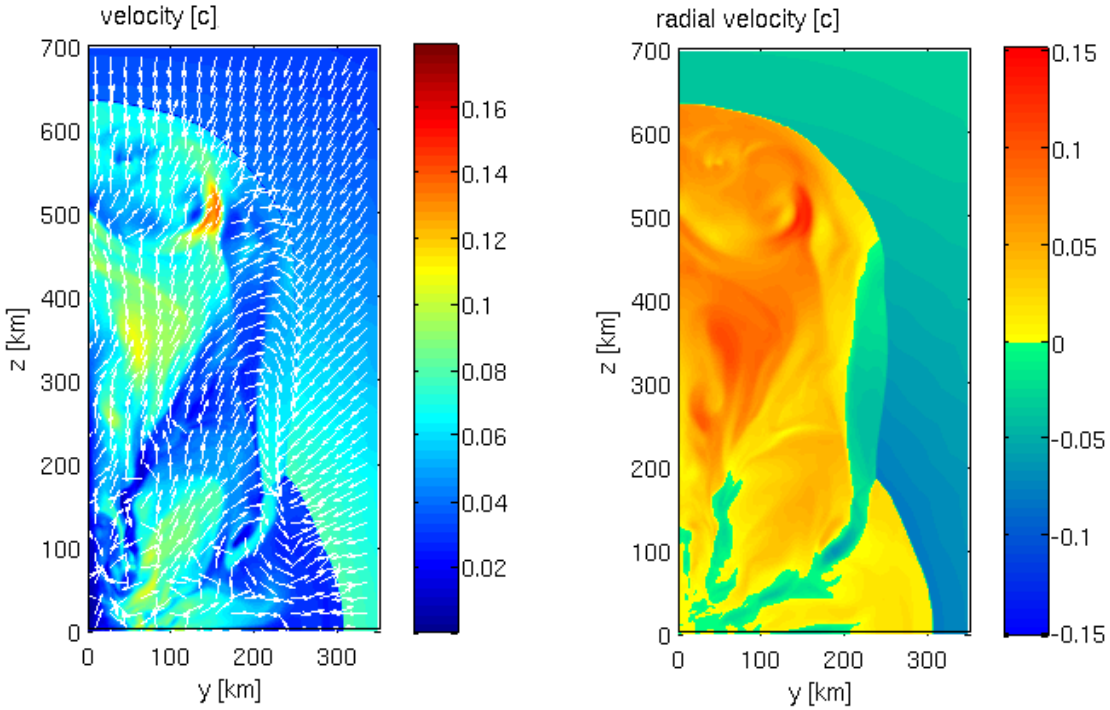

Figure 5.6: Vertical slices of the modulus and projected direction of the velocity (left panel), and of the radial velocity (right panel), 33 millisecond after bounce. After the formation and the expansion of the jets, the whole shock wave starts to expand, reducing the accretion on the protoneutron star. We can still notice streams of matter flowing inside, especially from intermediate latitudes. (Courtesy of R. Käppeli)

5.1.4 Nucleosynthesis

The nucleosynthesis calculations are performed with a new extended reaction network (Winteler, PhD thesis 2011) which represents an advanced (numerically and physically) update of the BasNet network (see, e.g., [160]). We use the reaction rates of [127, for the FRDM mass model]. We use the same weak interaction rates (electron/positron captures and β-decays) as in [3]. Additionally, we include neutron capture and neutron induced fission rates following [119] and β-delayed fission probabilities as described in [118].

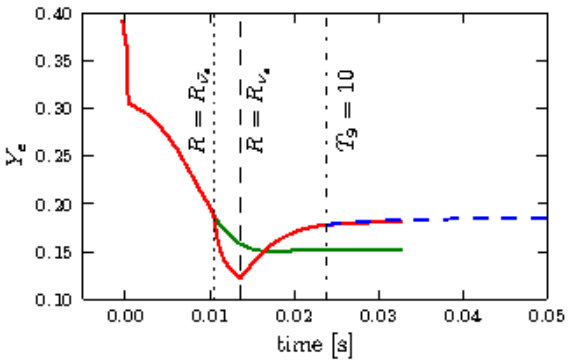

Figure 5.7: Time evolution of Y_e from a single tracer in green (red) for the original data (with neutrino absorption estimate). The blue dashed line represents Y_e evolved by the network. Vertical dotted (dashed) lines correspond to the time when $\bar{\nu}_e$ (ν_e) neutrinosphere is crossed; the dot-dashed vertical line when $T = 10\,\mathrm{GK}$ (Courtesy of C. Winteler).

The tracer particles obtained from the simulation provide density, temperature, and electron fraction for the nuclear network, as well as position and velocity, from the beginning to the end of the simulation ($t = t_f$). After t_f, thermodynamic variables are evolved following the prescription in [46]. [111] have shown that the details of the expansion only have a minor impact on the final abundances. For the post-processing we only consider gravitationally unbound tracer particles (see Section 5.1.2). In order to obtain mass integrated abundances we distribute the total ejected mass equally among all ejected tracers. It could be shown that this yields very similar results to post-processing calculations based on the conditions in the unbound cells at the final time (Winteler, PhD thesis 2011).

Equation (5.2) is applied as long as $T_{10} > 1$; below this temperature, an extended version of the network, including also neutrino reactions, is used. These weak reactions need the neutrino fluxes and the mean energies as input. Inside the simulation, these data are provided by the leakage scheme; in the tracer extrapolation, they are assumed to be constant and equal to the final values from the simulations.

The electron fraction is a key input for the nucleosynthesis and strongly depends on details of the challenging neutrino transport. In particular, neutrino absorption outside the neutrinosphere is crucial to determine the exact value of Y_e at the onset of the nucleosynthesis. Nevertheless, it is not yet included in the hydrodynamical simulations (where it is expected to have a minor impact on the dynamics), as pointed out in Section 5.1.2. Therefore, we present two different nucleosynthesis calculations: 1) Y_e is taken from

the original tracer particles and no neutrino interactions are included in the network, 2) the effects of the neutrino absorption on Y_e are estimated and neutrino reactions are included also in the network. In this second approach, we post-process the data from the tracers and we use the neutrino information obtained with the leakage scheme (Section 5.1.2).

The spectral neutrino luminosities (both for the energy and particle) are obtained as the radial integral of the local emission rates along the radial ray in which the tracer is located. Considering that the scheme does not take into account the thermalization process occurring to high energy neutrinos coming from the deepest part of the star, we reduce the local emission rates by an exponential factor of the optical depth, $\exp(-\tau/\beta)$, where β is a free parameter which has been set to 25 after comparing the output of spherically symmetric simulations with detailed Boltzmann transport and with our leakage scheme. In this approximation, we use integrated neutrino luminosities and we update only the electron fraction (i.e. neglecting the effect of neutrino energy deposition on the matter temperature) outside the neutrinosphere. The ratio between the energy- and particle-luminosities provides a good estimation of the mean neutrino energy, which is typically higher for anti-neutrinos ($\langle E_{\bar{\nu},e}\rangle \sim 10$MeV) than for neutrinos ($\langle E_{\bar{\nu}_e}\rangle \sim 8$MeV). The different opacities and mean energies lead to a larger neutrinosphere for ν_e (~ 70km) than for $\bar{\nu}_e$ (~ 60km). The electron fraction of the tracer is evolved considering neutrino emission and absorption on nucleons. If λ_{n,e^+} (λ_{p,e^-}) is the rate of $\bar{\nu}_e$ (ν_e) emission from neutrons (protons) and λ_{n,ν_e} ($\lambda_{p,\bar{\nu}_e}$) the rate of ν_e ($\bar{\nu}_e$) absorption on neutrons (protons), Y_e changes according to (see e.g. [59]):

$$\begin{aligned}\dot{Y}_e = {} & Y_n\lambda_{n,e^+} - Y_p\lambda_{p,e^-} + Y_n\lambda_{n,\nu_e} - Y_p\lambda_{p,\bar{\nu}_e} \approx \\ & 9.12\cdot 10^{-3}\, T_{10}^5\left((1-Y_e)F_4(-\eta_e) - Y_e F_4(\eta_e)\right) + \\ & 2.31\, r_7^{-2}\left((1-Y_e)\frac{\langle E_{\nu_e}\rangle L_{\nu_e,52}}{\langle \mu_{\nu_e}\rangle} - Y_e\frac{\langle E_{\bar{\nu}_e}\rangle L_{\bar{\nu}_e,52}}{\langle \mu_{\bar{\nu}_e}\rangle}\right)\end{aligned} \tag{5.2}$$

where T_{10} is the temperature in units of 10^{10}K, F_k the Fermi integral of order k, η_e the electron degeneracy parameter, r_7 the tracer radius in unity of 10^7cm, $\langle E_\nu\rangle$ the mean energy in MeV,$\langle \mu_\nu\rangle$ the neutrino flux factor [163, 59]. $L_{\nu_e,52}$ ($L_{\bar{\nu}_e,52}$), defined as the (anti-)neutrino luminosity in units of 10^{52}erg/s, are set to zero inside the neutrinospheres; outside, they smoothly increase to their full values on a lenghtscale of ~ 10 km.

In both approaches, the network calculations start when the temperature decreases to 10^{10} K. In the second one, equation (5.2) is applied as long as $T_{10} > 1$; below this temperature, neutrino capture cross sections on nucleons/nuclei are included also in the network [43]. These reactions require neutrino fluxes and mean neutrino energies. In the simulation, these quantities are provided by the leakage scheme; in the tracer extrapolation, they are assumed to be constant and equal to the values at $t = t_f$. Therefore, the decrease in the reaction rates is then solely given by their $R(t)^{-2}$ dependence.

The evolution of Y_e is presented in Figure 5.7 for the original simulation data and for the estimate of neutrino absorption. In the latter, high energy $\bar{\nu}_e$ captures on protons decrease Y_e outside the $\bar{\nu}_e$-neutrinosphere. However, beyond the ν_e-neutrinosphere, ν_e absorption on neutrons dominates and Y_e increases. The fast expansion and the relatively low neutrino mean energy limit the effect of the absorption. This trend is confirmed also by the network for $T \lesssim 10$ GK.

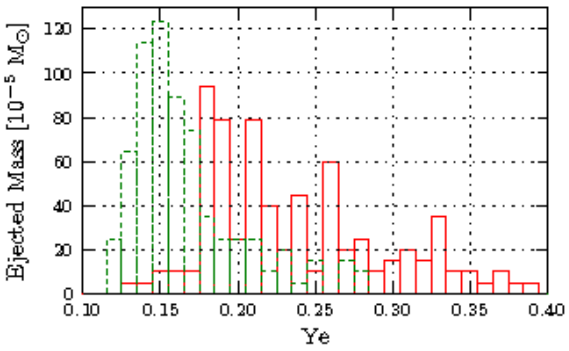

Figure 5.8: Ejecta masses vs. Y_e for the original simulation without neutrino captures (green) and including a simplified prescription for neutrino heating (red). The width of a Y_e bin is chosen to be $\Delta Y_e = 0.01$ (Courtesy of C. Winteler).

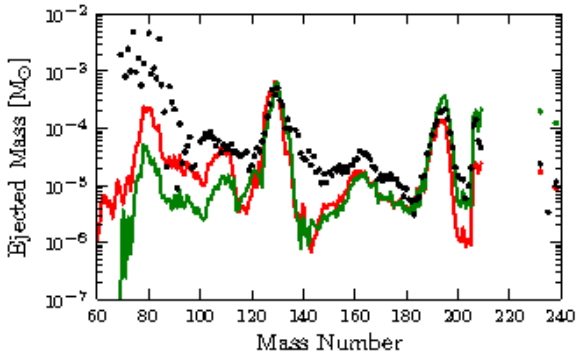

Figure 5.9: Integrated mass fractions for nucleosynthesis calculations with (red)and without (green) neutrino heating. Black dots represent solar r-process element abundances [153] scaled to fit the red line at $A = 130$ (Courtesy of C. Winteler).

Figure 5.8 shows the ejected mass as a function of Y_e for the original simulation data and for the case including neutrino absorption. These corrections shift the peak distribution from ~ 0.15 to ~ 0.17 and broaden it toward higher Y_e. In both approaches, at the onset of the nucleosynthesis, the density is still relatively high, $\rho \approx 10^9 \mathrm{gcm}^{-3}$, and the electron fraction rather low, $Y_e \approx 0.15 - -0.3$. This leads to an initial nuclear statistical equilibrium composition rich in neutrons and neutron-rich nuclei. Such conditions are closer to neutron star mergers than to the high entropy wind, which is characterized by an alpha-rich freeze-out with few nuclei close to stability and small amount of neutrons.

Mass integrated abundances are presented in Figure 5.9 for the two treatments of the electron fraction and compared to solar r-process abundances (e.g., [153]). Nuclei around the second ($A = 130$) and third ($A = 195$) r-process peaks, as well as the Pb region, can be synthesized in the jets. Note that the improvements in the electron fraction calculation result only in minor variations of the abundances. Moreover, the position of the peaks nicely agrees with solar system abundances. However, the agreement is not equally good for all mass numbers as the nuclei between peaks are slightly under-produced. Note also that the large trough in the mass range $140 - -160$ is mainly due to the strong $N = 82$ shell-closure of the FRDM mass model. Similar deficiencies were discussed by [111] and can be cured by using a different mass model. Nuclei in the region below the second

peak are produced mainly by charged-particle reactions which occur only in the tracer particles with relatively high electron fraction. This also explains the lower abundances in the range $A = 80 - 100$ for the case of Y_e without neutrino absorption (Figure 5.9). This calculation reaches lower Y_e which leads to higher neutron densities and a more abundant third peak and Pb region.

5.1.5 Discussion and Outlook

Magneto-rotationally driven supernovae suffer one main critique point: the simultaneous presence of fast rotation and strong magnetic fields in the progenitor before collapse. Recent progenitor models computed by [52] suggest that these special conditions are not reached in common evolutionary paths of massive stars. However, the low-metallicity models of [169] indicate that for a fraction, perhaps 1%, of all massive stars, favorable conditions can appear under special circumstances. This rarity of progenitors with these special initial conditions can also be put into accordance with the observed scatter of r-process element abundances at low metallicity, combined with the high r-process production of $\sim 6 \times 10^{-3}\, M_\odot$ per event. This indicates that these elements have been produced in relatively scarce but efficient events [153]. Therefore, the rare progenitor configurations used here could naturally provide a strong r-process site in agreement with observations of the early galaxy chemical evolution.

Currently, the aim to perform long-term global 3D simulations of CCSNe, including possibly a sophisticated radiative transfer of neutrinos, and the aim to simulate the local flow instabilities, leading to magnetic field amplification, seem to be mutually exclusive [113]. Given this difficulty, we followed here the common approach in the literature by taking sufficiently strong initial magnetic fields. By doing so, it is hypothesized that there is a physical process that can sufficiently quickly amplify the magnetic field to dynamic importance by extracting the free rotational energy in differential rotation. This motivates our choice of the high initial poloidal field strength, which by flux compression and rotational winding leads to magnetic fields whose magnitude roughly agree with those expected from the magnetorotational instability at saturation [113].

There are additional shortcomings in the treatment presented here. This includes that thermodynamic properties of tracer particles are only extrapolated beyond the end of the MHD calculation and the nucleosynthesis results were not yet tested with several nuclear mass models. But the main outcome of this investigation is that full 3D calculations can support the emergence of bipolar jets and that these are not artifacts of up to now axisymmetric approaches [111, 46]. Such explosions, resulting from the individual evolution of massive stars rather than complicated binary histories of neutron star mergers, could explain strong r-process features during early galactic evolution as observed in many low metallicity stars. The r-process production is very efficient, a factor of 100 more than expected on average from supernovae, if they would be responsible for solar r-process abundances. The question remains: whether magnetars — with the magnetic fields required for this outcome — result from about 1% of all core collapses or are rarer events. Apparently present knowledge permits this option [68].

The magnetorotationally driven supernova simulation presented here provides a scenario for a strong r-process site seemingly consistent with observations of the early chemical evolution of our Galaxy.

5.2 3D core collapse supernova simulations with SPHYNX & ASL

The numerical implementation of fluid dynamics has been typically treated within a grid, where the physical magnitudes are evaluated through the flux balance between adjacent cells, and their derivatives calculated using finite difference methods. The FISH code, which has been used in this work to study the aftermath of neutron star mergers and magneto-rotationally driven supernovae is actually a Cartesian grid code.
Nevertheless, many astrophysical scenarios have physical magnitudes ranging within several orders of magnitude, which demands a high adaptive behavior of the codes. Moreover, they usually develop highly-deformed asymmetric geometries that can pose a problem for Eulerian methods, adaptive or not, due to the numerical diffusion induced by the advective term. Such difficulty can be overcome using a grid that evolves with the fluid, i.e. a Lagrangian description where the advective term disappears. In this respect, an interesting choice when having distorted geometries is to switch from grids and use a particle (purely Lagrangian) method, where the mesh is replaced by a set of interpolation points that follow the fluid. The Smoothed Particle Hydrodynamics technique (widely known as SPH) belongs to this last group.

In this section, we will present the first results of simulations of core collapsing stellar core, performed with an SPH code, denominated SPHYNX and developed by Ruben Cabezon. For extensive reviews on the SPH technique we refer to [104] and, more recently, to [105] and [135]. The hydrodynamical evolution is coupled with a three dimensional neutrino treatment, based on the ASL scheme. It includes all the cooling part, but not the heating one, very similarly to what has been presented in the MHD simulation of the previous section. From the hydrodynamical scheme, we know that from the position of the SPH particles we can compute the local density and internal energy:

$$(\rho_i, u_i)_{\text{SPH}} \tag{5.3}$$

We add to each particle also information about the chemical composition, introducing the electron fraction, Y_e:

$$(\rho_i, u_i, Y_{e,i})_{\text{SPH}} \tag{5.4}$$

Assuming a NSE equation of state (which is here Lattimer-Swesty EOS), from the new set of SPH quantities, we can derive the nuclear composition provided by the EOS itself (neutrons, protons, alpha particles and a representative nucleus). In order to model neutrinos according to the ASL treatment, we add to the each particle also the neutrino abundances and the related neutrino energy, representing the neutrino trapped component, for each of the relevant neutrino species ($k = \nu_e, \bar{\nu}_e, \nu_{\mu,\tau}$). In this way, the full set of SPH quantities becomes

$$(\rho_i, u_i, Y_{e,i}, Y_{\nu_k,i}, Z_{\nu_k,i})_{\text{SPH+ASL}} \tag{5.5}$$

The goal of the treatment is to calculate the neutrino source terms, which then enter the hydrodynamics equations, and to evolve the abundances associated to each particle. From the neutrino treatment, the quantities that we calculate are:

$$\left(\dot{Y}_{e,i}, \dot{u}_i, \dot{Y}_{\nu_k,i}, \dot{Z}_{\nu_k,i}\right)_{\text{leak out}} \tag{5.6}$$

The internal energy variation for the fluid is considered as a source term in the energy equation. The electron fraction of each particle (and similarly the neutrino abundances and neutrino energies) is evolved explicitly, according to

$$Y_{e,i}(t + \mathrm{d}t) \approx Y_{e,i}(t) + \dot{Y}_{e,i}(t)\mathrm{d}t \tag{5.7}$$

The energy density provided by the neutrino radiation field (ρZ_ν) gives an extra contribution to the fluid pressure:

$$P_{\mathrm{tot}} = P_{\mathrm{gas}} + \frac{1}{3}\frac{\rho}{m_b}\sum_k Z_{\nu_k} \tag{5.8}$$

Because of this, in the momentum and energy equations we use the total pressure P_{tot}, instead of the only gas pressure P_{gas}. This inclusion should take into account the neutrino stress, which was explicitly calculated in the general ASL presentation.

Most of the quantities which are needed to compute these source terms are local, so the implementation in the SPH structure was straightforward and required no modification in the algorithm. The only non-local quantity which was implemented was the spectral optical depth: $\tau_{\nu,\mathrm{cl}}(\mathbf{x}, E)$ and $\tau_{\nu,\mathrm{eff}}(\mathbf{x}, E)$. To compute it in a simple way, we used the expected quasi-spherical symmetry of a collapsing stellar core: we defined a one dimensional radial grid, and on this grid we calculated the spherical averages of the neutrino spectral mean free paths (which was computed locally, at each SPH particle), directly from the SPH data. Then, we integrated $1/\lambda(R, E)$ radially, from the external edge up to each radial position, according to (2.99), to obtain the radial optical depth. Finally, the spherically symmetric optical depth was mapped back on the three dimensional SPH particles, interpolating with respect to the distance from the center of mass. To discretized the energy spectrum, we used 20 energy bins in the range $3\,\mathrm{MeV} \leq E \leq 300\,\mathrm{MeV}$, as we did in the spherically symmetric CCSN models. All the reactions listed in chapter 2 have been included.

5.2.1 Results

As a first test for the SPHYNX code with the ASL neutrino treatment, we set up a CCSN SPH simulation with 500,000 particles, using Newtonian gravity. We take a $15M_\odot$ spherically symmetric progenitor model from [52] that we map into a three dimensional quasi-random Sobolev distribution of equal mass particles. This are the initial conditions of the SPH simulation. We simulate $\sim 1.65M_\odot$ of mass, corresponding to the whole iron core and to a fraction of the silicon shell, up to $2,000\,\mathrm{km}$ in radius, and we run the simulation including all neutrino flavors (ν_e, $\bar{\nu}_e$ and $\nu_{\mu,\tau}$). Qualitatively, the dynamics of the collapse and of the early postbounce phase are the ones expected. The collapse proceed increasingly fast, raising the central density and temperature, and deleptonizing matter through electron captures on protons and nuclei. The produced neutrinos are initially emitted almost freely. After neutrino trapping, the core deleptonization stops and a gas of ν_e forms. The electron fraction decreases further and reaches $Y_e \sim 0.32$. When the central density becomes $\sim 4 \cdot 10^{14}\mathrm{g/cm}^3$, the core bounces and a shock wave forms at the surface of the newly born protoneutron star. The shocks moves out, traveling through the iron core, photodisintegrating matter and further deleptonizing it. We studied the expansion of the shock wave up to $\sim 100\,\mathrm{ms}$ after bounce, when the shock has reached

a distance of $\sim$ 160km.

In Figure 5.10, we can see the radial profiles of density (left column), electron fraction

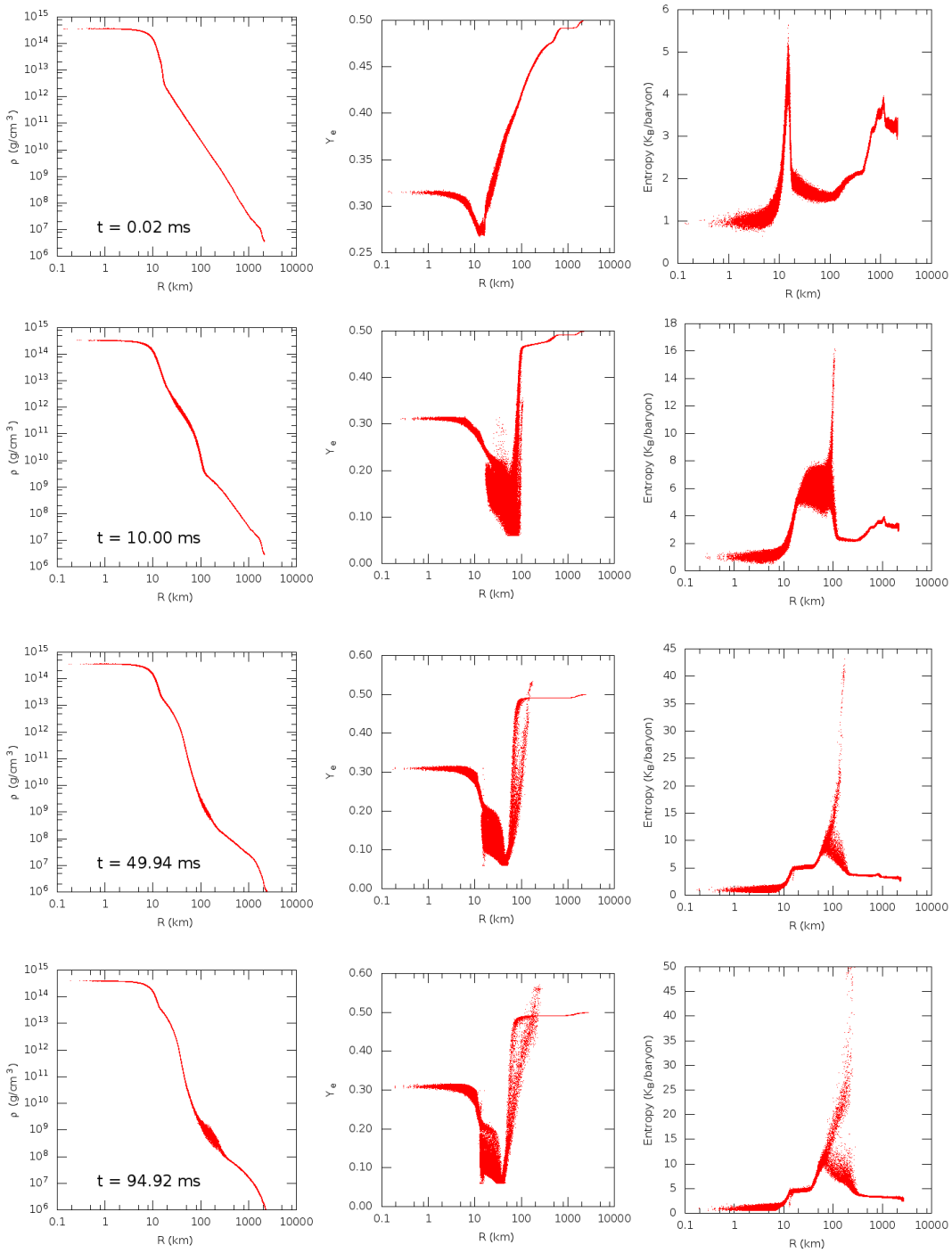

Figure 5.10: Radial profiles of density (left panels), electron fraction (central panels) and entropy, obtained directly from the SPH CCSN model fo a $15M_\odot$ progenitor model. Each red point correspond to a SPH particles. Four different simulation times are presented ranging from bounce up to $t_{\rm pb} \approx 95\,$ms (Courtesy of R. Cabezon).

(central column) and entropy (right column), at four different times: in the first row, we visualize results at bounce; in the second row, ten milliseconds after; then at fifty (third

row) and one hundred milliseconds (forth row). Each point in the panels represents one of the SPH particles. From the profiles at bounce, we can see that the collapse keeps a good spherical symmetry, as expected. We notice the position of the shock wave from the entropy spike and from the corresponding starting deleptonization in the Y_e profile. As the shock proceeds, multidimensional effects and inhomogeneities start to appear and to grow, especially inside the shocked material. This effect can be seen from the spread particles in the Y_e and entropy profiles. At the shock position, we notice that there is a strong increase in the entropy of a small amount of particles increase their entropy. We are currently investigating this aspect, and we think that it is linked with the form of the artificial viscosity, that it is not able to prevent certain particles to "surf" behind the shock front. As a consequence, they suffer of an extended period of shock heating. The corresponding increase in temperature induces larger neutrino emission rates and, consequently, lower electron fractions. However, even if we neglect these features, we can clearly see how perturbations and instabilities grow and affect the dynamics of matter inside the shock wave. Even the shape and the propagation of the shock break the spherical symmetry. This effect can be seen, for example, in the density radial profile, at the end of the simulation: the dispersion in density, corresponding to the shock position, has an extended range, that spans more than 50km.

The shape and the evolution of multidimensional instabilities can be better seen in Figure 5.11. In this figure, we project all the particles included in a thin layer of 20 km around the equatorial plane ($z = 0$), on a xy plane, of 200 km side. The physical quantities, which are color coded, are the temperature (left upper quadrant), the logarithm of the density (right upper quadrant), the electron fraction (left lower quadrant) and the entropy (right lower quadrant). For the first plot (upper left panel), we choose $t \approx 1.58$ms after bounce, instead of exactly bounce, to visualize the very beginning of hydrodynamical instabilities. In the second plot, we can see turbulences inside the protoneutron star and at the shock front (which is still visible): matter infalling radially reduces its free fall speed and form non-radial and non-symmetric flows towards the central compact object. In the lower two panels, all the represented particles are inside the shock; we can see large convective modes and flows of particles coming from the shock front and accreting on the protoneutron star. In Figure 5.12 we can see the temporal evolution of the total neutrino luminosities, directly calculated during the simulation with the ASL scheme. The obtained results agree with our expectations. We can distinguish all the relevant expected features: the luminosity rise during the collapse, the effect of neutrino trapping just before bounce; the neutrino burst a few milliseconds after bounce, where L_{ν_e} peaks at $\sim 6.5 \cdot 10^{53}$erg/s, and the decrease to an almost stationary value ($\sim 0.9 \cdot 10^{53}$erg/s) during the accretion phase. Regarding electron antineutrinos, $L_{\bar{\nu}_e}$ rises, as expected, after bounce, and, on a short timescale (~ 0.02s), it reaches an almost stationary value, similar to the one of ν_e luminosity. After bounce $\nu_{\mu,\tau}$ luminosity increases as well. Even if it rises slightly before the electron antineutrino one, it keeps a lower value during the accretion phase. This is due to the fact that electron flavor neutrino luminosities come mainly from charged current reactions on the shock accreting matter (mostly free protons and neutrons), while $\nu_{\mu,\tau}$ are produced by neutral weak current processes, converting thermal energy in neutrino pairs of all kinds. Other features which look already interesting and which deserve a deeper investigation in the future, are the oscillation in the luminosities: they appear in all three curves and they may be related with oscilla-

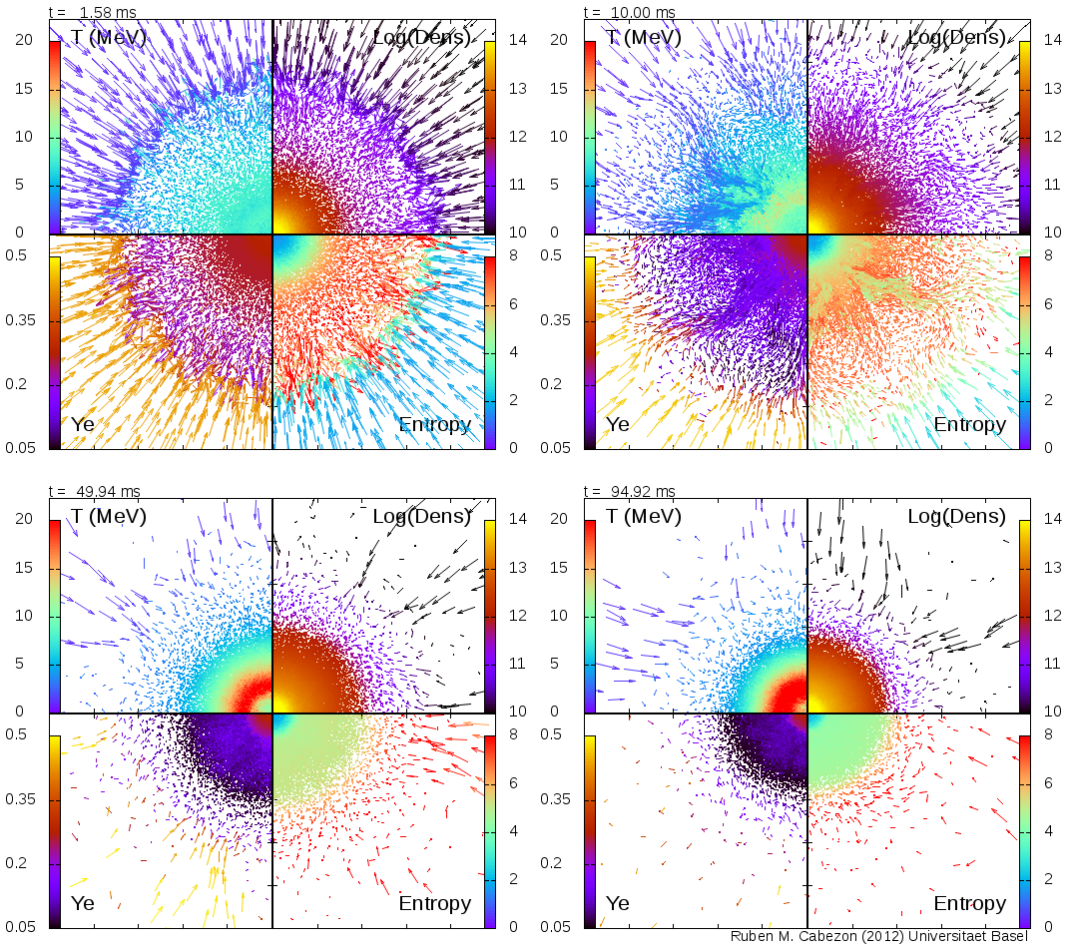

Figure 5.11: In this figure, we plot a projection on the xy plane of the SPH particles included in a thin layer of 20 km across the $z = 0$ plane. Four relevant quantities (starting from the upper left quadrant and proceeding in the clockwise direction, temperature, density, entropy and electron fraction) are color coded. We choose the same moments we used for the figure 5.10, with the exception of the first one, which was take not exactly at bounce, but 1.58 ms after it. Several multidimensional effects (like convection and matter streams) can be seen already after bounce, inside the shock, before growing and expanding on larger scales (Courtesy of R. Cabezon).

tions of the protoneutron star and/or with variations in the accretion rate induce by multi-dimensional effects.

A full comparison with a corresponding `AGILE-BOLZTRAN` calculation has not been done yet. Nevertheless, from a broad comparison with a similar model, we notice a good quantitative agreement, even if the deleptonization inside the shock wave is more effective here, enhancing slightly the luminosities.

5.2.2 Discussion and outlook

With respect to grids codes, SPH hydrodynamical schemes present an adaptive resolution, which follows directly (i.e., by construction) the matter density profile. In our

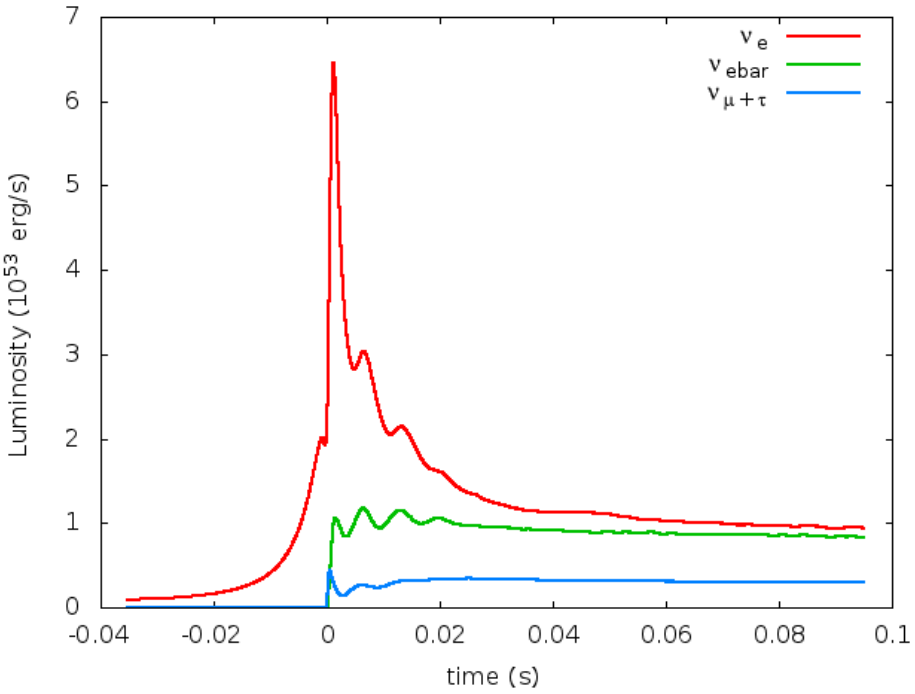

Figure 5.12: Temporal evolution of the neutrino luminosities, obtained from the SPH CCSN model with the ASL neutrino treatment, for all the three modeled neutrino species: ν_e (red line), $\bar{\nu}_e$ (green line) and $\nu_{\mu,\tau}$ (blue line) (Courtesy of R. Cabezon).

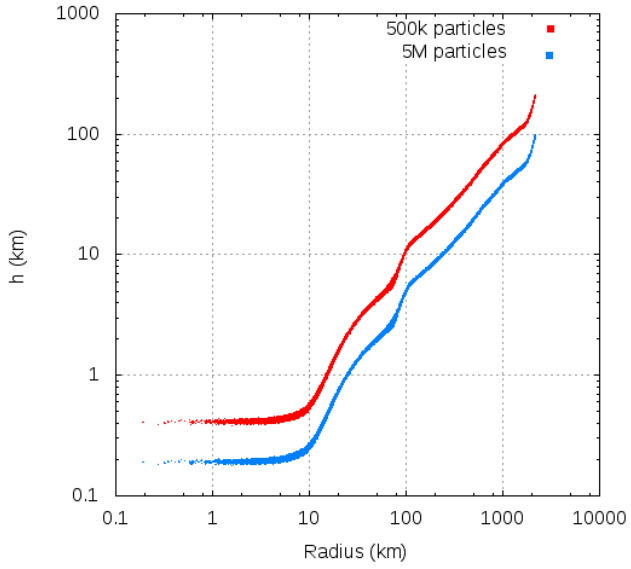

Figure 5.13: Smoothing length h from the core collapse SPH model, as a function of the radial position from the center. The red points correspond to the data taken from the SPH simulation with 500k particles. The blue points are the expected ones for a simulation with 5 millions particles; they are scaled from the red ones, according to $h_{5\mathrm{M}} = h_{500\mathrm{k}}/10^{1/3}$ (Courtesy of R. Cabezon).

models, this behavior can be seen in Figure 5.13, where we plot the smoothing length obtained from one simulation (the one with 500k particles, red points) as a function

of the radial coordinate, and the expected smoothing length from a model with 10 times more particles (5M particles, blue points), obtained from the previous ones as $h_{5M} = h_{500k}/10^{1/3}$. It is clear that most of the resolution is focused on the forming PNS, while the outer part of the system have a fast decreasing resolution. This simple consideration is one of the major arguments against the usage of SPH codes to explore CCSN models: if the shock looses rapidly resolution when it proceeds from the inner to the outer part of the domain, it is difficult to model with accuracy the physics of the shock and of its expansion. Assuming a fix density profile, a significant increase in resolution at large radii needs a very large increase in the number of particles, due to the fact that most of the particles will always sit in the forming PNS. Nevertheless, SPH has been widely used in CCSN models (see, for example, [45] and references therein). On the other hand, the same argument guarantees that the central object is the better resolved part of the simulation. Thus, this model seems to be naturally well suited to study the formation and the very early evolution of the PNS. For example, such an extreme resolution allows to study in details the oscillations of the newly born NS and their impact on the neutrino luminosities. Moreover, it could allow the investigation of convection inside the PNS in three dimensions, with very high spatial resolution (see, for example, [64, 100, 101, 14]) and with respect to the EOS used [131]. The conservation of linear momentum, angular momentum and energy, which is guarateed by SPH codes is another very strong point, which favors the inclusion of rotation and (eventually) magnetic field in the models, to study their impact on the neutrino emission and on the properties and dynamics of the PNS. Finally, the dynamics and the interaction of the PNS with the shock accreting matter in three dimensions could be studied, to find connections with the generation of NS spins and kicks.

5.3 Spherically symmetric supernova explosion with PUSH

Self-consistent models of spherically symmetric core collapse supernova, with detailed neutrino transport and General Relativity do not produce explosions (see, for example, [86]). However, spherically symmetric models of exploding stars are, at the moment, the easiest and almost the only possible way to study the expansion of the shock wave in the outer layer of the star, for a large sample of initial models (varying, for example, metallicity and mass of the progenitor star). The major goals of these simulations are 1) the extraction of important information about the thermodynamical properties of the expanding matter, after the passage of the shock wave. They are necessary to calculate the explosive nucleosynthesis and the composition of the ejected material (see, for example, [126, 43, 2]); 2) the study of the connection between the progenitor stars and the supernova remnants (BH or NS; see for recent examples [114, 167]).
Historically speaking, the explosion of the star has been artificially caused in different ways:

1. by thermonuclear bombs; this method consists in injecting a certain amount of internal energy, at a chosen position and at a certain time after bounce, increasing locally the matter temperature. If the injection is large enough, the added pressure is able to push matter away and, finally, trigger an explosion (see, for example,

[161]);

2. by piston models, in which a piston is placed at a chosen position in the star model (pre or post bounce) and moved, according to a certain velocity prescription. This prescription mimics first the free fall of the mass element, and later the explosive expansion of the formed Supernova shock (e.g. [179, 180]);

3. by modifications of the neutrino absorption rates, which are usually increased by a factor in the range $5 - 8$ (e.g.[43, 37]);

4. imposing a boundary condition in the innermost part of the simulation, which consists in the removal of the PNS and in the imposition of an analytical prescription for the neutrino luminosity. Allowing neutrinos to be re-absorbed behind the shock, specific choices of neutrino luminosities and spectra at the inner boundary can trigger an explosion (e.g. [146, 2, 167]).

In the following, we will present a new method, called PUSH, which avoids some of the drawbacks of the methods that have been used up to know. In particular, it allows the possibility for a fraction of the neutrino luminosity emitted as ν_μ, $\bar{\nu}_\mu$, ν_τ and $\bar{\nu}_\tau$, to be re-absorbed by the fluid, behind the shock. This extra-deposition of energy can trigger an explosion. Physically, we do not expect $\nu_{\mu,\tau}$ neutrinos to be re-absorbed (at least, considering only standard neutrino processes). Their luminosity is just considered as an energy resevoir, which can locally increase the energy gained by the fluid, absorbing ν_e and $\bar{\nu}_e$ neutrinos. Differently from other methods, the intensity of the used luminosity ($L_{\nu_{\mu,\tau}}$) is directly obtained from the dynamics of the system and, in particular, of the hot PNS.
Comparing in more details with the previous methods,

1. there are no external injections of energy;

2. there is no super-imposed motion of specific mass elements;

3. there are no alterations of the reactions rates regarding ν_e and $\bar{\nu}_e$, which are crucial to obtain a correct Y_e;

4. there is no need of internal boundary conditions and controlled neutrino luminosities at this boundary.

Nevertheless, we stress that this method is as artificial as the other, because it triggers an explosion adding an element which should not be included in the simulation.

5.3.1 Description of the model

We set up a spherically symmetric core collapse supernova model, using the code `AGILE-IDSA` [88]. This code has already been introduced in Chapter 2: `AGILE` is an adaptive mesh, general relavitistic, spherically symmetric hydrodynamical code. IDSA is an approximated spectral transport scheme for ν_e and $\bar{\nu}_e$. The publicly available version of this code includes the possibility to take into account the cooling provided by $\nu_{\mu,\tau}$, using the grey leakage scheme described in Chapter 2. We modified this version, including also the ASL treatment to model $\nu_{\mu,\tau}$. This modification was done mainly to retain spectral

information about the luminosity of these neutrinos, which is an essential ingredient for PUSH.
In table 5.2 and 5.3 we report the neutrino reactions which have been included and the values of the free parameteres of the ASL treatment we are typically using.

Reactions	Currents	Main Role	ν treatment	Reference
$e^- + p \rightarrow n + \nu_e$	CC	P, T, O	IDSA	[12]
$e^+ + n \rightarrow p + \bar{\nu}_e$	CC	P, T, O	IDSA	[12]
$e^- + (A, Z) \rightarrow \nu_e + (A, Z-1)$	CC	P, T, O	IDSA	[12]
$N + \nu \rightarrow N + \nu$	NC	O	IDSA & ASL	[12]
$(A, Z) + \nu \rightarrow (A, Z) + \nu$	NC	O	IDSA & ASL	[12]
$e^+ + e^- \rightarrow \nu_{\mu,\tau} + \nu_{\mu,\tau}$	NC & NC	P, T	ASL	[12],[102]
$N + N \rightarrow N + N + \nu_{\mu,\tau} + \bar{\nu}_{\mu,\tau}$	NC	P, T	ASL	[51]

Table 5.2: Table with the relevant neutrino reactions included in the models of `AGILE-IDSA` with ASL for the $\nu_{\mu,\tau}$ and with PUSH to trigger an explosion. In the reactions column, N represents nucleons. In the current column, NC stands for neutral current, while CC for charged current reactions. In the Main Role column, P stands for production, T for thermalization and O for opacity.

Considering that the goal of this model is not only to trigger the explosion, but also to follow the evolution of the shock far from the core, we extended the standard treatment of the EOS and of the connected chemical composition of matter:

- we used a new set of EOS tables for matter in NSE [53]; a consistent extension for the non-NSE conditions have been included. The transition between the two regimes is done by a linear combination of the thermodynamical properties in a tiny temperature interval, between $T_1 = 0.44\,\mathrm{MeV}$ and $T_2 = 0.48\,\mathrm{MeV}$. For temperatures above T_2, NSE is assumed; for temperature below T_2, non-NSE is considered. The upper limit T_2 can be increased in order to fulfill the important termodynamical constraint $\partial E/\partial T > 0$. This part of the work has been done by Matthias Hempel, at the University of Basel.

- We model the abundances of 25 different nuclear species, in the non-NSE regime and they are advected with the fluid. In the transition from non-NSE to NSE, the nuclear equilibrium takes care of their modification; in the opposite transition (which is relevant in case of mass elements ejected by an explosion), NSE compositions are mapped consistently into the 25 considered species. This part of the

Name of the parameter	Values
α_{diff}	6.00
β_{rec}	2.00
α_{int}	5.00
$\alpha_{\nu_{\mu,\tau},\mathrm{cut}}$	20.0
β_{cut}	$L_{\nu,\mathrm{N}}$

Table 5.3: Table with the values of all the free parameters of the $\nu_{\mu,\tau}$ ASL scheme used in the models.

work has been done by Matthias Hempel and Kevin Ebinger, at the University of Basel.

- We include a simplified treatment for the evolution of the abundances of a selected set of nuclear species out of NSE, due to nuclear burning processes. This treatment is based on the direct estimation of the burnign timescales from nuclear reaction rates [39], and it has been documented in Kevin Ebinger's Master thesis.

The idea behind PUSH was first suggested by Matthias Liebendörfer and Carla Fröhlich in 2007. Then, it was further developed by Kevin Ebinger in 2011-2012 in the `AGILE-BOLZTRAN` code (Master Thesis). We developed it further and we implemented it in `AGILE-IDSA` with ASL for $\nu_{\mu,\tau}$.
As it was already anticipated, the main idea behind PUSH is to allow a part of the $\nu_{\mu,\tau}$ luminosity to be re-absorbed by matter. This is performed introducing a local heating term $Q^{+}_{\mathrm{PUSH}}(R)$ [erg/g/s], calculated as

$$Q^{+}_{\mathrm{PUSH}}(t,R) = \left(\int_0^{+\infty} q^{+}_{\mathrm{PUSH}}(R,E)\,\mathrm{d}E\right)\,\mathcal{G}(t) \tag{5.9}$$

$$q^{+}_{\mathrm{PUSH}}(R,E) \equiv \frac{k_{\mathrm{PUSH}}}{4m_b}\,\sigma_0\left(\frac{E}{m_e c^2}\right)^2\left(\frac{\mathrm{d}L_{N,\nu_{\mu,\tau}}}{\mathrm{d}E}(R,E)\right)\frac{1}{4\pi R^2}\cdot\mathcal{F}(R,E). \tag{5.10}$$

In equation (5.10) σ_0 is the typical neutrino cross section 1.7, the usual neutrino energy dependence ($\propto E^2$) has been included, and $\mathrm{d}L_{N,\nu_{\mu,\tau}}/\mathrm{d}E$ is the spectral $\nu_{\mu,\tau}$ number luminosity. The product $(\mathrm{d}L_{N,\nu_{\mu,\tau}}/\mathrm{d}E)/(4\pi R^2)$ is just the particle number flux. k_{PUSH} is a free parameter which has to be set and which estabiliches the relative strenght of PUSH. An higher parameter correspond to a higher extra-energy deposition rate. The function $\mathcal{F}(R,E)$ is a term which has to be designed in order to apply PUSH just where we want it to be applied. To do this, we consider the following guidelines: according to the neutrino-driven explosion paradigm, deposition of energy by neutrino absorption above the neutrinosphere and behind the shock front can revive it. Multidimensional effects, like convection and large scales instabilities, can enhance the heating rates, ultimately favouring the explosion which is missing in spherically symmetric models. Then, we decide to apply PUSH in the neutrino transparent region, where the heating rate from ν_e and $\bar{\nu}_e$ is expected to dominate over cooling rate, (i.e., where $\dot{e}_{\nu_e,\bar{\nu}_e} > 0$ and for $\tau(R,E) > 2/3$), and where convection can occur (e.g., where $\mathrm{d}s/\mathrm{d}R < 0$). A possible expression for $\mathcal{F}(R,E)$ is, for example,

$$\mathcal{F}(R,E) = \begin{cases} 0 & \text{if } \mathrm{d}s/\mathrm{d}R > 0 \text{ or } \dot{e}_{\nu_e,\bar{\nu}_e} < 0\,, \\ \exp\left(-\tau_{\nu_e}(R,E)\right) & \text{otherwise.} \end{cases} \tag{5.11}$$

We decided to apply PUSH only after bounce (before bounce it is expected to do nothing), and, once an explosion has been detected, we switch it off smoothly, using a time dependent exponential cut:

$$\mathcal{G}(t) = \begin{cases} \exp\left(-\frac{t-t_{\mathrm{expl}}}{t_{\mathrm{cut}}}\right) & t_{\mathrm{bounce}} < t < t_{\mathrm{exp}} \\ 0 & \text{otherwise} \end{cases} \tag{5.12}$$

where t_{expl} is the simulated time at which the explosion is launched, t_{bounce} the time of bounce and t_{cut} is a cut timescale. The explosion is detected where the velocity radial

profile becomes somewhere positive, after the shock wave has turned into an accretion shock front.

5.3.2 Results

In the following, we will show results from some test runs we performed. We set up a simulation taking a $15M_\odot$ star progenitor, with Solar metallicity from [52]. We take an extended domain, that includes $M_{\rm sim} = 3.5M_\odot$ and initially extends radially up to $10,000$km. We choose the EOS denominated by TM1 [53] (which is the closest one to the relativistic Shen EOS). We compare two different simulations, the first one with a $k_{\rm PUSH} = 1.2$ and a second one with $k_{\rm PUSH} = 1.4$. Apart from the standard output of the code, we designed a tracer tool to analize the data in the comoving frame of single mass elements. This tracer interpolates linearly all the relevant quantities expressed on the adaptive grid (and, in some cases where the magnitude can change significantly from zone to zone, like the density, their logarithms) on a certain set of fixed mass shells. We calculate also the mass integrated total energy at each possible enclosed mass in the simulation domain, according to the expression (8) and (9) of [37]:

$$E_{\rm tot}(t,M) = \int_M^{M_{\rm tot}} E_{\rm specific}(t,m)\,{\rm d}m = \int_M^{M_{\rm tot}} \left(\Gamma e + \frac{2}{\Gamma+1}\left(\frac{v^2}{2} - G\frac{m}{r(m)}\right)\right)\,{\rm d}m, \tag{5.13}$$

where m is the enclosed mass, $r(m)$ is the corresponding radial position, e the specific internal energy, v the fluid radial velocity, and the Γ function is defined as

$$\Gamma(t,m) = \sqrt{1 - \frac{2Gm}{c^2\,r} + \left(\frac{v}{c}\right)^2}. \tag{5.14}$$

If we consider $t \gg t_{\rm expl}$, once we have detected the innermost mass shell which is ejected $m_{\rm expl,in}$, the explosion energy of the supernova and the number of baryons inside the PNS can be determined as:

$$E_{\rm expl} = E_{\rm tot}(t \gg t_{\rm expl}, m_{\rm expl,in})\,, \tag{5.15}$$

$$N_{\rm PNS} = m_{\rm expl,in}/m_b. \tag{5.16}$$

In the computation of the total energy we take into account also the total energy of the outer part (i.e., the progenitor outer shells, which have not been included in the simulation). We consider it as a static boundary condition,

$$E_{\rm tot}(t,M) = \int_M^{M_{\rm sim}} E_{\rm specific}(t,m)\,{\rm d}m + \int_{M_{\rm sim}}^{M_{\rm tot}} E_{\rm specific}(t=0,m)\,{\rm d}m. \tag{5.17}$$

For example, in our cases, if we split the total energy into internal, kinetic and potential energy,

$$E_{\rm int}(t=0,M_{\rm sim}) = 1.140\cdot 10^{50}{\rm erg}\,, \tag{5.18}$$

$$E_{\rm kin}(t=0,M_{\rm sim}) = 3.707\cdot 10^{44}{\rm erg}\,, \tag{5.19}$$

$$E_{\rm grav}(t=0,M_{\rm sim}) = -1.942\cdot 10^{50}{\rm erg}\,; \tag{5.20}$$

so that

$$E_{\rm tot}(t=0, M_{\rm sim}) = -0.803 \cdot 10^{50}{\rm erg}. \tag{5.21}$$

The tests we have performed differ by the PUSH constant $k_{\rm PUSH}$, which has been set to 1.0 (model A), 1.2 (model B) and 1.4 (model C). In all models, we set $t_{\rm cut} = 0.200$s. They all explode, but at different time and with different properties. In table 5.4 we report some relevant properties regarding the explosion and the remnant PNS, for each of the three analyzed models. As expected, the model that explodes earlier (0.128 s post

Name	$k_{\rm PUSH}$	$t_{\rm expl}$ [s]	$E_{\rm exp}$ [10^{51}erg]	$N_{\rm PNS}$ [10^{57}]	$M_{\rm PNS}$ [$M_\odot$]
A	1.0	0.478	0.350 (1.119 s)	2.067	1.575
B	1.2	0.201	0.740 (1.743 s)	1.904	1.462
C	1.4	0.128	0.986 (0.977 s)	1.836	1.414

Table 5.4: Table with a summary for the properties of the three exploding models. First column: the PUSH factor $k_{\rm PUSH}$. Second column, the explosion time, defined as the time after bounce at which the stalling accretion shock turns into an expanding ejecting shock (i.e., when $v_r > 0$ in the shock). Third column, the explosion energy, defined as (5.15); in brackets, we report the time after $t_{\rm expl}$ at which the explosion energy as well as the other following quantities) have been estimated. Forth column, the number of bayons inside the PNS. Fifth column, the expected NS gravitational mass (calculated for the TM1 EOS, at $T = 0$).

bounce) and with a larger explosion energy (almost 10^{51} erg) is model C, followed by model B (0.201 s and $0.7 \cdot 10^{51}$ erg) and model A (0.478 s and $0.35 \cdot 10^{51}$ erg). The explosion time is defined as the time after bounce when, after having turned into an accretion shock front, the shock wave expands and matter inside it has a positive radial velocity. In all three cases, the explosion is caused by the deposition of energy just below the shock radius: the difference is that in case B the deposition is more gradual and distributed than in case C. As a consequence, the shock starts to expand radially before developing positive velocities and the entropy increases more sensibly everywhere above the neutrinosphere. These two effects are much more evident in case A, where the shock expands from ~ 150 km up to ~ 500 km in ~ 0.4 s, very slowly at the beginning, and accelerating after due to the reduced ram pressure of the accreting matter (as density decreases, going radially). In Figure 5.14 we compare the cumulative amount of energy deposited by PUSH in the fluid (left) and the corresponding deposition rates (right), between the three different tests. As expected, at the beginning model C shows a sistematically higher deposition rate, which is able to trigger soon the explosion. The amount of energy that is deposited is, then, relavitely low and comparable with the final explosion energy. On the other hand, in case A, PUSH has to supply much more energy, definitely larger than the final explosion energy, on a much longer time, with a constantly, but slowly decreasing rate. This energy is only partially used to explode the star. Most of it heats matter below the shock, and is partially re-radiated in form of neutrinos.

The different radial configurations at $t = t_{\rm expl}$ can be seen in Figure 5.15, where the velocity, density, entropy and electron fraction profiles are compared. We can notice how the different explosion time affects the structure of the core, below the radius where the explosion develops. The model A had more time to cool and to accrete matter; thus,

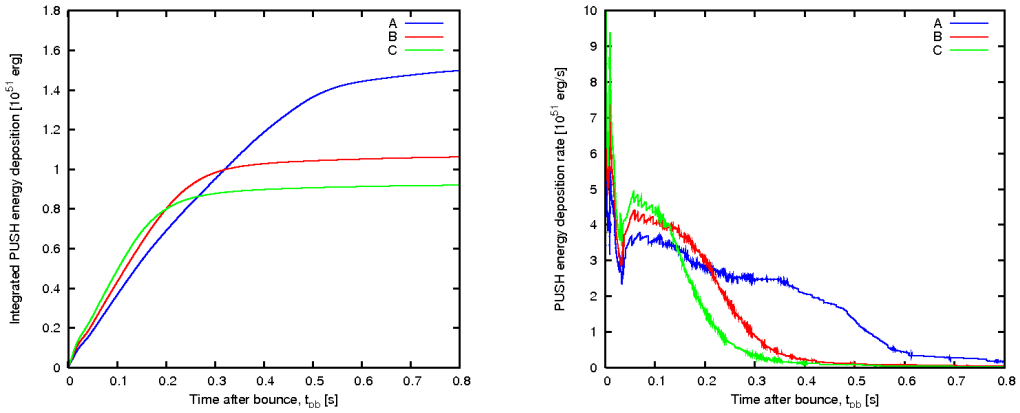

Figure 5.14: Comparison of the cumulative energy deposited by PUSH during the simulations between the different runs (left panels), and of its derivative (deposition energy rate, right panel), expressed as a function of time after bounce, when PUSH is active.

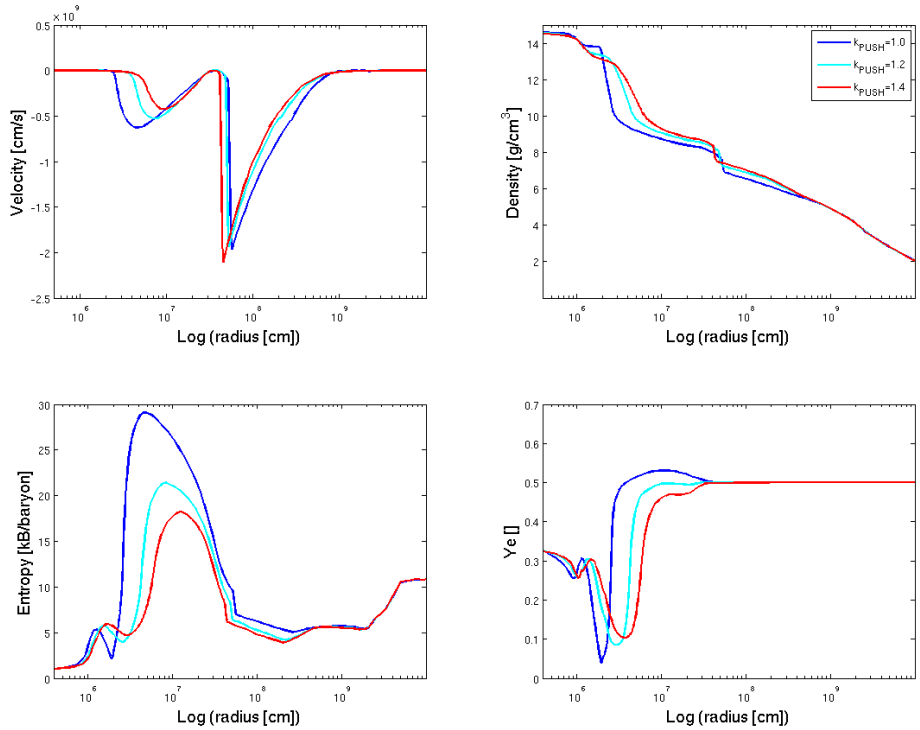

Figure 5.15: Comparison of the radial profiles of velocity (upper left panels), density (upper right panel), entropy (lower left) and electron fraction (lower right panels) for the three different models, at $t = t_{\rm expl}$.

the remnant is more compact and more massive at the explosion time. Neutrino spectra are harder and the luminosities higher; then, ν_e and $\bar{\nu}_e$ absorptions had already a visible effect in increasing the electron fraction in the expanding shock above 0.5 . In Figures 5.16 - 5.18 we report the temporal evolution of the radial profiles at different times (0.2, 0.5 and 0.7 seconds), after the explosion. Overall, the three cases show a similar evolution. However, it is quite clear that case A presents more differences, compared

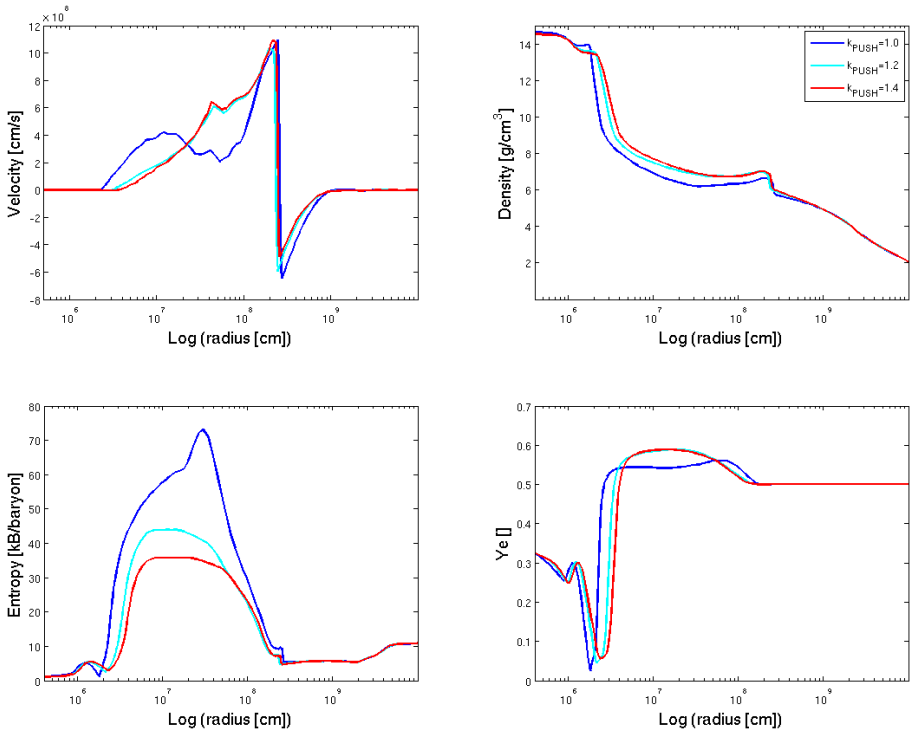

Figure 5.16: Same as Fig 5.15, but at $t = 0.2\,\mathrm{sec}$ after the explosion.

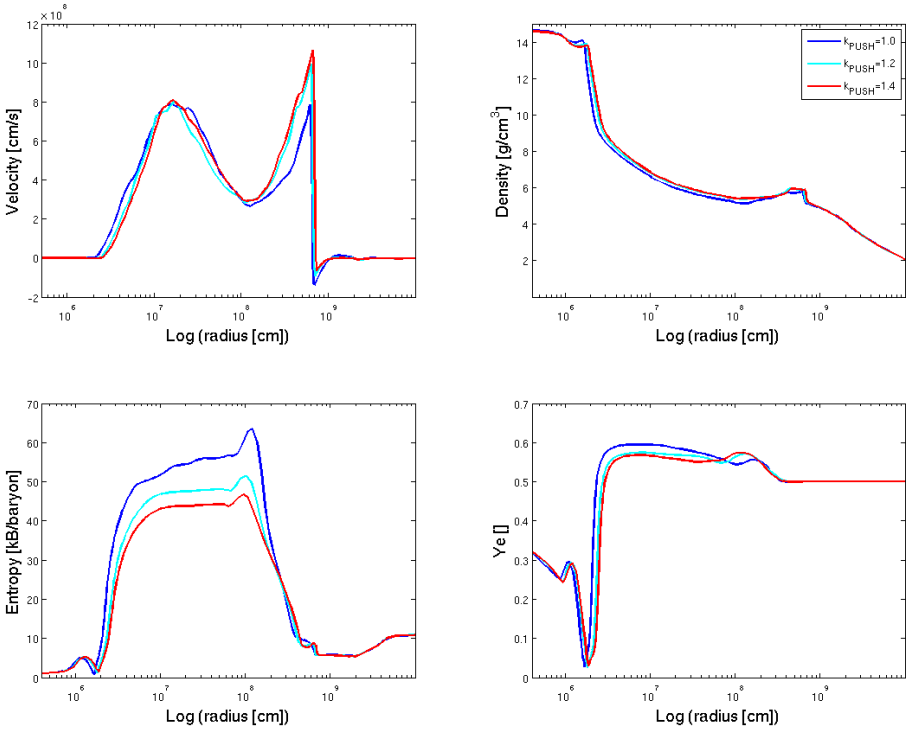

Figure 5.17: Same as Fig 5.15, but at $t = 0.5\,\mathrm{sec}$ after the explosion.

with cases B and C: it usually presents a higher entropy and a larger Y_e, results of the longer heating phase, and a faster decreasing radial velocity. Model B and C are very

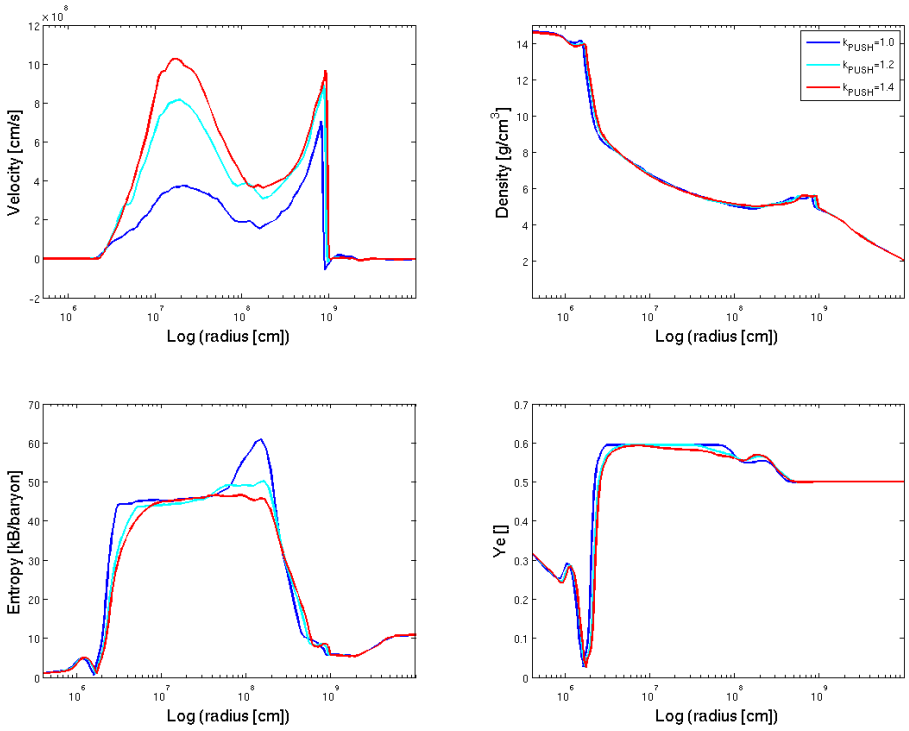

Figure 5.18: Same as Fig 5.15, but at $t = 0.7$ sec after the explosion.

similar; the difference in their explosion energy is, in any case, visible in the velocity and in the entropy profiles at late times, where those of C are systematically higher than those of B. We notice, in the Y_e profiles, that the electron fraction reaches the table limit ($Y_e = 0.6$). An increase in the electron fraction above 0.55 is expected also from detailed spherically symmetric models ([37, 55]), but less than what we obtain. We think that this larger effect can be linked with harder neutrino spectra, which we found, probably due to the absence of the neutrino-electron scattering process, which is very efficient at thermalizing neutrinos just below the neutrinosphere, and/or to an excess of cooling, due to the ASL scheme. Both aspects are currently under investigation. In Figure 5.19 we report the temporal evolution of the neutrino luminosities (left panel) and mean energies (right panel), for all the three species and for all the three runs. Up to 0.1 s after bounce, the three models do not show meaningful differences. The situation changes when the explosion sets in: due to the sudden decrease in the accretion rate on the PNS, all luminosities decrease (more drastically for ν_e and $\bar{\nu}_e$), and set to a (almost) common value, that represents the initial cooling rate of the PNS. The decrease in luminosities happens before for the C model, and later for the other two runs. Due to the longer accretion phase and PUSH action, the spectra of run C are harder; this has a direct link with the higher Y_e observed in the radial profiles. Finally, in Figure 5.20 we plot the radial position of selected mass shells as a function of time (after bounce), for run B. This results have been obtained using the tracer tool; similarly, the temporal evolutions of all interesting quantities can be obtained, as well. The mass corresponding to the PNS is represented by the lines which undergo collapse and sit steadily inside a radius of ~ 18 km. Intermediate mass shells ($1.60 M_\odot \lesssim m \lesssim 1.61 M_\odot$) experience the

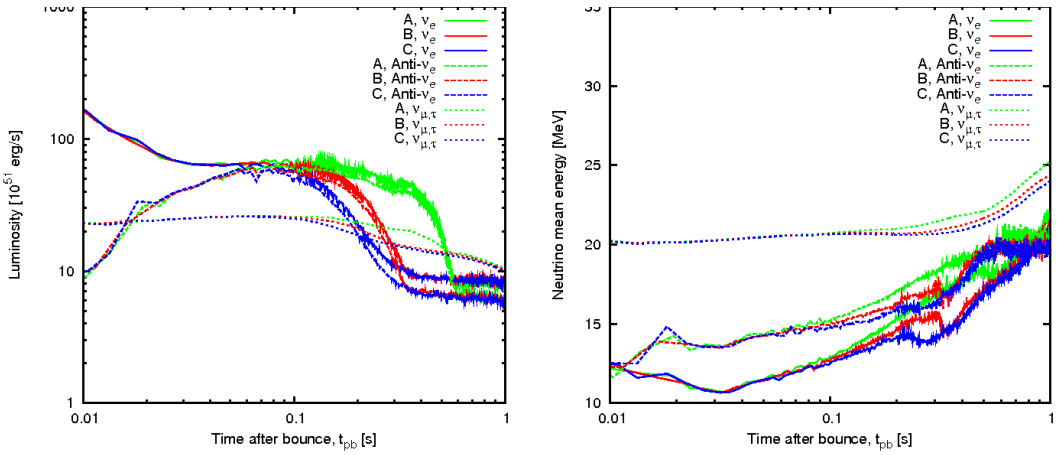

Figure 5.19: Temporal evolution of the neutrino luminosities (left panel) and mean energies (right panel), for all the three species (ν_e solid lines, $\bar{\nu}_e$ dashed lines, $\nu_{\mu,\tau}$ dotted lines) and for all the three runs (A green, B red, C blue).

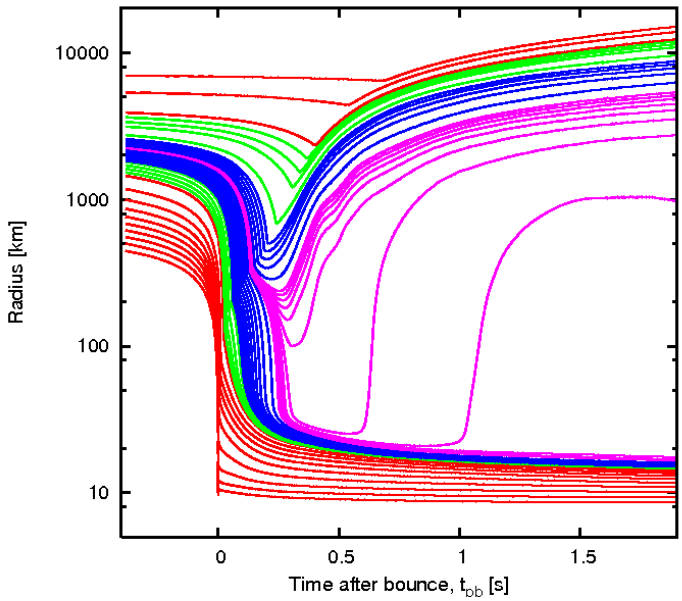

Figure 5.20: Temporal evolution of the radial position of selected mass shells, in the case of run B. Different colors refer to different resolutions. The first red line (in the bottom part of the picture) represents an enclosed baryon mass of $0.5\,M_\odot$; then each red line a mass shell incremented by $0.1\,M_\odot$, up to $1.3\,M_\odot$. The green lines start at $1.425\,M_\odot$ and finish at $1.500\,M_\odot$, with increments of $0.025\,M_\odot$. The blue lines start at $1.510\,M_\odot$ and finish at $1.590\,M_\odot$, with increments of $0.01\,M_\odot$. The region corresponding to the surface of the PNS is the better resolved one in the picture: the magenta lines start at $1.595\,M_\odot$ and finish at $1.606\,M_\odot$, with increments of $0.001\,M_\odot$. Then, the blue lines start at $1.610\,M_\odot$ and finish at $1.660\,M_\odot$, with increments of $0.01\,M_\odot$. The green lines start at $1.685\,M_\odot$ and finish at $1.785\,M_\odot$, with increments of $0.025\,M_\odot$. Finally, the external red lines start at $1.82\,M_\odot$ and finish at $1.85\,M_\odot$, with increments of $0.1\,M_\odot$

collapse inside the accreting shock front, before being quickly expelled by the expanding shock. The outer part $m \gtrsim 1.61 M_\odot$ are pushed outwards by the explosion, once they are reached by the shock, during their infalling motion. Very interestingly, neutrino-driven wind from the PNS surface cen be recognized. The termodynamical conditions inside the wind (mainly, electron fraction and entropy) are currently being investigated, to compare it with other existing models and to figure out the kind of nucleosynthesis expected in the ejecta (M. Hempel, private communication).

Chapter 6

Summary and Conclusions

The study of merging compact objects and collapsing stars is a fascinating topic in modern astrophysics. It involves all fundamental interactions and it requires large and complex numerical simulations, which can push even modern supercomputers to their limits, both in memory and computational power requirements. Differently from many other situations, neutrinos of all flavors play a central and crucial role in the dynamics and in the observables which characterize those systems. The requirement of producing multidimensional (magneto-)hydrodynamical models with detailed radiative transfer is challenging numerical astrophysicists since decades. Solutions of the Boltzmann transport equation is nowadays available in spherically symmetric models of core collapse supernovae; but its extension to less symmetric models seems at the moment difficult, due to computational limitation, more than conceptual problems. As a consequence, several different approximate neutrino transport schemes have been developed and coupled with different hydrodynamical codes. Today, accurate neutrino treatments are getting available also for three dimensional simulations. However, their computational cost is still relatively high. The parameter space of the modeled objects (neutron stars or massive star at the end of their life) is extremely wide; this large variability in the initial conditions and geometries (and partially in the still uncertain input physics) requires the development of less detailed, but also less demanding, approximate neutrino treatments. This type of schemes should not be used to answer fundamental questions where details of the neutrino transport are the essential ingredients to be modeled (like the ultimate proof of the viability of the delayed neutrino-driven explosion mechanism in Core Collapse Supernovae). Nevertheless they can be widely used

- for a less computationally demanding and broader parameter space exploration; in this respect, these approximated models can probably already distinguish between different general behaviors and trends, comparing different sections of the parameter space;

- for astrophysical systems where, due to more complicated geometry configurations, a detailed neutrino transport is still not available in three dimensions;

- for models where neutrinos are expected to play an important role, but where details of the transport become secondary;

- for new types of models (for example, those using new hydrodynamical schemes or

those solving full general relativistic equations), where a slim neutrino treatment is preferable.

In this respect, the major focus of my PhD at the University of Basel, in the Nuclear Astrophysics group of Prof. Thielemann and under the supervision of Dr. Matthias Liebendörfer, was the development, testing and implementation in several contexts of a new approximated, but computationally inexpensive scheme. This scheme belongs to the group of the so called *leakage schemes*, which have been developed and exploited since 1970s'. Usually, these treatments are based on formulations of the transport problem where the integration over the neutrino energy has already been performed (typically, assuming some well motivated hypothesis about their spectrum). As a consequence, they are called grey leakage schemes. Their outcome is, in most of the cases, an estimation of the rates at which neutrinos are locally released out of the system (both particles and energy rates). Then, the main focus of the treatment is often the cooling aspects connected with the production and the diffusion of radiation. One of the peculiar points of these schemes is their *effective* character: this means that the scheme is not really based on the solution of transport or diffusion equations, but it tries to mimic the effect of the expected solutions, according to the knowledge of some crucial quantities, like the local reaction rates, the local mean free paths or the neutrino optical depths.
One of the major goals of the project was to improve this type of schemes, increasing their accuracy and their physical completeness. This objective was achieved mainly passing from a grey to a spectral treatment (with respect to the neutrino energy), and including the evolution of the neutrino fractions and energy according to simple prescriptions, based on estimated relevant timescales. Another related aim was the inclusion of a physically motivated neutrino heating contribution. The major difficulties regarding this point are linked with 1) the non-local aspects of any heating process involving a localized radiating source; and 2) the necessity of having reliable spectral information about the radiation emitted from the source. Both these requirements are very challenging without a real transport scheme.
In Chapter 2, we showed the present version of the scheme, with a detailed description of the ingredients that have been included. In the second part of the chapter, several tests, with increasing input physics included, are discussed. The role of these tests is, not only to compare passively the obtained results with other, more accurate solutions, but also to provide a guide in the development of the scheme and the necessary determination of some important free parameters. In this sense, the scheme is effective: it needs a reference solution to be shaped on. Of course, one of the most challenging parts is to define a set of parameters and ingredients that are well suited for different situations (for example, for a whole core collapse supernova model, ranging from the collapse phase, up to the cooling of the PNS). The final result of this work is an Advanced Spectral Leakage (ASL) treatment, suited for all neutrino flavors (the actual modeled flavors are ν_e, $\bar{\nu}_e$ and $\nu_{\mu,\tau}$) and tested against detailed Boltzmann neutrino transport, in spherically symmetric Core Collapse Supernova simulations.
Considering the importance of the optical depth in the ASL treatment and its non-local character, we designed also a geometry-free algorithm to calculate the optical depth in multidimensional simulations with no special symmetry. This algorithm (MODA) has been described in Chapter 3 and some positive tests (both based on analytical initial data and on data obtained from actual astrophysical simulations) have been shown. The

implemented version has been OpenMP parallelized, and the related performances are discussed.
Parallel to the definition and to the refinement of the ASL scheme, we started to implement the treatment in different multidimensional astrophysical simulations. The models differ both for the physical contexts and for the coupled hydrodynamical codes. They have been reported in Chapter 4 and 5.
A first application has been done in the context of magneto-rotationally driven core collapse supernovae: assuming that the core of the progenitor star has an initial high rotation rate and a large enough polar magnetic field, the free rotational energy can be converted in magnetic energy. As a consequence, the related magnetic pressure lifts matter in polar jets, which expand fast and ultimately disrupt the star. In this scenario, neutrinos are expected to play a sub-dominant role concerning the dynamics of the explosion, but they still are essential to model the composition of the ejecta. We included the cooling features of the ASL scheme in three dimensional, Cartesian magnetohydrodynamical simulations. We performed a hybrid implementation of the scheme: most of the necessary quantities are calculated locally on the three dimensional grid; while the optical depth is calculated along linear path, with a ray-by-ray approach and assuming axisymmetry. First results of these simulations, obtained in collaboration with Roger Käppeli and Christian Winteler at the University of Basel, show (for some initial configuration) the formation of a jet explosion. Due to the extreme neutron richness of matter in the jets, the nucleosynthesis calculations, based on the obtained trajectories, make this scenario as one of the most promising site for the production of r-process elements, especially in the Early Universe.

A second scenario where the ASL treatment is being applied is the aftermath of neutron star merger. When two neutron stars in a binary system merge, after an inspiraling phase due to the emission of gravitational waves, a hyper massive neutron star is formed in the center, surrounded by a torus of dense accreting matter. The HMNS will collapse to a black hole, on a timescale which is still quite debated. Before this happens, a strong neutrino emission is supplied by the SMNS and by the inner part of the disc. We modeled the disk dynamics, the neutrino emission and their mutual interaction. Such a system is expected to have potential observables (for example, r-process nucleosynthesis, neutrino and gravitational wave signatures), as well as a strong connection with short GRBs.
To model the wind, we have performed for the first time 3D Newtonian hydrodynamics simulations, covering an interval of $\approx 100\,\mathrm{ms}$ after the merger, and a radial distance of $\gtrsim 1500\,\mathrm{km}$ from the HMNS, with high spatial resolution inside the wind. Neutrino radiation has been treated by a computationally efficient, multi-flavour Advanced Spectral Leakage scheme, which includes consistent neutrino absorption rates in optically thin conditions. Our initial configuration is obtained from the direct re-mapping of the matter distribution of a 3D SPH simulation of the merger of two non-spinning $1.4 M_\odot$ neutron stars [141, and references therein], at ≈ 15 ms after the first contact. The consistent dimensionality and the high compatibility between the two models does not required any global average nor any ad hoc assumption for the matter profiles inside the disc. Our 3D results show a good qualitative agreement with the 2D results obtained by [29] for a similar initial configuration, especially for the neutrino emission and the

wind dynamics. Meaningful quantitative differences are still present, probably related with the different accretion history inside the disc. Our major findings are:

1. the wind provides a substantial contribution to the total mass lost in a BNS merger. At the end of our simulation (≈ 100 ms after the merger), we compute $2.12 \times 10^{-3} M_\odot$ of neutron-rich ($0.2 \lesssim Y_e \lesssim 0.4$) ejected matter, corresponding to 1.2% of the initial mass of the disc. We distinguish between a high-latitude ($50° - 90°$) and a low-latitude ($30° - 50°$) component of the ejecta. The former is subject to a more intense neutrino irradiation and is characterized by larger Y_e, entropies and expansion velocities. We estimate that, on the longer disc lifetime, the ejected mass can increase to $3.49 - 4.87 \times 10^{-3} M_\odot$, where the smaller (larger) value refers to a quick (late) HMNS collapse after the end of our simulation.

2. The tendency of Y_e to increase with time above 0.3, especially at high latitudes, suggests a relevant contribution to the nucleosynthesis of the weak r-process elements from the wind, in the range of atomic masses from the first to the second peak.

3. A significant fraction of the neutrino luminosity is provided by the accretion process inside the disc. This fraction is expected to power a (less intense) baryonic wind also if the HMNS collapses to a BH before the disc consumption. According to our calculations, the collapse time scale has a minor impact on the possible observables (electromagnetic counterparts and nucleosynthesis yields), at least if the collapse happens after the wind has formed and weak equilibrium had time to establish inside it.

More recently, the ASL has been applied to two other different models. In the first one, the cooling part of the scheme has been implemented in a three dimensional SPH code by Rubén Cabézon, to model core collapse supernova. The very first tests are able to reproduce qualitatively and also partially quantitatively the expected results for collapse, bounce and post bounce phases, including an adeguate deleptonization and neutrino luminositis. Further developments are still necessary; but, taking into account the natural good conservation properties of SPH, and its high resolution in the high density regions, this scheme will provide a new tool to investigate relevant aspects of this astrophysical scenario with an approach complementary to grid codes. In particular, it can be a powerful tool for studing, for example, convection and kicks of PNS from a multidimensional, highly resolved point of view.
In the second recent application, done in collaboration with Matthias Hempel and Kevin Ebinger at the University of Basel, the ASL treatment for $\nu_{\mu,\tau}$ has been included in the publicly available spherically symmetric grid code `AGILE-IDSA` to model Core Collapse Supernovae. The code has been modified in order to include 1) a new Equation of State treatment for the part of the domain which is not in Nuclear Statistical Equilibrium, 2) as well as a simplified treatment for the evolution of the chemical composition of this part; 3) a new way to trigger an explosion depositing a fraction of the luminosities carried away by $\nu_{\mu,\tau}$ (PUSH). This scheme has just two additional free parameters, which can be tuned to obtain the expected values for the explosion timescale, the explosion energy and the mass of the remnant for some specific cases. The relatively low computational cost of each run ensures the possibility of large progenitor space exploration

(both in masses and metallicities), in particular for studying the effect of more detailed nuclear physics and neutrino interactions inputs.

Overall, the development of the new ASL neutrino treatment has reached a satisfactory level of accuracy and completeness. Coupled with a sophisticated algorithm to model optical depth in multidimensions (like the MODA algorithm), it can be used as a powerful tool to investigate neutrino emission and absorption in astrophysical scenarios with no defined symmetry. It has also shown a remarkable suppleness, which allows it to be implemented to model different astrophysical situations, with different hydrodynamical codes and different geometries.
However, much work has still to be done to improve further the treatment and to lead the multiple applications we have exposed to a satisfactory level, before being used for extensive and interesting scientific investigations.

From a personal point of view, the field of nuclear astrophysics and, in particular, the topics Core Collapse Supernovae and Neutron star Mergers have represented challenging and very stimulating subjects for my studies. They require very broad physical and computational abilities, together with patience and perseverance. This is particularly true when elusive neutrinos are involved.
The group in Basel has represented, personally and scientifically speaking, an ideal and stimulating working environment. Possibilities to develop internal collaborations, to access available resources and to visit other groups and start external collaborations have been always permitted and, even more, recommended.
My hope for the future is to continue on the path I have started, contributing to this fascinating field and, if possible, transmitting these feelings and knowledge to other persons.

Albino Perego

E-mail: albino.perego@physik.tu-darmstadt.de
Phone: 0049 6151 1675665

Birthday: September 23rd, 1983
Place of birth: Lecco, Italy
Citizenship: Italian

Current affiliation: Institute of Nuclear Physics (IKP),
Technische Universität Darmstadt
Schlossgartenstrasse 2, 64289 Darmstadt, Germany

Education and employments

2013- **Post-Doctoral position**, *TU-Darmstadt*, Darmstadt, Germany.
Post-Doctoral position at the Technische Universität Darmstadt, in the Theoretical Astrophysical group of Prof. Dr. Almudena Arcones (Helmholtz Young Investigator Group).

2008-2012 **Philosophiae Doctor degree**, *University of Basel*, Basel, Switzerland, *Summa cum Laude*.
PhD student at the University of Basel, in the Astro-Theoretical group, under the supervision of Professor Matthias Liebendörfer and Professor Friedrich-Karl Thielemann

2008 **Scholarship**, *University of Milano-Bicocca*, Milano, Italy.
Three months scholarship at the University of Milano-Bicocca, under the supervision of Professor Monica Colpi.

2005-2008 **Laurea magistrale**, *Università degli Studi di Milano*, Milano, Italy, *110/110 cum laude*.
Italian Master Degree in Physics, Curriculum of Theoretical Physics

2002-2005 **Laurea triennale**, *Università degli Studi di Milano*, Milano, Italy, *110/110 cum laude*.
Italian Bachelor Degree in Physics

1996-2002 **Diploma**, *Liceo Giovanni Battista Grassi*, Lecco, Italy, *100/100 cum encomio*.
Diploma at a scientific high school

2002-2008 **University lectures**.
During my studies I attended lectures from: Prof. M. Bersanelli, Prof. G. Bertin, Prof. P.F. Bortignon, Prof. A. Bracco, Prof. A. Carati, Prof. G. Coló, Prof. E. Colombo, Prof. E. Fabrici, Prof. R. Ferrari, Prof. S. Forte, Prof. F. Gallone, Prof. A. Guglielmetti, Prof. D. Klemm, Prof. L. Lanz, Prof. C. Maderna, Prof. N. Manini, Prof. M. Maugeri, Prof. L. Paganoni, Prof. N. Piovella, Prof. P. M. Pizzochero, Prof. E. Spoletini, Prof. M. Vignati, Prof. D. Zanon, Prof. L. Zetta

Experiences

Research

Since December 2009 **The aftermath of neutron star merger**.
I have been working with PD Dr. Matthias Liebendorfer (University of Basel), Professor Stephan Rosswog (Jacobs University Bremen) and Professor Almudena Arcones (Techinische Universität Darmstadt) on the study of the aftermath of neutron star merger and on its neutrino emission. Since April 2011, this work is computationally supported by the Swiss National Supercomputing Center (CSCS) under the production project s414.

Since December 2008 **Weak processes and numerical simulations of core collapse supernova**.
I have been working with Professor Matthias Liebendorfer, the nuclear astrophysics group (University of Basel), Achim Schwenk (TU Darmstadt) and Chris Pethick (NORDITA) on the improvement of weak processes and approximated neutrino treatments in the contest of dense and hot matter, in particular during supernova explosion and in magnetically driven supernova explosions. These projects are currently computationally supported by CSCS (production projects s414).

January 2010-December 2012 **Supernova HP2C project: Productive 3D Models of Stellar Explosions**.
I have been working with the Computational Astro-Nuclear group at the University of Basel (Principal Investigator: Matthias Liebendörfer), in collaboration with the Computational group at the University of Geneve (Principal Investigator: Martin J. Gander) at the HP2C project "Supernova".

Since May 2007 **Temporal evolution of massive black hole mass and spin, during cosmic evolution**.
I have been working with Professor Monica Colpi (University of Milano-Bicocca), Doctor Massimo Dotti and Professor Marta Volonteri (University of Michigan, Ann Arbor). We studied, with an analitical approximated model, the alignment process of the spin of a supermassive black hole with the orbital angular momentum of its accretion disc.

April 2005 - October 2005 **Production of W particles and jets in hadron colliders**.
I worked under the supervision of Doctor Alessandro Vicini and Professor Stefano Forte (University of Milano) on the calculation of the hadronic cross section for the production of W particles in proton-proton colliders, using different partonic distributions for the nucleon structure.

Presentations and seminars

July 2014 **Neutrino-driven wind in the aftermath of neutron star mergers**, *The r-process, status and challenges, INT Workshop*, Seattle, USA.

April 2014 **Neutrino-driven wind from the aftermath of neutron star mergers**, *XVII Nuclear Astrophysics Workshop*, Ringberg, Germany.

March 2014 **Neutrino-driven wind from the aftermath of neutron star mergers**, *NS from Birth to Death, conference*, Firenze, Italy.

November 2013 **Neutrino-driven wind in the aftermath of neutron star merger**, *GRBS in Kyoto, conference*, Kyoto, Japan.

June 2013 **The inner working of core collapse supernovae**, *Oskar Klein Centre, University of Stockholm*, Stockholm, Sweden.

January 2013 **Neutrino emission from the aftermath of neutron star merger**, *XLI Workshop on Gross Properties of Nuclei and Nuclear Excitations*, Hirschegg, Austria.

June 2012 **Neutrino transport in multi-dimensional core collapse supernova simulations**, *TU Darmstadt*, Darmstadt, Germany.

May 2012 **Neutrino transport in multi-dimensional core collapse supernova simulations**, *North Carolina State University*, Releigh, USA.

April 2012 **3D magneto-rotationally driven supernovae**, *Jacobs University Bremen*, Bremen, Germany.

March 2012 **A new approximated neutrino treatment for astrophysical simulations**, *XVI Nuclear Astrophysics Workshop*, Ringberg, Germany.

May 2011 **An approximated neutrino treatment for multi-D astrophysical simulations**, *Compstar 2011 workshop*, Catania, Italy.

October 2010 **Neutrinos in CCSN**, *Jacobs University Bremen*, Bremen, Germany.

March 2010 **A NLO leakage scheme for neutrino in CCSN**, *Ringberg Castle*, XV Nuclear Astrophysics Workshop, Ringberg, Germany.

February 2010 **Spin and mass evolution during BH spin alignment**, *Jacobs University Bremen*, Bremen, Germany.

December 2009 **The role of neutrinos in CCSN**, *LUTh, Observatoire de Paris*, Meudon, France.

August 2009 **μ and τ neutrinos in CCSN simulations**, *MICRA workshop, Niels Bohr Institute*, Copenhagen, Denmark.

June 2009 **SMBH spin and mass evolution during spin alignment**, *Insubria University*, Como, Italy.

Posters

September 2012 **Spectral neutrino emission in the aftermath of 3D neutron star mergers**, *CSCS Users day*, In collaboration with Dr. Ruben Cabezon, Lugano, Switzerland.

September 2011 **Numerical Simulation of Magnetically Driven Core-Collapse Supernovae**, *CCCS Fair PhD students day and CSCS users day*, in collaboration with R. Käppeli, Basel and Luzern, Switzerland.

September 2009 **Observables and Models of Stellar Explosions**, *CSCS Users day*, Luzern, Switzerland.

Teaching

Nov 2013-Oct 2014 **Master project supervision**, *TU Darmstadt*.
Supervision of the master project of Paul Mekhedjian on "Neutrino transport in CCSN".

Spring 2013 **An Introduction to Theoretical Astrophysics**, *TU Darmstadt*.
Exercises tutor for students (Lecturer: Prof. Dr. Almudena Arcones).

Spring 2012 **Nuclear Astrophysics II**, *University of Basel*.
Exercises tutor for master students (Lecturer: Prof. Dr. Thomas Raucher). Best Tutor award.

Autumn 2011 **Nuclear Astrophysics I**, *University of Basel*.
Exercises tutor for master students (Lecturer: Prof. Dr. Thomas Raucher). Best Tutor award.

Spring 2011 **Electrodynamics**, *University of Basel*.
Exercises tutor for bachelor students (Lecturer: Prof. Dr. Friedrich-Karl Thielemann).

Autumn 2010 **Introduction to Astrophysical Plasma**, *University of Basel*.
Exercises tutor for master students (Lecturer: Prof. Dr. Matthias Liebendörfer). Best Tutor award.

Spring 2010 **Nuclear Astrophysics II**, *University of Basel*.
Exercises tutor for master students (Lecturer: Prof. Dr. Thomas Raucher).

Autumn 2009 **Mathematical Method III**, *University of Basel*.
Exercises tutor for bachelor students (Lecturer: Prof. Dr. Andreas Aste).

Spring 2009 **Nuclear Astrophysics II**, *University of Basel*.
Exercises tutor for master students (Lecturer: Prof. Dr. Thomas Raucher).

Languages

Language Italian
Level Mother tongue

Language English
Level Advanced knowledge of written and spoken English (C1)

Language German
Level Basic knowledge of written and spoken German (B1)

Language French
Level Elementary knowledge of written and spoken French (A2)

Computer skills

Operating Systems Linux, Windows
Languages C, Fortran 77/90, LaTeX, OpenMP, MPI
Mathematical software Mathematica, Matlab

Publications

Authors Perego A., Rosswog S., Cabezón R., Korobkin O., Käppeli., Arcones A., Liebendörfer M.
Title Neutrino-driven winds from neutron star merger remnants
Accepted by A&A, 2014

Authors Perego A., Gafton E., Cabezón R., Rosswog S., Liebendörfer M.
Title MODA: a new algorithm to compute optical depths in multidimensional hydrodynamic simulations
Accepted by MNRAS, 2014

Authors Maio U., Dotti M., Petkova M., Perego A., Volonteri M.
Title Effects of Circumnuclear Disk Gas Evolution on the Spin of Central Black Holes
Accepted by ApJ, 2013

Authors Dotti M., Colpi M., Pallini S., Perego A., Volonteri M.
Title On the Orientation and Magnitude of the Black Hole Spin in Galactic Nuclei
Accepted by ApJ, 2013

Authors Bacca S., Hally K. R., Liebendörfer M., Perego A., Pethick C., Schwenk A.
Title Neutrino Processes in Partially Degenerate Neutron Matter
Accepted by ApJ, 2012

Authors Winteler C., Käppeli R., Perego A., Arcones A., Vasset N.,Nishimura N., Liebendörfer M., Thielemann F.-K.
Title Magnetorotationally Driven Supernovae as the Origin of Early Galaxy r-process Elements?
Accepted by ApJ Letter, 2012

Authors Dotti M., Volonteri M., Perego A., Colpi M., Ruszkowski M., Haardt F.
Title Dual BHs in merger remnants - II: spins evolution and gravitational recoil
Accepted by MNRAS 2010

Authors Liebendörfer M., Fischer T., Hempel M., Käppeli R., Pagliara G., Perego A., Sagert, I., Schaffner-Bielich J., Scheidegger S., Thielemann F.-K., Whitehouse S.C.
Title Neutrino Radiation-Hydrodynamics: General Relativistic versus Multidimensional Supernova Simulations
Progress of Theoretical Physics Supplement, 2010

Authors Perego A., Dotti M., Colpi M., Volonteri M.
Title Mass and spin coevolution during the alignment of a black hole in a warped accretion disc
Accepted by MNRAS, 2009

Bibliography

[1] E. Abdikamalov, A. Burrows, C. D. Ott, F. Löffler, E. O'Connor, J. C. Dolence, and E. Schnetter. A New Monte Carlo Method for Time-dependent Neutrino Radiation Transport. *ApJ*, 755:111, August 2012.

[2] A. Arcones, H.-T. Janka, and L. Scheck. Nucleosynthesis-relevant conditions in neutrino-driven supernova outflows. I. Spherically symmetric hydrodynamic simulations. *Astronomy and Astrophysics*, 467:1227–1248, June 2007.

[3] A. Arcones and G. Martínez-Pinedo. Dynamical r-process studies within the neutrino-driven wind scenario and its sensitivity to the nuclear physics input. *PhRvC*, 83(4):045809, April 2011.

[4] D. Argast, M. Samland, F.-K. Thielemann, and Y.-Z. Qian. Neutron star mergers versus core-collapse supernovae as dominant r-process sites in the early Galaxy. *Astronomy and Astrophysics*, 416:997–1011, March 2004.

[5] S. Bacca, K. Hally, M. Liebendörfer, A. Perego, C. J. Pethick, and A. Schwenk. Neutrino Processes in Partially Degenerate Neutron Matter. *ApJ*, 758:34, October 2012.

[6] A. M. Beloborodov. Hyper-accreting black holes. In M. Axelsson, editor, *American Institute of Physics Conference Series*, volume 1054 of *American Institute of Physics Conference Series*, pages 51–70, September 2008.

[7] H. A. Bethe. Supernova mechanisms. *Reviews of Modern Physics*, 62:801–866, October 1990.

[8] H. A. Bethe, G. E. Brown, and J. Cooperstein. Convection in supernova theory. *ApJ*, 322:201–205, November 1987.

[9] G. S. Bisnovatyi-Kogan, I. P. Popov, and A. A. Samokhin. The magnetohydrodynamic rotational model of supernova explosion. *Astrophysics and Space Science*, 41:287–320, June 1976.

[10] J. M. Blondin, A. Mezzacappa, and C. DeMarino. Stability of Standing Accretion Shocks, with an Eye toward Core-Collapse Supernovae. *ApJ*, 584:971–980, February 2003.

[11] J. S. Bloom, J. X. Prochaska, D. Pooley, C. H. Blake, R. J. Foley, S. Jha, E. Ramirez-Ruiz, J. Granot, A. V. Filippenko, S. Sigurdsson, A. J. Barth, H.-W. Chen, M. C. Cooper, E. E. Falco, R. R. Gal, B. F. Gerke, M. D. Gladders,

J. E. Greene, J. Hennanwi, L. C. Ho, K. Hurley, B. P. Koester, W. Li, L. Lubin, J. Newman, D. A. Perley, G. K. Squires, and W. M. Wood-Vasey. Closing in on a Short-Hard Burst Progenitor: Constraints from Early-Time Optical Imaging and Spectroscopy of a Possible Host Galaxy of GRB 050509b. *ApJ*, 638:354–368, February 2006.

[12] S. W. Bruenn. Stellar core collapse - Numerical model and infall epoch. *ApJS*, 58:771–841, August 1985.

[13] S. W. Bruenn, A. Mezzacappa, W. R. Hix, J. M. Blondin, P. Marronetti, O. E. B. Messer, C. J. Dirk, and S. Yoshida. 2D and 3D Core-Collapse Supernovae Simulation Results Obtained with the CHIMERA Code. *ArXiv e-prints*, February 2010.

[14] S. W. Bruenn, E. A. Raley, and A. Mezzacappa. Fluid Stability Below the Neutrinospheres of Supernova Progenitors and the Dominant Role of Lepto-Entropy Fingers. *ArXiv Astrophysics e-prints*, April 2004.

[15] R. Buras, H.-T. Janka, M. T. Keil, G. G. Raffelt, and M. Rampp. Electron Neutrino Pair Annihilation: A New Source for Muon and Tau Neutrinos in Supernovae. *ApJ*, 587:320–326, April 2003.

[16] R. Buras, M. Rampp, H.-T. Janka, and K. Kifonidis. Two-dimensional hydrodynamic core-collapse supernova simulations with spectral neutrino transport. I. Numerical method and results for a $15M_{\odot}$ star. *Astronomy and Astrophysics*, 447:1049–1092, March 2006.

[17] A. Burrows, L. Dessart, E. Livne, C. D. Ott, and J. Murphy. Simulations of Magnetically Driven Supernova and Hypernova Explosions in the Context of Rapid Rotation. *ApJ*, 664:416–434, July 2007.

[18] A. Burrows, E. Livne, L. Dessart, C. D. Ott, and J. Murphy. A New Mechanism for Core-Collapse Supernova Explosions. *ApJ*, 640:878–890, April 2006.

[19] A. Burrows, E. Livne, L. Dessart, C. D. Ott, and J. Murphy. Features of the Acoustic Mechanism of Core-Collapse Supernova Explosions. 655:416–433, January 2007.

[20] A. Burrows, J. Nordhaus, A. Almgren, and J. Bell. The potential role of spatial dimension in the neutrino-driving mechanism of core-collapse supernova explosions. *Computer Physics Communications*, 182:1764–1766, September 2011.

[21] A. Burrows and T. A. Thompson. Neutrino-Matter Interaction Rates in Supernovae: The Essential Microphysics of Core Collapse. *ArXiv Astrophysics e-prints*, November 2002.

[22] O. L. Caballero, G. C. McLaughlin, and R. Surman. Neutrino Spectra from Accretion Disks: Neutrino General Relativistic Effects and the Consequences for Nucleosynthesis. *ApJ*, 745:170, February 2012.

[23] A. G. W. Cameron. Some Nucleosynthesis Effects Associated with r-Process Jets. *ApJ*, 587:327–340, April 2003.

[24] S. A. Colgate and R. H. White. The Hydrodynamic Behavior of Supernovae Explosions. *ApJ*, 143:626, March 1966.

[25] J. Cooperstein, L. J. van den Horn, and E. A. Baron. Neutrino flows in collapsing stars - A two-fluid model. *ApJ*, 309:653–666, October 1986.

[26] M. B. Davies, W. Benz, T. Piran, and F. K. Thielemann. Merging neutron stars. 1. Initial results for coalescence of noncorotating systems. *ApJ*, 431:742–753, August 1994.

[27] P. B. Demorest, T. Pennucci, S. M. Ransom, M. S. E. Roberts, and J. W. T. Hessels. A two-solar-mass neutron star measured using Shapiro delay. *Nature*, 467:1081–1083, October 2010.

[28] L. Dessart, A. Burrows, E. Livne, and C. D. Ott. Multidimensional Radiation/Hydrodynamic Simulations of Proto-Neutron Star Convection. *ApJ*, 645:534–550, July 2006.

[29] L. Dessart, C. D. Ott, A. Burrows, S. Rosswog, and E. Livne. Neutrino Signatures and the Neutrino-Driven Wind in Binary Neutron Star Mergers. *ApJ*, 690:1681–1705, January 2009.

[30] M. Duez. New results in black hole-neutron star merger models. In *APS Northwest Section Meeting Abstracts*, page H1010, October 2010.

[31] R. C. Duncan, S. L. Shapiro, and I. Wasserman. Neutrino-driven winds from young, hot neutron stars. *ApJ*, 309:141–160, October 1986.

[32] D. Eichler, M. Livio, T. Piran, and D. N. Schramm. Nucleosynthesis, neutrino bursts and gamma-rays from coalescing neutron stars. *Nature*, 340:126–128, July 1989.

[33] R. I. Epstein and C. J. Pethick. Lepton loss and entropy generation in stellar collapse. *ApJ*, 243:1003–1012, February 1981.

[34] J. Faber. Status of neutron star-black hole and binary neutron star simulations. *Classical and Quantum Gravity*, 26(11):114004, June 2009.

[35] K. Farouqi, K.-L. Kratz, B. Pfeiffer, T. Rauscher, F.-K. Thielemann, and J. W. Truran. Charged-particle and Neutron-capture Processes in the High-entropy Wind of Core-collapse Supernovae. *ApJ*, 712:1359–1377, April 2010.

[36] T. Fischer, I. Sagert, M. Hempel, G. Pagliara, J. Schaffner-Bielich, and M. Liebendörfer. Signals of the QCD phase transition in core collapse supernovae - microphysical input and implications on the supernova dynamics. *Classical and Quantum Gravity*, 27(11):114102, June 2010.

[37] T. Fischer, S. C. Whitehouse, A. Mezzacappa, F.-K. Thielemann, and M. Liebendörfer. Protoneutron star evolution and the neutrino-driven wind in general relativistic neutrino radiation hydrodynamics simulations. *Astronomy and Astrophysics*, 517:A80, July 2010.

[38] T. Foglizzo. Non-radial instabilities of isothermal Bondi accretion with a shock: Vortical-acoustic cycle vs. post-shock acceleration. *Astronomy and Astrophysics*, 392:353–368, September 2002.

[39] W. A. Fowler, G. R. Caughlan, and B. A. Zimmerman. Thermonuclear Reaction Rates, II. *Annual Review of Astronomy and Astrophysics*, 13:69, 1975.

[40] D. B. Fox, D. A. Frail, P. A. Price, S. R. Kulkarni, E. Berger, T. Piran, A. M. Soderberg, S. B. Cenko, P. B. Cameron, A. Gal-Yam, M. M. Kasliwal, D.-S. Moon, F. A. Harrison, E. Nakar, B. P. Schmidt, B. Penprase, R. A. Chevalier, P. Kumar, K. Roth, D. Watson, B. L. Lee, S. Shectman, M. M. Phillips, M. Roth, P. J. McCarthy, M. Rauch, L. Cowie, B. A. Peterson, J. Rich, N. Kawai, K. Aoki, G. Kosugi, T. Totani, H.-S. Park, A. MacFadyen, and K. C. Hurley. The afterglow of GRB 050709 and the nature of the short-hard γ-ray bursts. *Nature*, 437:845–850, October 2005.

[41] D. A. Frail, S. R. Kulkarni, R. Sari, S. G. Djorgovski, J. S. Bloom, T. J. Galama, D. E. Reichart, E. Berger, F. A. Harrison, P. A. Price, S. A. Yost, A. Diercks, R. W. Goodrich, and F. Chaffee. Beaming in Gamma-Ray Bursts: Evidence for a Standard Energy Reservoir. *The Astrophysical Journal Letters*, 562:L55–L58, November 2001.

[42] C. Freiburghaus, S. Rosswog, and F.-K. Thielemann. R-Process in Neutron Star Mergers. *The Astrophysical Journal Letters*, 525:L121–L124, November 1999.

[43] C. Fröhlich, G. Martínez-Pinedo, M. Liebendörfer, F.-K. Thielemann, E. Bravo, W. R. Hix, K. Langanke, and N. T. Zinner. Neutrino-Induced Nucleosynthesis of A¿64 Nuclei: The νp Process. *Physical Review Letters*, 96(14):142502, April 2006.

[44] C. L. Fryer and M. S. Warren. The Collapse of Rotating Massive Stars in Three Dimensions. 601:391–404, January 2004.

[45] C. L. Fryer and M. S. Warren. The Collapse of Rotating Massive Stars in Three Dimensions. *ApJ*, 601:391–404, January 2004.

[46] S.-i. Fujimoto, N. Nishimura, and M.-a. Hashimoto. Nucleosynthesis in Magnetically Driven Jets from Collapsars. *ApJ*, 680:1350–1358, June 2008.

[47] N. Gehrels, E. Ramirez-Ruiz, and D. B. Fox. Gamma-Ray Bursts in the Swift Era. *Annual Review of Astronomy and Astrophysics*, 47:567–617, September 2009.

[48] P. Goldreich and S. V. Weber. Homologously collapsing stellar cores. *ApJ*, 238:991–997, June 1980.

[49] S. Goriely, A. Bauswein, and H.-T. Janka. r-process Nucleosynthesis in Dynamically Ejected Matter of Neutron Star Mergers. *The Astrophysical Journal Letters*, 738:L32+, September 2011.

[50] F. Hanke, A. Marek, B. Müller, and H.-T. Janka. Is Strong SASI Activity the Key to Successful Neutrino-driven Supernova Explosions? *ApJ*, 755:138, August 2012.

[51] S. Hannestad and G. Raffelt. Supernova Neutrino Opacity from Nucleon-Nucleon Bremsstrahlung and Related Processes. *ApJ*, 507:339–352, November 1998.

[52] A. Heger, S. E. Woosley, and H. C. Spruit. Presupernova Evolution of Differentially Rotating Massive Stars Including Magnetic Fields. *ApJ*, 626:350–363, June 2005.

[53] M. Hempel, T. Fischer, J. Schaffner-Bielich, and M. Liebendörfer. New Equations of State in Simulations of Core-collapse Supernovae. *ApJ*, 748:70, March 2012.

[54] R. D. Hoffman, S. E. Woosley, and Y.-Z. Qian. Model Independent r-Process Nucleosynthesis - Constraints on the Key Parameters. *Nuclear Physics A*, 621:397–400, February 1997.

[55] L. Hüdepohl, B. Müller, H.-T. Janka, A. Marek, and G. G. Raffelt. Neutrino Signal of Electron-Capture Supernovae from Core Collapse to Cooling. *Physical Review Letters*, 104(25):251101, June 2010.

[56] R. A. Hulse and J. H. Taylor. Discovery of a pulsar in a binary system. *The Astrophysical Journal Letters*, 195:L51–L53, January 1975.

[57] N. Itoh, H. Hayashi, A. Nishikawa, and Y. Kohyama. Neutrino Energy Loss in Stellar Interiors. VII. Pair, Photo-, Plasma, Bremsstrahlung, and Recombination Neutrino Processes. *ApJS*, 102:411, February 1996.

[58] H.-T. Janka. Implications of detailed neutrino transport for the heating by neutrino-antineutrino annihilation in supernova explosions. *Astronomy and Astrophysics*, 244:378–382, April 1991.

[59] H.-T. Janka. Conditions for shock revival by neutrino heating in core-collapse supernovae. *Astronomy and Astrophysics*, 368:527–560, March 2001.

[60] H.-T. Janka, K. Langanke, A. Marek, G. Martínez-Pinedo, and B. Müller. Theory of core-collapse supernovae. *Physics Reports*, 442:38–74, April 2007.

[61] H.-T. Janka and E. Mueller. Neutrino heating, convection, and the mechanism of Type-II supernova explosions. *Astronomy and Astrophysics*, 306:167, February 1996.

[62] R. Kaeppeli, S. C. Whitehouse, S. Scheidegger, U. -. Pen, and M. Liebendoerfer. FISH: A 3D parallel MHD code for astrophysical applications. *ArXiv e-prints 0910.2854*, October 2009.

[63] R. Käppeli, S. C. Whitehouse, S. Scheidegger, U.-L. Pen, and M. Liebendörfer. FISH: A Three-dimensional Parallel Magnetohydrodynamics Code for Astrophysical Applications. *ApJS*, 195:20, August 2011.

[64] W. Keil, H.-T. Janka, and E. Mueller. Ledoux Convection in Protoneutron Stars—A Clue to Supernova Nucleosynthesis? *The Astrophysical Journal Letters*, 473:L111, December 1996.

[65] R. W. Klebesadel, I. B. Strong, and R. A. Olson. Observations of Gamma-Ray Bursts of Cosmic Origin. *The Astrophysical Journal Letters*, 182:L85+, June 1973.

[66] O. Korobkin, S. Rosswog, A. Arcones, and C. Winteler. On the astrophysical robustness of neutron star merger r-process. *ArXiv e-prints*, June 2012.

[67] K. Kotake, K. Sato, and K. Takahashi. Explosion mechanism, neutrino burst and gravitational wave in core-collapse supernovae. *Reports on Progress in Physics*, 69:971–1143, April 2006.

[68] C. Kouveliotou, S. Dieters, T. Strohmayer, J. van Paradijs, G. J. Fishman, C. A. Meegan, K. Hurley, J. Kommers, I. Smith, D. Frail, and T. Murakami. An X-ray pulsar with a superstrong magnetic field in the soft γ-ray repeater SGR1806 - 20. *Nature*, 393:235–237, May 1998.

[69] C. Kouveliotou, C. A. Meegan, G. J. Fishman, N. P. Bhat, M. S. Briggs, T. M. Koshut, W. S. Paciesas, and G. N. Pendleton. Identification of two classes of gamma-ray bursts. *The Astrophysical Journal Letters*, 413:L101–L104, August 1993.

[70] T. Kuroda, K. Kotake, and T. Takiwaki. Fully General Relativistic Simulations of Core-collapse Supernovae with an Approximate Neutrino Transport. *ApJ*, 755:11, August 2012.

[71] J. M. Lattimer and F. Douglas Swesty. A generalized equation of state for hot, dense matter. *Nuclear Physics A*, 535:331–376, December 1991.

[72] J. M. Lattimer, F. Mackie, D. G. Ravenhall, and D. N. Schramm. The Decompression of Cold Neutron Star Matter. *ApJ*, 213:225, 1977.

[73] J. M. Lattimer and M. Prakash. Neutron star observations: Prognosis for equation of state constraints. *Physics Reports*, 442:109–165, April 2007.

[74] J. M. Lattimer and M. Prakash. What a Two Solar Mass Neutron Star Really Means. *ArXiv e-prints*, December 2010.

[75] J. M. Lattimer and D. N. Schramm. Black-hole-neutron-star collisions. *The Astrophysical Journal Letters*, 192:L145–L147, September 1974.

[76] J. M. Lattimer and D. N. Schramm. The Tidal Disruption of Neutron Stars by Black Holes in Close Binaries. *ApJ*, 210:549, 1976.

[77] J. M. LeBlanc and J. R. Wilson. A Numerical Example of the Collapse of a Rotating Magnetized Star. *ApJ*, 161:541–+, August 1970.

[78] W. H. Lee, E. Ramirez-Ruiz, and D. López-Cámara. Phase Transitions and He-Synthesis-Driven Winds in Neutrino Cooled Accretion Disks: Prospects for Late Flares in Short Gamma-Ray Bursts. *ApJL*, 699:L93–L96, July 2009.

[79] E. J. Lentz, A. Mezzacappa, O. E. Bronson Messer, M. Liebendörfer, W. R. Hix, and S. W. Bruenn. On the Requirements for Realistic Modeling of Neutrino Transport in Simulations of Core-collapse Supernovae. *ApJ*, 747:73, March 2012.

[80] C. D. Levermore and G. C. Pomraning. A flux-limited diffusion theory. *ApJ*, 248:321–334, August 1981.

[81] M. Liebendörfer. A Simple Parameterization of the Consequences of Deleptonization for Simulations of Stellar Core Collapse. *ApJ*, 633:1042–1051, November 2005.

[82] M. Liebendörfer, T. Fischer, M. Hempel, R. Käppeli, G. Pagliara, A. Perego, I. Sagert, J. Schaffner-Bielich, S. Scheidegger, F. Thielemann, and S. C. Whitehouse. Neutrino Radiation-Hydrodynamics: General Relativistic versus Multidimensional Supernova Simulations. *Progress of Theoretical Physics Supplement*, 186:87–92, 2010.

[83] M. Liebendörfer and M. J. Gander. Supernova - productive 3d models of stellar explosions.

[84] M. Liebendörfer, O. E. B. Messer, A. Mezzacappa, S. W. Bruenn, C. Y. Cardall, and F.-K. Thielemann. A Finite Difference Representation of Neutrino Radiation Hydrodynamics in Spherically Symmetric General Relativistic Spacetime. 150:263–316, January 2004.

[85] M. Liebendörfer, A. Mezzacappa, F.-K. Thielemann, O. E. B. Messer, W. R. Hix, and S. W. Bruenn. Probing the gravitational well: No supernova explosion in spherical symmetry with general relativistic boltzmann neutrino transport. 63, 2001.

[86] M. Liebendörfer, M. Rampp, H.-T. Janka, and A. Mezzacappa. Supernova Simulations with Boltzmann Neutrino Transport: A Comparison of Methods. *ApJ*, 620:840–860, February 2005.

[87] M. Liebendörfer, S. Rosswog, and F.-K. Thielemann. An Adaptive Grid, Implicit Code for Spherically Symmetric, General Relativistic Hydrodynamics in Comoving Coordinates. *ApJS*, 141:229–246, July 2002.

[88] M. Liebendörfer, S. C. Whitehouse, and T. Fischer. The Isotropic Diffusion Source Approximation for Supernova Neutrino Transport. *ApJ*, 698:1174–1190, June 2009.

[89] A. Marek, H. Dimmelmeier, H.-T. Janka, E. Müller, and R. Buras. Exploring the relativistic regime with Newtonian hydrodynamics: an improved effective gravitational potential for supernova simulations. *Astronomy and Astrophysics*, 445:273–289, January 2006.

[90] G. C. McLaughlin and R. Surman. Prospects for obtaining an r process from Gamma Ray Burst Disk Winds. *Nuclear Physics A*, 758:189–196, July 2005.

[91] D. L. Meier, R. I. Epstein, W. D. Arnett, and D. N. Schramm. Magnetohydrodynamic phenomena in collapsing stellar cores. *ApJ*, 204:869–878, March 1976.

[92] O. E. B. Messer, S. W. Bruenn, J. M. Blondin, W. R. Hix, and A. Mezzacappa. Multidimensional, multiphysics simulations of core-collapse supernovae. *Journal of Physics Conference Series*, 125(1):012010–+, July 2008.

[93] P. Mészáros. Gamma-ray bursts. *Reports on Progress in Physics*, 69:2259–2321, August 2006.

[94] B. D. Metzger, A. Arcones, E. Quataert, and G. Martínez-Pinedo. The effects of r-process heating on fallback accretion in compact object mergers. *MNRAS*, 402:2771–2777, March 2010.

[95] B. D. Metzger, A. L. Piro, and E. Quataert. Time-dependent models of accretion discs formed from compact object mergers. *MNRAS*, 390:781–797, October 2008.

[96] B. S. Meyer. Decompression of initially cold Neutron Star Matter: A Mechanism for the r-Process. *ApJ*, 343:254, 1989.

[97] B. S. Meyer and J. S. Brown. Survey of r-Process Models. *ApJS*, 112:199, September 1997.

[98] A. Mezzacappa and S. W. Bruenn. A numerical method for solving the neutrino Boltzmann equation coupled to spherically symmetric stellar core collapse. *ApJ*, 405:669–684, March 1993.

[99] A. Mezzacappa and S. W. Bruenn. Stellar core collapse - A Boltzmann treatment of neutrino-electron scattering. 410:740–760, June 1993.

[100] A. Mezzacappa, A. C. Calder, S. W. Bruenn, J. M. Blondin, M. W. Guidry, M. R. Strayer, and A. S. Umar. An Investigation of Neutrino-driven Convection and the Core Collapse Supernova Mechanism Using Multigroup Neutrino Transport. *ApJ*, 495:911, March 1998.

[101] A. Mezzacappa, A. C. Calder, S. W. Bruenn, J. M. Blondin, M. W. Guidry, M. R. Strayer, and A. S. Umar. The Interplay between Proto–Neutron Star Convection and Neutrino Transport in Core-Collapse Supernovae. *ApJ*, 493:848, January 1998.

[102] A. Mezzacappa and O. E. B. Messer. Neutrino transport in core collapse supernovae. *Journal of Computational and Applied Mathematics*, 109:281–319, September 1999.

[103] S. G. Moiseenko and G. S. Bisnovatyi-Kogan. Outflows from Magnetorotational Supernovae. *International Journal of Modern Physics D*, 17:1411–1417, 2008.

[104] J. J. Monaghan. SPH without a Tensile Instability. *Journal of Computational Physics*, 159:290–311, April 2000.

[105] J. J. Monaghan. Smoothed particle hydrodynamics. *Reports on Progress in Physics*, 68:1703–1759, August 2005.

[106] E. Mueller and W. Hillebrandt. A magnetohydrodynamical supernova model. *Astronomy and Astrophysics*, 80:147–154, December 1979.

[107] B. Müller, H.-T. Janka, and H. Dimmelmeier. A New Multi-dimensional General Relativistic Neutrino Hydrodynamic Code for Core-collapse Supernovae. I. Method and Code Tests in Spherical Symmetry. *ApJS*, 189:104–133, July 2010.

[108] E. Müller, H.-T. Janka, and A. Wongwathanarat. Parametrized 3D models of neutrino-driven supernova explosions. Neutrino emission asymmetries and gravitational-wave signals. *Astronomy and Astrophysics*, 537:A63, January 2012.

[109] T. Nakamura and K. Oohara. Gravitational Radiation from Coalescing Binary Neutron Stars. IV —Tidal Disruption—. *Progress of Theoretical Physics*, 86:73–88, July 1991.

[110] N. Nishimura, T. Fischer, F.-K. Thielemann, C. Fröhlich, M. Hempel, R. Käppeli, G. Martínez-Pinedo, T. Rauscher, I. Sagert, and C. Winteler. Nucleosynthesis in Core-collapse Supernova Explosions Triggered by a Quark-Hadron Phase Transition. *ApJ*, 758:9, October 2012.

[111] S. Nishimura, K. Kotake, M.-a. Hashimoto, S. Yamada, N. Nishimura, S. Fujimoto, and K. Sato. r-Process Nucleosynthesis in Magnetohydrodynamic Jet Explosions of Core-Collapse Supernovae. *ApJ*, 642:410–419, May 2006.

[112] J. Nordhaus, A. Burrows, A. Almgren, and J. Bell. Dimension as a Key to the Neutrino Mechanism of Core-collapse Supernova Explosions. 720:694–703, September 2010.

[113] M. Obergaulinger, P. Cerdá-Durán, E. Müller, and M. A. Aloy. Semi-global simulations of the magneto-rotational instability in core collapse supernovae. *Astronomy and Astrophysics*, 498:241–271, April 2009.

[114] E. O'Connor and C. D. Ott. Black Hole Formation in Failing Core-Collapse Supernovae. *ApJ*, 730:70, April 2011.

[115] C. D. Ott, E. Abdikamalov, P. Moesta, R. Haas, S. Drasco, E. O'Connor, C. Reisswig, C. Meakin, and E. Schnetter. General-Relativistic Simulations of Three-Dimensional Core-Collapse Supernovae. *ArXiv e-prints*, October 2012.

[116] C. D. Ott, A. Burrows, L. Dessart, and E. Livne. Two-Dimensional Multiangle, Multigroup Neutrino Radiation-Hydrodynamic Simulations of Postbounce Supernova Cores. *ApJ*, 685:1069–1088, October 2008.

[117] B. Paczynski. Gamma-ray bursters at cosmological distances. *The Astrophysical Journal Letters*, 308:L43–L46, September 1986.

[118] I. V. Panov, E. Kolbe, B. Pfeiffer, T. Rauscher, K.-L. Kratz, and F.-K. Thielemann. Calculations of fission rates for r-process nucleosynthesis. *Nuclear Physics A*, 747:633–654, January 2005.

[119] I. V. Panov, I. Y. Korneev, T. Rauscher, G. Martínez-Pinedo, A. Kelić-Heil, N. T. Zinner, and F.-K. Thielemann. Neutron-induced astrophysical reaction rates for translead nuclei. *Astronomy and Astrophysics*, 513:A61, April 2010.

[120] W. H. Press, S. A. Teukolsky, W. T. Vetterling, and B. P. Flannery. *Numerical recipes in FORTRAN. The art of scientific computing*. 1992.

[121] D. J. Price and S. Rosswog. Producing Ultrastrong Magnetic Fields in Neutron Star Mergers. *Science*, 312:719–722, May 2006.

[122] J. Pruet, R. D. Hoffman, S. E. Woosley, H.-T. Janka, and R. Buras. Nucleosynthesis in Early Supernova Winds. II. The Role of Neutrinos. *ApJ*, 644:1028–1039, June 2006.

[123] Y.-Z. Qian and S. E. Woosley. Nucleosynthesis in Neutrino-driven Winds. I. The Physical Conditions. *ApJ*, 471:331, November 1996.

[124] G. G. Raffelt. *Stars as laboratories for fundamental physics : the astrophysics of neutrinos, axions, and other weakly interacting particles*. 1996.

[125] G. G. Raffelt. Mu- and Tau-Neutrino Spectra Formation in Supernovae. *ApJ*, 561:890–914, November 2001.

[126] T. Rauscher, A. Heger, R. D. Hoffman, and S. E. Woosley. Hydrostatic and explosive nucleosynthesis in massive stars using improved nuclear and stellar physics. *Nuclear Physics A*, 718:463–465, May 2003.

[127] T. Rauscher and F.-K. Thielemann. Astrophysical Reaction Rates From Statistical Model Calculations. *Atomic Data and Nuclear Data Tables*, 75:1–351, May 2000.

[128] L. Rezzolla, L. Baiotti, B. Giacomazzo, D. Link, and J. A. Font. Accurate evolutions of unequal-mass neutron-star binaries: properties of the torus and short GRB engines. *Classical and Quantum Gravity*, 27(11):114105–+, June 2010.

[129] L. Rezzolla, B. Giacomazzo, L. Baiotti, J. Granot, C. Kouveliotou, and M. A. Aloy. The Missing Link: Merging Neutron Stars Naturally Produce Jet-like Structures and Can Power Short Gamma-ray Bursts. *The Astrophysical Journal Letters*, 732:L6+, May 2011.

[130] L. F. Roberts, D. Kasen, W. H. Lee, and E. Ramirez-Ruiz. Electromagnetic Transients Powered by Nuclear Decay in the Tidal Tails of Coalescing Compact Binaries. *The Astrophysical Journal Letters*, 736:L21, July 2011.

[131] L. F. Roberts, S. Reddy, and G. Shen. Medium modification of the charged current neutrino opacity and its implications. *ArXiv e-prints*, May 2012.

[132] L. F. Roberts, S. E. Woosley, and R. D. Hoffman. Integrated Nucleosynthesis in Neutrino Driven Winds. *ApJ*, 722:954, April 2010.

[133] J. W. Rohlf. *Modern physics from [alpha] to Z*. 1994.

[134] S. Rosswog. Mergers of Neutron Star-Black Hole Binaries with Small Mass Ratios: Nucleosynthesis, Gamma-Ray Bursts, and Electromagnetic Transients. *ApJ*, 634:1202–1213, December 2005.

[135] S. Rosswog. Astrophysical smooth particle hydrodynamics. *New Astronomy Reviews*, 53:78–104, April 2009.

[136] S. Rosswog, M. B. Davies, F.-K. Thielemann, and T. Piran. Merging neutron stars: asymmetric systems. *Astronomy and Astrophysics*, 360:171–184, August 2000.

[137] S. Rosswog and M. Liebendörfer. High-resolution calculations of merging neutron stars - II. Neutrino emission. *MNRAS*, 342:673–689, July 2003.

[138] S. Rosswog, M. Liebendörfer, F.-K. Thielemann, M. B. Davies, W. Benz, and T. Piran. Mass ejection in neutron star mergers. *Astronomy and Astrophysics*, 341:499–526, January 1999.

[139] S. Rosswog, T. Piran, and E. Nakar. The multi-messenger picture of compact object encounters: binary mergers versus dynamical collisions. *ArXiv e-prints*, April 2012.

[140] S. Rosswog and D. Price. MAGMA: a three-dimensional, Lagrangian magnetohydrodynamics code for merger applications. *MNRAS*, 379:915–931, August 2007.

[141] S. Rosswog and D.J. Price. Magma: a magnetohydrodynamics code for merger applications. *MNRAS*, 379:915 – 931, 2007.

[142] S. Rosswog, E. Ramirez-Ruiz, and M. B. Davies. High-resolution calculations of merging neutron stars - III. Gamma-ray bursts. *MNRAS*, 345:1077–1090, November 2003.

[143] M. Ruffert, H.-T. Janka, and G. Schaefer. Coalescing neutron stars - a step towards physical models. I. Hydrodynamic evolution and gravitational-wave emission. *Astronomy and Astrophysics*, 311:532–566, July 1996.

[144] M. Ruffert, H.-T. Janka, K. Takahashi, and G. Schaefer. Coalescing neutron stars - a step towards physical models. II. Neutrino emission, neutron tori, and gamma-ray bursts. *Astronomy and Astrophysics*, 319:122–153, March 1997.

[145] I. Sagert, T. Fischer, M. Hempel, G. Pagliara, J. Schaffner-Bielich, A. Mezzacappa, F.-K. Thielemann, and M. Liebendörfer. Signals of the QCD Phase Transition in Core-Collapse Supernovae. *Physical Review Letters*, 102(8):081101–+, February 2009.

[146] L. Scheck, K. Kifonidis, H.-T. Janka, and E. Müller. Multidimensional supernova simulations with approximative neutrino transport. I. Neutron star kicks and the anisotropy of neutrino-driven explosions in two spatial dimensions. *Astronomy and Astrophysics*, 457:963–986, October 2006.

[147] S. Scheidegger, R. Käppeli, S. C. Whitehouse, T. Fischer, and M. Liebendörfer. The influence of model parameters on the prediction of gravitational wave signals from stellar core collapse. *Astronomy and Astrophysics*, 514:A51+, May 2010.

[148] F. A. Scott. Energy Spectrum of the Beta-Rays of Radium E. *Physical Review*, 48:391–395, September 1935.

[149] N. I. Shakura and R. A. Sunyaev. Black holes in binary systems. Observational appearance. *Astronomy and Astrophysics*, 24:337–355, 1973.

[150] S. L. Shapiro and S. A. Teukolsky. *Black Holes, White Dwarfs and Neutron Stars: The Physics of Compact Objects*. June 1986.

[151] H. Shen, H. Toki, K. Oyamatsu, and K. Sumiyoshi. Relativistic equation of state of nuclear matter for supernova and neutron star. *Nuclear Physics A*, 637:435–450, July 1998.

[152] M. Shibata and K. Taniguchi. Coalescence of Black Hole-Neutron Star Binaries. *Living Reviews in Relativity*, 14:6, August 2011.

[153] C. Sneden, J. J. Cowan, and R. Gallino. Neutron-Capture Elements in the Early Galaxy. *Annual Review of Astronomy and Astrophysics*, 46:241–288, September 2008.

[154] K. Sumiyoshi, S. Yamada, H. Suzuki, H. Shen, S. Chiba, and H. Toki. Postbounce Evolution of Core-Collapse Supernovae: Long-Term Effects of the Equation of State. *ApJ*, 629:922–932, August 2005.

[155] R. Surman, G. C. McLaughlin, and W. R. Hix. Nucleosynthesis in the Outflow from Gamma-Ray Burst Accretion Disks. *ApJ*, 643:1057–1064, June 2006.

[156] R. Surman, G. C. McLaughlin, M. Ruffert, H.-T. Janka, and W. R. Hix. r-Process Nucleosynthesis in Hot Accretion Disk Flows from Black Hole-Neutron Star Mergers. *The Astrophysical Journal Letters*, 679:L117–L120, June 2008.

[157] E. M. D. Symbalisty and D. N. Schramm. *Astrophys. Lett.*, 22:143, 1982.

[158] T. Takiwaki, K. Kotake, and K. Sato. Special Relativistic Simulations of Magnetically Dominated Jets in Collapsing Massive Stars. *ApJ*, 691:1360–1379, February 2009.

[159] J. H. Taylor, L. A. Fowler, and P. M. McCulloch. Measurements of general relativistic effects in the binary pulsar PSR 1913+16. *Nature*, 277:437–440, February 1979.

[160] F.-K. Thielemann, A. Arcones, R. Käppeli, M. Liebendörfer, T. Rauscher, C. Winteler, C. Fröhlich, I. Dillmann, T. Fischer, G. Martinez-Pinedo, K. Langanke, K. Farouqi, K.-L. Kratz, I. Panov, and I. K. Korneev. What are the astrophysical sites for the r-process and the production of heavy elements? *Progress in Particle and Nuclear Physics*, 66:346–353, April 2011.

[161] F.-K. Thielemann, M.-A. Hashimoto, and K. Nomoto. Explosive nucleosynthesis in SN 1987A. II - Composition, radioactivities, and the neutron star mass. *ApJ*, 349:222–240, January 1990.

[162] T. A. Thompson, A. Burrows, and J. E. Horvath. μ and τ neutrino thermalization and production in supernovae: Processes and time scales. *PhRvC*, 62(3):035802, September 2000.

[163] T. A. Thompson, A. Burrows, and B. S. Meyer. The Physics of Proto-Neutron Star Winds: Implications for r-Process Nucleosynthesis. *ApJ*, 562:887–908, December 2001.

[164] T. A. Thompson, A. Burrows, and P. A. Pinto. Shock Breakout in Core-Collapse Supernovae and Its Neutrino Signature. *ApJ*, 592:434–456, July 2003.

[165] F. X. Timmes and F. D. Swesty. The Accuracy, Consistency, and Speed of an Electron-Positron Equation of State Based on Table Interpolation of the Helmholtz Free Energy. *The Astrophysical Journal Supplement Series*, 126:501–516, February 2000.

[166] D. L. Tubbs and D. N. Schramm. Neutrino Opacities at High Temperatures and Densities. *ApJ*, 201:467–488, October 1975.

[167] M. Ugliano, H.-T. Janka, A. Marek, and A. Arcones. Progenitor-explosion Connection and Remnant Birth Masses for Neutrino-driven Supernovae of Iron-core Progenitors. *ApJ*, 757:69, September 2012.

[168] E. P. J. van den Heuvel. The Formation and Evolution of Relativistic Binaries. In M. Colpi, P. Casella, V. Gorini, U. Moschella, and A. Possenti, editors, *Astrophysics and Space Science Library*, volume 359 of *Astrophysics and Space Science Library*, page 125, 2009.

[169] S. Wanajo. The r-Process in Proto-Neutron Star Winds with Anisotropic Neutrino Emission. *The Astrophysical Journal Letters*, 650:L79–L82, October 2006.

[170] S. Wanajo and H.-T. Janka. The r-process in the Neutrino-driven Wind from a Black-hole Torus. *ApJ*, 746:180, February 2012.

[171] S. Wanajo, H.-T. Janka, and B. Müller. Electron-capture Supernovae as The Origin of Elements Beyond Iron. *The Astrophysical Journal Letters*, 726:L15, January 2011.

[172] J. M. Weisberg, D. J. Nice, and J. H. Taylor. Timing Measurements of the Relativistic Binary Pulsar PSR B1913+16. *ApJ*, 722:1030–1034, October 2010.

[173] J. M. Weisberg and J. H. Taylor. The Relativistic Binary Pulsar B1913+16: Thirty Years of Observations and Analysis. In F. A. Rasio and I. H. Stairs, editors, *Binary Radio Pulsars*, volume 328 of *Astronomical Society of the Pacific Conference Series*, page 25, July 2005.

[174] S. Whitehouse and M. Liebendörfer. Neutrino transport in 3D simulations of core-collapse supernovae. In *Nuclei in the Cosmos (NIC X)*, 2008.

[175] S. C. Whitehouse and M. Liebendörfer. A new approach to neutrino transport in 3d simulations of core-collapse supernovae. *PoS(NIC X)243*, 2008.

[176] C. Winteler, R. Käppeli, A. Perego, A. Arcones, N. Vasset, N. Nishimura, M. Liebendörfer, and F.-K. Thielemann. Magnetorotationally Driven Supernovae as the Origin of Early Galaxy r-process Elements? *The Astrophysical Journal Letters*, 750:L22, May 2012.

[177] S. E. Woosley and J. S. Bloom. The Supernova Gamma-Ray Burst Connection. *Annual Review of Astronomy and Astrophysics*, 44:507–556, September 2006.

[178] S. E. Woosley, A. Heger, and T. A. Weaver. The evolution and explosion of massive stars. *Reviews of Modern Physics*, 74:1015–1071, November 2002.

[179] S. E. Woosley and T. A. Weaver. The Evolution and Explosion of Massive Stars. II. Explosive Hydrodynamics and Nucleosynthesis. *ApJS*, 101:181, November 1995.

[180] W. Zhang, S. E. Woosley, and A. Heger. Fallback and Black Hole Production in Massive Stars. *ApJ*, 679:639–654, May 2008.